UNIVERSITÉ D'ORLÉANS
POLITECNICO DI MILANO

ÉCOLE DOCTORALE SCIENCES ET TECHNOLOGIES
DOTTORATO IN ENERGETICA

Institut de Combustion, Aérothermique, Réactivité et Environnement

THÈSE présentée par :

Silvana DE IULIIS

soutenue le : *16 décembre 2009*

pour obtenir le grade de : **Docteur de l'université d'Orléans**

Discipline : cinétique chimie appliquée

Etude de la vitesse de formation des suies à partir de l'éthylène en présence d'hydrogène par les méthodes du tube à choc et du brûleur au moyen de différentes techniques optiques

---

THÈSE dirigée par :
Claude-Etienne PAILLARD   Professeur émérite –Université d'Orléans
Aldo COGHE   Professeur – Université de Milan

RAPPORTEURS :
Jean-François MULLER   Professeur émérite, Université de Metz
Jacques VANDOOREN   Professeur émérite, Université Catholique de Louvain,

_____

JURY :
Jean-François MULLER   Professeur émérite, Université de Metz
Jacques VANDOOREN   Professeur émérite, UCL, B, Président du Jury
Aldo COGHE   Professeur –Institut Polytechnique de Milan, Italie
Robert George SANTORO   Dir. of the Propulsion Eng. Res. Center, Penn State Univ., USA
Giorgio ZIZAK   Directeur de recherche, CNR-IENI, Milan, Italie
Nabiha CHAUMEIX   Directeur de recherche, ICARE,CNRS, Orléans
Claude-Etienne PAILLARD   Professeur émérite – ICARE, Université d'Orléans

POLITECNICO DI MILANO

UNIVERSITÉ D'ORLÉANS

UNIVERSITÉ
FRANCO
ITALIENNE

Joint Doctoral Program in Energy – 22nd Cycle

A Shock Tube and Burner Study on Soot Growth Rate from Ethylene in presence of Hydrogen by different Optical Diagnostics

Supervisors:

Prof. Aldo Coghe, Politecnico di Milano

Prof. Claude-Etienne Paillard, Université de Orléans

Head of the Doctoral program in Energy:

Prof. Adriano Muzzio, Politecnico di Milano

Silvana De Iuliis

2010

To Vincenzo and Renato,

with gratefulness and love

Acknowledgments

I would like to express my sincere gratitude to my supervisors, Prof. Aldo Coghe (Politecnico di Milano) and Prof. Paillard (Université d'Orléans) for their constant support, fruitful discussion and friendship during the entire period of the thesis.

I am very grateful to my tutor dr Nabiha Chaumeix (researcher at CNRS-CARE, Institute de Combustion, Aerothermique, Reactivite et Environment in Orleans) for her never-ending enthusiasm, positive approach to scientific problems and sincere and warm friendship.

I would like to thank dr Giorgio Zizak (Research Director, National Research Council, Istituto per l'Energetica e le Interfasi in Milano) for his continuous support and help in any occasion since the beginning of my scientific career.

A special thanks to dr Francesco Cignoli and dr Silvia Maffi (researchers at CNR-IENI in Milano) for their valuable advice and friendly help.

I am very grateful to dr Mamhoud Idir (Engineer at CNRS-ICARE in Orleans) for the constant scientific and technical support.

I would extend my warmest thanks to all people in the labs of CNR-IENI in Milano and CNRS-ICARE in Orleans for their unconditioned help. I was very lucky to meet them and to work with them.

My sincere and special gratitude goes to my parents for their continuous support.

Silvana

Table of contents

Etude de la vitesse de formation des suies à partir de l'éthylène en présence d'hydrogène par les méthodes du tube à choc et du brûleur au moyen de différentes techniques optiques

Résumé

Cette thèse a pour objet d'améliorer la connaissance du mécanisme de formation de suie. Deux méthodes ont été utilisées pour produire des particules de suie dans des conditions contrôlées : le brûleur à flamme plat où les particules se forment par combustion de mélanges d'éthylène/air riches et le tube à choc dans lequel la suie est produite par pyrolyse de C_2H_4 à haute pression (5 bar) et dans un large domaine de température (1850-2100 K). Ces deux systèmes ont été équipés avec un dispositif original de diffusion laser à trois angles couplé à l'extinction laser pour suivre la croissance de particules, identifier les différentes étapes de leur mécanisme de formation et en déduire l'évolution de la fraction volumique des suies, leur rendement, leur structure et leur morphologie. Dans la flamme, l'addition de H_2 entraîne une réduction globale de la concentration des suies, de leur diamètre moyen des particules et leurs agglomérats, de la densité en nombre de particules. Dans le tube à choc, on n'observe pas de dépendance significative du délai d'induction à la formation des particules par addition de H_2. La courbe de rendement en suie en fonction de la température présente la même forme avec et sans hydrogène mais le rendement maximal est fortement abaissé en présence d'hydrogène pour une concentration initiale fixée en atomes de carbone. Le rôle de l'hydrogène sur la croissance des particules et les caractéristiques des suies est discuté en comparant les resultats obtenus dans le cas de flamme de premelange et derrière l'onde de choc réfléchie respectivement.

Mots clés: Formation des suies, Ethylène, Hydrogène, Diffusion laser à trios angles, Extinction laser.

A Shock Tube and Burner Study on Soot Growth Rate from Ethylene in Presence of Hydrogen by Different Optical Diagnostics

Abstract

The aim of this thesis was to improve the knowledge of the soot formation mechanism. Two methods have been used to produce soot particles in controlled conditions: flat flame burner where particles were formed by combustion of rich ethylene/air mixtures and shock tube in which soot was produced by C_2H_4 pyrolysis at high pressure (5 bar) and in a large range of temperature (1850-2100 K). Both systems have been equipped with a novel technique of scattering at three angles coupled with laser extinction device in order to follow particles growth, to identify different steps of their formation mechanism and to deduce soot volume fraction evolution, soot yield, structure and morphology. In the flame, an overall reduction of soot concentration, mean volume diameter, particles number density was observed when hydrogen was added to combustible mixture. In shock tube, induction delay time of particle formation does not depend on H_2 addition. The typical curves of soot yield versus temperature present the same shape with and without H_2 ; the maximum yield occurs at the same temperature (near 2000 K) but the yield is strongly lower in presence of H_2 for a given C atom concentration. The role of hydrogen on particles growth rate and soot characteristics was discussed by comparing the results obtained respectively in the premixed flames and behind reflected shock waves.

Keywords : Soot formation, ethylene, hydrogen, laser extinction, laser scattering at three angles

Studio in un Tubo d'Urto e in un Bruciatore della crescita della Fuliggine da Etilene in presenza di Idrogeno per mezzo di diverse Tecniche Diagnostiche.

Riassunto

Scopo del presente lavoro di tesi è stato lo studio dei meccanismi di formazione della fuliggine, detta comunemente soot. Sono stati utilizzati due diversi metodi per produrre particelle di fuliggine in condizioni controllate: un bruciatore che da origine a fiamme dette "flat", caratterizzate da una distribuzione radiale uniforme di temperatura e di specie chimiche, alimentato da una miscela etilene/aria, e un tubo d'urto in cui la fuliggine è generata dalla pirolisi di etilene ad alta pressione (5 bar) e in un ampio intervallo di temperatura (1850-2100 K). In entrambi i sistemi una nuova tecnica diagnostica è stata applicata: essa si basa sull'accoppiamento di misure di scattering a tre angoli con misure di estinzione. In questa maniera è possibile seguire il processo di formazione della fuliggine e valutare i parametri caratteristici del soot, sia riguardo alla concentrazione che alla morfologia. In fiamma, l'aggiunta di idrogeno nella miscela combustibile determina una sostanziale riduzione della frazione volumetrica di fuliggine, della conversione in soot degli atomi di carbonio nella miscela iniziale, del diametro medio in volume, della densità numerica delle particelle primarie. Misure nel tubo d'urto hanno permesso di ottenere il seguente importante risultato: non c'è alcuna variazione del tempo di ritardo dell'induzione con l'aggiunta di idrogeno. Inoltre le corrispondenti curve tipiche del rendimento della fuliggine presentano la stessa struttura, il massimo allo stesso valore di temperatura (2000 K circa) e una significativa riduzione del rendimento con l'aggiunta di idrogeno. Il ruolo dell'idrogeno sulla crescita del particolato e i parametri caratteristici della fuliggine è stato discusso confrontando i risultati ottenuti rispettivamente nelle fiamme premiscelate e al di là dell'onda d'urto riflessa.

Parole chiave: Formazione della fuliggine, etilene, idrogeno, estinzione laser, scattering della radiazione laser a tre angoli.

INTRODUCTION

Recently major task of the combustion community has been the improvement of the combustion processes in order to preserve clean environment and to reduce energy consumption. To this aim, the study of pollutants formation derived from combustion, and in particular of soot particles, have gained increasing interest. Soot particles are the products of incomplete combustion processes and consequently are associated to a reduction in the combustion efficiency. In addition, due to the fact that they present, adsorbed on the surface, molecules as the polycyclic aromatic hydrocarbon, some of which are carcinogenic, they are dangerous for the human health and for the environment. For these reasons many efforts by the combustion community have been devoted, and still are, to the comprehension of the chemical and physical mechanisms describing soot formation, in dependence on the different parameters, as the fuel, the presence of air/oxygen, the temperature and the pressure and the design of the combustion apparatus.

Hydrogen has received increasing attention as a potential alternative for fuel-based power generation. Although the interest for hydrogen economy has lowered with respect to recent past years, its possible role as a clean and abundant energy carrier can not be neglected.

From the other side, many drawbacks (concerning production, distribution and storage) still prevent its extensive use in practical systems.

According to the Energy Information Administration, in 2005 85% of the primary energy production in the world came from burning fossil fuels.

Then, in order to cover the large gap between conventional fossil fuels and cleaner environment in an hydrogen society, blending hydrocarbons with hydrogen can represent a medium-term solution.

From a combustion point of view, hydrogen has many advantages compared with other hydrocarbon fuels. In fact, it presents a wide range of flammability limits, a low ignition energy, and low ignition temperature (750-800 K), an high energy mass density (1.2 *10 J/Kg). Then, its addition to hydrocarbon fuels can produce effects on chemical and physical mechanisms involved in combustion processes. These are not predictable in simple way, due to the non-linear nature of chemical kinetics.

Particularly interesting is the investigation of the role of hydrogen addition in such mixtures concerning the tendency of the fuel to produce soot. To this purpose, while some details on the general improvements of the combustion characteristics obtained with hydrogen addition have been observed and reported in the literature, very few works can be found concerning the influence on soot formation. The few papers, moreover, are restricted to a poor selection of experimental conditions.

Several projects are addressed to the characterization of the hybrid fuels. In this context, a new term was introduced, Hythane®, to indicate a blend of 20% hydrogen and 80% natural gas, already commercially available and distributed in the US. According to the company involved, this alternative fuel, used directly to fill vehicles, has been found to produce significantly lower emissions than diesel or natural gas. It is interesting to study more deeply such issue.

The aim of this thesis is the study of hybrid fuels in terms of their tendency to produce soot, and, in particular, the role of hydrogen in soot formation mechanisms once it is added to hydrocarbon fuels.

Soot formation mechanisms are different according to the device in which the investigation is carried out. Considering premixed conditions, like in laboratory premixed flames, soot is produced only in rich mixtures, with equivalence ratio greater than one. On the other hand, considering diesel engine, the fuel is introduced at liquid phase. Combustion

occurs around droplets, which are progressively vaporized in a high temperature medium. Soot is here formed essentially under near pyrolytic conditions.

To study soot formation in the case of premixed mixture combustion, in this work the investigation is performed with a McKenna, widely used by the Combustion community to produce a premixed flat flame. The study of soot formation in near-pyrolysis conditions is performed with the shock tube method. In both cases ethylene was the hydrocarbon chosen for the blending. The choice is due to the following reasons. To work with burners, the use of a gas results to be more suitable and simple to perform. Ethylene has been widely studied in flames, as reported in the literature. For comparison, in this work measurements in the shock tube were performed with the same fuel.

The investigation of soot formation can be experimentally performed by applying optical diagnostics techniques, which, being non-intrusive, allow to carry out in-situ measurements. In this work in order to characterize soot particles in terms of concentration, dimension and eventually structure, the scattering/extinction technique is employed. Such technique has been widely applied in laboratory flames, while very few works are reported in the literature on the application on shock tubes. In this last device, in fact, measurements are not straightforward, as the shock wave takes a short period of time and the observation interval lasts few milliseconds.

In order to develop the technique, first measurements were performed in the premixed flames. Here a new methodology is developed on the basis of the fractal theory to derive, coupling scattering measurements at three angles with extinction, soot parameters, such as the radius of gyration, primary particle diameter and soot yield.

The applicability of the scattering/extinction technique to the shock tubes was verified in a 38 mm i.d. shock tube. The technique was properly assessed both for the experimental part and for the processing procedure applied to retrieve soot parameters. The limitations of the technique are discussed.

The previously assessed technique was then applied to a 78 mm shock tube, best suited to study the influence of hydrogen addition on soot formation. Scattering measurements performed at three angles and global parameters, as soot yield and induction delay time, as well as soot structure characteristics, as soot diameter and aggregation, are obtained. The influence of hydrogen on these parameters are analyzed.

Moreover, considering the extinction technique, an analysis is performed, both in the flame and in the shock tube, on the influence of the wavelength of the used source on soot concentration measurements.

In brief the aim of the thesis can be summarize as follows:

- to develop a scattering/extinction technique to describe fractal-like soot structure in flames;
- to analyze the influence of the wavelength on extinction;
- to implement the scattering/extinction technique in the shock tube;
- to study the role of hydrogen addition on soot formation both in premixed and in pyrolysis conditions.

In the first Chapter, the theoretical background is outlined. Generally, the main characteristics of soot, the formation models and the apparatus used for the analysis are presented. The role of hydrogen is briefly considered on the general combustion performances. Concerning the diagnostics tools, it is described an overview of the techniques applied to study soot formation, while a deep presentation is given for the scattering/extinction technique as applied in this study.

In the second Chapter the two facilities are described: the burner bench and the shock tube. Details on the experimental equipments and the optical layout are given. In order to point out the experimental difficulties, the alignment procedure is shown, together with the calibration step needed to process the data. Finally, in both cases the experimental conditions chosen are presented.

The third Chapter is addressed to the measurements performed in the flame. The non-doped premixed flame and the one with hydrogen addition have been characterized as for the soot formation. Besides, the processing procedures applied to obtain the results concerning soot parameters are presented.

In the fourth Chapter are reported measurements performed in the shock tube in a way similar to the one for flames. The processing procedure developed and applied to the shock tube is deeply discussed. Then, we present the results obtained and the influence of hydrogen both on global soot parameters and on soot structure.

The work is a co-tutele thesis between the Universitè d'Orleans and Politecnico di Milano (Department of Energy). The research activity was made in the frame of a collaboration between two laboratories: IENI-CNR (Istituto per l'Energetica e le

Interfasi)/Politecnico di Milano and ICARE-CNRS (Institute de Combustion, Aerothermique, Reactivite et anveronemnt) in Orleans.

In Milano investigation on premixed flames has been performed. The CNR-IENI laboratory is well known to have gained over many years experience on the development of diagnostics techniques applied on combustion systems.

The shock tube investigation has been carried out in Orleans. The French laboratory boasts great knowledge and expertise recognized by the scientific community on chemical kinetics.

I. State of knowledge on Soot Formation Mechanisms

INTRODUCTION

In this chapter a general background on the main topics of this work is presented.

In the first part, an overview of the particulate matter delivered in the atmosphere and, in particular, of the combustion-generated nanoparticles is given, taking into account the impact on the environment and on the human health. The main characteristics of the formation and growth models of soot particulate are described as well as the main laboratory reactors used to perform such investigations. Then, the influence of additives like hydrogen on the combustion performance and, in particular, on soot formation, is presented by considering the work reported in the literature on this subject.

The second paragraph is focused on the description of the diagnostics techniques developed to study soot formation in different set-ups. The optical techniques, being non-intrusive, allow such investigation in an hostile environment as the combustion one. The main physical characteristics and the related basic theory of these techniques are given. Moreover, considering their main features, a comparison of the different diagnostics is presented, trying

to point out the need to use one instead of the other technique in relation to the particular conditions under study.

In the third paragraph, a wide dissertation is given on the scattering/extinction technique, which is the diagnostic applied in this work. Besides the classical method and further improvements in the case when the polydispersity of the primary particles diameter cannot be considered negligible, the fractal-like approach is taken into account.

1   Particulate matter and soot

As it will be illustrated below, soot is a major source of atmospheric particulate. Nevertheless, the mechanisms involved in soot formation are quite peculiar with respect to other sources. Then, in this introduction the two will be discussed separately.

1.1   Particulate matter - classification

The term "particulate matter", PM or also known as particle pollutants, is used to describe a complex mixture of extremely small particles and liquid droplets. It is made up of a number of components, including acids (such as nitrates and sulfates), organic chemicals, metals and soil or dust particles. The typical dimension is in the range from micron to about 20 nm, which corresponds to the molecular size. For that, a full description of atmospheric particles requires specification of concentration, size, chemical composition, phase and morphology.

According to the U.S. Environmental Protection Agency (EPA) [1] atmospheric particles can be classified as follows:

- Ultrafine: particles with an aerodynamic diameter lower than 0.1 μm
- Fine: particles with an aerodynamic diameter in the range 0.1 – 2.5 μm such as those found in smoke and haze
- Coarse: particles with an aerodynamic diameter in the range 2.5 – 10 μm, such as those found near roadways and dusty industries
- Supercoarse: particles with an aerodynamic diameter higher than 10 μm

A further classification of particles performed by EPA is given as:

- Total Suspended Particulate Matter (TSP): particles ranging in size from 0.1 μm to about 30 μm
- PM10: particulate matter with an aerodynamic diameter less than or equal to 10 μm
- PM2.5: particulate matter with an aerodynamic diameter less than or equal to 2.5 μm
- Nanoparticles: particles with diameters below 50 nm

According to this classification, particulate matter is regulated and tested. Since PM indicates only mass concentrations, there are considerations for further parameters, such as particle number and toxicity, which might be respected for future limit values (Nussbaumer et al. [2]).

Fig. I.1.1 displays a typical size distribution of atmospheric particulate matter that combines the two classification schemes discussed above.
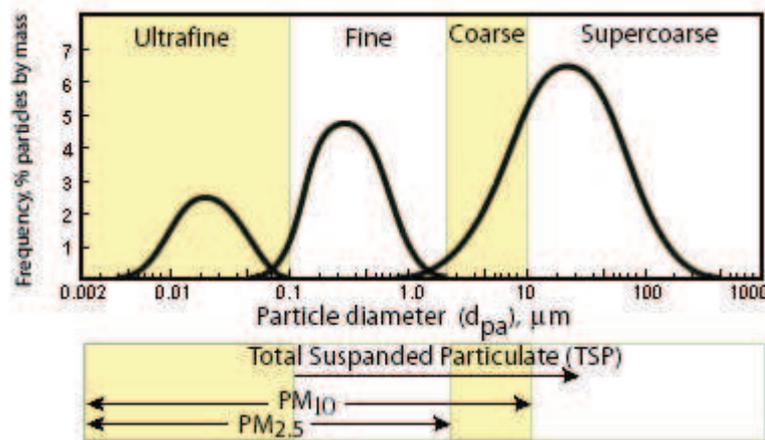
Fig. I.1.1: *Ambient Particulate Matter size distribution [1].*

The sources of atmospheric particles can be both natural and human. The major natural cause is represented by dust, volcanoes, and forest fires, while for human sources combustion processes are the main candidate. Typical examples are the burning of fuels in internal combustion engines, power plants, incineration plants and heating plants.

Some particles, known as primary particles, are directly emitted from a source to the atmosphere (primary emissions), such as construction sites, unpaved roads, fields, smokestacks or fires. In other cases gases are emitted and, in the atmosphere, complicated reactions of chemicals such as sulfur dioxides and nitrogen oxides take place, leading to the formation of further particles (secondary emissions). These last are responsible of the fine particle pollution. In both cases, combustion processes are heavily involved: e.g. diesel engines and biomass combustion for primary emissions, and stationary combustion systems (energy, industry, domestic fuel) for secondary emissions.

In the ambient air, as a result, a mixture of directly emitted primary aerosols and secondary aerosols formed in the atmosphere is present.

The interest of the scientific community in particulate matter is essentially due to environmental aspects and adverse effects on human health. In fact, in the environment, climate can be affected. By scattering or absorbing solar radiation, a change in cloud properties can result, which causes rain or snow fall. Over the past decades different studies suggest that by increasing the air pollution in the urban area, an increasing of respiratory and cardiovascular mortality is observed (Chalupa et al. [3]). In particular, ultrafine particles are dangerous as they present a higher predicted pulmonary deposition, greater potential to induce pulmonary inflammation, large surface area, and enhanced oxidant capacity.

As already observed, combustion of fossil fuels involved in transport, home appliances and power generation is considered as a major source of production of airborne species responsible of atmosphere pollution. This is particularly important in those zones of the earth with high population and industrialization density. In fact, according to the Energy Information Administration (IEA), in 2005, 85% of the primary energy production in the world came from burning fossil fuels. The other sources are hydroelectric (3%), nuclear (6%) and others: geothermal, solar and wind (IEA [4]).

As pollution has been becoming an increasingly serious problem in the last 20 years, all industrialized countries have introduced stringent regulations about the limitation of particulate emission by major combustion systems. As already observed, the regulations have been applied to nanoparticles mass and no indication on the total number of particles is given. Moreover, after-treatment devices, utilized in order to reduce the particles mass concentration at diesel vehicles exhaust, with a significant reduction in particles size, cause the emission of higher numbers of nanoparticles. For that, the future regulations, imposed and defined by the EC, will take into account this aspect.

1.2   Combustion-generated nanoparticles

In ideal conditions, combustion of hydrocarbons leads to the formation of carbon dioxide and water. Unfortunately in any practical system, combustion is not complete and other undesired species are formed and emitted, depending on combustion conditions. In this case, an overall reduction of the efficiency of the combustion process is involved.

Diesel particulate matter is a complex aggregate of solid and liquid material. It is mainly composed by carbonaceous particles generated in the engine cylinder during the combustion. The primary carbon particles form larger agglomerates and they combine with other

components of diesel exhaust, both organic and inorganic. Generally, the diesel PM is divided into three basic fractions:

- Solids - dry carbon particles, commonly known as soot;
- SOF - Soluble Organic Fraction; heavy hydrocarbons adsorbed and condensed on the carbon particles;
- SO_4 - sulphate fraction, hydrated sulphuric acid.

The actual composition of diesel PM depends on the particular engine and its load and speed conditions. "Wet" particulates can contain up to 60% of the hydrocarbon fraction (SOF), while "dry" particulates consists mostly of dry carbon. The amount of sulphates is directly related to the sulphur contents of the fuel (Kittelson et al. [5]). A small amount of inorganic ash is composed by metal compounds in the fuel (if metallic additives are present) and lubrication (Kittelson [6], Jung [7]).

Concerning soot particles, even if pure soot is physiologically inert, it presents toxic characteristics due to the presence on it of aromatics, some of which carcinogenic and with mutagenic properties. Aromatics molecules, besides being incorporated into soot, are emitted in the environment both free or condensed on the soot surface. Moreover, due to the particulate dimension, soot particles can be easily inhaled and deposited on lungs, resulting in respiratory problems.

The effort of the combustion community is the improvement of the combustion processes in all practical systems: diesel and gasoline engines, gas turbines, burners for domestic or industrial boilers. Due to the complexity of the systems, efforts are still required for a detailed understanding of the chemical and physical processes responsible for aerosol formation, at the basis of the conversion of hydrocarbon molecules, generally containing only few carbon atoms, to agglomerate of soot particle.

1.3   Main Soot Characteristics

As observed by different authors as Wander Wal [8], Xu et al. [9] and Koylu et al. [10], transmitted electron microscope (TEM) analysis allows to gain information about soot structure, reported in Fig. I.1.2.
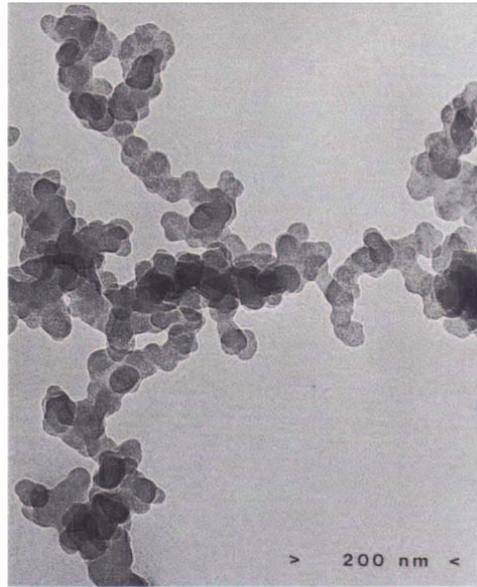
Fig. I.1.2: *Typical picture of soot structure obtained with TEM analysis [this work].*

Soot is composed of aggregates of hundreds or more primary spherules, known as primary particles, nearly spherical with a diameter in the range of 5-60 nm. The aggregates can be more or less complex, from straight or branched chains, to fractal-like structures. Soot particles contain, besides carbon atoms, hydrogen in an amount which depends on the particles residence time in the combustion environment. Usually the terms young and mature soot are used, the last exhibiting lower hydrogen amount. Typically, the C/H ratio is in the order of 8, much larger than that of parent fuel molecules. The average density of soot particles is about 1.8 g/cm^3. The parameters used to characterize soot particles are the following:

- The soot volume fraction, f_v, which represents the volume occupied by soot particles in a unit volume (cm^3/cm^3)
- The total number of particles per unit volume, N_p, expressed in #/cm^{-3}
- The mean diameter of the soot primary particle.

1.4   Soot formation and growth modelling

Soot formation is a complex process, occurring through many chemical and physical steps. Although efforts are spent to understand these processes (Lahaye et al.[11], Wagner

[12], Haynes et al. [13], Smith [14], Bockhorn [15]), much work is still needed to gain a complete picture. Generally a detailed kinetic model of soot formation contains two parts: a gas-phase chemistry and a solid-phase one. In Fig. I.1.3, a schematic picture of soot modeling is shown as proposed by Lighty et al. [16].
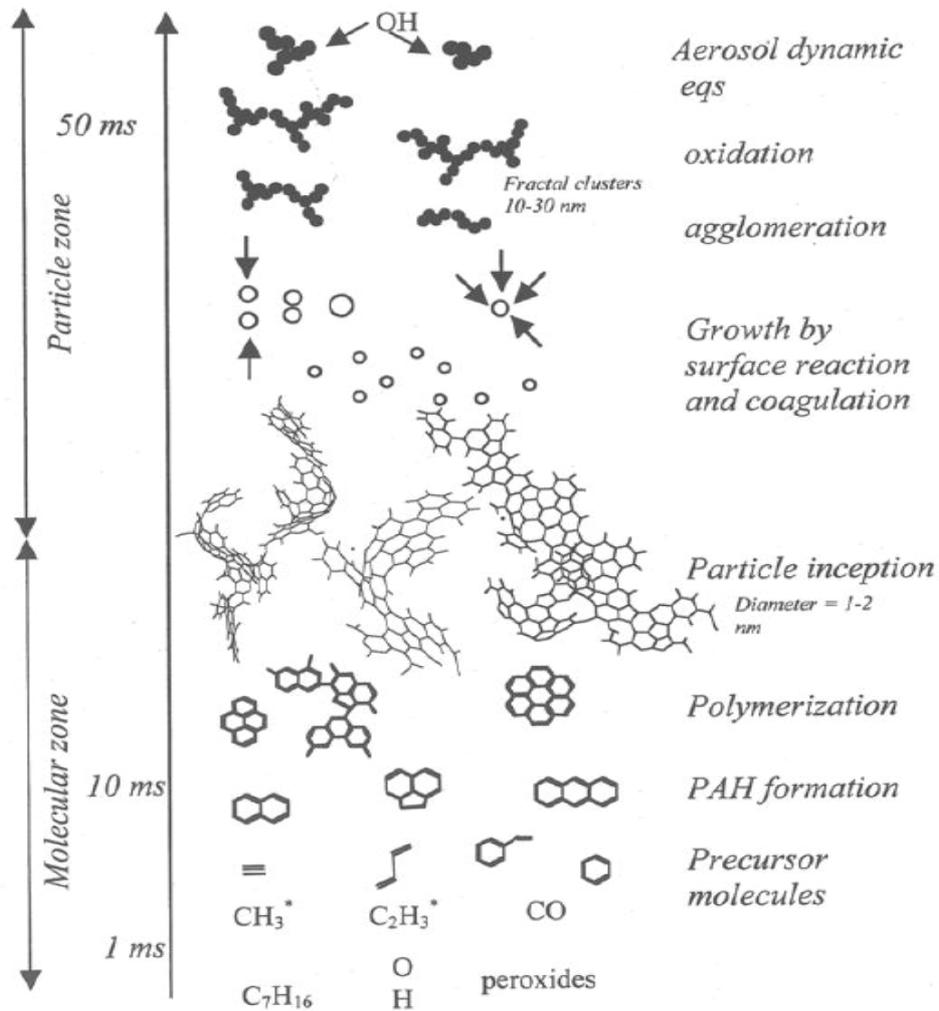
Fig. I.1.3: *Schematic modeling of soot formation processes [16].*

According to a review article on chemical reaction pathways by Richter and Howard [17], the main steps can be summarized as follows:

Gas-phase
- Pyrolysis of fuel molecules
- Formation of aromatic structures and heavy hydrocarbons

$$Solid\ phase \begin{cases} \text{- Nucleation and growth reactions} \\ \text{- Surface growth reactions} \\ \text{- Coagulation} \\ \text{- Agglomeration} \end{cases}$$

1.4.1 Gas phase

In the gas phase, fuel pyrolysis and formation of the precursors take place. Many suggestions have been made regarding the nature of possible soot precursors, and both experimental and modeling observations allow to infer that polycyclic aromatic hydrocarbon (PAHs) is the most feasible candidate class (Richter et al. [17], Dobbins et al. [18]).

As a first step, fuel breaks down into smaller hydrocarbon molecules and free radicals either by pyrolysis and oxidation reactions. In an oxygen deficient environment, this leads to the formation of significant amounts of C_2H_2. Other species, containing two, three or four carbon atoms are also involved in the formation of stable aromatic rings. The relative contribution of the different types of growth reactions seems to depend strongly on the fuel structure, that is aromatic or aliphatic.

The benzene ring, which exhibits relatively high thermodynamic stability, is widely accepted as building block of soot particulate. Different chemical pathways leading to the first benzene ring have been discussed in the literature.

In the following the main developed mechanisms are presented.

Formation of the first aromatic ring

1. Frenklach mechanism

The most popular mechanism has been proposed by Frenklach and Wang. They found that the main candidate to the formation of benzene is acetylene and the related compounds obtained by addition of acetyl radical (C_2H) and vinyl (C_2H_3) on double bonds.

In Fig. I.1.4 (Frenklach et al. [19], [20], [21]) is shown the suggested mechanism. Two chemical pathways are possible depending on the temperature range. At high temperature, we have the formation of vinyl-acetylene (C_4H_4), by H-abstraction n-C_4H_3 is formed, at which acetylene is added. At low temperature, the addition of acetylene to vinyl results in n-C_4H_5 formation, which upon addition of acetylene produces benzene. Benzene and phenyl are converted to one another by the H-abstraction reaction and its reverse.

Fig. I.1.4: *Formation pathways of benzene according to Frenklach et al [19]*

2. Miller and Melius mechanism

A different mechanism was proposed by Miller and Melius [22]. In fact, they observed by comparing different model predictions with experimental measurements performed on acetylene premixed flames that the contributions of reactions involving C_4H_3 and C_4H_5 are not sufficient to explain the formation of benzene.

Then, considering both structural and thermodynamic observations, these authors found that more additional pathways were necessary to explain the formation of the first ring and proposed the Resonantly Stabilized Free Radical (RSFR) as propargyl (C_3H_3) as the main precursor. As these radicals are very stable, due to the stabilization induced by the resonance, they are characterized to have a long life time. Consequently they are present in a high concentration, which allow them to react according to the following pathway:

$$C_3H_3 + C_3H_3 \leftrightarrow C_6H_5 + H \tag{I.1.1}$$

$$C_3H_3 + C_3H_2 \leftrightarrow C_6H_5 \tag{I.1.2}$$

They concluded that the recombination of two C_3H_3 molecules represents a more attractive source of benzene.

3. Ciclopentadiene mechanism

Both mechanisms: $C_2 + C_4$ and $C_3 + C_3$ seems to lead to the formation of the first aromatic ring. However, despite the high number of works a generally accepted consensus about the

dominant benzene formation pathway does not seem to have been reached. Other compounds, in fact, can have relevance as precursors in PAH formation without passing through benzene as intermediate. The formation of naphthalene, a compound with two aromatic rings, via the reaction of two cyclopentadienyl radicals was firstly included by Dean [23] in a kinetic model describing the methane pyrolysis. This resonantly stabilized free radicals was also proposed by Miller and Melius [22]. The same conclusion was obtained by Marinov et al. [24] and Castaldi et al. [25], based on combined experimental and kinetic modeling studies of PAH formation in methane and ethylene flames.

Aromatic growth in PAH

1. HACA mechanism

Once the first benzene ring is formed, the modeling of PAH growth up to particle inception is essentially based on the addition of small units, as C_2H_2, to the first ring. To describe this growth process, a widely accepted model is introduced by Franklach et al [19, 20, 2121], which is based on the extraction of an hydrogen radical and absorption of C_2H_2. This mechanism is known as HACA (Hydrogen-Abstraction / C_2H_2-addition). In Fig. I.1.5, a schematic picture of this mechanism is presented.
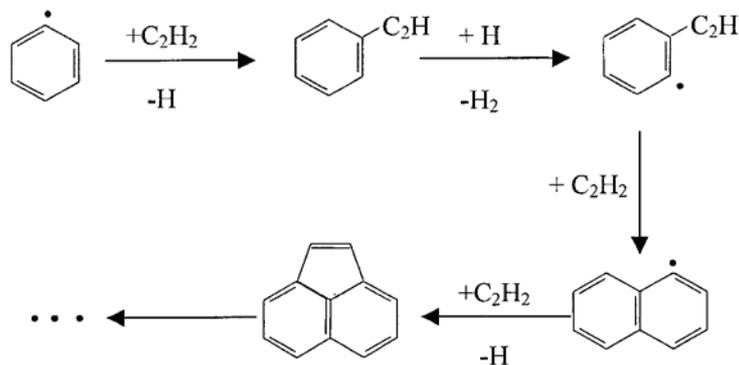
Fig. I.1.5: *HACA sequence for PAH growth (Frenklach et al. [19]).*

In this figure the first steps of the sequence correspond to the formation of naphthalene and acenaphthylene. Then, the sequence continues to form larger PAHs.

2. Miller and Melius mechanim

Miller and Melius [22] and Marinov et al. [24] found that the growth mechanism HACA proposed by Frenklach resulted to be too much slow to take into account the growth rate of

soot formation. They proposed that in such growth processes resonantly stabilized radicals and polymerization reactions, that is radicals addition on double bonds, can explain the fast growth in aromatic structures. These mechanisms can account for the formation of highly de-hydrogenated complex molecules. This subject is still a matter of discussion in the combustion community.

1.4.2 Solid phase

The formation and growth of soot particles in solid phase can be divided in the following steps: *soot particle inception*, *surface growth* and *oxidation, coagulation*, and *agglomeration.*

The *soot particle inception* is a homogeneous process occurring in the gas phase environment, when heavy PAH molecules coalesce to form particles. According to different authors (Wagner et al. [12], Haynes et al.[13], Bockhorn [15], Glassman [26], Kennedy [27], Richter et al. [17]), this happens when the molecular mass is in the range 500-1000 a.m.u. Above these values the PAHs can be considered as solid particles rather than molecules. The first soot particles are roughly spherical in shape, with a diameter of about 1.5 nm and have a C/H ratio of about 2. Once particles are formed, the growth processes can be due to the other mentioned mechanisms.

The bulk of soot yield is generated by the *surface growth* process, which can be described by heterogeneous chemical kinetics. It consists in the attachment of gas-phase species to the surface of the particle and, consequently, their incorporation in the particle itself. As growth species are chemically bounded on soot, radical sites are present on these particles. Acetylene and PAH are the main responsible of this growth process (McKinnon et al. [28], Frenklach [29]). As a consequence of these mechanisms, the surface growth process is characterized by an increase of the particle diameter and of the soot volume fraction, while the total number of the primary particles remains constant. In order to describe this process, a growth rate is defined in correspondence of the surface reactions, which can be represented by a first-order growth model, according to Bockhorn et al. [30] and Matzing et al. [31]. The following expression is given:

$$\frac{df_v}{dt} = k_g \left(f_\infty - f_v \right) \tag{I.1.3}$$

where f_V is the soot volume fraction, f_∞ is its asymptotic value relative to long reactions times and k_g is the surface growth constant.

During *coagulation*, sticking collision takes place, which results in an increase of the average particle size, a decrease in the total number of primary particles, while the total soot amount remains the same. In the case of particles with small diameter, collision frequencies are high and isotropic. The resulting particles are statistically spherical. Considering this coagulation mechanism, a corresponding soot growth rate can be defined (Graham et al. [32]). To this purpose, the following assumptions have to be considered:

- particles are in the free molecular regime;
- for each collision a coagulation results;
- all particles are spherical.

Then, according to the Smoluchowski equation, the decrease of the number of soot particles, N_{tot}, satisfies the relationship:

$$\frac{dN_{tot}}{dt} = -K_c(dp)N_{tot}^{\;2} \tag{I.1.4}$$

where K_c is a constant, which depends on the particle diameter. In the case of particles with diameter less than the free mean path length of the gas (Knudsen number >10) the coagulation growth rate results to be (Graham et al. [32]):

$$\frac{dN_{tot}}{dt} = -\frac{6}{5} K_{theor} f_v^{\;1/6} N_{tot}^{\;1/6} \tag{I.1.5}$$

where

$$K_{theor} = \frac{5}{12}\left(\frac{3}{4\pi}\right)^{1/6}\left(\frac{6K_B T}{\rho}\right)^{1/2} G\,\alpha \tag{I.1.6}$$

In the previous equation K_B is the Boltzmann constant, ρ the density of soot particles, G accounts for the enhancement of the collision rate density due to dispersion forces, α the distribution function of the particles size for free molecular coagulation.

Parallel to the surface growth, soot *particle oxidation*, which is a kind of surface reaction, takes place. As an effect of the oxidation reactions the mass of these carbonaceous species decrease through the formation of CO and CO_2. The main oxidation reactants are OH, O and O_2; usually OH under fuel-rich conditions and O_2 under fuel-lean conditions.

Finally, when particles are not very chemically reactive, *aggregation* processes begin with the formation of open clusters.

Although these processes are described and shown in the picture separately, usually there is an overlapping of the steps, some of which being competitive.

1.5   Hydrogen-hydrocarbon hybrid fuels

In order to improve the overall combustion performance, an increasing interest is given by the scientific community to the use of additives into hydrocarbon fuels (Oh et al. [33], Liu et al. [34]). In this context, hydrogen/hydrocarbon blended fuels have been proved to match this task. The behavior of these blended fuels is due to the main combustion characteristics of hydrogen. In fact, hydrogen presents a wide range of flammability, a low ignition energy, an high energy mass density (1.2 *10 J/Kg) and low ignition temperature (750-800 K). Then, with hydrogen addition to hydrocarbons, different effects on the chemical and physical processes involved in combustion can result. Unfortunately, these effects are not predictable due to the complex and non-linear nature of chemical kinetics.

One of the first studies has been performed by Tesner in 1958 [35] and consisted in diluting natural gas with hydrogen. A slowdown of carbon black formation was found during thermal decomposition. After this observation, several works can be found in the literature on the investigation of the improvement of combustion features. Generally the influence of hydrogen addition is investigated in different set-ups according to the following points: combustion ignitability, flame stability, visible flame appearance, temperature field, soot and pollutants emission. These aspects, and especially the stability problems, are particularly important for industrial applications, e.g. in gas turbines, where a lean condition is present.

In particular, by adding hydrogen an increase in the flammability limits has been observed in different conditions, as in jet diffusion flame (Karbasi et al. [36]), in swirling turbulent flame (Schefer [37]) (by performing OH PLIF measurements), in a lean-premixed counter-flow flame (Jackson et al. [38]) and in a non-premixed natural gas swirl-stabilized flame (Cozzi et al. [39]). An improvement in the stability was observed as a result of an

increase in the flame speed both in diffusion flame (Yu et al. [40]) and on a lean high pressure premixed turbulent flame (Halter et al. [41]). A similar result has been derived also from numerical approach (Tseng [42]). As a further interesting point, by adding hydrogen, significant changes in the flame structure, flow field and temperature field were also observed by Cozzi et al. [39].

Concerning the influence of hydrogen addition on soot formation very few studies can be found in the literature. In the work of Choudhuri [43], it was found that increasing natural gas or propane in the mixture the flame luminosity and length increase, due to soot concentration and CO emission. Anyway, a reduction of NO and NOx was found.

In diffusion flames, the influence of hydrogen on temperature field and soot formation was experimentally studied on methane, ethylene, propane and butane (Migliorini et al. [44], Gulder et al. [45]). The relative influence of dilution and direct chemical interaction on soot formation was analyzed by comparing hydrogen addition results with the ones obtained with helium addition. No changes of the temperature field was detected in both cases. On the contrary, for soot formation a significant effect was observed, strongly dependent on the investigated fuel. By using propane and butane, hydrogen and helium addition reduces soot by the same amount showing that hydrogen has mainly a dilution effect. In the ethylene flame soot reduction is more consistent with hydrogen than helium, indicating also the presence of a chemical route for soot reduction, while, in the case of methane flame, an opposite behavior is observed.

Recently Guo et al. [46] performed a numerical investigation on the effect of H_2 and He on the flame experimentally investigated by Gulder et al. [45], using a detailed reaction mechanism. The results presented by Gulder have been numerically well reproduced.

To conclude we can infer that the effect of hydrogen addition on hydrocarbon fuels can be summarized as follows:

- extension of stability limits
- increase of burning velocity
- significant change in flame structure and flow field
- decrease of soot production.

Generally, looking at the literature, we can infer that an exhaustive characterization of such hybrid fuels is far from being achieved and much work is still needed. In particular concerning the investigation of hydrogen addition on soot formation, very few data are available. In fact, as reported above, this study has been performed only in diffusion flames and no information is available in other different reactors. Anyway, the observed reduction of soot with hydrogen addition sounds to be obvious due to a reduction in the hydrocarbon content (for example in a diffusion flame), and consequently in carbon atom concentration. It is, instead, interesting to estimate in which proportion the soot yield, obtained by normalizing the soot volume fraction to the carbon atom concentration, is decreasing.

1.6   Laboratory Combustion reactors

In order to study soot formation mechanisms from hydrocarbons in different experimental conditions, different experimental set-ups have been implemented by many authors. The main investigated reactors can be summarized as follows:

- well-stirred reactor
- fast compression machine
- laboratory flames (diffusion and premixed)
- shock tube

The *well-stirred reactor* is widely used to investigate the formation of soot precursors, starting from the first benzene ring (Yahyaoui et al. [47], Dagaut [48]) . These studies are usually carried out by coupling different diagnostics as gas-chromatography and mass-spectroscopy. The apparatus is particularly interesting for chemical kinetic studies, as mono-dimensional approach can be applied.

The fast compression machine is a reactor which allows to simulate diesel engine-like conditions. The apparatus creates accurately controlled conditions at the end of compression (uniform mixture, temperature, and well-defined mixture composition) and, by decoupling chemistry with mixing, provides an unambiguous data interpretation for kinetics study (Kitsopanidis et al. [49]). With this reactor, self-ignition delay of hydrocarbons can be studied, which is important for gas-phase modeling in soot formation mechanisms.

Laboratory flames allow to investigate mechanisms of formation and growth of soot particles and their precursors.

As for the _premixed flame_, fuel and oxidizer are mixed before the combustion process takes place. If the reactant gases have a laminar flow, the flame speed is dominated by the chemistry. The flame structure consists essentially of four distinct regions (Glassman [26]):

1. unburned
2. preheat
3. reaction
4. burned gases.

Initially the fresh unburned mixture at ambient condition approaches the flame front and it is heated up by conduction and radiation from the flame front. Once temperature is high enough to sustain combustion, in the reaction zone chemical reactions start. The gases emerging from this zone enter the burned gas region.

In a premixed flame the relative amount of fuel and oxidizer can be regulated. To this purpose, a parameter is introduced, called the equivalence ratio, defined as:

$$\Phi = \frac{\left(\dfrac{x_{fuel}}{x_{oxigen}}\right) in\ work\ mixture}{\left(\dfrac{x_{fuel}}{x_{oxigen}}\right) in\ stoichiometric\ mixture} \tag{I.1.7}$$

where the ratio of gas and oxidizer at the work conditions are compared with the corresponding ratio at the stoichiometry (x_i being the molar fraction of the species i). A flame with an equivalence ratio larger than one is called fuel-rich, and fuel lean if Φ is less than one. Passing from lean- to rich-flame conditions soot is formed. This condition is called sooting point. Another quantity used to characterize a premixed flame is C/O ratio, defined as the ratio of the numbers of carbon atoms to oxygen atoms in a mixture. In the combustion community, a Mckenna burner is widely used to produce premixed flames. The burner has been properly designed to produce a "flat" flame, that means with a uniform distribution of the major species and temperature radially across the flame. This allows to consider the flame mono-dimensional and to perform the investigation only on the axis. For this reason, in lean

condition, this burner is considered a standard for calibration (Clauss et al. [50], Cheskis [51], Chen et al. [52], Barlow et al. [53], Meier et al. [54], Prucker et al. [55], Sutton et al. [56]). As reported by many authors, measurements performed by using several optical and sampling techniques result to be very helpful for the implementation and validation of chemical kinetics codes (D'Alessio et al. [57], Xu et al. [58, 59], Tregrossi et al. [60], Atakan et al. [61], Apicella et al. [62], Menon et al. [63]). In particular, the McKenna burner was recently proposed and utilized as a standard burner for the development of the Laser-Induced Incandescence (LII) technique (Axelsson et al. [64], Kruger et al. [65], Schultz et al. [66]).

Concerning the *diffusion flame*, the fuel and the air are initially unmixed (Glassman, [26]). They are separate and form the reaction zone at their interface. As the gases move upstream the mixing layer increases in thickness, until a uniform mixture of products is formed. In this flame, combustion is sustained by the diffusion of the fresh mixture in the flame zone, instead of the chemical kinetics of the system as in the premixed flame. As at the beginning no oxygen is present in this case, the fuel is pyrolysed or broken down to smaller molecules and radicals, which results in the formation of soot. Approaching the flame zone, the presence of oxygen allows the products of the pyrolysis to react. The resulting flame zone is substantially thicker than in the premixed flame.

The shock tube is an ideal totally adiabatic reactor where, due to the passage of a shock wave, the mixture under study is brought almost instantly to a known and controlled high temperature and pressure. Then, the main advantage of this reactor is the capability to study soot formation and its precursors in precise conditions of temperature and pressure, up to high values typical of internal combustion engines. For this reason, it allows to perform a parametric study of the processes. In the following paragraphs, details on this reactor are presented and an overview on the experimental studies regarding soot formation will be discussed.

2 Optical diagnostics techniques

Diagnostics techniques are powerful tools to investigate soot formation and growth in practical systems. Essentially, they can be divided in intrusive and non-intrusive techniques. The intrusive techniques are characterised by a perturbation of the system under investigation,

which is particularly strong for hostile combustion systems. A typical example is given by the probe sampling of soot for the Transmitted Electron Microscope analysis (TEM) (Koylu et al. [67], Janzen et al. [68], Dobbins et al. [69], Cai et al. [70]). In fact, considering this technique applied to an atmospheric flame, a strong perturbation can result from a fast insertion of the probe in the flame itself. Moreover, the interaction of this probe with soot in the flame can also produce non-controlled chemical effects.

The optical techniques and, in particular, laser diagnostics, being non-intrusive, allow to overcome these problems. Thanks to the application of more and more powerful lasers, measurements of species concentration and temperature field can be carried out with high spatial and temporal resolution. These techniques are widely applied also to the investigation of soot formation and growth. Soot particles are, in fact, particularly suited to be detected with such techniques thanks to the features of the gray body emission.

In this paragraph it is given an overview of the following soot optical diagnostics techniques, which are also the most common:

1. Extinction technique
2. Two-colour emission technique
3. Laser-Induced Incandescence (LII)
4. Extinction/Scattering technique (scattering at one or multi-angles)

Concerning the extinction/scattering technique, only general information is given here. In fact, as this diagnostics is implemented in this thesis, it is widely discussed in the next paragraph.

The techniques listed above are based on different physical phenomena and, for that, they are complementary, allowing to obtain different information. The application of one technique instead of another depends on the experimental conditions involved. Just to give an example, classical extinction, being integral, can be applied to obtain average value of soot concentration in practical systems, with a limitation on the detection level. Then, it is useful for industrial application when the soot load is particularly important. On the contrary, LII, which requires more efforts to be performed, allows to have local measurements with high sensitivity and spatial resolution. For that, it is a powerful tool to detect carbonaceous particulate matter in turbulent flames.

Moreover, attention has to be paid to the interpretation of the results, which are not always straightforward, in order to derive from the experimental measurements the right evaluation of soot parameters.

2.1 Extinction technique

Extinction is a well-established technique and is based on the measurement of a monochromatic light intensity transmitted through a given medium. Generally, a laser source or a lamp coupled with a coloured filter is used. In the following, the description refers to the laser application, which is the configuration used in the present study.

The monochromatic transmittance TR_λ, given by the natural logarithm of the ratio between the intensity of the emerging (I_L) and the incident (I_o) laser beam, is related to the extinction coefficient K_{ext} (expressed in cm^{-1}) according to the Lambert- Beer's law as follows

$$TR_\lambda = \ln\left(\frac{I_L}{I_0}\right) = -K_{ext}L \qquad (I.2.1)$$

where L is the path length in the medium producing the extinction. The absorbing medium is considered uniform all along the pathway. The extinction coefficient can be expressed as follows:

$$K_{ext} = N_p(C_{scatt} + C_{abs}) = K_{scatt} + K_{abs} \qquad (I.2.2)$$

where N_p [#/cm3] is the particle number density and C_{abs} and C_{scatt} are the cross sections for absorption and scattering, respectively. In most practical cases, the scattering contribution can be assumed to be negligible, with a coincidence of the extinction and absorption coefficients $K_{ext} = K_{abs}$. In the Rayleigh limit of the Mie theory, when the particle size is much smaller than the wavelength of the incident radiation, the absorption coefficient can be expressed as a function of the soot volume fraction, f_v, according to the following relationship

$$K_{abs} = \frac{6\pi E(m)f_v}{\lambda} \qquad (I.2.3)$$

where $E(m)$ is a function of the real, n, and imaginary, k, part of the refractive index m ($m=n -ik$) according to this expression

$$E(m) = \frac{1}{6} \text{Im}\left(\frac{m^2 - 1}{m^2 + 2} \right) = \frac{nk}{\left(n^2 - k^2 + 2 \right) + 4n^2 k^2}$$

(I.2.4)

Considering the definition of the soot volume fraction, f_v, in terms of the total number of primary particles per unit volume and the soot particle diameter, d_p, as:

$$f_v = \frac{\pi}{6} d_p^{\;3} N_p$$

(I.2.5)

and by taking into account the previous expressions, the value of f_v can be determined by the classical working formula:

$$f_v = \frac{-\ln\left(\frac{I_L}{I_0} \right) \lambda}{6\pi L E(m)}$$

(I.2.6)

If L is expressed in meters and λ in microns then f_v is obtained expressed in ppm, which indicates the millionths of the volume occupied by soot.

Being the extinction a line-of–sight technique, only an average value of f_v along the pathway of the investigated medium is derived, without any spatial resolution along the laser beam direction. In the case of axial-symmetric geometry of the system, an Abel inversion procedure (Dasch [71]) can be applied. From chordal profiles of extinction measurements, a local extinction coefficient, and consequently a local soot concentration in the system are obtained. This optical diagnostic is experimentally simple, with only the limitation of the point-to-point nature of the measurements. For this reason, it is quite difficult to probe soot volume fraction in non-homogeneous distribution as in turbulence flames. For such an application, the technique was extended to the two-dimensional arrangements (Greenberg et al. [72], Snelling et al. [73]), which allow to have a 2D distribution of the soot volume fraction with a single measurement.

A further discussion is required for the particular laser wavelength used, according to the experimental conditions employed (in terms of the gas used, temperature and pressure range). As the technique is based on the absorption of the laser light and the absorption spectral features depend on the particular species present in the system, care has to be taken in discriminating soot concentration from other "non-solid" species. In fact, considering for example laboratory flames, gas species, and particularly polycyclic aromatic hydrocarbon, exhibit strong absorption spectra ranging from UV up to the visible region. Depending on the experimental conditions, as for example in premixed rich flames, these spectra can be competitive with soot broad-band grey body absorption. On the contrary, different behaviour is obtained for diffusion flames. Extinction measurements to evaluate soot volume fraction performed at different wavelengths in a shock tube (Graham [74], Graham et al. [75]) and in reach premixed flames (Migliorini et al. [76]) confirm this behavior, showing that with the use of UV or visible light an overestimation of f_v is obtained. Then, the use of an infrared source should allow to completely neglect the contribution of other non-solid species to soot absorption. This point will be discussed further on, in a following chapter, by showing our results of f_v obtained with different wavelengths.

2.2   Two-color emission technique

This technique is essentially based on the gray body emission of soot at high temperature. For that, it is largely applied both in luminous flames (Siddal et al. [77]) and in internal combustion engines (Matsui et al. [78]). The simplicity of this technique is attractive under many of the severe constraints imposed in most practical systems. It readily allows to evaluate the averaged values of soot volume fraction and temperature, which are the most significant parameters in engineering purposes. In Fig. I.2.1, a typical experimental apparatus implemented for this kind of measurements is shown (Cignoli et al. [79]). Practically, it is a two-colour pyrometry technique: soot radiation emitted from the flame is detected at two different wavelengths (the two colored filters in the figure, blue and red) and compared with the radiation emitted from a calibrated light source at the same wavelengths. The yellow plate shown in the figure is an anti-heat filter, which allows to remove the IR component in the signal.
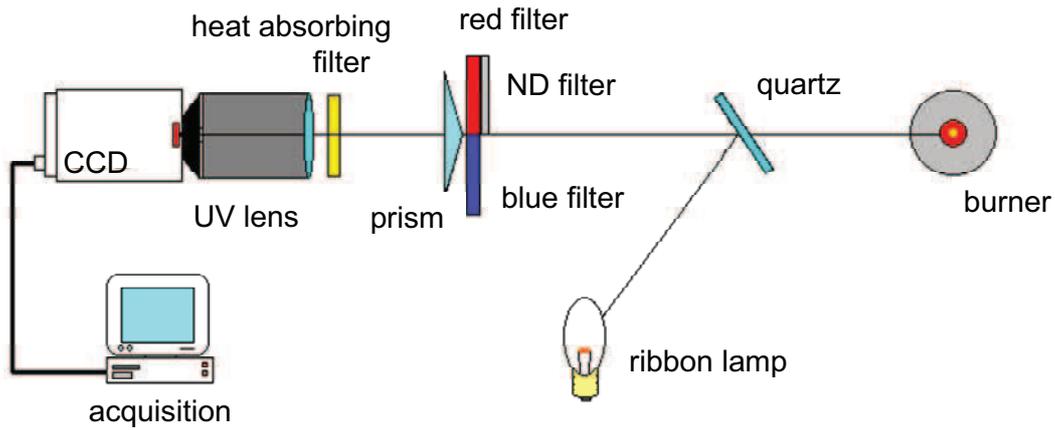
Fig. I.2.1: *Experimental set-up for light emission measurements (Cignoli et al. [79]).*

The light intensity emitted from soot can be described by the Planck's radiation law weighted by the emissivity of the soot particles, as:

$$I_s = \varepsilon_s(\lambda, f_v) I_{BB}(\lambda, T_s) \eta_{s\lambda}$$

(I.2.7)

where $\eta_{s\lambda}$ is a calibration constant, which takes into account the overall instrumental function of the set-up. The function $\varepsilon_s(\lambda, f_v)$ is the soot emissivity, which depends on the wavelength and on the soot volume fraction. In the previous equation, I_{BB} is the spectral blackbody radiation intensity at the soot temperature T_s given by Plank's law

$$I_{BB} = \frac{C_1}{\lambda^5} \frac{1}{\exp\left(\dfrac{C_2}{\lambda T_s}\right) - 1}$$

(I.2.8)

where C_1 and C_2 are the first and the second Planck's constants.

By considering the Kirchhoff's law, for a uniform soot layer of length L and volume fraction f_v, the emissivity is given by:

$$\varepsilon_S(\lambda, f_V) = 1 - \exp(-K_{abs} \ L)$$

(I.2.9)

In the previous equation, K_{abs} is the absorption coefficient (see Eq. (I.2.3)), which can be expressed also as follows:

$$K_{abs} = \frac{6\pi E(m) f_v}{\lambda} = \frac{f_v}{l_{abs}}$$

(I.2.10)

where l_{abs} is the natural length of absorption. This parameter is defined as the thickness of pure soot ($f_v=1$) with a transmittance equals to 1/e and depending only on soot characteristics (De Iuliis et al. [80]).

The radiation intensity emitted from a calibrated lamp can be expressed as:

$$I_L = \varepsilon_L(\lambda, T_L) I_{BB}(\lambda, T_L) \eta_{L\lambda}$$

(I.2.11)

In this equation the emissivity of the calibrated lamp, ε_L, is known as a function of wavelength and temperature, and $\eta_{L\lambda}$ is the wavelength-dependent calibration constant, which could differ from $\eta_{s\lambda}$ at most for components that can be assumed to be neutral in the considered wavelength region. Then, by writing the two Eqs. (I.2.7) and (I.2.11) at the two wavelengths λ_1 and λ_2, and taking the ratio, it is verified that

$$\frac{\eta_{S\lambda_1}}{\eta_{S\lambda_2}} = \frac{\eta_{L\lambda_1}}{\eta_{L\lambda_2}}$$

(I.2.12)

From the previous relationships, both the soot volume fraction and the temperature can be derived. First of all considering that $f_v L/l_{abs} \ll 1$ an expansion in the Taylor series of the Planck's law, Eq. (I.2.8), is performed and, consequently, the exponential function can be neglected. Then, by considering the relationship in Eq. (I.2.12) the soot temperature can be easily derived. Once this term is known, by simply comparing the light intensity emitted from soot and the one from the calibrated lamp at the same wavelength, the soot volume fraction is obtained. In the following the two analytical expressions are reported:

$$T_S = -c_2\left(\frac{1}{\lambda_1} - \frac{1}{\lambda_2}\right)\left[\ln\left(\frac{I_S(\lambda_1)}{I_S(\lambda_2)}\frac{I_L(\lambda_2)}{I_L(\lambda_1)}\frac{\varepsilon_L(\lambda_1, T_L)}{\varepsilon_L(\lambda_2, T_L)}\frac{l_{abs1}}{l_{abs2}}\right) + \frac{c_2}{T_L}\left(\frac{1}{\lambda_2} - \frac{1}{\lambda_1}\right)\right]^{-1}$$

(I.2.13)

$$fv = -\frac{l_{abs}}{L}\ln\left(1 - \varepsilon_L(\lambda,T_L)\frac{I_S(\lambda)}{I_L(\lambda)}\exp\left(-\frac{c_2}{\lambda}\left(\frac{1}{T_L} - \frac{1}{T_S}\right)\right)\right) \qquad (I.2.14)$$

Like extinction, the two-colour emission is an integral technique, and only in the case of axial symmetric geometry of the system, the local values of f_v and of the temperature can be obtained by performing the inversion procedure. The extension to the two-dimensional case is important especially in turbulent conditions (Cignoli et al. [79]). This technique is simple and robust with the need of only simple optics and without a laser, and it allows to deliver a significant amount of data in a short time. Uncertainties may be attribute to the presence of cold soot regions in the flame, whose corresponding low emission gives a different weighted contribution to the overall soot radiation intensity (Cignoli et al. [79]). Other considerations have been made concerning the focusing optical system, especially in the case of flames with wide width (usually diameter bigger than five centimetres). In fact, in this case, if the f number is not large enough, the regions in the flame beyond and before the focal length axis give different contribution to the signal.

Moreover, it is important to underline that the most significant uncertainties of all optical techniques are due to the spread in the values of the soot refractive index. In the paragraph 2.5 we report an analysis of the refractive index and the different data taken from the literature, as obtained at different wavelengths, and measured in different experimental conditions. Particularly interesting values are proposed by Chand and Charalampopoulos [81] who gave a dependence of both the real and imaginary part of the refractive index on the wavelength. Using these functions, De Iuliis and colleagues proposed the extension of the two-colour emission technique to the case of multiwavelength detection [80]. The agreement of these measurements with previous extinction ones performed in the same experimental conditions (De Iuliis et al. [80]) allow to prove the validity of this choice of the refractive index at least in the visible spectral region.

2.3 Laser Induced Incandescence (LII) technique

During the 90's the laser-induced Incandescence (LII) has become popular within the combustion community, as it is a promising tool that allows temporally and spatially resolved measurements for the characterization of soot in combustion systems.

The technique is based on the absorption of a high power laser pulse, resulting in an increase of the internal energy, and on the release of this energy with the emission of a typical grey body thermal radiation. During the laser pulse, the particles reach a temperature well above the flame temperature.

In order to develop a time-dependent model, some hypotheses have to be made. First of all, the aggregates are idealized as composed by particles with the same diameter and touching at one point (Melton [82]). Although soot is usually regarded as agglomerates of primary spherical particles, a model for LII technique can be based on energy and mass balances for one spherical particle rather than for the whole aggregate. This viewpoint requires that all the particles in an aggregate have the same temperature; in addition, they have to be considered small enough to neglect internal temperature gradients. In this approach, individual monosized primary particles are considered.

As proposed in the pioneering work of Melton [82], and Eckbreth [83], several physical phenomena have to be taken into account. In Fig. I.2.2, a schematic representation of the phenomena involved and the energy balance equation are reported.
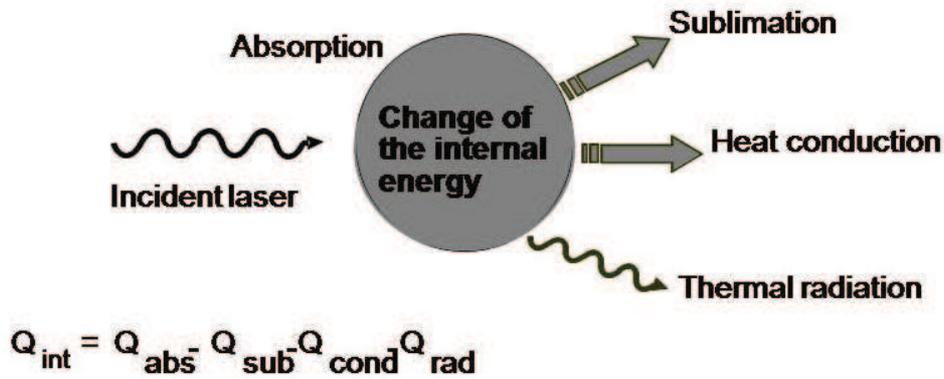
Fig. I.2.2: *Energy balance description of a laser-heated soot particle.*

By using thermodynamic principles, the balance equation can be expressed as:

$$K_{abs} \frac{\pi}{4} d_p{}^2 q(t) - \pi d_p{}^2 (T - T_0)\Lambda - \left(\frac{\Delta H_V}{W_s}\right)\frac{dM}{dT} - q_{rad} - 1/6 \pi d_p{}^3 \rho C_s \frac{dT}{dt} = 0 \qquad (I.2.15)$$

The different terms represent, respectively:

1. the absorption rate of laser energy where

- K_{abs} is the absorption coefficient of soot
- d_p is the particle diameter
- $q(t)$ is the temporal profile of the laser pulse;

2. the rate of heat transfer to the ambient by conduction where

- Λ is the particle thermal conductivity toward the surrounding gases
- T is the particle temperature
- T_0 is the ambient gas temperature;

3. the energy expended in vaporization of soot carbon where

- ΔH_v is the heat of vaporization of carbon
- W_s is the molecular weight of carbon vapor species
- dM/dt is the rate of mass vaporization;

4. q_{rad} the rate of energy loss by black body radiation;

5. the rate of internal energy raise where

- c_s is the specific heat of carbon
- ρ is the soot density.

The mass conservation equation is:

$$\frac{dM}{dt} = \pi \frac{d_p^{\,2}}{4} \rho \frac{d_p}{dt} = \pi \, dp^2 \rho \, U_v \qquad (I.2.16)$$

where U_v indicates the thermal velocity (Eckbreth [83]). Eqs. (I.2.15) and (I.2.16) are a set of coupled differential equations numerically solvable in order to obtain particle dimension $d_p(t)$ and temperature $T(t)$ versus time depending on the specific exciting wavelength, ambient gas temperature T_0 and particle initial diameter d_{p0}.

Finally the LII signal must be calculated taking into consideration the density of primary particles and the spectral bandwidth of detection, $\Delta\lambda$, around a central wavelength λ_0

$$LII(\lambda_0 t) = N_p \, \pi \, d_p^{\,2}(t) \frac{C_1 \varepsilon(t) \Delta\lambda}{\lambda_0^{\,5} \left[\exp\left(\dfrac{C_2}{\lambda_0 \, T(t)} \right) - 1 \right]}$$

(I.2.17)

A typical example of the resulting time-dependent LII signal is shown in Fig. I.2.3 (De Iuliis et al. [84]).
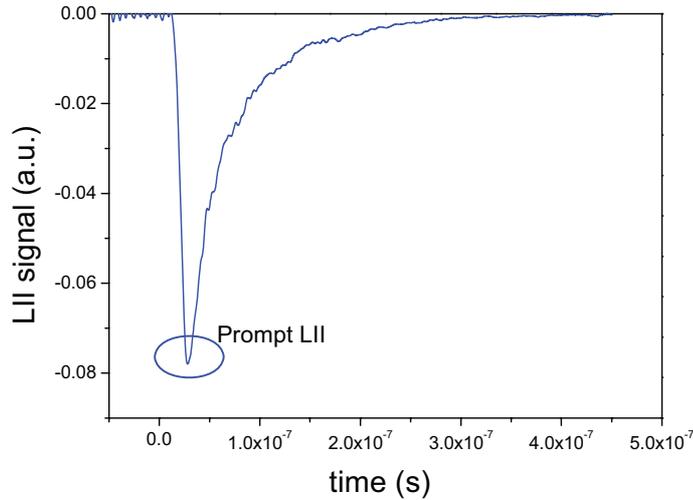
Fig. I.2.3: *Typical laser-induced incandescence signal versus time (De Iuliis et al. [84])*

The signal is negative as it is measured with a photomultiplier. In correspondence of the absorption of the laser pulse, the incandescence intensity increases up to a maximum value, and then, soon after the laser, decreases with a typical decay time scale of some hundreds of nanoseconds.

According to Melton's theory, the signal temporal decay depends on the particles size. In fact, smaller particles are responsible of faster decay. Moreover as for the peak of LII signal, usually called "prompt" LII, the following relationship was originally proposed by Melton [82]:

$$prompt \, LII \cong N_p \, d_p^{\,x}$$

(I.2.18)

where the exponent x is given by:

$$x = 3 + \frac{154}{\lambda_0 \, (nm)} \qquad\qquad (I.2.19)$$

For a detection wavelength λ_0 in the visible, this exponent is about 3 and the prompt LII signal is proportional to the soot volume fraction (Melton [82]).

In order to have absolute measurements, a calibration procedure of the incandescence signal is required. As for soot volume fraction measurements, these are carried out by scaling the peak of the incandescence intensity with the value of f_v obtained with other optical techniques, as for example with the classical extinction one (Shaddix et al. [85], Axelsson et al. [86]). Recently (De Iuliis et al. [84], Snelling et al. [87]), a two-color laser induced incandescence approach is adopted, which is an extension of the pyrometry technique. The prompt LII signals are detected at two wavelengths (the more far away from each other are, the more sensitive the technique) and compared with the emission from a calibrated lamp, with the care of keeping the collection system identical in both cases. In this context, as the methodology of the technique is the same as the two-color pyrometry (Paragraph 2.2) details on the equations used are not reported here.

Many works are reported in the literature concerning the development and the application of the two-color LII technique. As for the evaluation of the prompt LII, a procedure is proposed by de Iuliis et al., based on a statistical analysis, to determine the suitable gate width over which the integral signal should be evaluated [84]. It was found that an integration over a gate width of 4 ns (1 ns before and 3 ns after the peak of the incandescence signal) allows to have a prompt value close to the absolute peak value and with the highest signal to noise ratio. Another important point is the choice of the value of the laser fluence to be used, which is the laser pulse energy divided by the section surface (W/cm^2). To this purpose, the dependence on the laser fluence of the peak of the incandescence signal detected at the two wavelengths and, consequently, the related incandescence temperature obtained with the calibration is considered. Fig. I.2.4 shows this dependence for methane and ethylene (De Iuliis et al. [88]).

As it can be seen, the behavior is the same for both fuels: temperature linearly increases with the laser fluence up to a threshold value (250-300 mJ/cm^2). Above this threshold the temperature remains quite constant up to a certain value after which, due to the sublimation, a slightly decrease is observed (not shown in the figure).

In order to obtain these results it is mandatory to have a proper feature of the laser beam cross section in the probe volume.
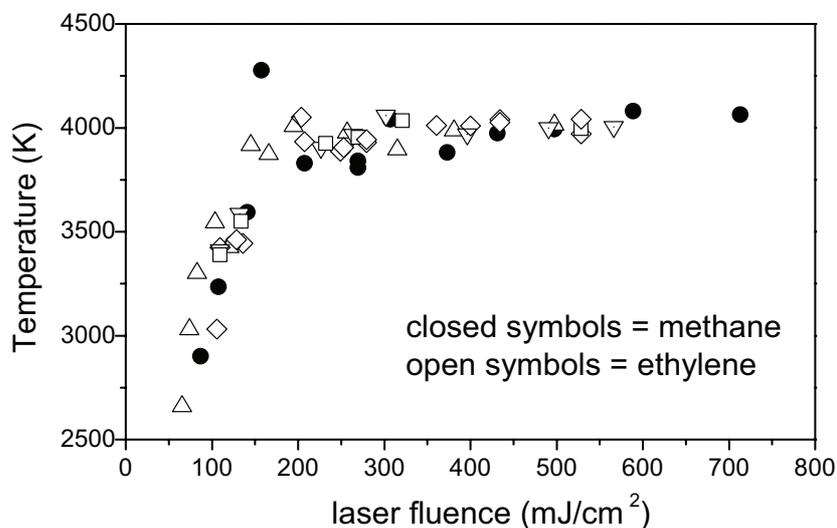
Fig. I.2.4: *Dependence of soot LII temperature on the laser fluence (De Iuliis et al. [88])*

The laser spot has to present a quite uniform intensity across the section, with well defined edges. In this way, it is possible to avoid wing effects, which causing a continuous increase of the probe volume prevent the saturation plateau to be reached.

Moreover, the uniformity of laser intensity assures to reach uniform value of temperature across the probe volume. Thanks to the convenient behavior of the temperature with the laser fluence (see Fig. I.2.4), this can be obtained for a wide range of the laser fluence. For these considerations we can infer that LII measurements should be carried out just above 300-350 mJ/cm^2, where the saturation occurs, but sublimation still can be considered negligible.

The technique is punctual and very sensitive. Moreover, as it is based on incandescence phenomena, it is possible to select and discriminate carbonaceous particles with respect to other "non-solid" species. The extension to the two-dimensional case is possible even if not straightforward: a critical issue is the possibility of obtaining a uniform laser sheet in terms of the shape and the fluence (De Iuliis et al. [89]).

Although in the last decades a lot of works can be found in the literature both for what concerns measurements (Snelling et al. [90], Michelsen et al. [91]) and for modeling (Michelsen et al. [92]), many efforts are still required for an accurate description of the physical and chemical processes involved in nanosecond heating of soot particles.

36

2.4   Generality of Laser Scattering/extinction technique

With the techniques presented up to now, measurements of the soot volume fraction and soot temperature field (obtained with the emission) can be carried out. Except to LII, which allows to measure soot particle sizing, no information about soot particle characterization and morphology can be derived. Reviews of the scattering-extinction technique of the laser light reported in the literature show how this method can be used to determine soot structure characteristics (Charalampopoulos [93] and Sorensen [94]).

In the Rayleigh approximation of Mie's theory, which means for diameter much smaller than the wavelength of the incident radiation, by combining the scattering signal with the extinction measurements it is possible to evaluate both the diameter and the number density of soot particles. In this regime, the particles are assumed to be isolated, with no aggregation processes involved. The corresponding vertically polarised component of the scattering intensity presents an angular pattern which is independent on the scattering angle.

On the contrary, in highly sooting conditions, a dependence of the scattering intensity from the angle is observed. Thanks to thermophoretic sampling and TEM analysis a complex morphology of soot particulate is shown, as for example in coannular ethylene-air diffusion flames (Dobbins et al. [69], Megaridis et al. [95]). These and other observations pointed out that the growth of soot particles is due not only to surface processes by also via agglomeration. Chain-like or more complex clusters are the typical features, consisting of primary spherules of about 20-50 nm diameter; individual clusters may contain many thousands of such primary particles. Depending upon these structures, different angular patterns are obtained. For quite highly ramified structure, a fractal-like approximation is used to analyse scattering measurements carried out at multiple angles (Dobbins et al. [96], Bonczyk et al. [97], Puri et al. [98]). In this case information about aggregation in terms of fractal dimension and radius of gyration are obtained.

Moreover, the polidispersity of the aggregation is considered in order to take into account the number of primary particles in an aggregate, according to a distribution function. Being this technique the basis of the present thesis a further chapter completely focused on this topic is devoted.

2.5   Some consideration about soot refractive index

As already observed in the previous paragraphs, the most important uncertainty of all optical measurements is given by the spread of the wavelength-dependent soot refractive index. Several works are reported in the literature regarding measurements of *m* obtained in different experimental conditions. In order to compare all these data and to give an idea on the effect of this spread on our measurements, the function E(m) is evaluated and traced in Fig. I.2.5 as obtained from literature data in the range of wavelength up to 3 μm.
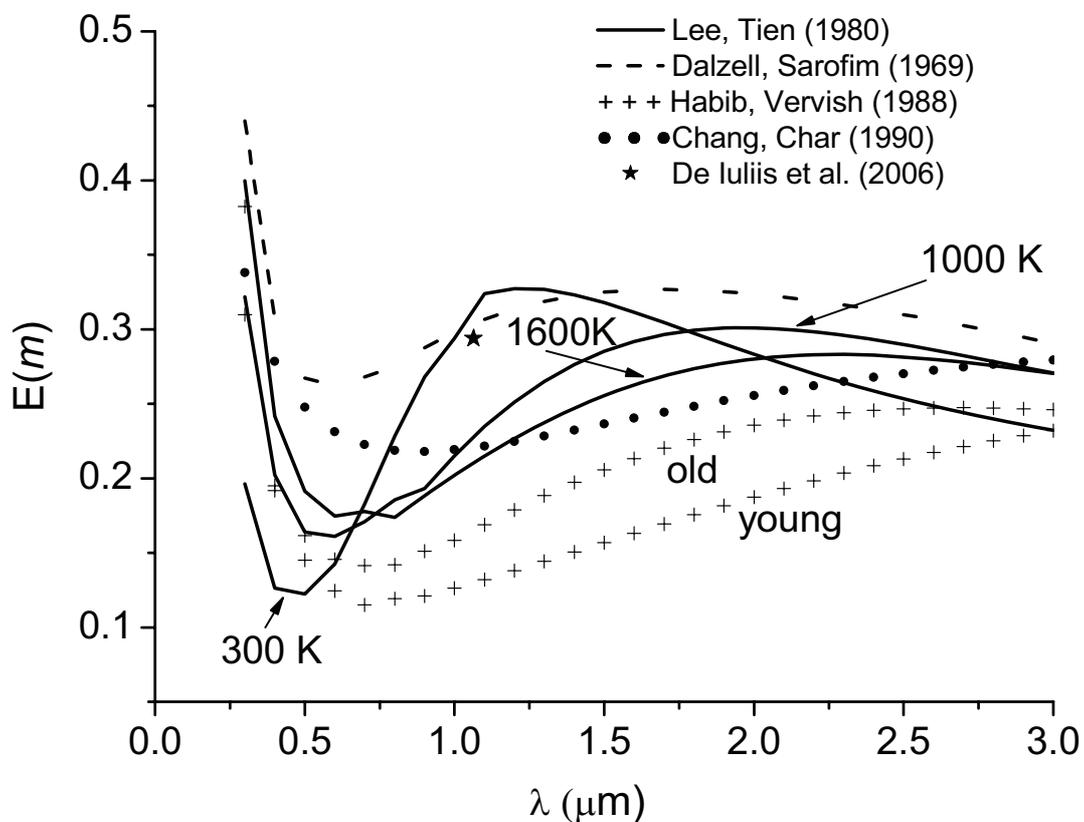
Fig. I.2.5: *Dependence of E(m) on the wavelength up to 3 μm (De Iuliis et al. [88]).*

As it is evident, a significant spread of the curves is shown, which can be justified by the following observations. These results have been obtained in experimental and numerical studies carried out in a period lasting several years. In the case of experimental measurements, then, different experimental conditions (in flames, in the overfire region, or after collection from flames) as well as different techniques and methodology were used. Moreover, different soot properties and structures are here involved.

For example, a significant change of E(m) is obtained for any wavelength by changing soot temperature from 300 K up to 1600 K (Lee and Tien [99]), or considering soot of different age (Habib and Vervish [100]) (old or young as shown in the figure). Particularly interesting are the values of the refractive index proposed by Chang and Charalampopoulos [81] and used in the present work. In fact, the corresponding curve of E(m) traces an average behavior of such a dependence. The refractive index is given at any wavelength through a polynomial expressions of both the real, n, and the imaginary part, k, as:

$$n = 1.811 + 0.1263\ln\lambda + 0.027(\ln\lambda)^2 + 0.0417(\ln\lambda)^3 \tag{I.2.20}$$

$$k = 0.5821 + 0.1213\ln\lambda + 0.2309(\ln\lambda)^2 - 0.01(\ln\lambda)^3 \tag{I.2.21}$$

In the same figure there are also reported the values from Dalzell and Sarofim [101], as largely used in the literature. These curves, anyway, accounting for the variation of m and reported in Fig. I.2.5, are only few examples of the data that can be found in the literature.

In Fig. I.2.6, the values of E(m) limited to the visible region is represented. Here more data taken from the literature are added. Even in the visible region, the spread in E(m) is significant, and again the values proposed by Chang and Charalampopoulos [81] fall close to the average. The same observations already made for Fig. I.2.5 is valid in the visible range. Moreover, almost all data are obtained from soot investigation, with the exception of the one by Pluchino et al. [102] relative to carbon particles.

It has been widely proved that the refractive index values from Chang and Charalampopoulos [81] are reliable for measurements in the visible spectral region, as verified by applying different optical techniques. However, this is not always the case. Laser-Induced Incandesce measurements performed by De Iuliis et al. [88] on a diffusion flame suggested to use higher values of E(m) in the infrared, exactly 0.29 at 1064 nm, which is the star reported in Fig. I.2.5. All data reported in the figure are in the range 0.1-0.3. In the work of Snelling et al. [87] a constant value of 0.4 in all the visible spectral region was suggested.

To conclude, due to the strong influence on the results, here we suggest to always declare the refractive index used to pursuit soot measurements.
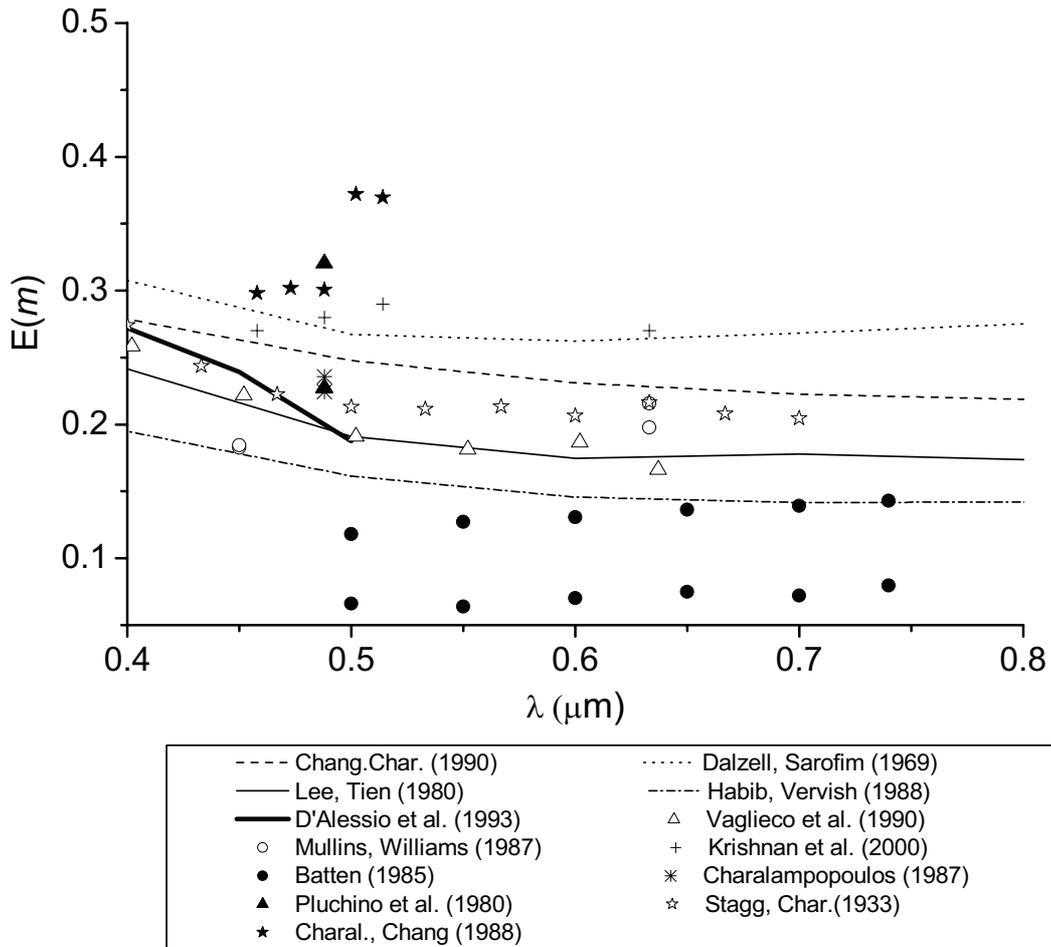
Fig. I.2.6: *E(m) against wavelength in the visible region. The data are taken from the following references: Vaglieco et al. [103], Pluchino et al. [102], Batten [104], Mullins and Williams [105], Charalampopoulos [106], Charalampopoulos and Chang [107], Stagg and Charalampopoulos [108], D'Alessio et al. [109], Krishnan et al. [110].*

3 Scattering/extinction technique

In this paragraph an extensive study on the scattering/extinction technique is presented. Starting from the classical method, which allows to derive soot particle diameter and number density applied to a system of isolated and monodisperse spherical monomers, improvements are considered in order to describe more and more complex structures. As it is verified that particle diameter follows a distribution function, the polydispersity has to be taken into account. The technique of the dissymmetry ratios allows to investigate the aggregation

processes involved in the soot formation and growth mechanisms. The fractal-like theory is commonly implemented to describe soot structure, which presents the typical fractal cluster behaviour.

Finally, the sampling technique for transmission electron microscope analysis is presented. With such a technique, soot size can be determined, which is an important parameter for the validation of *ex situ* optical measurements.

3.1   Classical method

In the scattering technique a vertically polarized laser light is sent into the probe volume under investigation and the vertically polarized scattered light, usually collected at 90°, is detected (Kerker [111]).

In the Rayleigh regime, the scattering cross section of a single particle is given by (Dobbins et al. [96] and Koylu and Faeth [112]):

$$C_{VV}^{P} = x_p^6 \frac{F(m)}{K^2} = \frac{\pi^4 dp^6}{4\lambda_{scatt}^4} F(m) \tag{I.3.1}$$

where the particle size parameter is $x_p = \pi\, dp/\lambda_{scatt}$, $K = 2\pi/\lambda_{scatt}$ is the incident wave vector and $F(m)$ is a function of the refractive index of soot, given by

$$F(m) = \left| \frac{m^2 - 1}{m^2 + 2} \right|^2 \tag{I.3.2}$$

From Eq. (I.3.1) the scattering cross section depends on the 6th power of the particle diameter and inversely on the 4th power of the scattering wavelength. Applying the Rayleigh scattering approximation to an ensemble of primary particles and assuming that the individual primary particles act independently, the scattering coefficient becomes:

$$K_{VV} = N_p\, C_{vv}^p \tag{I.3.3}$$

where N_p is the number of primary particles per unit volume. The scattering intensity measured at the detector is simply given as:

$$I_{VV} = \eta I_0 N_p C_{VV}^P \tag{I.3.4}$$

where I_o is the incident laser intensity and η is the instrumentation factor.

Combining the extinction (see Par.2.1 in this Chapter) with the scattering measurements the particle diameter and the number density can be determined. Here, the expression for the absorption coefficient is recalled:

$$K_{abs} = \frac{6\pi E(m) f_v}{\lambda_{abs}} \tag{I.2.3}$$

where for clarity the subscript *abs* is added to the wavelength as it could be different from the one used for scattering measurements.

By ratioing Eqs (I.2.3) and (I.3.5) the following relationships for d_p and N_p can be obtained:

$$d_p = \left(\frac{\lambda_{scatt}^{4}}{\lambda_{abs}} \right)^{1/3} \left(\frac{4 E(m) K_{vv}}{\pi^2 F(m) K_{abs}} \right)^{1/3} \tag{I.3.5}$$

$$N_p = \frac{6 f_v}{\pi d_p^{3}} \tag{I.3.6}$$

3.2   Primary particle polydispersity

Within the probe volume, however, particles of different size can be present (De Iuliis et al. [80], Kelleler et al. [113]).

In order to describe a population of primary particles of different size, it is necessary to introduce a probability distribution function (PDF) $p(d_p)$, which gives the number of the

monomers exhibiting a diameter in the range $d(d_p)$ normalized to the total number of particles, ($\int_0^\infty p(d_p)d(d_p) = 1$). Usually a lognormal distribution is used as given by the expression

$$p(d_p) = \frac{\exp\left[-\frac{1}{2}\left(\frac{\ln(d_p/dp_m)}{\ln(\sigma_g)}\right)\right]}{\sqrt{2\pi} N_p \ln(\sigma_g)} \tag{I.3.7}$$

where dp_m is the geometric mean of the distribution and σ_g is the corresponding standard deviation. A generalized mean diameter or moment ratio of the *PDF* is introduced and defined as:

$$dp_{mn} = \left[\frac{\int_0^\infty p(d_p)d_p{}^m d(d_p)}{\int_0^\infty p(d_p)d_p{}^n d(d_p)}\right]^{1/(m-n)} \tag{I.3.8}$$

where the integral is extended from 0 to infinity. As an example, the first order moment, d_{10}, is, by definition, the average diameter $\overline{d_p}$.

By taking into account the polydispersity, the average diameter, the soot volume fraction, the scattering and the absorption coefficients of an ensemble of polydisperse particles become

$$dp_{10} = \int_0^\infty p(d_p)d_p\, d(d_p) \tag{I.3.9}$$

$$f_v = \frac{\pi}{6} N_p\, dp_{30}{}^3 \tag{I.3.10}$$

$$K^a_{vv} = \frac{F(m)}{4}\left(\frac{\pi}{\lambda_{scatt}}\right)^4 N_p \int_0^\infty p(d_p)d_p{}^6 d(d_p) = \frac{F(m)}{4}\left(\frac{\pi}{\lambda_{scatt}}\right)^4 N_P\, dp_{60}^6 \tag{I.3.11}$$

$$K_{abs} = -\frac{\pi^2}{\lambda_{ext}} \text{Im}\left\{\frac{m^2-1}{m^2+1}\right\} N_P \, dp_{30}^3 \qquad (I.3.12)$$

The corresponding relationships for the particle number density and an average value of the particle diameter, dp_{63}, obtained by rationing this time Eqs. (I.3.11) and (I.3.12), are:

$$N_p = \frac{6f_v}{\pi \, dp_{30}^3} \qquad (I.3.13)$$

$$dp_{63} = \overline{d_p} = \lambda \left(\frac{4E(m)\,K_{vv}}{\pi^2 F(m)\,K_{abs}}\right)^{1/3} \qquad (I.3.14)$$

where dp_{63} is given by the following moments ratio:

$$dp_{63} = \left(\frac{dp_{60}^{\,6}}{dp_{30}^{\,3}}\right)^{(1/3)} \qquad (I.3.15)$$

The previous relationship shows that particle number concentration N_p can be derived only if d_{63} can be related to d_{30}, once the size distribution is known. In the work performed by Douce et al. [114], the size distribution of the primary particle diameter have been measured in the case of soot formed behind reflected shock waves and for different hydrocarbons, highly diluted in argon. Table I.3.1 summarizes these results. It was shown that the distribution can be considered as log-normal with a standard deviation reaching a maximum of 0.17.

Different results have been obtained by Baurle et al [115], who found a value for σ_g of 0.2. From TEM measurements performed on benzene/acetylene, and acetylene/hydrogen mixtures diluted in Argon, Knorre et al. [116] obtained a value of $\sigma_g = 0.15 \pm 0.05$.

Hydrocarbon	T_5 (K)	P_5 (kPa)	d_p (nm)	σ_g
Toluene	1560	1333	31.7	0.12
"	1700	1714	25.9	0.15
"	2000	1433	17.8	0.10
n-Hexadecane	1702	879	22	0.13
"	1840	995	23.9	0.15
"	1911	697	20	0.14
n-Heptylbenzene	1630	751	18.5	0.13
"	1769	834	20.4	0.14
"	1960	914	16.4	0.17

Table I.3.1: *Mean diameter of the primary particles measured behind reflected shock waves using TEM analysis (Douce et al. [114])*

By taking into account these literature data, in this work an average value of $\sigma_g = 0.17$ for the geometric standard deviation of the distribution is used. These small values confirm the very narrow width of the primary particles size distribution.

The corresponding ratio $(dp_{63}/dp_{30})^3$ can be easily calculated by considering the definition of the moment ratio given in Eq. (I.3.8), giving a value of about 1.29. Then the particle number concentration results to be

$$N_p = \frac{6}{\pi} \frac{f_v}{\overline{d_p}^3} 1.29 \tag{I.3.16}$$

It is important to specify that dp_{63} is a definition of an average value, which is different from the arithmetic mean of the particle diameter. For simplicity, in the following paragraphs the average particle diameter will be indicates as $\overline{d_p}$.

3.3 Dissymmetry ratio optical technique

The Rayleigh scattering technique presented in the previous section allows to derive soot particle diameter and number density by considering isolated soot spherules of relatively small diameter. However, TEM analysis of soot morphology shows that soot is mainly composed by aggregates of individual primary particles. In order to investigate soot morphology and the aggregation process, in this paragraph another technique is presented.

To this purpose, we introduce the following definitions. The dissymmetry ratio $R_{pp}(\theta)$ is defined in terms of the ratio of differential scattering cross-sections at the angles θ and $180°-\theta$ as (Fussey et al. [117], Felske et al. [118], di Stasio et al. [119, 120, 121]):

$$R_{pp}(\vartheta) = \frac{C_{pp}(\vartheta)}{C_{pp}(180-\vartheta)} \tag{I.3.17}$$

where pp refers to a polarization combination (of the source and the detection). In the literature a general definition can also be found, concerning the ratio of the scattering cross-section at two different and generic scattering angles:

$$R_{pp}(\vartheta_1/\vartheta_2) = \frac{C_{pp}(\vartheta_1)}{C_{pp}(\vartheta_2)} \tag{I.3.18}$$

In the last case the two angles, with the subscript 1 and 2, have to be specified. The dissymmetry ratio is proved to be quite insensitive to the variation of the soot optical properties (n, k) in the range of the values typical of soot (di Stasio [121]). For this reason, it results to be a powerful tool to characterize the scattering pattern in relation to its dependence on the scattering angle. In the Rayleigh regime, the vertical-vertical Rayleigh scattered intensity presents no dependence on the scattering angle, resulting in no dissymmetry: $R_{VV}=1$. Even with sphere-like particles usually the dimensions are such that no measurable dissymmetry is produced. For example, with $x_p \leq 0.25$ the deviation of R_{VV} from 1.0 is within the usual limits of experimental error for measurements in flames (Felske et al. [118]). In this case, the combination of the scattering and the extinction measurements allows to derive the dimension of the soot primary particle, as shown in the previous paragraph. When aggregation effects occur and soot is characterized by chain-like or cluster structures, the

scattering pattern changes significantly with respect to the Rayleigh regime. According to soot morphology, different shapes of the angular distribution of the scattering light are obtained. In Fig. I.3.1, the numerical results obtained by di Stasio et al. [119] with the same number N_p of primary particles of different diameters and different structure of the aggregate are reported. As it is evident from this figure a strong dependence on the morphology is obtained, changing from 1D linear chain up to the fractal cluster. For each morphology, a significant dependence on the particle size is also shown. It is observed that the forward scattering intensity (angles between 0 and 30°) is independent of the diameter of the spherules and it gives directly the number of primary particles in the aggregate.
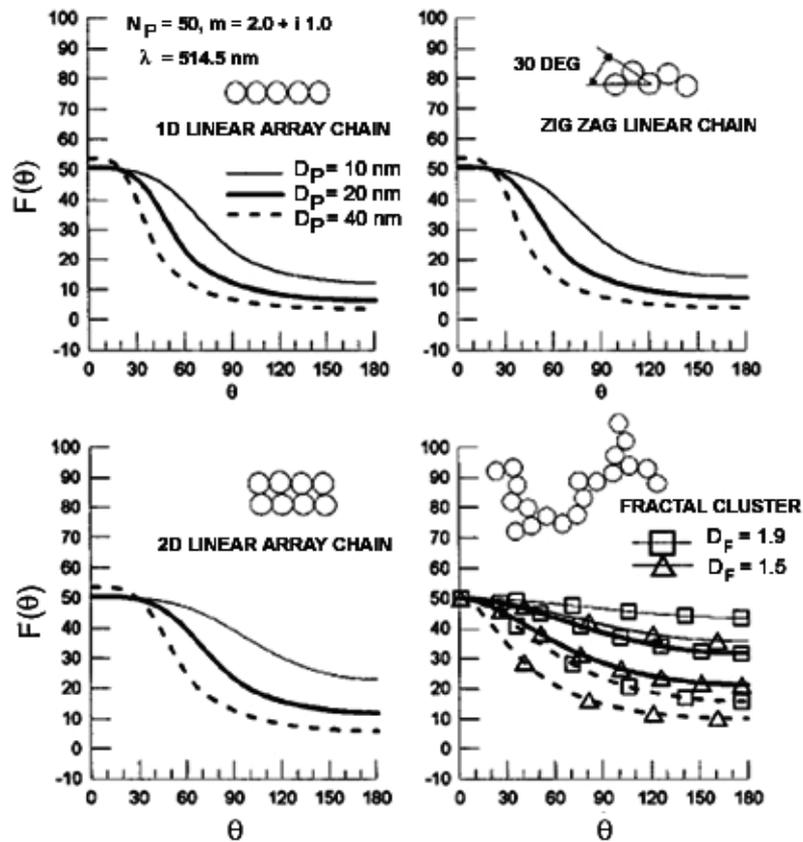
Fig. I.3.1: *Structure factor versus scattering angle for different soot morphology (di Stasio et al. [119]).*

Strictly related to the scattering patterns are the dissymmetry ratios, as reported Fig. I.3.2. Here the dependence of the dissymmetry with respect to the number density N_p is shown for d_p=10 nm (panel a, on the left) and d_p = 40 nm (panel b, on the right). In each panel different ratios are reported in relation to different scattering angles. As it can be seen, depending on the particular behavior of the scattering intensity versus the scattering angle,

one can evaluate the morphology with a proper choice of the angles at which the dissymmetry ratios are considered.
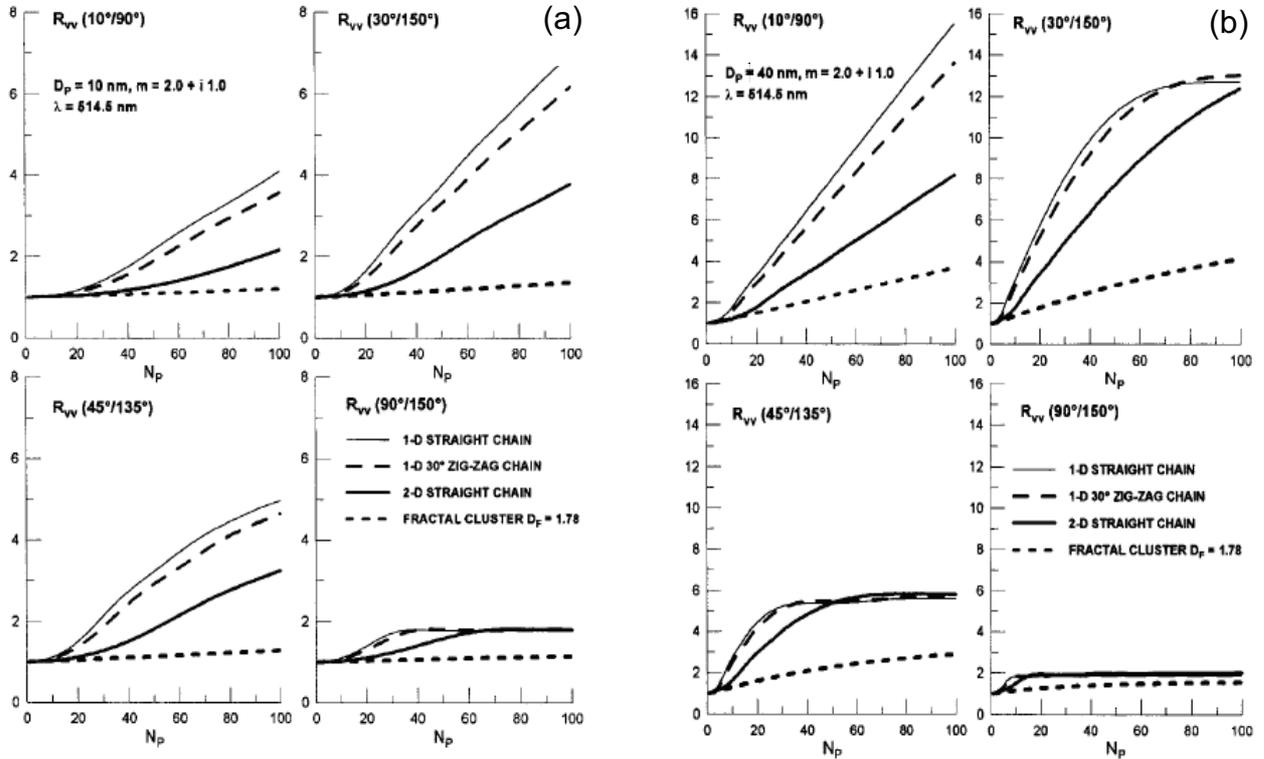
Fig. I.3.2: *Values of dissymmetry ratio at different angles versus N_p and for small $(d_p=10$ nm$)$ and large $(d_p=40$ nm$)$ particle diameter (di Stasio [119]).*

This is evident in Fig. I.3.2. The more regular the increasing of the dissymmetry ratio with the number N_p, the higher the sensitivity of R_{vv} to the morphology. Then, we can infer that $R_{vv}(10°/90°)$ is the most sensitive curve. This trend is the same independently of the particle diameter considered. Considering the other curves, we can see that moving at higher N_p a bending in the trend is detected. For this reason, the dissymmetry ratio $R_{vv}(30°/150°)$ is more sensitive than $R_{vv}(45°/135°)$, while $R_{vv}(90°/150°)$ exhibits a lower sensitivity, due to the bending in its trend with N_p.

From these observations it is clear that the choice of a number of certain scattering angles, and the corresponding dissymmetry ratios, can be considered a feature which allows to identify unambiguously soot morphology and aggregation. In the work of di Stasio et al. [119], by comparing numerical approach with experimental data taken from other authors, it was also found that the selection of three scattering angles is enough to yield such information.

3.4   Fractal-like approach

Investigations of soot morphology performed by means of thermophoretic sampling and TEM analysis have shown that soot particles in some environments as in flames consist of ramified aggregates of primary particles. These monomers are approximately spherical, non-overlapping, and with a quite uniform diameter. As these clusters present a fractal-like character, in order to derive soot morphology parameters the use of optical properties of mass fractals have been proposed by many authors in conjunction with Rayleigh-Debye-Gans (R-D-G.) theory (Dobbins et al. [96], Kerker [111], Koylu and Faeth [112]). With this approach, each primary particle acts as a dipole source for scattering radiation and the difference in phase of the light scattered from separate particles determine the overall scattered field. The fractal description was found to be appropriate even in the case of a small number of primary particles (Np=5) (Megaridis et al. [95], Mountain et al. [122]).

According to the mass fractal approximation, the relationship between the primary particle diameter and the number of these particles within an aggregate (N) is given by Botet and Jullien [123]:

$$N = k_f (R_g / d_p)^{D_f} \qquad (I.3.19)$$

where R_g is the radius of gyration of an aggregate, D_f the fractal dimension (or Hausdorf dimension), and k_f a constant fractal prefactor. The radius of gyration is defined as:

$$R_g{}^2 = \frac{1}{n} \sum_i r_i{}^2 \qquad (I.3.20)$$

where r_i is the distance of the ith primary particle to the center of mass of the aggregate. As reported in the literature from TEM measurements, the value of D_f is found to be in the range of 1.7-1.9 (Oh et al. [124], Samson et al. [125]); anyway, in premixed flames a lower value is obtained (Chakrabarty et al. [126]).

According to R-D-G theory (Dobbins et al. [96], Kerker [111], Koylu and Faeth [112]), the scattering cross section of a vertically polarized light scattered from an aggregate results to be:

$$C_{vv}^a = C_{vv}^p N^2 S(qR_g)$$

(I.3.21)

In this equation, the relationship $S(qR_g)$ is the optical structure factor, which depends on the radius of gyration and the scattering angle through the scattering wave vector q. This last parameter is defined as:

$$q = \frac{4\pi}{\lambda} \sin \theta / 2$$

(I.3.22)

A typical cluster characteristic is the squared dependence of the cross section on N. In other words, the total scattering from an aggregate is N times larger than the scattering from an aggregate at the Rayleigh limit.

The vertically polarized scattering intensity from N_a monodisperse aggregates per unit volume is given by adding the contribution from individual aggregates

$$I_{VV}^m(\theta) = \eta I_0 N_a C_{vv}^p N^2 S(qR_g)$$

(I.3.23)

As for the structure factor, two limiting cases are well known in the literature: the Guinier function, which describes the scattering behavior at small angles, and the power-law regime for large angles (Puri et al. [98], Dobbins et al. [96], Koylu and Faeth [112, 127], Dobbins et al [128]). The two analytical expressions are given by

$$S(qR_g) = \exp\left(-\frac{q^2 R_g^2}{3}\right) \qquad \textit{Guinier regime,} \quad q^2 R_g^2 \ll 1$$

(I.3.24a)

$$S(qR_g) = (qR_g)^{D_f} \qquad \textit{power-law regime,} \quad q^2 R_g^2 \gg 1$$

(I.3.24b)

An exhaustive study of several expressions for the structure factor can be found in the literature, covering the whole range of qR_g (Sorensen et al. [129]). In the same paper Lin et al. have proposed the following expression:

$$S(qR_g) = \left[1 + \sum_{s=1}^{4} C_s (qR_g)^{2s} \right]^{-D_f/8} \tag{I.3.25}$$

where $C_1=8/(3D_f)$, $C_2=2.5$, $C_3=-1.52$ and $C_4=1.02$. This polynomial function, valid for whatever scattering angles, almost overlaps other curves reported in the same work.

Recently, Teng and co-workers [130] proposed another expression for the structure factor, which has the same structure as Eq.(I.3.25), but with only two terms (the first and the fourth), and the relative coefficient given by $C_1=8/(3 D_f)$ and $C_4=1$.

Then, if one is able to derive the value of the radius of gyration from such scattering measurements, the parameters characterizing the soot particles as the primary particle diameter and number density can be deduced.

In the literature different approaches have been applied. The most common is to perform scattering measurements at different angles. Then, the expressions of the structure factor given by Eqs. (I.3.24a) (I.3.24b) are used (Charalampopoulos [93], Megaridis et al. [95], Dobbins et al. [96], Sorensen et al. [129]). Generally from the Guinier relationship the radius of gyration is determined, while in the power regime, the measurement of the fractal dimension can be derived. In the following this procedure is described.

In the Guinier regime, measurements performed at small angles, in the forward scattering direction, are taken into account. Eq.(I.3.24a) is expanded in the Taylor's series. Being the scattering intensity proportional to the structure factor, according to Eq. (I.3.23), the following relationship is obtained:

$$I^m{}_{VV}(\theta) \approx 1 - \frac{q^2 R_g{}^2}{3} \tag{I.3.26}$$

The scattering intensity is plotted versus q^2 and fitted with a straight line, whose angular coefficient gives the radius of gyration.

Now the scattering signal in the backward direction is considered. In this regime, the scattering intensity is proportional to the relationship given in Eq. (I.3.24b).

$$I^m{}_{VV}(\theta) \approx \left(q^2 R_g{}^2 \right)^{-D_f/2} \tag{I.3.27}$$

By taking the logarithmic of both the right and the left sides the following expression can be written:

$$\ln(I_{VV}(\theta)) \approx -D_f \ln(qR_g)$$ (I.3.28)

This equation is plotted in double logarithmic scale and fitted with a straight line. From the slope, the fractal dimension can be derived.

Up to now, in these relationship the polydispersity has been neglected. As different aggregates consist of a different number of monomers, the polydisperse population of aggregates has to be taken into account. For that, it is necessary to introduce a probability distribution function $p(N)dN$, which gives the fraction of aggregates with a number N of primary particles. From *TEM* analysis it was found that the function which reproduces quite well such a probability distribution is a lognormal. The relative expression is the same as Eq.(I.3.7) written in terms of N (Cai et al. [70], Megaridis et al. [95], Koylu and Faeth [112], Koylu et al. [131]), that is:

$$p(N) = \frac{\exp\left[-\frac{1}{2}\left(\frac{\ln(N/N_m)}{\ln(\sigma)}\right)^2\right]}{\sqrt{2\pi}N\ln(\sigma)}$$ (I.3.29)

where N_m is the geometric mean of the primary particles per aggregate and σ is the standard deviation. The value of $\sigma = 2.1$ is widely accepted by other authors (Dobbins et al. [96], Koylu and Faeth [112]). The related qth moment of the probability density function is defined as:

$$\overline{m_q} = \int_0^\infty N^q p(N)dN$$ (I.3.30)

From this definition, $\overline{m_1}$ is the mean value of the number density of the monomers in a cluster. The averaged scattering signal from a polydisperse ensemble of aggregates results to be (Dobbins et al. [96]):

$$I_{VV}^{p}(\theta) = \eta I_0 C_{vv}^{p} N_a \int N^2 S(qR_g) p(N) dN \tag{I.3.31}$$

By considering the expressions of the structure factor given in the right side of Eqs. (I.3.26) (I.3.27), Eq. (I.3.31) can be re-write in the two regimes as follows:

$$I_{VV}^{p}(\theta) \approx \int \left(1 - \frac{q^2 R_g^{\ 2}}{3}\right) p(N) dN \approx 1 - \frac{1}{3} q^2 \int R_g^{\ 2} p(N) dN = 1 - \frac{1}{3} q^2 \overline{R_g^{\ 2}} \tag{I.3.32}$$

$$I_{VV}^{p}(\theta) \approx \int \left(q^2 R_g^{\ 2}\right)^{-D_f/2} p(N) dN \approx \left(q^2 \overline{R_g^{\ 2}}\right)^{-D_f/2} \tag{I.3.33}$$

In the previous relationship a new definition of the mean radius of gyration is introduced, which can be expressed as:

$$\left(\overline{R_g^{\ 2}}\right)^{1/2} = \left(\int R_g^{\ 2} p(N) dN\right)^{1/2} \tag{I.3.34}$$

According to the polydispersity, extinction and scattering coefficients can be written as:

$$K_{abs,pol} = \frac{\pi^2 dp^3}{\lambda_{abs}} E(m) N_a \overline{m_1} \tag{I.3.35}$$

$$K_{vv,pol}(\theta) = C_{VV}^{a} N_a = C_{vv}^{p} N_a \overline{m_2} S(q^2 \overline{R_g^{\ 2}}) = \frac{\pi^4 dp^6}{4\lambda_{scatt}^{\ 4}} F(\lambda) N_a \overline{m_2} S(q^2 \overline{R_g^{\ 2}}) \tag{I.3.36}$$

Then, a volume-mean diameter D_{30}, that is the volume of the sphere which gives the same contribution to the scattering as the cluster, is considered and defined as:

$$D_{30}^{\ 3} = dp^3 \overline{m_1} \tag{I.3.37}$$

Taking the ratio between scattering (Eq.(I.3.35)) and absorption coefficient (Eq.(I.3.36)) D_{30} can be calculated as follows

$$D_{30} = \frac{1}{\pi} \left(\frac{\lambda_{scatt}^{\;4}}{\lambda_{ext}} \right)^{1/3} \left[\frac{4\pi E(m) \, K_{vv,pol}(\vartheta)}{F(m) f_n S\left(q^2 \overline{R_g^{\;2}}\right) K_{abs,pol}} \right]^{1/3}$$

(I.3.38)

where f_n is given by:

$$f_n = \overline{m_2} / \left(\overline{m_1}\right)^2$$

(I.3.39)

While D_{30} is linked to the size of the scatterer, the radius of gyration is related to the structure of the aggregate, and their combination allows to derive the diameter of the soot primary particle. In fact, considering Eq. (I.3.37) and (I.3.19), written taken into account the polydispersity, d_p is derived:

$$d_p = \frac{D_{30}^{\;3}}{H \overline{R_g^{\;2}}}$$

(I.3.40)

where H is a complex moments ratio, given by

$$H = \frac{K_f \overline{m_1} \, \overline{m_2}}{\overline{m_3}}$$

(I.3.41)

when the fractal dimension is close to 2, which is the case for soot particles.

It is important to stress once more that the methodology presented in this paragraph and applied by many authors require to perform scattering measurements at different angles. A different, more suitable and less-time consuming approach will be addressed in this study and will be presented in the Chapter III.

3.5 Support from ex-situ analysis: soot sampling and TEM analysis

Transmission electron microscopy investigation of projected images from a set of aggregates allows to unambiguously evaluate size of the primary particles, geometric

dimensions, and projected areas of the aggregates. Soot particle diameter is derived by measuring the area of a particle usually placed at the periphery of aggregates. Due to the narrow primary particle size distribution, usually we refer to a single mean radius.

Let us consider each aggregate and define the geometric dimensions as the maximum projected length (L) and width perpendicular to L (W). The number of primary particles in an aggregate is related to the aggregate projected area ($A_a = \pi R_a^2$) and the mean primary particle cross section ($A_p = \pi a^2$) as follows:

$$N = k_a \left(\frac{A_a}{A_p} \right)^{\alpha} = k_a \left(\frac{R_a}{a} \right)^{2\alpha} \tag{I.3.42}$$

where k_a and α are empirical constants and R_a represents the area-equivalent radius. Extensive morphology analysis performed by Koylu [132] suggested that $k_a = 1.15$, while in other experimental investigations (Megaridis et al. [95], Koylu et al.[131]), it was used the value of $\alpha = 1.08$-1.09.

In order to determine the fractal dimension, the actual radii of gyration of the aggregates are required, whose value is not easily measured from the projected images. Several studies proved that for the estimation of D_f any other characteristic dimension of the aggregates can be used. As suggested by Koylu et al. [132], as the maximum length L scales with R_g in a regular manner, the outer radius of an aggregate ($R_L = L/2$) is used to this purpose. Then, the mass fractal relationship becomes

$$N = k_L \left(\frac{R_L}{a} \right)^{D_f} \tag{I.3.43}$$

Considering the log-log plot of N vs R_L/a and the least-squares fit, a linear trend is obtained where the slope is the fractal dimension and the intercept the logarithm of the correlation constant k_L. By comparing Eq (I.3.19) with Eq.(I.3.43) the following relationship can be easily derived:

$$\frac{k_f}{k_L} = 2^{D_f} \left(\frac{R_L}{R_g} \right)^{D_f} \tag{I.3.44}$$

where, in the right hand side the coefficient 2^{Df} results from considering in Eq. (I.3.19) the diameter d_p instead of the radius of the primary particle a. The evaluation of the radius of gyration is obtained according to the relationship:

$$\left(\frac{R_L}{R_g}\right) = \left[\frac{(D_f + 2)(D_f + 5)}{2D_f(D_f + 1)}\right]^{1/2} \tag{I.3.45}$$

which has been derived as follows. Hurd and Flower [133] proposed to introduce an exponential cutoff to the density autocorrelation function in order to take into account that this function falls to zero at the cluster perimeter. Finally, considering Eq. (I.3.44) and Eq. (I.3.45), the value of k_f can be calculated.

In principle, from TEM analysis information about all soot parameters, that is d_p, N, D_f, R_g and k_f can be derived. This technique, anyway, is characterized to be intrusive, difficult to be applied in hostile environment, and also time-consuming. For that, usually it is implemented only to perform a validation of optical techniques, for example in few positions of the system under study.

4 Soot formation and role of hydrogen addition: short overview

In the last few decades, many efforts have been spent to understand the formation and growth mechanisms of soot particles under different conditions. In this paragraph an overview of the works reported in the literature is given, relatively to the reactors employed in this study, the premixed flame and the shock tube, and to the gas used, ethylene. Moreover, work carried out on the role of additives, like hydrogen, in the soot formation mechanisms performed in such apparatus, are also presented.

4.1   Premixed flames

A great number of studies on soot in rich premixed flames are reported in literature. These studies are mainly devoted to the understanding of the chemical kinetics mechanisms for

- soot precursors and soot nucleation
- soot growth and oxidation
- fuel structure and additives
- coagulation and aggregation

The main goal of these studies is the development of models able to predict species concentration and soot yield in a variety of experimental conditions. Because of the hazard for human health of soot emission from combustion systems many studies are also devoted to understand some physical process such as

- coalescence of ultrafine nanoparticles in larger primary particles during or after the nucleation process
- aggregation of soot primary particles in large fractal aggregates.

All these physical and chemical phenomena are strictly linked together and, in spite of the enormous amount of experimental, theoretical and numerical studies, a clear picture of all the mechanisms is not yet achieved.

<u>Soot precursors and soot nucleation</u>

The influence of PAH and other species on the early stages of soot formation was investigated by optical techniques (D'Alessio et al. [134] and by on-line gas chromatography and mass spectrometry (Marinov et al. [135], Tregrossi et al. [136], Melton et al. [137]). Combinations of scattering, extinction and fluorescence in the UV and VIS part of the spectrum were used to study PAH, high molecular weight species and nanoparticles in premixed flames of different fuels (Ciajolo et al. [138], D'Alessio et al. [139], Minutolo et al. [140], Ciajolo et al. [141]).

It was early recognized from spectroscopic measurements that carbonaceous nanoparticles originating from the condensation of precursors in the nucleation region are different from soot at later stages of growth (Minutolo et al. [142, 143, 144]). Aromatic

structures, absorbing in the UV, are formed at a C/O ratio well below the soot formation threshold (Minutolo et al. [143]). These structures are attributed to 1- and 2-ring functionalities present as polymeric structures with typical size around 2 nm in the pre-inception zone. These structures polymerize through resonantly stabilized radicals forming open structures that grow to yield nanoparticles that subsequently dehydrogenate to form soot. The inception of soot particles consists in the progressive aromatization of the initially "transparent" structures. The massive growth of soot particles takes place only when the aromatization has largely progressed. The 2-3 nm sized organic carbon (OC) particulates was also detected by extra situ sampling showing an higher solubility in water than both soot particles and mature aromatic particles transforming into soot with spectral signatures in agreement with the one in flames (Sgro et al. [145, 146]).

In order to further elucidate the mechanism of soot inception by PAHs molecules the molecular-beam high resolution mass-spectrometry and REMPI (resonance enhanced multiphoton ionization) technique (Weilmunster et al. [147]) have been applied.

These and other studies contributed to the understanding of the detailed chemistry mechanisms for soot formation (Richter et al. [148], Appel et al.[149], D'Anna et al. [150], Krestinin [151], Richter et al. [152]).

Soot growth and oxydation

A wide discussion about the gas molecules responsible of soot growth is reported in the literature. Early experimental studies (Bonne et al. [153], Homann et al. [154]), based on mass spectral measurements of post flame gases, indicated that only the largest observed polyacetylenes (as C_8H_2 and $C_{10}H_2$), were important as surface growth species. Lahaye et al. [11] suggested that polyacetylenes or polyaromatics could be important for surface growth, while D'Alessio et al. [155] was not in agreement with such observations.

The role of the acetylene was also studied by Harris on a premixed ethylene/air flames. The increased growth rate was explained by the increased surface area available for growth. The reaction of acetylene with soot particles is the major mechanism.

In most of these early studies optical techniques have been developed and applied (D'Alessio et al. [155, 156], Flower [157]). Detailed modeling of soot particle nucleation and growth in laminar premixed flames, taking into account fuel pyrolysis, PAH formation, their planar growth and coagulation into spherical particles and finally surface growth and particle oxidation, were developed (Frenklach [29]). The model predicts the formation of PAHs, their coagulation into clusters and cluster coagulation, and surface growth due to chemical and

physical process. The model also predicts the classical structure of soot particles: a less dense particle core, composed by randomly oriented PAH oligomers, and a more dense concentrically-arranged particle shell.

The state of the art of the soot formation studies was summarized in a fundamental book (Bockhorn [15]) where the hydrogen-abstraction/carbon-addition (HACA) mechanism was used to predict surface growth rates (Frenklach et al. [29]). Several experimental studies confirmed the validity of the HACA mechanism in premixed flames of different fuels (Xu et al. [58, 59]. More recent studies have proposed a polymerization mechanism in parallel with the HACA mechanism.

Fuel structure and additives

Early studies were devoted to understand the effects of metal containing fuel additives on soot emission (Bonczyk [158]). The formation of metal oxides, particularly with iron addition, and their subsequent oxidation of solid carbon to CO and CO_2 has been proposed as a soot reduction mechanism especially in the soot burnout zone (Hahn et al. [159]).

Different fuels and additives are also used to elucidate particular pathways for soot formation (Atakan et al. [61], Menon et al. [63]).

Oddly, in spite of the great interest in hydrogen blended fuels for increased flame stability and pollutant reduction, studies on H_2 hybrid fuels in premixed flames can not be found. There are several papers dealing with diffusion and turbulent flames but, to our knowledge, no one devoted to the investigation of the effects of hydrogen addition on soot formation mechanisms.

Coagulation and aggregation

The characterization of soot particle in rich-conditions premixed flames have been carried out by applying optical diagnostics technique as LII, scattering/extinction as well as sampling and TEM analysis. Many works are reported in the literature on this subject. Concerning scattering/extinction, the fractal approach in conjunction with the R-D-G theory have been applied, as reported in this Chapter. With such measurements, information about soot yield, primary particles and aggregation are derived (Dobbins et al. [96]).

As for the coagulation, this process is studied by applying the theory of Brownian coagulation with the Smoluchowski equation with particular emphasis to high pressure conditions (Holdges et al. [160], Kazakov et al. [161]).

4.2   Shock tubes

The soot tendency of a given fuel (or mixture of fuels) is assessed, experimentally, in shock tubes through measurements of different parameters that are characteristics of different processes in the soot production:

1. the induction delay time, that is the time needed in order to form, from the initial gaseous fuel, the first nuclei of solid particles;

2. the soot growth rate, through the evaluation of the soot surface growth constant which defines the rate at which soot increase in size by surface chemistry through the contribution of gaseous species that stick to the surface of the soot;

3. the soot yield, this parameter indicates the efficiency of carbon conversion from the fuel to soot

These parameters can be easily deduced if the soot volume fraction is measured as a function of time.

If samples are taken at the end of the process, by using a transmission electron microscope at different magnifications, one can derive both:

1. the aggregate arrangement and size,

2. the average diameter of the primary particles,

3. the structure of the primary particles, which is the arrangement of the carbon layers that constitute the soot itself.

In this part, a review of these different parameters will be done for ethylene based mixtures when possible and for aliphatic fuels. Moreover, a description of the diagnostic techniques applied to the shock tube to derive soot parameters is presented.

Soot induction Delay Times

One of the most important parameter to characterize a fuel tendency to form soot is the induction delay time. This delay is defined as the interval time between the moment at which the fuel mixture is heated to a given temperature and the moment where soot particles appear. This delay (labeled τ_{ind}) depends on the fuel nature, the mixture equivalence ratio and, finally, at a lower extent, on the pressure.

A large number of studies have been performed using shock tube, the first one goes back to 1958 (Hooker [162]) and concerned acetylene tendency to form soot. Since then,

numerous studies have assessed this parameter for aliphatic compounds, from methane (Fussey et al. [117], Kelleler et al. [163, 164]) up to n-heptane (Kelleler et al. [163, 164]) and even heavier fuels such as n-decane and 2,2,4,4,6,8,8-heptamethylnonane (Mathieu et al. [165]) as well as aromatic ones such as toluene (Wang et al. [166], Alexiou [167], Douce et al. [168], Mathieu et al. [169]) and heavier ones such as α-methylnaphtalene Douce et al. [169].

From these studies, the general trend can be drawn: soot induction delay times decrease exponentially as the temperature is raised. Usually, they are expressed using a modified form of the Arrhenius Law:

$$\tau_{ind} = A[HC]^a \cdot [O_2]^b \cdot [Diluent]^c \cdot \exp\left(\frac{E}{RT}\right) \qquad (I.4.1)$$

with τ_{ind} the induction delay time of soot formation; R the perfect gas constant; T the temperature; E the activation energy; [HC] the hydrocarbon concentration; [O$_2$] the oxygen concentration; [Diluent] the diluent concentration and a, b, c the exponents over the concentrations.

In the pyrolysis configuration where there is no oxygen in the mixture, the exponent over the hydrocarbon concentration is negative, between -1 and 0, which indicates that increasing the hydrocarbon concentration lowers the induction delay time, as for the diluents' exponent, in most of the studies, it is fixed to zero. The activation energy varies according to the nature of the hydrocarbon and varies between 100 and 250 kJ mol^{-1}.

When oxygen is present in the mixture, depending on the type of fuel a decrease or a slight increase of the induction delay time is observed, usually the exponent over the oxygen is positive but lower than 1. The activation energies, in this case, are slightly higher than the ones obtained in pyrolysis conditions, between 160 and 270 kJ mol^{-1}.

As for ethylene based mixtures, the same tendency has been observed by different authors (Fussey et al. [117], Muller et al. [170], Kelleler et al. [163, 164]). However, Bauerle et al [115] did not see any effect of the carbon concentration on soot induction delay times, while Fussey et al [117] and Kellerer et al. [163] have shown a promoter effect as resulted from negative coefficient over the fuel (Table I.4.1). As for the activation energy, it seems that there is a disagreement between two groups of authors, Muller et al [170] and Kellerer et al [163] give an activation energy around 130 kJ mol^{-1}, while Bauerle et al [115] and Tanke

[171] found values twice higher than the previous authors. The pressure domain does not seem to be the key factor in this disagreement.

Ethylene / Argon Mixtures				
Authors	A $(s.(mol.m^{-3})^{-a})$	a	E_{ind} $(kJ.mol^{-1})$	P (bars)
Fussey et al. [117]	/	-0,23	/	1-2 et 10-12
Müller et al. [170]	/	/	125	40
Bauerle et al. [115]	/	/	215	50
Tanke [171]	$3,24.10^{-10}$	< 0,4	216	6 et 110
Kellerer et al. [113]	$3,15.10^{-8}$	-0.45	141	15-100

Table I.4.1: *Summary of the Arrhenius parameters of the induction delay time expression*

in the case of ethylene pyrolysis, $\tau_{ind} = A[C_2H_4]^a \exp\left(\dfrac{E}{RT}\right).$

<u>Soot Growth Constant</u>

Following the nucleation phase that leads to the first soot nuclei, the soot load will increase by coagulation of the small primary particles, leading to new spherical ones, and by the growth of each particles due to surface reactions between the gaseous species and the soot itself. This last process is generally described assuming a first order law (Matzing et al. [172], Bohm et al. [173], Tanke [171], Kelleler et al. [163], Baurle et al. [115]) already reported in this chapter.

The soot growth constant K_g, which depends strongly on the particle diameter, is then expressed as:

$$k_g = A_g [HC]^a \exp\left(-\frac{E_g}{RT}\right) \tag{I.4.2}$$

with A_g the pre-exponential factor, *a* the exponent over the fuel concentration, E_g the activation energy, *R* the perfect gas constant and T the temperature.

Most of the studies, in which the surface soot growth constant has been derived, were performed for the pyrolysis conditions. The soot growth constant usually does not vary monotonically with the temperature. In the case of ethylene pyrolysis, the soot growth constant reaches a maximum between 1900 and 2000 K (Tanke [171], Knorre et al. [116]). Then, two different activation energies of opposite signs can be derived as it is summarized in Table I.4.2.

Ethylene / Argon mixtures								
Authors	P (bars)	$[C_2H_4]$ (mol.m^{-3})	a	T_{max} (K)	A_g (s^{-1}.mol^{-1}.m^3)		E_g (kJ.mol^{-1})	
Bauerle et coll. (1994)	6-100	30-700	1	2000	/	/	~200	/
Tanke (1994)	25-100	3.9-12	1	1910	$2.09.10^8$	1.51	205	-93

Table I.4.2: *Summary of the Arrhenius parameters of soot growth constant expression in the case of ethylene pyrolysis,* $k_g = A_g [HC]^a \exp\left(-\dfrac{E_g}{RT}\right).$

Soot yield

After the fast soot volume fraction increase, the soot growth slows down and eventually stops after a period of time between 1 and 3 ms in shock tubes. From the maximum soot volume fraction obtained behind reflected shock waves, the amount of carbon atoms transformed as soot can be assessed assuming the following hypotheses:

- soot contains mainly carbon atoms, hydrogen contain being negligible,

- the primary particles are spherical,

- their size is small compared to the wavelength at which extinction is measured (usually 632.8 nm),

- the extinction signal can be inferred only to soot particles.

Given the initial carbon concentration, then the soot yield is derived by dividing the carbon concentration as soot by the initial carbon concentration in the gas phase (as fuel).

A great number of studies have addressed the characterization of the soot yield. Frenklach et al. [174] have shown the important effect of the temperature on the soot yield.

They have shown that the soot yield exhibits a bell-shape curve with the temperature. Hence, there is an optimal temperature for which the soot load is maximum. But also, below a given temperature (around 1400 K) no soot can be formed while there is no limit on the high temperature side (Douce et al. [168] and Mathieu et al. [169]). The same group has shown that this optimal temperature shifts towards lower values when the initial pressure is increased. In the early work of Graham et al. [32] it was shown that the soot load increases with the initial carbon concentration, and finally Bauerle et al. [115] demonstrated that increasing the initial pressure of the mixture will lead to an increase in the soot yield.

In the literature, one find mainly studies on linear hydrocarbon with a long chain (Hwang et al. [175], Tanke [171], Kelleler et al. [163, 164], Bauerle et al. [115]).

Concerning ethylene pyrolysis, Bauerle et al. [115] have shown that the optimal temperature is close to 1850 K.

Diagnostic techniques for soot measurements in the shock tube

A large part of the studies reported in the literature is focused on the application of light extinction technique to soot volume fraction measurements (Goos et al. [176], Mathieu [177], Douce et al. [168], Wang et al. [166], Frenklach et al. [174], Bauerle et al. [115], Alexiou et al. [167], Graham et al. [74, 75]). In this way, soot parameters (e.g. the induction delay time, the soot yield and soot formation rate) can be evaluated for different fuels under different conditions. For example, in the work of Bauerle et al. [115], measurements up to 100 bar have been performed. The extinction technique has been implemented by using the typical red line of the He-Ne laser or, as in some works (Knorre et al. [116], Graham [74]), using different infrared sources, like 1064 nm or 3.39 µm. To the same purpose, thermal radiation and extinction measurements were also carried out at different wavelengths (Tsuboi et al. [178], Emelianov et al. [179], Knorre et al. [116]), allowing to derive also soot temperature, as described in Chapter II.

For a deeper investigation of soot formation, knowledge about the soot particle sizing and growth is required. The application of a sampling technique and TEM analysis (Evans et al. [180]) allows to have information about soot particle only at the end of the shock wave run, and not to follow all the stages of soot growth. Optical non-intrusive diagnostics, such as the scattering/extinction technique, allow to overcome this limitation. Although this technique is well developed in both diffusion or premixed stationary flames (Dobbins et al. [128], Sorensen et al. [129], Teng et al. [130], Puri et al. [98], Kelleler et al. [164], De Iuliis et al. [181]), few works are present in the literature on the application in shock tubes. In the

seventies Graham [74, 75] was the first to introduce this method for measurements in a shock tube. In one of his papers, this author investigated light scattering behaviour of soot aerosol with an excitation laser modulated in polarization. The anisotropy of the particles allowed to study soot coagulation in the regime of free molecular flows. This method was also applied by di Stasio [119, 120] to analyze the morphology of soot aggregates at high pressures and temperatures. Many years later, an important contribution was given by Kellerer and co-workers [163182, 182]. They investigated pyrolysis and oxidation of different hydrocarbons in a wide range of pressure (up to 100 bar) and temperature. Anyway, even if a huge work was performed by these authors, a deep description of the diagnostics and the relative limitation was not clearly presented. To our knowledge, no other works are reported in the literature on these measurements, or simply on the application of the scattering diagnostics to the shock tube in other experimental conditions. This is probably due to the fact that this kind of diagnostics is not straightforward.

CONCLUSIONS

From the state of the art, we can infer that a comprehension of the mechanisms responsible of soot formation and the relative role of hydrogen is not completely achieved. A deeper investigation should still be performed concerning, for example, the structure of soot particulate in a wide range of experimental conditions. In brief, the following observation can be made.

1. The study of premixed flames in the fuel rich conditions is an important point for the development of chemical kinetics codes.

2. The influence of hydrogen addition on soot formation mechanisms is not well investigated. Few works concern the investigation on diffusion flames, while no data are available for example in a premixed flame and in a shock tube.

3. Besides the concentration, soot structure and morphology is not well studied under different conditions, as for example in the shock tube. The development of a proper diagnostic technique, as the scattering/extinction is mandatory.

Concerning the last point, it was already observed that the scattering/extinction has been widely applied in flames but few data are available in a shock tube. In this context, the main goal of this work thesis can be summarized as follows:

1. Development of a three angles scattering/ extinction technique applied on a premixed flame in order to investigate soot concentration, dimension and morphology.

2. Investigation of the role of the wavelength used for extinction measurements.

3. Extension of this diagnostic technique to the shock tube, analysing the difficulties and the limitation.

4. Investigation of the role of hydrogen addition on soot formation both in the premixed flame and in the shock tube.

Measurements in premixed flames are carried out in the CNR laboratory in Milano, where experimental facilities and experience in the application of optical diagnostics technique in combustion systems are widely available. For the shock tube, the measurements have been carried out in ICARE-CNRS laboratories in Orleans. The French researchers have been widely recognized to be expert in combustion and chemical kinetics.

Some considerations about the two laboratory reactors used are given. Shock tube and flame are quite different, and in some way complementary, as they allow to perform the study in different conditions of temperature and pressure. In Table I.4.3 some relevant characteristics of the two reactors are compared.

PREMIXED FLAME	SHOCK TUBE
Homogeneous Combustion (gas, p, Φ)	Homogeneous Combustion (gas, p, T, Φ)
Time/Temperature Coupling	Time/Temperature de-coupling
Not-resolved soot inception	Time-resolved soot formation
Flame front spatially identified	Single parameters analysis– for Kinetics

Table I.4.3: *Comparison between the two laboratory reactors.*

In the first line ϕ refers to the equivalence ratio, p and T are the pressure and the temperature.

Although flames are closer to practical systems, such investigation is not easy to perform, as a strong coupling of time and temperature is present.

Usually, in fact, the investigation is carried out along the flame axis, which corresponds to the reaction time, where strong temperature gradients are present. The limited region of the flame results in a low temporal resolution and the typical soot growth processes occur almost at the same time.

Then, it is difficult to detect unambiguously the soot inception region and aggregation processes can be important. As observed with TEM analysis, soot is more likely in the form of clusters, especially high in the flame, and the polydispersity of the number of primary particles per aggregate has to be considered. In contrast, the distribution of the primary particles diameter is approximated to be monodisperse. Moreover, depending on the experimental conditions problems of mixture inflammability and flame stability can result.

In the shock tube the experimental conditions, e.g. pressure and temperature, remain constant during the observation time (some milliseconds). During this period, it is possible to follow with a good resolution time the evolution of soot formation and growth. The main advantage of the shock tube is the ability to perform a parametric study of such mechanisms, that is particularly interesting for chemical kinetic modeling. In this context, it is easy to imagine, as it will be proved in this work, that inception and surface growth are more important than aggregates formation. For that, by applying the dissymmetry ratio technique, the polydispersity of soot primary particle diameters is taken into account and aggregation processes have been investigated.

II.   *Experimental*

INTRODUCTION

This chapter is divided in two sections according to the two experimental set-ups used for soot investigation: a laboratory flame and a shock tube. For both facilities details about the experimental equipments are given. In particular, the studies on a laboratory flame have been carried out on a McKenna burner used by the scientific community in order to obtained stable premixed flames. As for the shock tube studies, measurements are carried out on two different tubes characterised by different internal diameter and total length. The small one (38 mm internal diameter) has been previously used in order to assess the applicability and the limits of the scattering technique, while the other one was used for the study of the effect of hydrogen addition. For each run a given procedure has to be followed: to fill the tube properly, to start the shot, to open the tube in order to clean it and to close the tube for the next shot. All these steps require many efforts and time, so the use of relatively small volume and size makes this procedure easier. Finally the optical arrangements for the scattering/extinction technique employed in the two devices are deeply described.

1 McKenna Burner

1.1 Configuration of the Burner

Atmospheric laminar premixed flames are produced with a McKenna burner [183] (Holthius & Associated, Sebastopol, CA). In Fig. II.1.1, a schematic of this burner is shown. The main body consists of a water-cooled porous plug of 60 mm diameter. Water is used as cooling medium to facilitate rapid flame stabilization. Reactants gases (fuel and oxidizer) are introduced through the lower part of the burner. The flame is shielded from the surrounding air by using an inert gas (N_2), which flows through a 6 mm thick bronze porous ring concentric with respect to the main porous plate. For flame stabilization, a stainless steel plate of 60 mm diameter is placed at 20 mm height above the burner.
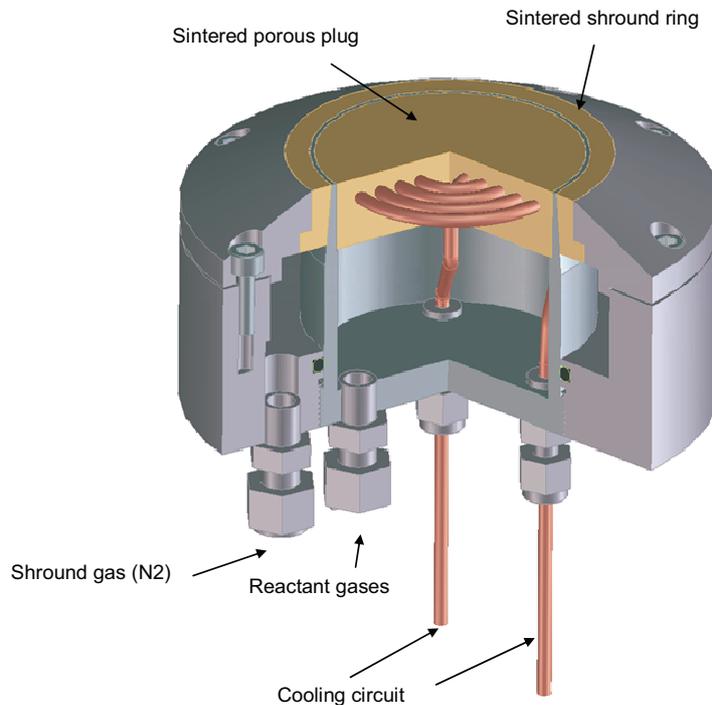

Fig. II.1.1: *Schematic of the McKenna burner [183].*

This burner is considered a standard in the lean and close-to-stoichiometric conditions, and used in several laboratories around the world for the development and calibration of optical diagnostics techniques (Clauss et al. [50], Cheskis et al. [51], Chen et al.[52], Barlow et al. [53], Meier et al. [184], Prucker et al. [55], Sutton et al. [56]). It is characterized by the fact that it produces a "flat" fame, that means with radial uniform concentration of

combustion species and temperature. Thanks to this feature the flame can be considered mono-dimensional, which is an important point in the modeling approach. For many years the flame flatness has been widely assumed to be verified also in rich conditions. In the work of Migliorini et al. [185] it has been proved that this is not always the case. Different models of this burner are commercially available, with a stainless steel or a bronze porous disk. Measurements of soot concentration performed radially across the flame by applying different optical diagnostics techniques have proved that only the bronze porous plug burner produces a flat distribution. On the contrary, the burner with stainless steel disk produces a skewed soot distribution, probably due to catalytic effects Migliorini et al. [185]. For this reason, in our laboratory the bronze burner is used for soot investigation in rich conditions

The burner is allocated on a XYZ motorized table in order to investigate the flame both axially and in the radial direction.

1.2 Optical Layout

In Fig. II.1.2, the experimental optical arrangement for scattering measurements is shown. The green beam (514 nm wavelength) of a cw Ar^+Kr^+ laser (Coherent Innova 70C spectrum) is used with the energy kept constant at 200 mW. The beam (2 mm diameter), vertically polarized, passes through two quartz prisms and is focused at the burner axis by means of a lens (800 mm focal length).

A proper goniometric rolling platform has been designed and implemented, which allows the detection of the light scattered at different angles. It consists in a fixed part, concentric with the burner, and clamped on the optical table, on which a mobile part can revolve. This last allows to carry the guide for holding the receiving optics. The light scattered from the flame is focused, with magnification 1, by means of a lens (150 mm focal length) on a slit (1 mm width) placed just in front of the photomultiplier (Hamamatsu R4220), equipped with an interference filter centered at 514 nm and with a bandwidth of 3 nm. A polarizer plate, placed on the pathway of the scattering signal, is used to select its vertically polarized component.

The signal is processed by means of a digital Lock-in amplifier (Stanford, model SR850 DSP) coupled with a mechanical chopper at the frequency of 300 Hz. In this way it is possible

to discriminate the scattered light against flame emission. The acquisition is driven by a personal computer.
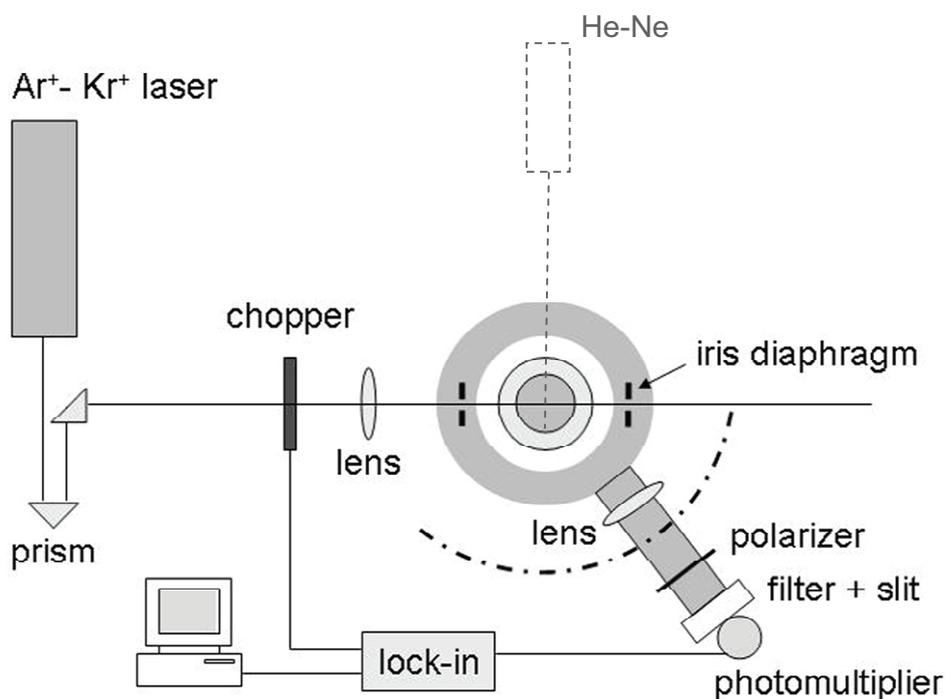

Fig. II.1.2: *Experimental apparatus for scattering measurements in flames.*

In the present work, the strategy proposed by di Stasio (described in the Chapter I) has been adopted. In fact, the aim of our scattering measurements is the investigation of the evolution in the time of soot morphology in terms of the occurrence of aggregation processes. To this purpose the choice of the three scattering angles has been performed in order to have the highest sensitivity of the corresponding dissymmetry ratios. In this work the angles of 30°, 90°, and 150° have been chosen for the scattering measurements in flames.

In Fig. II.1.3, the experimental set-up implemented for extinction measurements is shown. The 1064 nm beam of a cw Nd:YAG laser is focused on the flame axis and the transmitted intensity collected through a two-lens system on the entrance of an integrating sphere. This collecting apparatus allows to avoid beam steering due to thermal gradients at the flame edges. The signal is measured with a photosensor (Hammamatsu H5783-01) and processed by means of the same digital Lock-in amplifier used for scattering measurements, coupled with the mechanical chopper. The acquisition is driven by a personal computer.
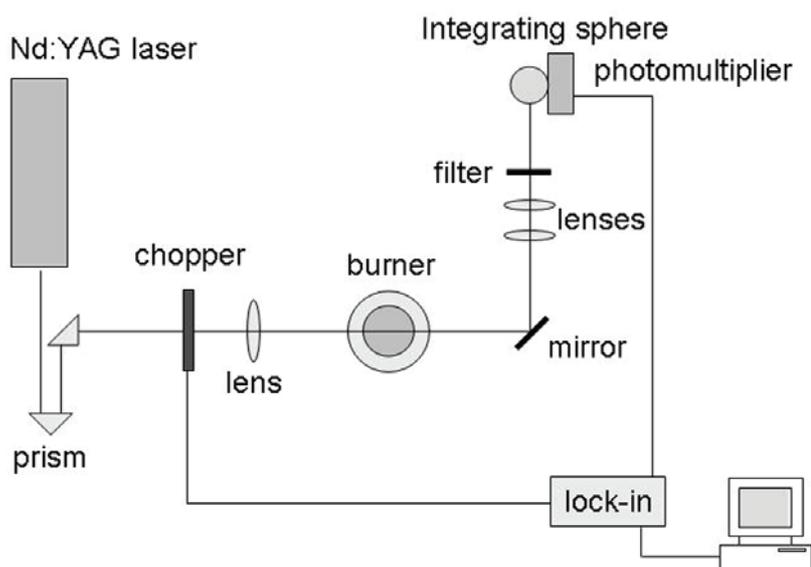
Fig. II.1.3: *Experimental apparatus for extinction measurements in flames.*

In order to improve the signal to noise ratio, each signal results from an average over 300 samples.

Alignment procedure

Care has to be taken for the overall alignment, which is particularly tricky to perform for scattering measurements in the present configuration. In order to be confident that, by rotating the optical table, the same flame location is investigated, the following points have to be verified:

- the goniometric platform has to be perfectly concentric with the position in the flame where measurements are performed,
- the laser beam has to pass exactly along the burner diameter.

The alignment procedure of the laser beam consisted of several steps. Two iris diaphragms are fixed on the goniometric table, placed along the diameter. For the receiving optics, another cw He Ne laser, reported in dotted line in the Fig. II.1.2, is used. A point diffuser is placed on the interception of the two laser beams (the Argon ion and the He-Ne), at the burner axis. The position of the scattering signal focused on the slit of the photomultiplier is checked at different scattering angles, by rotating the optical table.

Calibration procedure

In order to derive the scattering coefficient of soot, a calibration procedure has been performed. It consists in the measurement of the scattering signals of a gas of known scattering cross section performed in the same experimental conditions (optical and electronic components).

To this purpose, nitrogen and methane are used which have a cross section at 532 nm of $6.13*10^{-28}$ and $1.34*10^{-27}$ cm^2/sr, respectively at 532 nm. In order to evaluate the signal background, due to the spurious diffusion of the laser light in the apparatus, helium is used as it is characterized by a very low scattering cross section ($0.086*10^{-28}$ cm^2/sr) compared to other gases. For that, measurements performed with helium are assumed to be an approximation of the ones carried out in the vacuum.

The procedure employed for the calibration is the following. While the same optical arrangement is used to collect signal intensities, the burner is replaced by a simple tube where the gas, with known scattering cross section, is let flowing. In this way we are sure that no impurities are present.

- With the laser on, at 200 mW, which is the operating conditions employed for measurements in flames, and by flowing He, the signal intensity is collected. This corresponds to the background due to the spurious diffusion of the laser light.

- Once the signal background is measured, the scattering intensity from each gas (N$_2$ and CH$_4$) is collected.

- The scattering signal used for the calibration is given by the difference between the previous one (scattering from N$_2$ and CH$_4$ – background).

The evaluation of the soot scattering coefficient is obtained by considering that the intensity of the scattering radiation I_{vv} is given by the expression:

$$I_{vv} = I_0 \, \Delta\Omega \, \frac{\Delta V}{S} K_{vv} \eta \qquad\qquad (II.1.1)$$

where I_0 is the laser power (in Watts) , $\Delta\Omega$ is the solid angle aperture of the collecting optics, ΔV is the probe volume, S the cross section of the beam at the focal point and η is the optical efficiency of the collecting system.

The differential scattering coefficient of a calibration gas $K_{vv,gas}$ is given by:

$$K_{VV,gas} = N_{gas} \, C_{VV,gas} \qquad\qquad (II.1.2)$$

where $C_{vv,gas}$, is the gas scattering cross section and N_{gas} is the number density, $N_{gas}=2.69*10^{19}$ cm^{-3} at room temperature and atmospheric pressure.

By writing Eq.(II.1.2) both for the gas and for the soot particles and taking the ratio, it is possible to obtain:

$$K_{VV,soot} = K_{VV,gas} \frac{I_{VV,soot}}{I_{VV,gas}} = \frac{N_{gas} C_{VV,gas}}{I_{VV,gas}} I_{vv,soot} = \alpha \, I_{VV,soot} \qquad\qquad (II.1.3)$$

The soot scattering coefficient is expressed as a function of the gas scattering coefficient and the ratio of the signal intensity scattered from the soot particles and from the gas.

In Table II.1.1 are reported the values of the scattering cross sections and the measured intensities for the gases used in the calibration.

gas	$C_{vv} *10^{28}$ (cm^2) (@532 nm)	$C_{vv} *10^{28}$ (cm^2) (@514 nm)	$I_{back.}$ (mV)	I_{vv}, (mV) @ 90°	I_{vv}-I_{back} (mV)
N_2	6.13	7.03	0.01	0.039	0.029
CH_4	13.4	15.4	0.01	0.073	0.063

Table II.1.1: *Scattering cross section, measured scattering intensities and background for nitrogen and methane*

I_{back} refers to the background (measured with helium), while I_{vv} is the signal intensities collected with the two gases. The scattering intensities reported in the Table II.1.1 refer to measurements collected at 90°. During the calibration procedure, it was checked that, after the correction for the difference in the probe volume with the scattering angle, the same values was obtained for any other angles, as given by the Rayleigh scattering theory. This confirms that the calibration procedure was correctly performed.

The calibration values of α for the two gases resulted to be $\alpha = 6.58*10^{-7}$ W^{-1}.cm^{-1}.sr^{-1} and $6.53*10^{-7}$ W^{-1}.cm^{-1}.sr^{-1} To derive the soot scattering coefficient, the average value $\alpha = 6.55*10^{-7}$ W^{-1}.cm^{-1}.sr^{-1} is used.

1.3 Sampling for TEM analysis

1.3.1 Thermophoretic Sampling (TS)

In order to perform thermophoretic sampling (Wegner et al. [186]) a rapid insertion devise was built, and reported in Fig. II.1.4. It consists of a double-action piston carrying at the extremity of the shaft a TEM grid (ϕ=3mm). An electro-pneumatic driver allows to change the residence time in a wide range with 1 ms step.
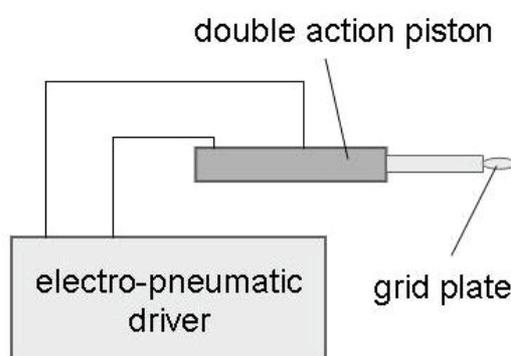

Fig. II.1.4: *The rapid insertion devise for thermophoretic sampling*

The grid-support system is driven by means of a couple of electrovalves fed by a digital control panel. Such panel allows varying the permanence of the probe inside the flame with the transit time depending on the applied pressure (usually 8 atm).

The effective period of permanence of the probe in flame has been exactly estimated by measuring, using an oscilloscope, the interruption time of a laser beam caused by the probe. Such beam was centered both on the burner and on a photodetector coupled with the oscilloscope. The more suitable residence time were in the order of tens milliseconds.

Actual residence time is 50 ms for the measurements performed in this work.

The thermophoretic deposition is driven by the presence of a temperature gradient, which is established by introducing briefly into the flame gases a probe surface, initially at room temperature. The probe exposure time should be long sufficiently for capture, and short enough to present a cold surface. In fact, in this way any reaction can be frozen.

1.3.2 TEM Image analysis

Image analysis wad carried out on the TEM micrographs using two different software.

With Photoshop, each particle was circled and with Image-Pro Plus, the automatic counting of the particles was performed. The software gave back information about particle diameter, projected area, perimeter. The diameter value here used was derived from the projected area, as some particles were not exactly spherical. From these values the particle size distribution (PSD) was built up and the average value evaluated.

1.4 Experimental conditions

This study has been carried out on an ethylene/air laminar premixed flame at atmospheric pressure with the addition of hydrogen at two different contents.

Ethylene was distributed by SAPIO, the purity was higher than 99.999%. Hydrogen was distributed by SAPIO with purity better than 99.999 %. The used air was compressed laboratory dry air.

Flow rates of fuel and oxidizer (air, in our case) are measured and controlled by using calibrated mass flow meters (Bronckhorst, AK Ruurlo, The Netherlands).

Table II.1.2 summarizes the experimental conditions. The pure ethylene/air flame is characterized by an equivalence ratio of 2.34 (flame A). This value has been chosen as it offers a good compromise between flame richness (that is soot content) and flame structure stability. In the same table the equivalence ratios related to the doped flames are also reported. In this case, instead of the definition reported in Eq. (I.1.7), in order to take into account the composition of a hybrid mixture, an *effective fuel equivalence ratio* is introduced according to the following relationship:

$$\phi = \frac{\dfrac{x_{FUEL}}{[x_{AIR} - x_{H_2}/(x_{H_2}/x_{AIR})_{ST}]}}{(x_{FUEL}/x_{AIR})_{ST}} \tag{II.1.4}$$

where x_{FUEL}, x_{AIR} and x_{H_2} are the molar fractions of fuel, air and hydrogen, respectively. The subscript ST refers to stoichiometric conditions.

The adiabatic temperature T_{ad} has been calculated, based on equilibrium calculation at constant pressure.

flame #	C_2H_4 [Nl/min]	H_2 [Nl/min]	H_2 /C_2H_4*100	Air [Nl/min]	Φ	T_{ad} (K)
A	1.400	0	0	8.60	2.34	1736
B	1.360	0.272	20	8.34	2.53	1711
C	1.328	0.531	40	8.14	2.76	1680

Table II.1.2: *List of the investigated premixed flames.*

As reported in the table, by adding hydrogen to the mixture only a slight decrease in the adiabatic temperature is calculated, being about 50 K with 40% H_2.

Hydrogen-doped flames are obtained by replacing a certain amount of ethylene/air mixture in the flame A with a corresponding amount of hydrogen. In this work 20% and 40% of hydrogen are considered, the following parameters are kept constant:

- total flow rate, equals to 10 Nl/min;
- cold gas flow velocities, that is 5.84 cm/s;
- C/O ratio, that is 0.775.

This criterion has been chosen in order to compare the three investigated flames concerning their tendency to produce soot.

2 Shock tube

2.1 Principles - Evaluation of the thermodynamic parameters

A shock tube is a totally adiabatic reactor, where the experimental gas is brought almost instantly to a known and controlled high temperature and pressure for a short time due to the passage of a shock wave in the gas (Gaydon [187]). In Fig. II.2.1-(a) a schematic picture of the tube is shown. In this device a plane shock wave is produced by the sudden bursting of a diaphragm which separates a gas at high pressure (driver tube) from the one at low pressure (driven tube).
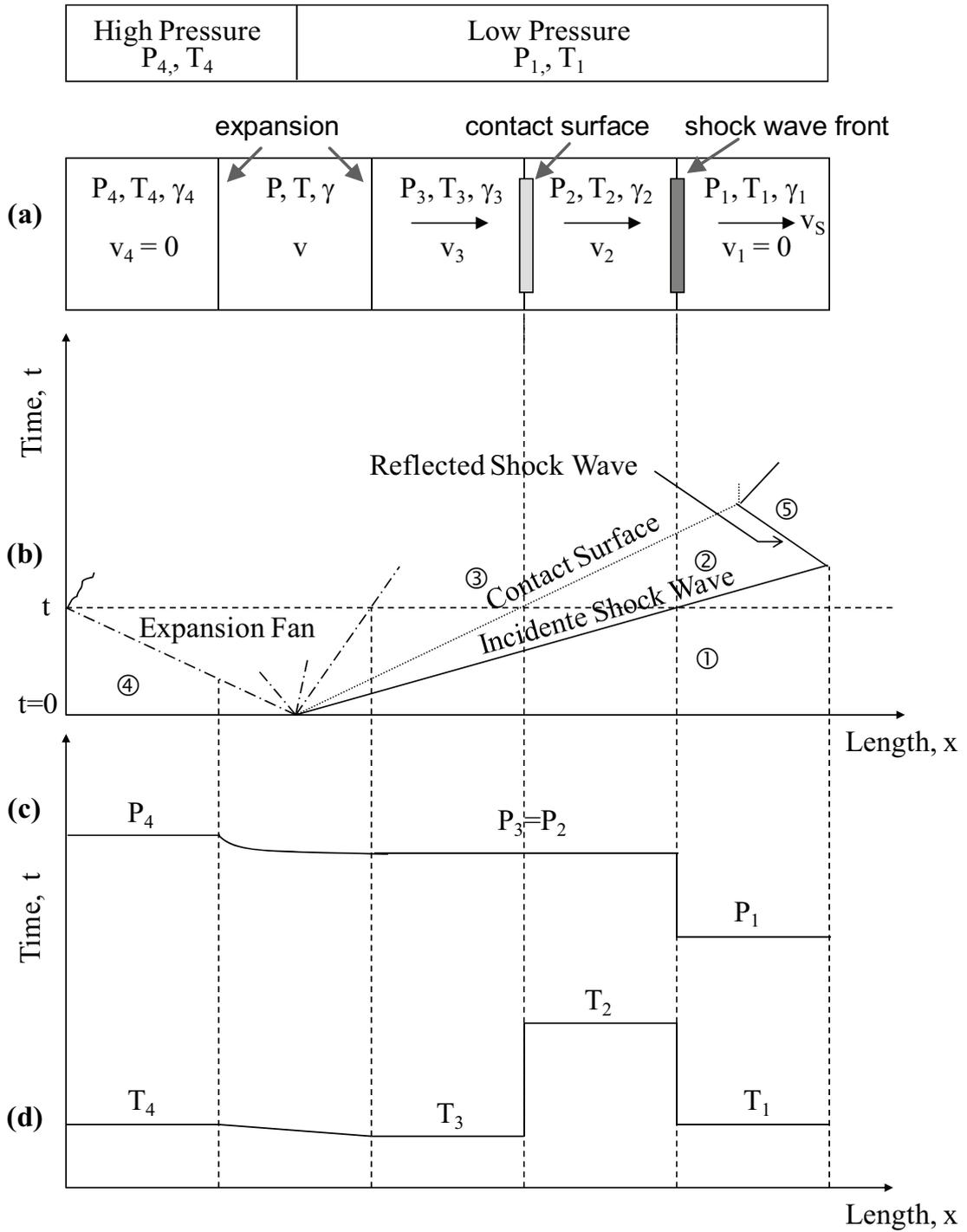
Fig. II.2.1: *(a) Schematic picture of shock tube; (b) An (x-t) diagram of the shock wave, expansion waves and contact surface separating driver and experimental gases; (c) variation of the pressure along the tube at fixed time; (d) variation of the temperature.*

In the high pressure section of the tube (left side), an inert gas is introduced, usually helium, at a temperature T_4 and a pressure P_4. In the low pressure side the gas under investigation, which is subjected to the shock wave, is introduced at a temperature T_1 and a pressure P_1. After the bursting of the diaphragm, a series of compression waves are developed in the low-pressure gas, forming a shock front which propagates along the tube at constant supersonic velocity. Simultaneously, an expansion or rarefaction wave moves back into the high-pressure gas at the speed of sound. The experimental gas and the driver gas make contact at the "contact surface", which moves rapidly along the tube behind the shock front. In Fig. II.2.1-(b) the temporal trend versus the position along the tube is reported for the shock front, the contact surface and the rarefaction wave. The variation of the pressure in Fig. II.2.1-(c) and of the temperature in Fig. II.2.1-(d) along the tube at a certain time are represented.

The following labels are commonly used for the temperature and the pressure:
- subscript 1 for the undisturbed experimental gas, resulting in T_1 and P_1;
- T_4 and P_4 refer to the initial conditions for the high pressure side;
- the subscript 2 for the region between the shock front and the contact surface;
- and T_3 and P_3 refer to the region between the surface contact and the rarefaction wave.

P_4 is greater than P_1, but usually $T_1=T_4$, which is the room temperature. The shock wave causes a fast increase in temperature and pressure of the gas under investigation. In an ideal gas, the temperature is characterized by a fast rise from the initial room temperature to a very high value at the shock front (T_2), a steady condition up to the contact surface, and, behind this, a quick fall to a value below the room temperature in the rarefaction region. When the incident shock wave reaches the end of the tube it is reflected back into the gas, resulting in an increase of the temperature and pressure, denoted in this region as T_5 and P_5. After a certain period of time, depending on the tube size, the reflected wave front meets the contact surface between driver and driven gas. As a result, a fast quenching of the reflected shock wave is obtained. The observation time where optical measurements are carried out is related to the distance between the end of the tube and the place where this reflected shock wave meets the contact surface. For that, the observation period at constant temperature and pressure depends on the tube length and the shock wave speed.

The reflected shock wave exhibits two important characteristics.

- It is a suitable tool to allow high temperature and density to be reached with not extremely high diaphragm pressure ratios.

- As the gas particles behind the reflected shock wave are at rest relative to the tube, the observations on a fixed group of particles throughout their heating and compression can be carried out.

In our measurements the following hypothesis are considered:

- the rupture of the membrane is instantaneous and complete

- no molecular transfer process or turbulence occur

- gas can be considered as perfect

In order to obtain the thermodynamics parameters behind the reflected shock wave the following hypothesis can be considered, in first approximation:

- the isentropic coefficient γ is constant with the temperature (as for monoatomic gases);

- effects due to the walls can be considered as negligible.

The gas parameters in the regions associated with a shock wave are the pressure, density, temperature of the gas, and the velocity v of the gas molecules relative to the shock tube. In most applications $v_1 = 0$. The velocity of the shock front relative to the tube is referred as W_s. Practically, it is more convenient to express the basic equations of the gas motion in relation to the shock front, which is considered at rest, that means taking into account a relative velocity u.

Now the equations of mass, momentum and energy conservation for the incident shock wave are considered. In this case, heat exchange in the shock wave can be neglected. In fact, as the time of flow is usually on the order of milliseconds, heat losses by conduction are negligible. Due to the low emissivity of the gas, radiation losses are negligible as well as convection since the gas flow is considered inviscid. The ratio of the shock parameters P_2/P_1 and T_2/T_1, known as Rankine-Hugoniot equations, can be easily obtained:

$$\frac{P_2}{P_1} = \frac{2\gamma M_1^2 - (\gamma - 1)}{\gamma + 1} \qquad \text{(II.2.1)}$$

$$\frac{T_2}{T_1} = \frac{\left(\gamma M_1^2 - \frac{\gamma - 1}{2}\right)\left(\frac{\gamma - 1}{2} M_1^2 + 1\right)}{\frac{\gamma + 1}{2} M_1^2} \qquad \text{(II.2.2)}$$

where M_1 is the Mach number of the incident shock wave, and γ the specific heat ratio. These relationships allow the determination of the temperature and the pressure of the incident shock wave through an ideal gas (T_2, P_2) by knowing the initial condition of the gas under investigation (T_1, P_1), and by measuring the speed of the shock wave W_s.

As for the reflected shock parameters in an ideal gas, a procedure is to derive pressure, temperature and density in the reflected shock wave in terms of the relative conditions in the incident one. Then by considering the equations (II.2.1) and (II.2.2), these properties can be related to the initial conditions as follows:

$$\frac{P_5}{P_1} = \left[\frac{2\gamma M_1^2 - (\gamma - 1)}{\gamma + 1}\right]\left[\frac{(3\gamma - 1)M_1^2 - 2(\gamma - 1)}{(\gamma - 1)M_1^2 + 2}\right] \qquad \text{(II.2.3)}$$

$$\frac{T_5}{T_1} = \frac{\left[2(\gamma - 1)M_1^2 + (3 - \gamma)\right]\left[(3\gamma - 1)M_1^2 - 2(\gamma - 1)\right]}{(\gamma - 1)^2 M_1^2} \qquad \text{(II.2.4)}$$

These relationships are valid only if γ is constant. In our experiments, the variation of γ as a function of the temperature is taken into account in a program developed at ICARE by Paillard and co-workers [188]. The uncertainties in the parameters T_5 and P_5 are related to the uncertainties on the Mach number determination and in the thermodynamics parameters of the investigated gases.

2.2 Description of the shock tubes used in this study

In Fig. II.2.2, the shock tube with 38 mm internal diameter is reported. It is made of stainless steel and consists of a driver tube of 1.59 m length and a 2.42 m long driven tube.
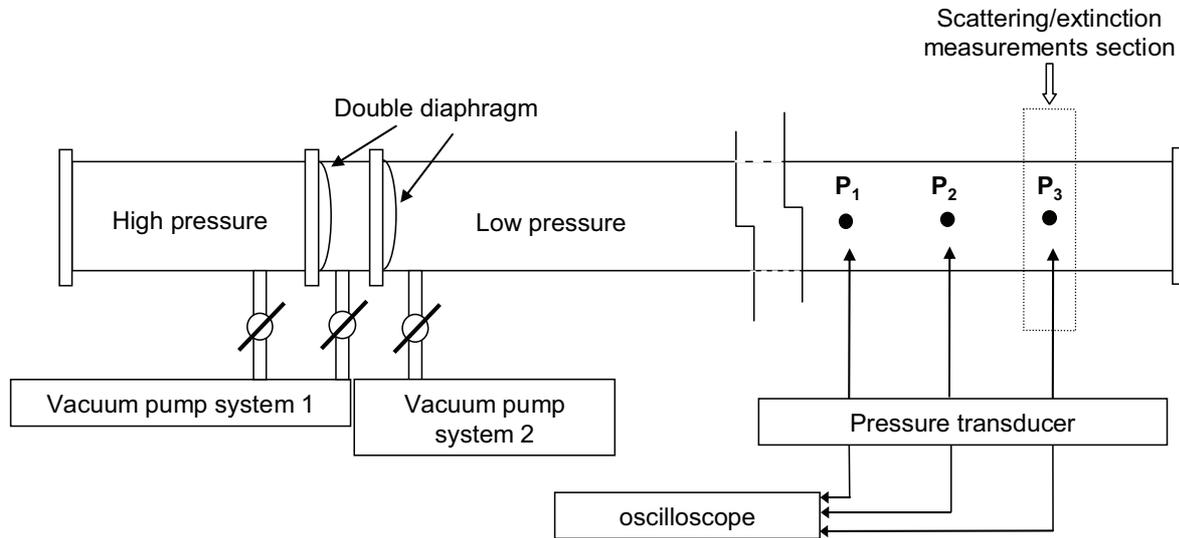

Fig. II.2.2: *Diagram of 38 i.d. shock tube and its accessories*

In order to measure the shock wave speed three pressure transducers (P_1, P_2, P_3) are placed as shown in the figure. The distance between first and second transducers is 200 mm, and the distance between second and third is 417 mm.

In the figure the section reported with gray line (in correspondence of the pressure transducer close to the tube end) refers to the part of the tube where the optical diagnostics arrangement is settled for the extinction/scattering measurements.

In Fig. II.2.3, the shock tube with 78 mm internal diameter is shown. It is made of stainless steel and characterized by a 890 mm long driver section and a 4.18 m driven part.

The tube is equipped with different pressure transducers positioned along the tube (grey circles) of which only four, closer to the tube end (C_1, C_2, C_3, C_4), are used to measure the shock velocity. As it is evident from the figure the tube consists of different sections, of which the closest to the tube-end has been properly designed to perform scattering/extinction measurements.
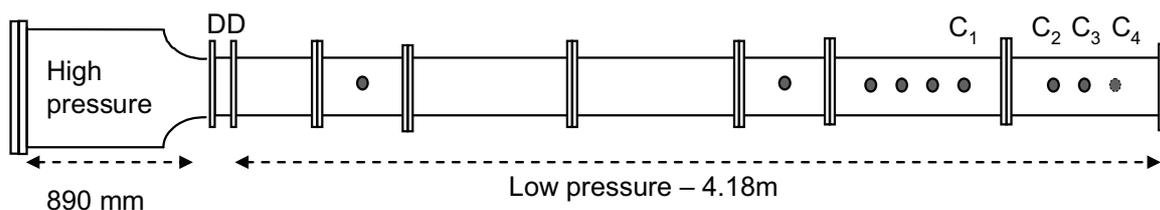
Fig. II.2.3: *Description of the 78 mm shock tube. C_1, C_2, C_3 and C_4 are the pressure transducers*

The distances between two consecutive pressure transducers are: C_1-C_2 = 323.5 mm, C_3-C_2 = 100.5, C_4-C_3 = 97 mm.

The basic procedure to start the shock waves is the same for both tubes. We refer to this system as double diaphragm. The driver and the driven tube are separated by means of an intermediate section with negligible volume with respect to the main parts. The intermediate part consists of a metallic cylindrical support where two membranes can be allocated. The pressure on each membrane is between P_4 and $P_4/2$. The two membranes are made of terphane (glycol ethylene polyterephtalate) of different thickness, depending on the range of pressure considered. As for the vacuum, the same system, shown for simplicity only in Fig. II.2.2, is used. One vacuum pump (system 1) is utilized for both the high pressure and the intermediate section, and the other one (system 2) for the low pressure side. A depressurisation cylinder (not shown in the figure) is also connected with the vacuum pump system 1 and the intermediate part. The inert gas, helium in our case, is introduced inside the intermediate and high pressure tubes (the relative inlet is also not reported in the figure).

The procedure carried out for each shock run can be summarised as follows: after the vacuum is made in the whole shock tube, the insertion of the driven and driver gases can be started. As for the low pressure tube, it is filled up to a given pressure with the gas under investigation (generally a mixture of this gas with argon). The inert gas (helium) is introduced both in the intermediate (up to a pressure of $P_4/2$) and in driver tube (filled up to P_4). The start of the shock wave is caused by opening a valve that allows the helium inside the intermediate tube to flow into the depressurisation cylinder, where the vacuum is done. This results in a very fast increase of pressure difference at the membranes and, as a consequence, in their rupture.

The main reasons of using the shock tubes of different length and diameter is the following. The time required to perform each run is strictly related to the volume and size of the tube used. Then, the analysis of the applicability and limitation of the scattering/extinction

technique to a shock tube has been carried out with the 38 mm i.d. tube. On the contrary, the study of hydrogen addition to the mixture has been performed on the 78 mm i.d. shock tube. In fact, in this last case the effects of the boundary layers can be considered negligible, which makes it more suitable to perform chemical kinetics studies.

The passage of the shock wave front is detected by the pressure transducers by means of a fast digital oscilloscope and, by knowing the distance between these detectors, the shock wave speed can be determined. This value together with the initial pressure condition and mixture composition allow the determination of the temperature and pressure behind the incident and the reflected shock wave as well as the Mach number, by using the SHOCK code (Mitchell et al. [189]) of the CHEMKIN II library (Kee et al. [190]).

2.3   Optical Layout

The experimental optical diagnostic set-up applied to the 78 mm i.d. shock tube is shown in Fig. II.2.4 and Fig. II.2.5. As for the 38 mm i.d. tube, a similar implementation is used and here not reported, with only the following differences:

- For extinction measurements an He:Ne laser at 632.8 nm was used,
- no scattering measurements were collected at 20° and 160°

In both tubes, the section where the optical set-up is allocated is characterized by having five quartz windows ($\varnothing$ = 3mm) placed on the tube surface, two along one diameter (180° each other apart) and the others at three angles (20°, 90° and 160°) with respect to the direction of the incident laser beam (Fig. II.2.5b). With this configuration, the scattering signal at the three angles can be measured.

For scattering measurements, the vertically polarized beam of a continuous Ar^+ laser (Spectra Physics, model 2017) at λ = 488 nm is used. The beam, which has a diameter of ϕ_L = 1.4 mm passes through a fast mechanical chopper (40 KHz), in order to discriminate the scattering signal against background emission. The laser beam is focused on the chopper plane with a lens (L_1 in Fig. II.2.4, 100 mm focal length) and collimated again with an identical lens (L_1). A periscope allows to adapt the beam height of the laser to the one of the shock tube axis and, consequently, to rotate the polarization of the beam from vertical to horizontal. Hence the beam is vertically polarized with respect to the scattering plane. The

upper mirror of the periscope is a dichroic mirror (DM$_1$), which allows to reflect the 488 nm beam and transmit the 810 nm beam used for extinction produced by a laser diode LD (see in the following).
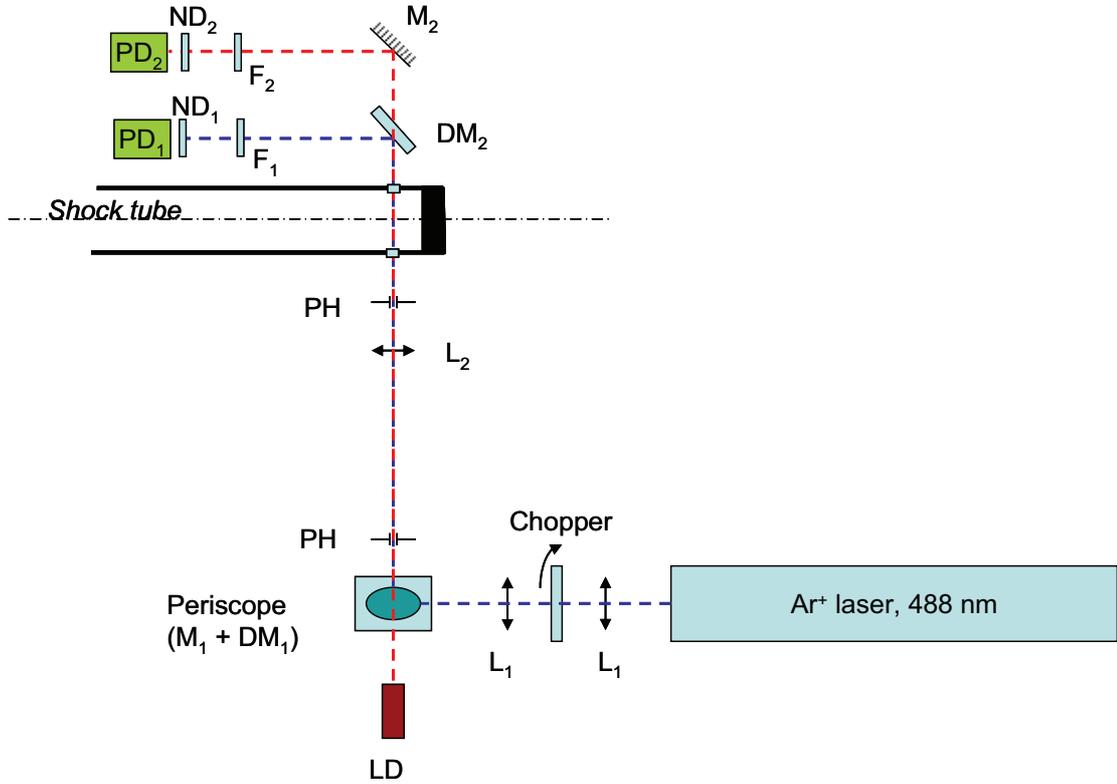

Fig. II.2.4: *Experimental apparatus applied to the shock tube for extinction measurements.*

The beam is then focused at the center of the shock tube using a lens (L$_2$ in Fig. II.2.4, f_2 = 250 mm focal length). Assuming the laser beam to be Gaussian, its diameter ϕ_f on the focal plane is given by :

$$\phi_f = \frac{4\lambda f_2}{\pi \phi_L} \approx 110 \ \mu m \tag{II.2.5}$$

After crossing the tube, the beam is reflected on a dichroic mirror (DM$_2$) and collected on a fast photodiode PD$_1$ (Thorlabs, PDA36A-EC model). In this way, extinction measurements at 488 nm can be performed. The photodiode is equipped with an interference filter (F$_1$), centered at 488 nm and with a bandpass of $\Delta\lambda$ = 10 nm, and with a neutral density

filter (ND$_1$) to avoid any saturation. The laser power, measured just before the focusing lens L$_2$, resulted to be 500 mW.
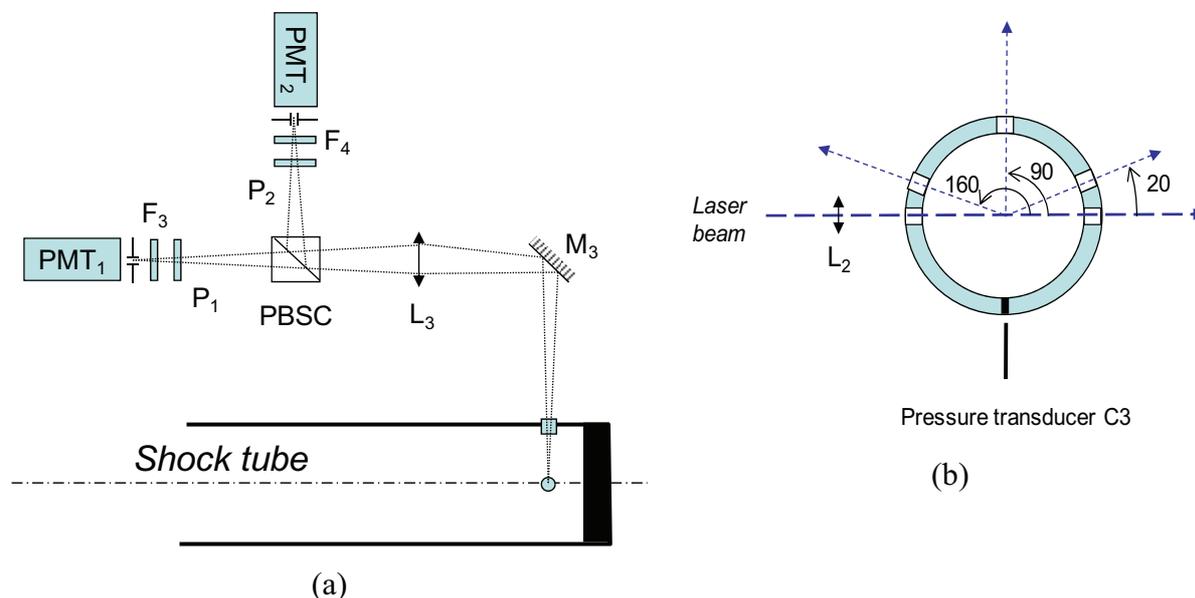

Fig. II.2.5: *Details of the optical collection setup for scattering measurements applied to the shock tube. (a) side view - (b) cross section view*

The scattered light from the focal point of the laser beam is collected, as shown in Fig. II.2.5 b, at the three angles (20°, 90° and 160°) by using three identical lenses (150 mm focal length). At each angle, the image of the probe volume is focused on a pinhole of 1 mm diameter, mounted in front of a photomultiplier tube (PMT$_1$) (Hamamatsu, R928 model). A polarizing plate (P$_1$) and a narrow-band ($\Delta\lambda$=1 nm) interference filter (F3) centered at 488 nm are also positioned in front of the PMT.

In order to analyze the non-polarized component of the signal collected at 90°, a polarizing splitting cube (PBSC) is placed on the pathway of the scattering receiving optics. The cube allows to transmit the parallel component of the signal polarization (scattering + emission) and to reflect the perpendicular one (emission). In this way, it is possible to discriminate the contribution of the emission from the one due to the scattering. The emission signal is also measured using another PMT (PMT$_2$) , which is equipped with a pinhole and an interference filter (488 nm centered, $\Delta\lambda$=10 nm bandpass). A 700 V power supply was used for each PMT.

For extinction measurements, a continuous laser diode, delivering a collimated 3 mm diameter beam at 810 nm, is positioned at the height of the shock tube axis, just behind the upper mirror of the periscope (Fig. II.2.4). This laser diode is mounted on an adjustable holder allowing the superimposition of the 810 nm laser beam onto the one of the Argon laser. To this purpose for such alignment, two pinholes (PH) mounted along the beams path way are used. The IR beam is focused at the center of the tube with the same lens L_2. The transmitted 810 nm beam is then collected on a fast photodiode (Thorlabs, DET10A model) by using a mirror. A high pass filter (760 nm cut) and a neutral density filter are mounted in front of this photodiode.

The implementation of these equipments around the shock tube is given in Fig. II.2.6.
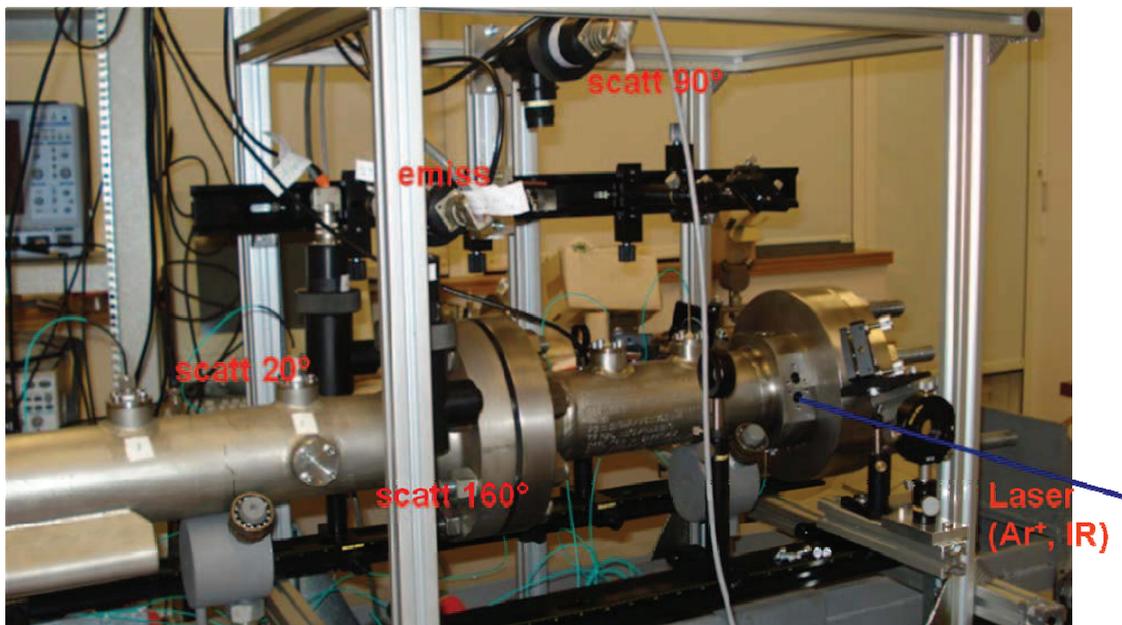
Fig. II.2.6: *Picture of the scattering/extinction set-up employed on the big shock tube.*

The pressure signals, the scattering and the transmitted intensities are synchronized and triggered by the pressure signal detected from the pressure transducer placed at the end of the tube. This allows to start the acquisition when the shock wave reaches the tube-end and to measure what happens behind the reflected shock wave. The acquisitions are carried out with fast digital oscilloscopes (Tektronix, TDS5034B model for scattering measurements; Tektronix 3014 model for extinction measurements and Agilent 54624A model to carry out transducer measurements).

As for the extinction, before each shock run, reference signals, corresponding to 0% and 100% transmittance (with the laser on and off) are collected and stored.

Alignment procedure

The alignment procedure of the whole experimental set-up required to be frequently checked, even every shots. The more sensitive part concerns the superimposition of the probe volume with the focal position of the laser beam. To this purpose, a home-made device is used, which is practically a half cylinder holding a needle. By placing this tool in the tube, the needle is positioned just at the center of the section, in the position of the lens focal point. The needle can be adjusted in height and along the tube axis so that the laser beam does not hit directly the needle, but licks at the tip.

Special care has also to be taken for the back reflections of the laser beam onto the tube window that can occur inside the tube. This can affect in a significant way background signals measured at 20 and 160°.

.

Calibration procedure

In order to derive the differential scattering coefficient at 90°, 20° and 160° from the scattering raw data, a calibration procedure was performed in a similar way as described for flame experiments. The gas used for this purpose is propane, with a quite high scattering cross section of $K_{vv,gas}$ = 104.1 $*10^{-28}$ cm^2 at 488 nm compared to the other gases,. For safety reason, propane was not used for the calibration procedure in flames, where lighter ones are instead chosen.

Due to the particular care that should be taken for such a calibration measurement, the proper procedure is here described.

1. After making the vacuum in the tube, the light diffused through the physical components of the apparatus (i.e. internal wall and windows of the tube), is detected. This signal represents the background.
2. The tube is filled up with a known concentration of propane (usually about 80 kPa), and the resulting signal is measured in the same experimental conditions of soot measurements, without running the shot.
3. The scattering due to propane is derived by taking the difference between the previous signals.

The pressure value used for propane is a compromise between safety and the request of high signal to noise ratio.

In Fig. II.2.7 are reported the signals when the tube is empty (vac_sig, blue line in the figure) and when it is filled up with propane (prop_sig, red line).
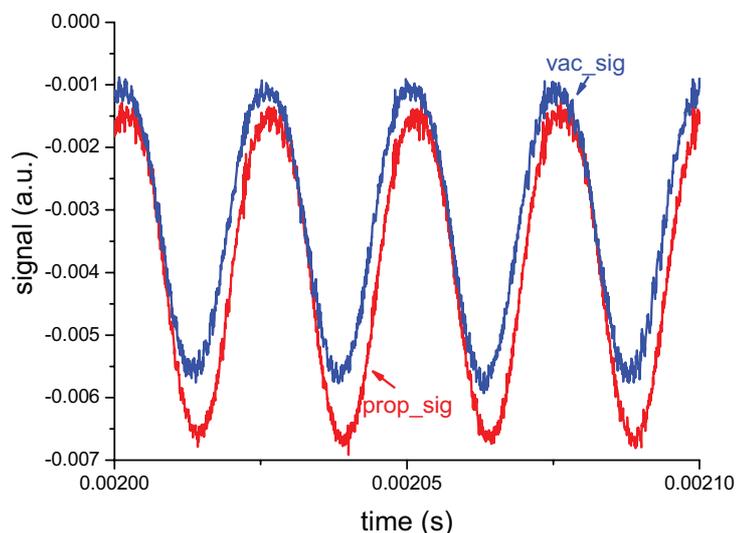

Fig. II.2.7: *Scattering signal in the vacuum (blue line) and with the tube filled up with propane (red line).*

Of course, due to the quite low level of such signals, a significant averaging procedure has to be performed in order to detect the scattering from the gas with a good signal to noise ratio.

Once the intensity of the scattering signal from propane is obtained, the soot scattering coefficient is calculated following the same procedure applied in the burner, by using Eq. (1.2.2).

2.4 Experimental conditions

The mixtures and the related experimental conditions investigated in this study are reported in Table II.2.1.

A first analysis is performed to assess the scattering/extinction technique concerning both the implementation of the optical apparatus and the procedure to process the data in order to derive soot parameters. For this purpose, measurements in the 38 mm tube are carried out. Ethylene and toluene mixtures are used as fuels at the conditions given in the table for T_5, P_5 and for the carbon atom concentrations.

Then, the study of the influence of hydrogen addition on soot formation is performed in the 78 mm shock tube. In this case, ethylene/argon mixtures is investigated at which 0.5% and 1% H_2 in volume with respect to the total mixture is added. It is important to observe that, in this last case, the amount in volume of hydrogen is the half than the amount of ethylene. In the table the corresponding experimental conditions are also given.

The mixtures have been prepared in a 10 l glass-bulb and stirred to ensure homogeneous composition, especially in the case when hydrogen is used.

Shock Tube diameter	Mixture	Temperature (T_5, K)	Pressure (P_5, kPa)	$[C] \times 10^{-17}$ atoms/cm^3
38 mm	3%C_2H_4 + 97%Ar	2070-2350	430-510	8.5-10
	0.3% C_7H_8 + 99.7%Ar	1616-1934	486-630	4 1 – 5.5
78 mm	2%C_2H_4 + 98%Ar	1850-2100	500	6.4 -8
	2% C_2H_4 + 0.5%H_2+97.5%Ar	1850-2100	500	6.6 – 7.87
	2% C_2H_4+1%H_2+97%Ar	1850-2100	500	6.7 -7.7

Table II.2.1: *List of the gas mixtures used in the two shock tubes.*

Ethylene, Hydrogen, Argon, Helium and Propane (for calibration) were distributed by Air Liquide, the purity was higher than 99.999%. Toluene was distributed by Sigma Aldrich, the purity was higher than 99.7%.

III. Flame Measurements: Results and Discussion

INTRODUCTION

In this chapter scattering/extinction measurements carried out in premixed flames are reported. The study is performed on ethylene/air premixed flame at atmospheric pressure, at which fixed percentages of hydrogen are added.

In order to study soot formation, a new approach based on scattering/extinction technique is developed in this work and here presented. On the basis of the fractal approach and of the Rayleigh-Debye-Gans scattering theory, the new procedure implemented to retrieve soot parameters is widely described relatively to the case of pure ethylene/air. Information about soot volume fraction, radius of gyration and soot particle diameter are presented. Then it is investigated the influence of hydrogen addition on soot formation, and in particular on these soot parameters. The uncertainties of the results obtained are evaluated together with the sensitivity of some assumptions (fractal prefactor and fractal dimension). Moreover, some considerations are given, and some results shown, for the dependence of the extinction measurements on the laser wavelength of the used source.

In order to compare and to validate optical measurements, sampling and transmission electron microscopy analysis has been carried out, and the optically-measured particle diameter compared with the sampling measurements.

1 Methodology

1.1 New Fractal Analysis

The basic principles and the relationships of the scattering/extinction technique have been summarized in Chapter 1 as deduced from the current literature. In this paragraph we will describe the methodology of the scattering/extinction technique developed and presented in this work as applied to the ethylene/air flame (A).

1.1.1 Extinction coefficient and soot volume fraction

First of all from extinction measurements, the extinction coefficient and the soot volume fraction are obtained.

The intensity of the emerging, I_L, and incident, I_0, laser beam at a certain location in the flame are collected in sequence in order to take into account the low-frequency thermal fluctuations of a cw laser beam. Each signal results from an average over 300 samples.

By applying Eqs. (I.2.1) and (I.2.6) reported in Chapter I, the extinction coefficient and the soot volume fraction, respectively, are calculated.

Being these measurements line-of sight, an averaged evaluation across the absorption pathway, that is in our case the flame thickness, is obtained. The average soot volume fraction results to be almost coincident with the corresponding value on the flame axis in the case of a radially uniform soot distribution across the flame. As it has been verified in our laboratory, this feature is obtained by using a McKenna burner with a bronze porous-plug (Migliorini et al. [185]).

In order to measure the flame thickness at different heights above the burner (HAB), 2D emission from flame is collected by using a CCD camera.

1.1.2 Scattering coefficient

Scattering measurements are carried out at 30°, 90° and 150° scattering angles, on the flame axis and at different heights above the burner. The limitation of HAB = 14 mm is due to the interference of the laser beam with the flame-stabilizing plate, where a thick layer of soot is formed.

By changing the scattering angle, a variation in the probe volume is obtained as it is shown in Fig. III.1.1. In this figure there are shown the laser beam (continuous line) and the collecting solid angle (dotted line) at α and 90°. In correspondence of the beam waist, the interception of the laser beam and the collecting solid angle defines the probe volume, which is different according to the scattering angle considered.


laser beam

α

Collecting optics

Collecting optics
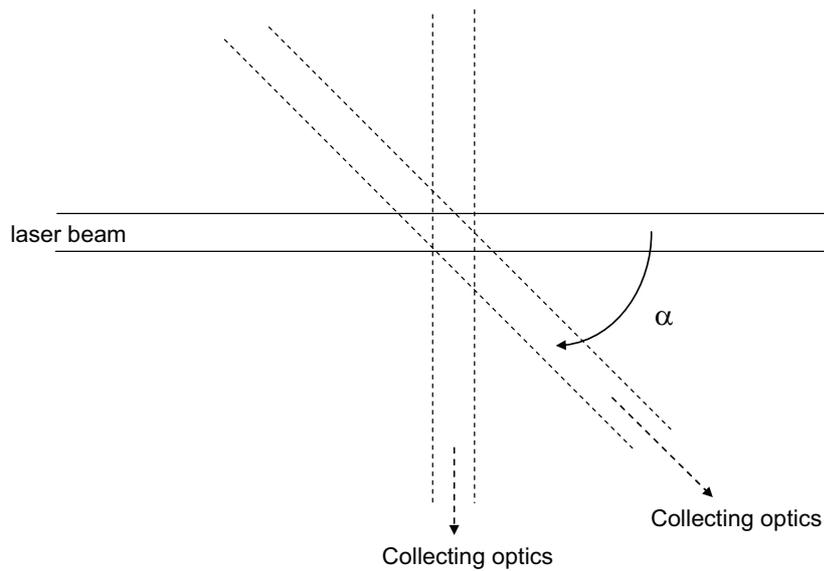
Fig. III.1.1: *Dependence of the probe volume on the scattering angle*

If *V* is the probe volume related to 90° measurements, ad *V'* the one observed at the scattering angle α, the following relationship is obtained:

$$V' = V / sen\alpha \tag{III.1.1}$$

The raw scattering signals have to be corrected for the factor given in Eq. (III.1.1). As the probe volume at the angle α is higher than the one at 90°, the corresponding raw scattering signal is higher as well.

In order to derive the scattering coefficient the calibration procedure described in the Chapter II is applied to the scattering signal.

1.1.3 Soot parameters: radius of gyration, volume-mean diameter, particle diameter

It is well known that soot growth is characterized by aggregation processes which can be described by the fractal theory. Based on this description, in this work a new numerical approach is proposed to evaluate soot particle parameters. To this purpose, the analysis performed by De Iuliis et al. [181] is here considered and further developed. It is essentially based on the evaluation of the ratio of the scattering signal measurements detected at two scattering angles.

As for the main parameters of the fractal theory, e.g. the radius of gyration and the structure factor, a full description is given in paragraph 3.4 of Chapter I. In this study, the expression of the structure factor of Lin et al. [129], already reported in Chapter I and here recalled, has been used:

$$S(qRg) = \left[1 + \sum_{s=1}^{4} C_s (qR_g)^{2s} \right]^{-D_f/8}$$ (III.1.2)

where $C_1=8/(3D_f)$, $C_2=2.5$, $C_3=-1.52$ and $C_4=1.02$. This polynomial function, chosen for simplicity as it describes scattering signal at any scattering angle, almost overlaps other curves reported in the same work. Recently, Teng and co-workers [130] proposed another expression for the structure factor, which has the same structure as Eq.(2.1.2), but with only two terms (the first and the fourth) in the addition, and the relative coefficient given by $C_1=8/(3\,D_f)$ and $C_4=1$. As it will be shown in the following even in this case a good overlapping of the two curves is obtained.

The probability distribution function $p(N)$, which gives the fraction of aggregates with a number N of primary particles, is described using a lognormal distribution (see Chapter I):

$$p(N) = \frac{\exp\left[-\frac{1}{2}\left(\frac{\ln(N/N_m)}{\ln(\sigma)} \right)^2 \right]}{\sqrt{2\pi} N \ln(\sigma)}$$ (III.1.3)

where N_m is the geometric mean of the primary particles per aggregate and σ is the standard deviation. In this work the value $\sigma = 2.1$ is used, as widely accepted by other authors (De Iuliis et al. [79] and Dobbins et al. [96]).

We remind that the related qth moment of the probability distribution function is defined as

$$\overline{m_q} = \int\limits_0^\infty N^q p(N) dN \tag{III.1.4}$$

where $\overline{m_1}$ is the mean value of the number density of the monomers in a cluster.

The averaged scattering signal from a polydisperse ensemble of aggregates results to be (De Iuliis et al. [181])

$$I_{VV}^p(\theta) = \eta I_0 C_{vv}^p N_a \int N^2 S(qR_g) p(N) dN \tag{III.1.5}$$

Considering the following definition for the average expression of the structure factor:

$$\overline{S(qR_g)} = \frac{\int N^2 S(qR_g) p(N) dN}{\int N^2 p(N) dN} \tag{III.1.6}$$

the integral in Eq.(III.1.5) can be written:

$$\int N^2 S(qR_g) p(N) dN = \overline{m_2} \ \overline{S(qR_g)} \tag{III.1.7}$$

From this relationship a mean value of the radius of gyration can be derived with the following assumption:

$$\overline{S(qR_g)} = S^*(qR_{gs}) \tag{III.1.8}$$

In other words, in order to describe the feature of the scattering signal from a polydisperse distribution of aggregates, a new relationship for the structure factor $S^*(qR_{gs})$

have to be introduced. This function can be written in terms of an averaged radius of gyration for scattering R_{gs}, which can be properly chosen.

Different definitions for the average R_{gs} can be considered (Mountain et al. [122]), which are all connected through moment ratios. Here the following relationship has been adopted

$$R_{gs} = R_{gm1} = d_p \, (\overline{m_1} / k_f)^{(1/Df)} \tag{III.1.9}$$

R_{gm1} is the radius of gyration of a fractal aggregate with a primary particle diameter d_p and an average value $\overline{m_1}$ for the number of monomers per unit volume.

The expression $S^*(qR_{gm1})$ in Eq. (III.1.8) is then derived thanks to the following numerical simulation. Considering the relationship of the structure factor by Lin et al. (Eq. (III.1.2)) as a function of the wave vector q, the corresponding integral of Eq. (III.1.7) is built up. The numerical integration, obtained by changing N_p from 0 to a maximum value (10,000 in our case), is evaluated for a given value of R_{gm1}. This is obtained with small particle size and a large average number of particles per aggregate, or vice versa. As for N_p, tests are carried out to check that increasing the maximum value over which the integral is performed no variation in the calculation was obtained.

In Fig. III.1.2, the two curves for small (d_p = 5 nm) and large (d_p = 25 nm) particle size, for a given value of R_{gm1}, are perfectly overlapped and consequently only one is visible.
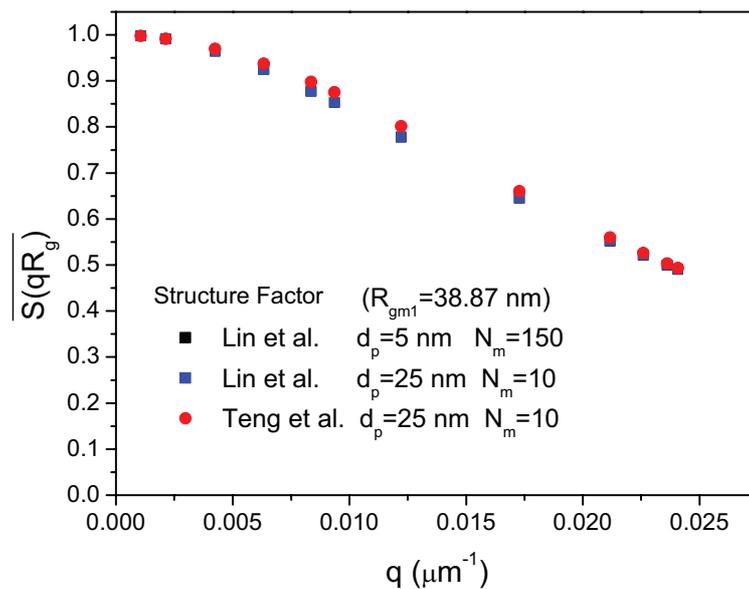

Fig. III.1.2: *Average structure factor versus q (De Iuliis et al. [181], Teng et al. [130]).*

In the same figure are also reported the values obtained by using the structure factor proposed by Teng et al. [130]. As already observed the difference between the graphs is almost negligible.

Finally by fitting $\overline{S(qR_g)}$ curve shown in Fig. III.1.2, a polynomial expression of the structure factor as a function of R_{gm1} is obtained

$$S^*(qR_{gm1}) = \frac{1}{1 + P_1(qR_{gm1}) + P_2(qR_{gm1})^2 + P_3(qRgm1)^3 + P_4(qR_{gm1})^4} \qquad \text{(III.1.10)}$$

where P_1, P_2, P_3, P_4 are the fitting parameters. The previous relationship, evaluated for a certain R_{gm1}, is satisfied whatever the radius of gyration. In fact, as the equation is expressed as a function of the product of R_{gm1} and the scattering wave vector, the curve of the structure factor will be more or less stretched along the x-axis, depending on the cluster dimension, but with the same analytical expression. Anyway, it is easy to numerically verify that this expression is valid whatever is the value of the radius of gyration.

Eq.(III.1.10) can be used to describe, at any angle, the scattering signal from a collection of polydisperse aggregates, with the following assumption:

- the validity of the Lin relationship for the structure factor [129],
- the lognormal distribution for the number of primary particles per aggregate,
- $\sigma = 2.1$ for the value of the standard deviation.

Using the expression (2.1.10), the novel approach proposed in this work allows the evaluation of the average radius of gyration Rg_{m1} from two-angle scattering measurements. To this purpose the scattering signal is collected at two angles (θ and $180°-\theta$) and the corresponding dissymmetry ratio is calculated.

The numerical simulation procedure performed is essentially parallel to the experimental one. The intensities $I_{VV,1}$ and $I_{VV,2}$ related to the two scattering angles are written according to Eq. (III.1.5). The corresponding ratio, that is the dissymmetry ratio is given by:

$$R_{VV}(\theta_1, \theta_2) = \frac{I_{VV}(\theta_1)}{I_{VV}(\theta_2)} = \frac{I_{VV,1}}{I_{VV,2}} = \frac{\int S(q_1 R_g) N^2 p(N) dN}{\int S(q_2 R_g) N^2 p(N) dN} = \frac{S^*(q_1 R_{gm1})}{S^*(q_2 R_{gm1})} \qquad \text{(III.1.11)}$$

where the subscript *1* and *2* refer to the two scattering angles used.

By considering Eq.(III.1.11), R_{gm1} is evaluated through a numerical inversion procedure. To this purpose, R_{gm1} is traced versus the dissymmetry ratio $I_{VV,1}/I_{VV,2}$, as shown in Fig. III.1.3, where the three curves correspond to $R_{vv}(20°/160°)$, $R_{vv}(45°/135°)$ and $R_{vv}(30°/150°)$.
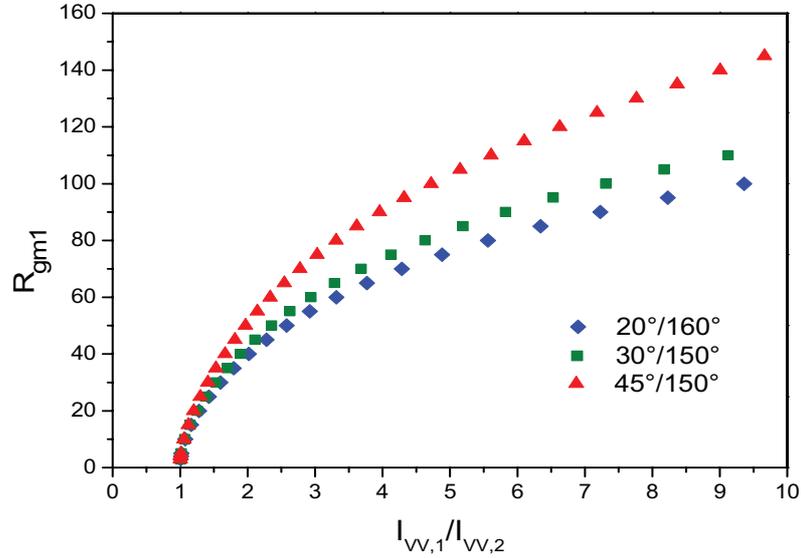
Fig. III.1.3: *Average radius of gyration vs dissymmetry ratios (evaluated at three angles).*

Almost the same trend is obtained for the three kinds of dissymmetry ratio. Due to the mechanical constraints of the optical arrangement, in this work scattering measurements in flames have been carried out at 30° and 150°. Then in the following the corresponding dissymmetry ratio $R_{vv}(30°/150°)$ will be taken into account. This curve is then fitted with a 6th order polynomial equation, given by the analytical expression:

$$R_{gm1} = \sum_{n=0}^{6} C_n (I_{VV,1} / I_{VV,2})^n \tag{III.1.12}$$

where the fitting coefficients are: C_0= -1843.57, C_1=6244.13, C_2=-8734.16, C_3=2669.25, C_4= 578.38 C_5=-51.48. The analytical function allows to evaluate, from the experimental measurements of the dissymmetry ratio, the average radius of gyration R_{gm1}.

This outcome represents the most important contribution of the present work. That is, the evaluation of the soot fractal parameter, as the radius of gyration, by measuring the scattering signal only at two angles. The drawback has been, however, the introduction of a new expression of the structure factor given by Eq. (III.1.10).

Once the average radius of gyration has been evaluated, the other soot parameters, as the volume-mean diameter and the primary particle diameter, are obtained in a similar way as the approach already described in the Chapter I and here briefly reported.

By knowing the average structure factor, the scattering coefficient from a polydisperse ensemble of aggregates results to be

$$K_{vv,pol} = C_{vv}^a N_a = C_{vv}^p N_a \overline{m_2} S^*(qRgm1) = \frac{\pi^4 d_P^6}{4\lambda_{scatt}^4} F(\lambda) N_a \overline{m_2} S^*(qR_{gm1}) \tag{III..1.13}$$

which is interesting to compare with Eq. (I.3.36). As for the absorption coefficient, the same expression as Eq. (I.3.35) is obtained. Considering the scattering coefficient at 90°, and coupling it with the absorption coefficient, the volume-mean diameter is obtained:

$$D_{30} = \frac{1}{\pi}\left(\frac{\lambda_{scatt}^4}{\lambda_{ext}}\right)^{1/3}\left[\frac{4\pi\,E(m)\,K_{vv,pol}(90°)}{F(m)f_n S^*\left(qR_{gm1}\right)K_{abs,pol}}\right]^{1/3} \tag{III.1.14}$$

which is similar to the expression given in Eq. (I.2.38), except for the structure factor.

Finally combining the definitions of both the radius of gyration R_{gm1} (Eq. (III.1.9) and the volume-mean diameter (Eq. (I.3.37), $D_{30}^3 = dp^3 \overline{m_1}$), soot primary particle diameter is given by

$$d_p^{3-D_f} = \frac{D_{30}^3}{k_f R_{gm1}^{D_f}} \tag{III.1.15}$$

In the present approach, some parameters as the fractal prefactor, K_f, and the fractal dimension, D_f, can not be derived from optical measurements. Then, these parameters have been experimentally measured from *ex situ* investigation by using transmission electron microscope (TEM) analysis. With this method the following values are obtained: $K_f= 6.3$ and $D_f= 1.68$.

Moreover, with TEM also the diameter of the primary particles can be measured, which are then compared with the *in situ* scattering measurements.

1.1.4 Conclusions on the methodology

In brief, here the methodology implemented to derive soot parameters by using angular scattering technique are synthesized in Fig. III.1.4. Sampling and TEM analysis have been performed only in one position in the flame
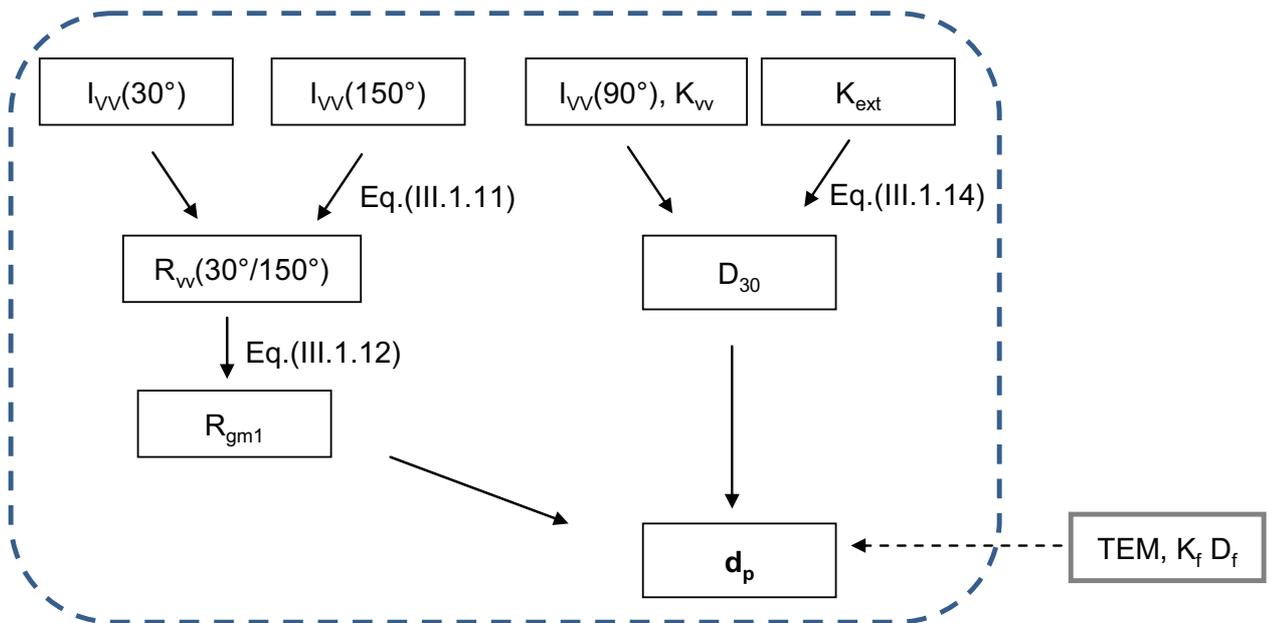

Fig. III.1.4: *Scattering/extinction measurements – processing procedure applied to flames*

The dotted contour is traced in order to separate optical measurements from TEM analysis. In our approach TEM measurements are considered only as a support at the optical data, allowing to obtain the values of K_f and D_f, which are, anyway, widely found in the literature.

The optically-determined soot primary diameter will be compared with the sampling data.

1.2 Uncertainties and sensitivity in scattering/extinction measurements

The evaluation of the uncertainties of our results is performed by considering the error in the raw data and applying the propagation theory. To this purpose, for the moment, the

fractal dimension and fractal prefactor are considered constant and the uncertainties of scattering/extinction measurements are taken into account.

As for extinction measurements, starting from the experimental data, the statistical relative error for I_L and I_0 is 0.4%. These are obtained by taking an average over 300 samples. By applying the propagation theory, for the monochromatic transmittance $TR_\lambda = I_L/I_0$ (see Eq. (I.2.1) in Chapter I) and for the extinction coefficient the following relationships are derived:

$$\frac{\Delta(TR_\lambda)}{TR_\lambda} = \sqrt{\left(\frac{\Delta I_L}{I_L}\right)^2 + \left(\frac{\Delta I_0}{I_0}\right)^2} \qquad (III.1.16)$$

$$\frac{\Delta K_{ext}}{K_{ext}} = \frac{1}{TR_\lambda} \frac{\Delta(TR_\lambda)}{\ln(TR_\lambda)} \qquad (III.1.17)$$

Then, the relative error of the monochromatic transmittance is 0.6%, and the one of the extinction 3%. As the soot volume fraction differs from K_{ext} for a constant factor of proportionality, the same uncertainty is obtained.

Considering scattering measurements, the signal is detected with an uncertainty of 2.5%. By combining scattering and extinction coefficients the error for D_{30} results to be 1.3% from the following relationship:

$$\frac{\Delta(D_{30)}}{D_{30}} = \frac{1}{3} \sqrt{\left(\frac{\Delta K_{VV}}{K_{VV}}\right)^2 + \left(\frac{\Delta K_{ext}}{K_{ext}}\right)^2} \qquad (III.1.18)$$

The radius of gyration is calculated from the dissymmetry ratio. The relative error of I_{VV1}/I_{VV2} (Eq. (III.1.12)) is 3.5%, and the corresponding value for R_{gm1} is 9.87%.

Finally the uncertainty on soot particle diameter can be derived from Eq.(III.1.15). In fact, applying the error propagation theory, we obtain

$$\frac{\Delta(d_p)}{d_p} = \frac{1}{3 - D_f} K_f \sqrt{3\left(\frac{\Delta D_{30}}{D_{30}}\right)^2 + \left(\frac{\Delta R_{gm1}}{R_{gm1}}\right)^2} \qquad (III.1.19)$$

The uncertainty for the particle diameter is calculated to be 10.4%.

As already observed, the numerical approach developed and presented in this work is based on the measurements of the fractal dimension and the prefactor by means of TEM analysis. Anyway, as different values of these parameters can be found in the literature, it is interesting to evaluate the sensitivity of the primary particle diameter according to such values.

The fractal dimension is found to vary in the range 1.68-1.9 (Xu et al. [9] and Koylu et al. [10]), which results in a variation of 10% on d_p.

More significant sensitivity is obtained for the fractal prefactor, as in the literature values in the range 5.8-9.4 are reported (Xu et al. [9], Koylu et al. [10]). Accordingly, soot particle diameter can vary as much as 35%.

It can be inferred that, even if the particle diameter is more sensitive to fractal prefactor value, such variation can still be acceptable.

1.3   Dependence of extinction measurements on laser wavelength

In this paragraph the dependence of the extinction on the spectral band region of the source used is analyzed. The aim is to point out that the choice of the wavelength is strictly linked to the particular experimental conditions under investigation, that means reactant gases, temperature and pressure range.

As extinction technique is applied to measure soot concentration, the contribution to the absorption of carbonaceous particles has to be discriminated against the one due to other species. A combustion system is a quite complex environment, characterized by the presence of different gas-phase species, as for example the polycyclic aromatic hydrocarbons. These molecules present typical wide absorption band in the UV-visible region. Depending on the experimental conditions, the contribution to the extinction from these absorbing species could not be negligible. To overcome this problem, wavelengths close to the IR spectral region should be chosen.

For this reason, the investigation of the dependence of extinction measurements on the spectral region is investigated both in flames and in shock tube. In this paragraph results concerning measurements in flames are presented, while the data in shock tube will be reported in the next Chapter.

To this purpose, in the ethylene/air premixed flame extinction measurements are carried

out with 632.8 nm (He-Ne) and 1064 nm (cw Nd:YAG). In Fig. III.1.5, the corresponding soot volume fraction f_v is reported versus the height above the burner.
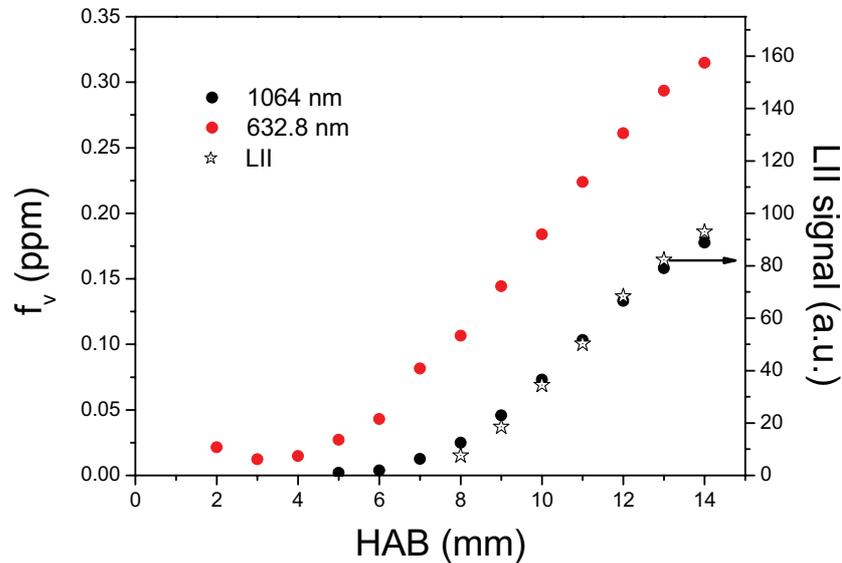

Fig. III.1.5: *Soot volume fraction axial profiles obtained using different sources: at 1064 nm and 632.8 nm. Comparison with LII measurements (this work).*

As it can be seen from the figure, the use of the red laser line gives values of f_v that are overestimated with respect to the ones obtained with the IR source.

In the same figure, for comparison, laser-induced incandescence measurements are also reported on the right y-axis. These measurements have been performed by using a Nd:Yag laser (1064 nm, 300 mJ/cm^2) and collecting the incandescence signal at 450 nm. More details on LII measurements are given in the work of Migliorini et al. [191]. The incandescence signal, reported in Fig. III.1.5, is not calibrated, and is traced by scaling it with the other measurements. As it can be observed, LII curve is almost overlapped with f_v measurements obtained with the IR source.

As already described in Chapter I Paragraph 2.3, LII technique allows to detect carbonaceous particles and to discriminate them against other species. Then, it is possible to infer that the infrared source used for the extinction is the one suitable to detect soot concentration, at least in the conditions under study.

In the next Chapter, we will show that a different result is obtained for the measurements in shock tube. In any case, the use of long wavelength sources for extinction measurements results to be safer whatever is the experimental condition.

2 Results

2.1 Ethylene / Air Flame

2.1.1 Flame structure

In Fig. III.2.1 a picture of the flame fuelled with ethylene / air mixture at an equivalence ratio of 2.34 (Flame A) is shown. The flame has been imaged by recording the light emission with a CCD camera coupled with an interference filter (λ=647 nm, $\Delta\lambda$ =10 nm). In the picture y-axis refers to the real height above the burner, being HAB = 0 the burner mouth and HAB = 20 mm the height at which the stabilizing plate is positioned. On the x-axis the radial position in the flame is reported. In the figure caption T_{ini} and P_{ini} represent the initial temperature of the fresh gases and pressure, respectively.
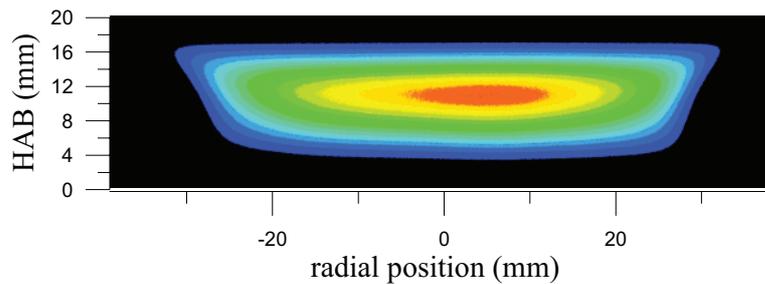
Fig. III.2.1: *2D light emission of ethylene / air flame (A) at an equivalence ratio of 2.34 (T_{ini} = 300 K, P_{ini} = 101.3 kPa).*

From this image, one can see that the flame presents, with a good approximation, an axisymetric geometry. As it is reported in the work of Migliorini et al. [185], the distribution of the soot volume fraction radially across this investigated flame is uniform, which is consistent with the 2D image shown in the figure.

In order to characterize the flame, temperature measurements performed along the flame axis are reported in Fig. III.2.2 (Migliorini et al. [192]).

These measurements have been carried out by using a 50 μm Pt/Pt-Rh(10%) uncoated thermocouple and are corrected for heat losses. Starting from the burner mouth the temperature increases in the first 2 mm, reaching a value of about 1700 K, which is very close to the adiabatic temperature reported in Table II.1.2. Moving upwards, towards the stabilized plate, a very slight decrease in temperature is detected.
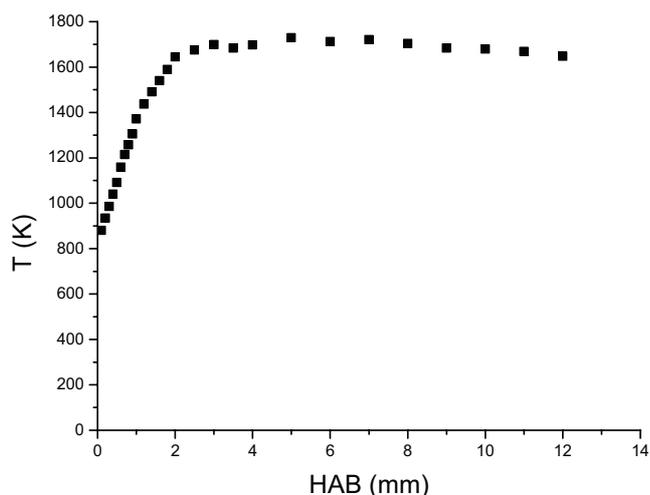
Fig. III.2.2: *Temperature measurements (T) versus HAB for ethylene / air flame at ϕ= 2.34.*

2.1.2 Soot parameters

In order to describe this flame in terms of soot formation the procedure presented in the Paragraph 2.1 and sketched in Fig. III.1.4 are now applied for each height above the burner.

Considering the scattering measurements, the three signals collected at three scattering angles have been corrected for the probe volume and processed with the calibration procedure reported in Chapter II. In Fig. III.2.3, the scattering intensity versus the height above the burner (HAB) is shown for the three scattering angles.
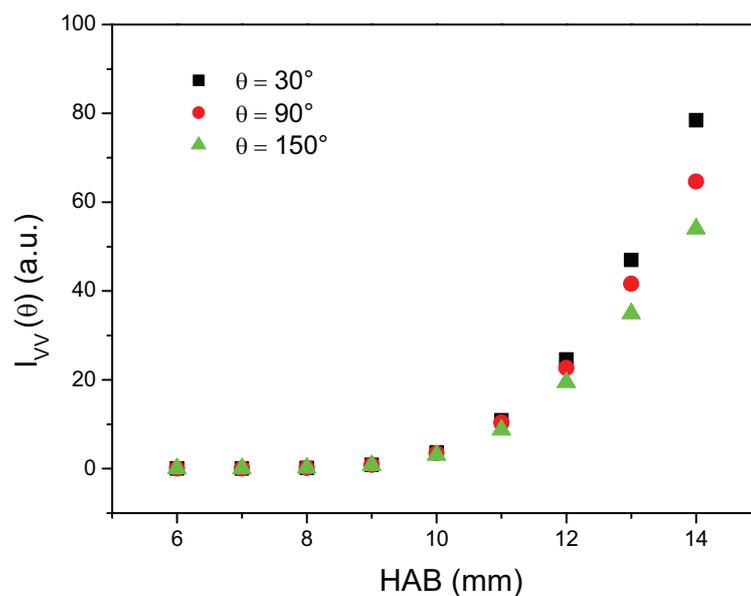

Fig. III.2.3: *Scattering intensity at three scattering angles vs HAB – ethylene/air flame.*

Significant scattering signals are detected starting from HAB = 6 mm (as shown in the figure). Just to give an idea, the scattering intensity at this height and at 90° resulted to be I_{VV} = 40 ± 1 mV, with respect to a corresponding measured background of 10 mV. Then, the values reported in Fig. III.2.3 and processed in the following have a good signal to noise ratio. Moving high in the flame, a fast increase of three scattering intensities of about two order of magnitude is observed. By comparing the signals at the three angles, it can be seen that low in the flame they are overlapped, and become spread out in the upper region.

In order to better analyze how the angular dependence of the scattering signal changes with the height, in Fig. III.2.4, the intensity versus the scattering angle is reported for each HAB.
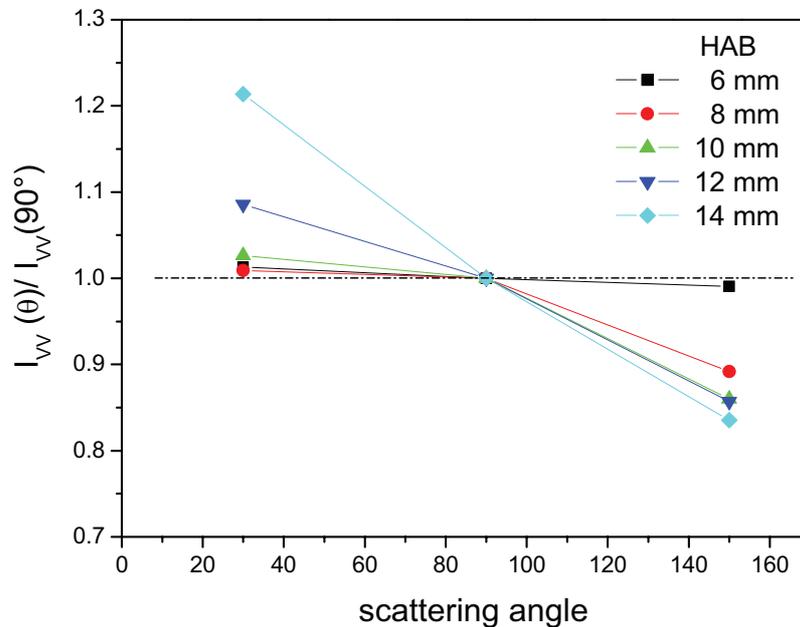

Fig. III.2.4: *Scattering intensity normalized at the value at 90° versus scattering angles at different HABs – ethylene/air flame*

All data are normalized to the scattering intensity at 90°. Although measurements are performed every millimeter along the flame axis, for clarity, the curves traced refer to signals collected every two millimeters. At HAB = 6 mm the trend is almost flat, with the intensities at the three angles presenting almost the same value. This behavior is typical of Rayleigh scattering regime. In order to understand weather, at this height above the burner, scattering signal is due to soot or to gas phase species extinction measurements are needed.

At HAB = 8 mm the presence of a dissymmetry in the trend is evident: the signal at 150° is definitely lower than 1, while the value at 30° is almost equal to the signal at 90°. At

this stage, carbonaceous particulate is already formed. Such a dissymmetry can be due to a non-perfectly spherical shape of the particle or to a beginning in the aggregation. Moving higher in the flame the dissymmetry ratio becomes more and more severe.

From extinction measurements, extinction coefficient and soot volume fraction are derived. In Fig. III.2.5 the scattering coefficient at 90° (right y-axis) and the extinction coefficient (left y-axis) are shown versus the height above the burner.
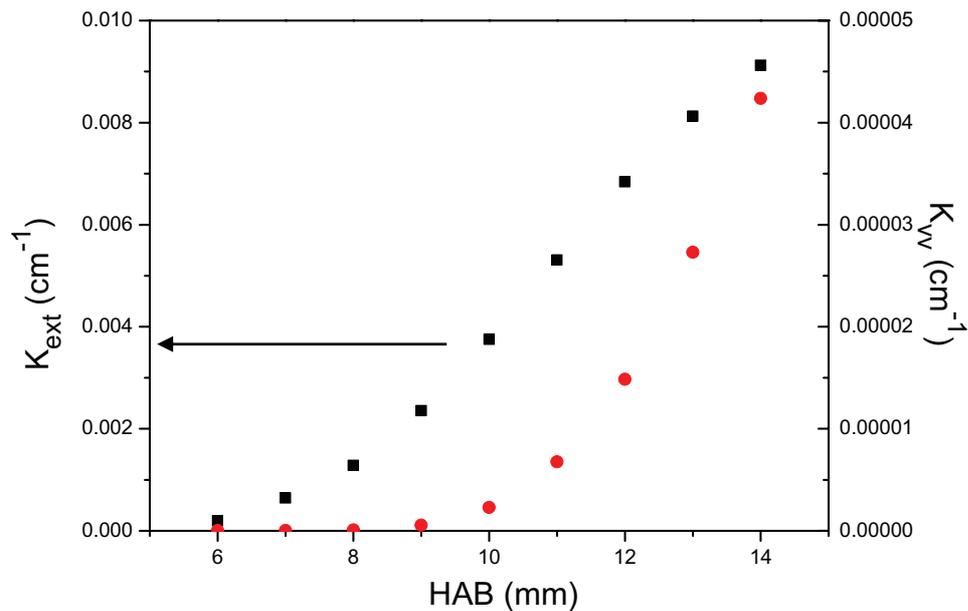

Fig. III.2.5: *Scattering and extinction coefficient K_{vv} and K_{ext}, respectively, versus height above the burner – ethylene/air flame at an equivalence ratio of 2.34 ($T_{ini} = 300$ K, $P_{ini} = 101.3$ kPa).*

As in flames the height above the burner is related to the residence time, one can say that the scattering coefficient starts with some delay with respect to the extinction. This behavior is due to the fact that the scattering is proportional to the 6th power of diameter. Since the particle size is relatively small at the beginning of soot formation, a low value of the scattering coefficient is obtained. This means that the delay can be probably due to a limited dynamic range of the scattering measurements.

In Fig. III.2.6 the soot volume fraction versus the height above the burner is reported. Due to the proportionality between the soot volume fraction and the extinction coefficient, again on the right y-axis the values of K_{ext} are reported. No extinction signal is detected below 6 mm height above the burner. The curve presents a monotonic increase with the flame height, reaching a maximum value at the highest level investigated in the flame, that is HAB

= 14 mm. Here, the extinction reaches the value of only 4%, corresponding to $K_{ext} = 0.01$ cm^{-1} and $f_v = 0.17$ ppm. In order to appreciate such low extinction level in its variations, a significant signal to noise ratio is required. In fact, as already reported in the paragraph 2.2 of this chapter, 300 sampling are collected in order to obtain an uncertainties in f_v of 3%.
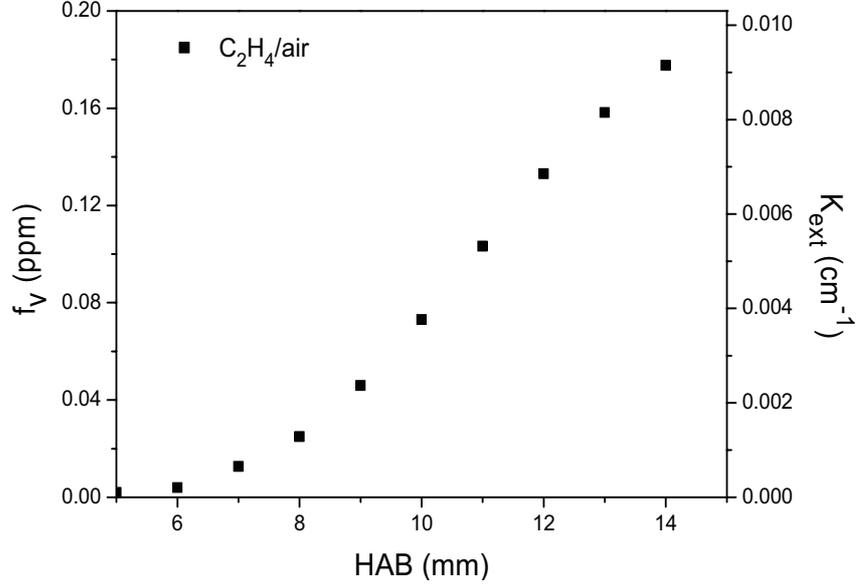

Fig. III.2.6: *Extinction coefficient (on the right-axis) and soot volume fraction (left-axis) versus the height above the burner for C$_2$H$_4$/air flame at an equivalence ratio of 2.34 (T$_{ini}$ = 300 K, P$_{ini}$ = 101.3 kPa).*

As soot formation depends on the carbon atom concentration in the initial mixture, in order to evaluate the conversion of these carbon atoms in the soot particles a normalization criterion has to be applied. The soot yield, Y_{soot}, is then introduced, as defined as:

$$Y_{soot} = \frac{[C]_{soot}}{[C]_{tot}} \qquad\qquad (III.2.1)$$

In the previous relationship, *[C]$_{soot}$* is the carbon atom concentration in the carbonaceous particulate and *[C]$_{tot}$* the relative value of the initial mixture. According to Graham's model [74] the soot yield can be expressed as:

$$Y_{soot} = \frac{N_{av}\rho}{12[C]_{tot}} f_v \qquad\qquad (III.2.2)$$

where ρ is the soot particle density and N_{av} the Avogadro's number.

In Fig. III.2.7 the soot yield versus the height above the burner is plotted. The maximum soot yield of 1.3 % is obtained at the height of 14 mm. The introduction of the soot yield is particularly required when the results obtained with hydrogen addition will be presented, as it will be discussed in the next paragraph. In fact, the normalization to the concentration of carbon atom in the initial mixture makes it possible to have a comparison between the results with and without hydrogen.
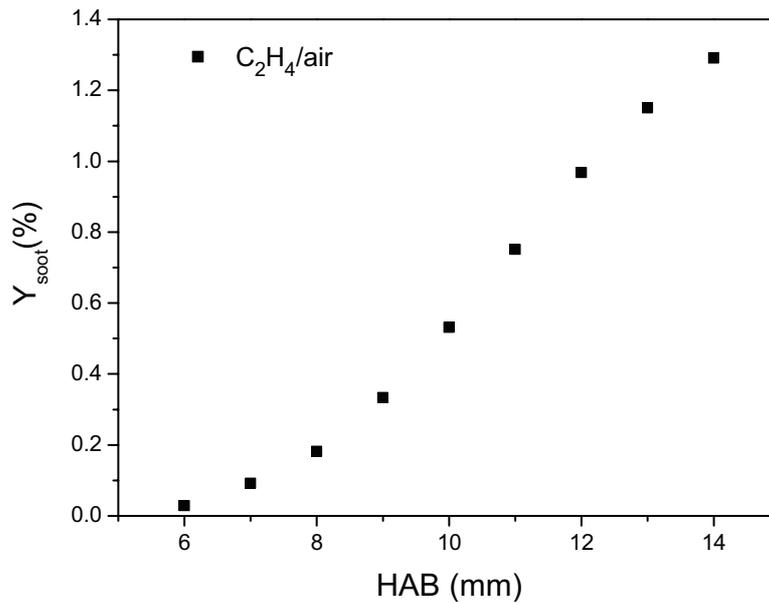

Fig. III.2.7: *Soot yield versus the height above the burner for C_2H_4/air flame at an equivalence ratio of 2.34 (T_{ini} = 300 K, P_{ini} = 101.3 kPa).*

From scattering measurements at 30° and 150° the dissymmetry ratio is calculated. Its behavior versus the height above the burner is shown in Fig. III.2.8. As a general trend, an increases of $R_{vv}(30°/150°)$ along the flame axis is detected. In particular, in the figure three different slopes can be observed: a first one is more likely an "abrupt discontinuity" between 7 mm and 8 mm height above the burner, a second increase occurs between 8 mm – 12 mm, and moving upwards a third rate is detected.

As the radius of gyration has been obtained through a polynomial equation of the dissymmetry ratio (see Eq. III.1.12), the same trend as $R_{vv}(30°/150°)$ is obtained for R_{gm1} (Fig. III.2.9).
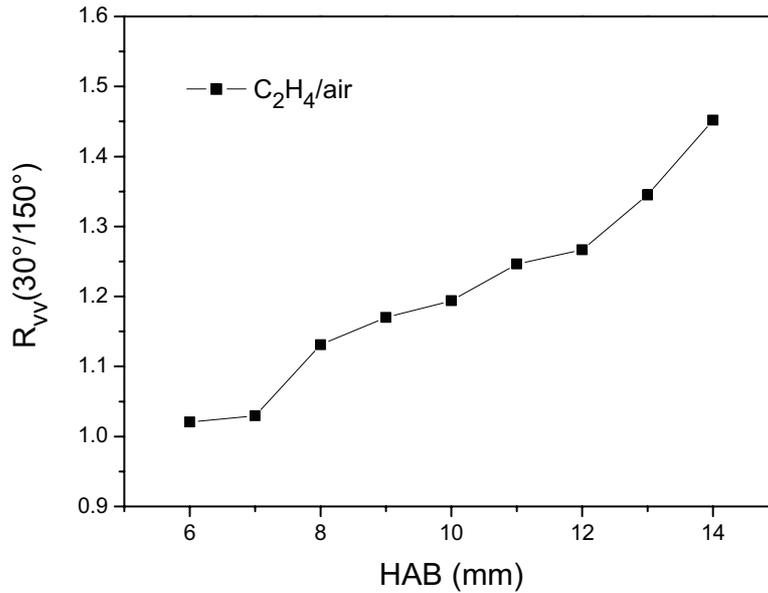
Fig. III.2.8: *Dissymmetry ratio versus the height above the burner for C_2H_4/air flame at an equivalence ratio of 2.34 ($T_{ini} = 300$ K, $P_{ini} = 101.3$ kPa).*
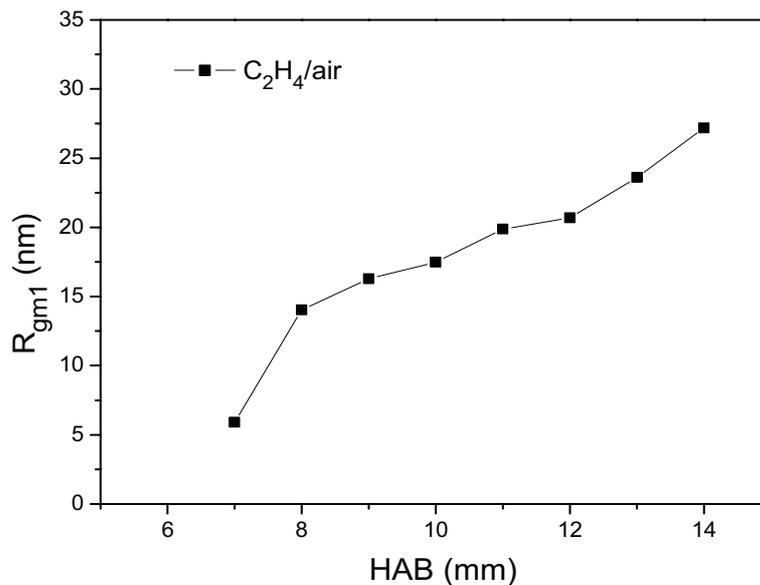

Fig. III.2.9: *Radius of gyration versus the height above the burner for C_2H_4/air flame at an equivalence ratio of 2.34 ($T_{ini} = 300$ K, $P_{ini} = 101.3$ kPa).*

Again, a fast growth process is observed from 7 to 8 mm HAB, then a slower one for HAB between 8 and 12 mm. Finally, a faster increase is observed for HAB higher than 12 mm.

From the interesting behavior of the radius of gyration reported in the figure, information about the aggregation can be obtained during the reaction time. In particular, such

behavior can be explained taking into account the occurrence of competitive growth processes, as surface growth and aggregation. This is evident considering the changing in the slope from 8 mm to 14 mm. In the first part, surface growth results to be more important then aggregation, while the inverse happens in the flame section above HAB = 12 mm. Moreover, considering the beginning of soot formation, it is difficult to understand if the "abrupt discontinuity" can be due to the starting of aggregation processes or to the presence of not spherical primary particles. For that other information are needed.

By combining scattering at 90° and extinction coefficients, the volume-mean diameter, $D_{30,}$ is calculated. In Fig. III.2.10 the axial profile is shown. As one can see, D_{30} exhibits a monotonic increases as a function of HAB, no changing slopes were observed as obtained for the dissymmetry ratio or for the radius of gyration.
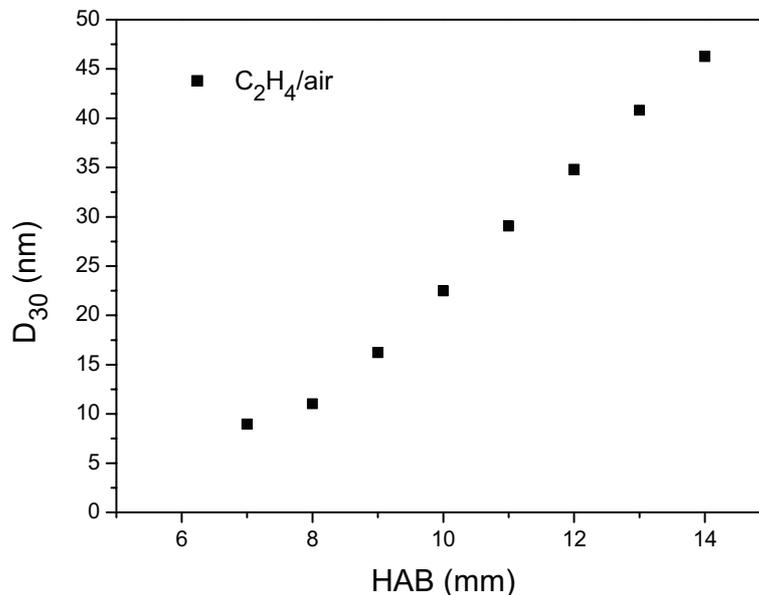

Fig. III.2.10: *Volume-mean diameter versus the height above the burner for C_2H_4/air flame at an equivalence ratio of 2.34 (T_{ini} = 300 K, P_{ini} = 101.3 kPa).*

By comparing the results of the volume-mean diameter and of the radius of gyration, it can be inferred that the first fast increase in the radius of gyration is due to aggregation process.

Finally, the axial profile of the soot particle diameter and the particle number density versus the height above the burner are reported in Fig. III.2.11 and Fig. III.2.12, respectively.
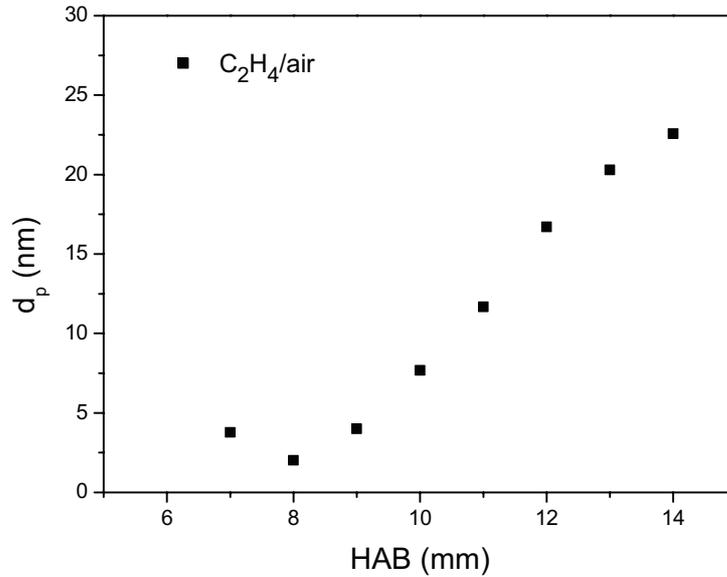
Fig. III.2.11: *Soot particle diameter versus the height above the burner for C_2H_4/air flame at an equivalence ratio of 2.34 (T_{ini} = 300 K, P_{ini} = 101.3 kPa).*
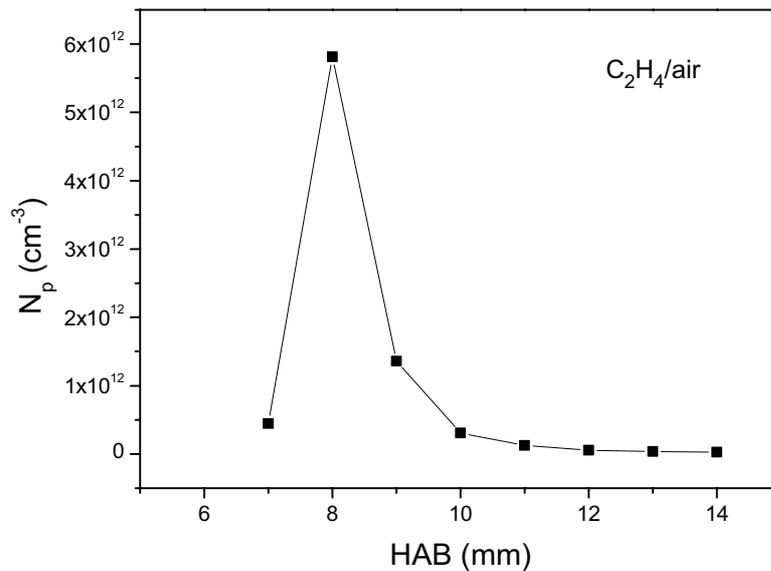

Fig. III.2.12: *Soot particle number density versus the height above the burner at an equivalence ratio of 2.34 (T_{ini} = 300 K, P_{ini} = 101.3 kPa).*

For HAB = 7-8 mm the soot primary particle diameter is almost constant and above this height increases regularly. The minimum detectable value of d_p results to be about 3 nm.

Correspondingly, the particle number density N_p presents a significant peak at HAB = 8 mm, which is due to the occurrence of nucleation processes. The following fast reduction in the number density is due to coagulation mechanisms.

2.2 Effect of Hydrogen Addition

In order to study the influence of hydrogen addition on soot formation, measurements are carried out on two additional flames, labeled B and C, reported in Table II.1.2.

2.2.1 Flame structure

In Fig. III.2.13 the pictures of the flames fuelled with ethylene/hydrogen/air are shown. They are obtained as the one in Fig. III.2.1, collecting the light emission with a CCD camera and an interference filter (λ=647 nm, $\Delta\lambda$ =10 nm).
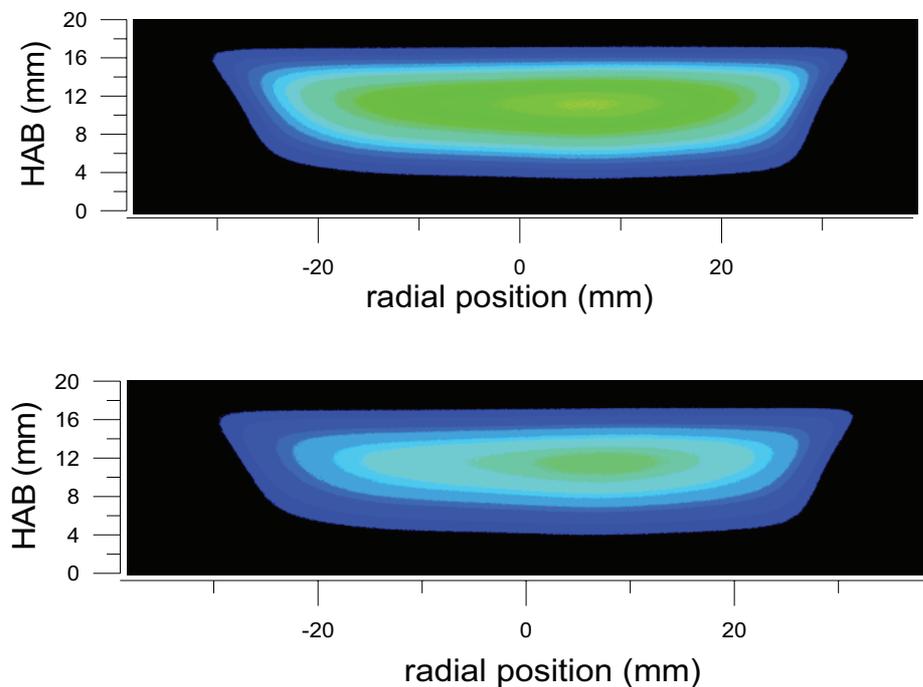
Fig. III.2.13: *2D light emission of ethylene /hydrogen / air flames. Flame B: with 20% of H_2, flame C: with 40% of H_2.*

With hydrogen addition, similar structure of the 2D light emission picture is observed, characterized to be, with a good approximation, axial symmetric.

As an overall behavior, it is clear from these figures that the emission intensity, in false color, decreases with the increasing of hydrogen addition.

As the radiation emitted from the flame can be due both to a reduction in the soot volume fraction and to a change in the temperature field, this observation is not sufficient to

derive any conclusions on the effect of hydrogen addition. A characterization of these flames in terms of temperature is necessary.

In Fig. III.2.14 the temperature versus the height above the burner is reported for the three flames under study (Migliorini et al. [192]). Temperature measurements were carried out by using the same thermocouple already employed in the non-doped flame. As it can be seen in the figure, the flames with hydrogen present values of temperature that are slightly lower than those obtained in the flame without hydrogen. Anyway, such difference results to be about 50 K at maximum. The maximum values of temperature measurements obtained in the two flames are in agreement with the corresponding adiabatic temperature values reported in Table II.1.2.

In the figure, moreover, it is possible to observe that the behavior of temperature versus HAB in the case of doped flames is flatter than in the case without hydrogen addition. This observation allows to infer that the equilibrium conditions is reached faster with hydrogen addition.
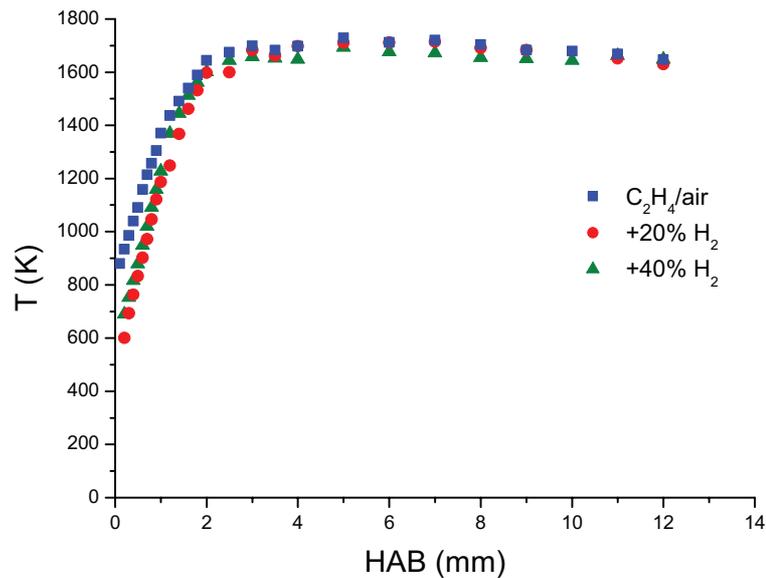

Fig. III.2.14: *Temperature measurements versus HAB for the three investigated flames: C₂H₄/air, C₂H₄/20%H₂/air and C₂H₄/40%H₂/air (Migliorini et al. [192]).*

2.2.2   Soot parameters

In the following, all soot parameters derived in the three flames under study will be compared.

Starting from extinction measurements, in Fig. III.2.15, extinction coefficient (on the right-axis) and soot volume fraction (on the left-axis) are reported versus the height above the burner.

The consideration about the low values of K_{ext} and consequently of f_v made in the previous paragraph, now is more severe. In fact, as for the non-doped flame, we have already observed that at HAB = 14 mm, f_v is less than 0.17 ppm (or correspondingly K_{ext} less than 0.01 cm^{-1} and the transmittance about 4%). By adding 40% H_2, at the same HAB, the soot volume fraction is about 0.05 ppm, corresponding to an extinction of only 1.5%.

It is clear that a high sensitivity of the technique with a good signal to noise ratio is required to appreciate such low signal level, especially in measurements low in the flame.
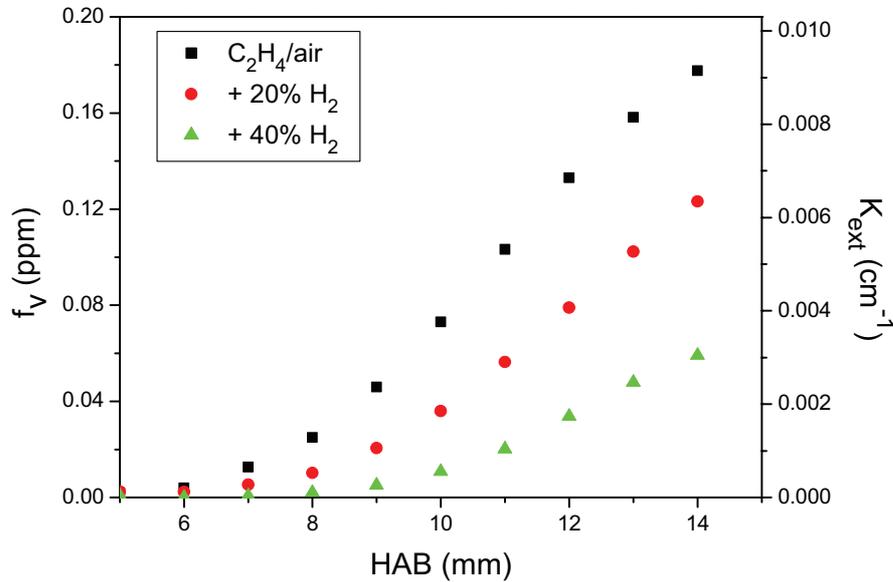
Fig. III.2.15: *Extinction coefficient (on the right-axis) and soot volume fraction (left-axis) versus the height above the burner for the three investigated flames: C₂H₄/air, C₂H₄/20%H₂/air and C₂H₄/40%H₂/air (see Table II.1.2).*

In order to evaluate the effective influence of hydrogen addition by comparing the flame with and without hydrogen, the soot yield is calculated. In fact, as reported in Table II.1.2, the flames are obtained by substituting an amount of ethylene/air with hydrogen, keeping constant the C/O ratio and the total mass flow rate. Then, for the comparison of the soot volume fraction, the normalization to the total carbon atom concentration in the initial mixture is mandatory. The soot yield versus the height above the burner is shown for the three investigated flames in Fig. III.2.16.
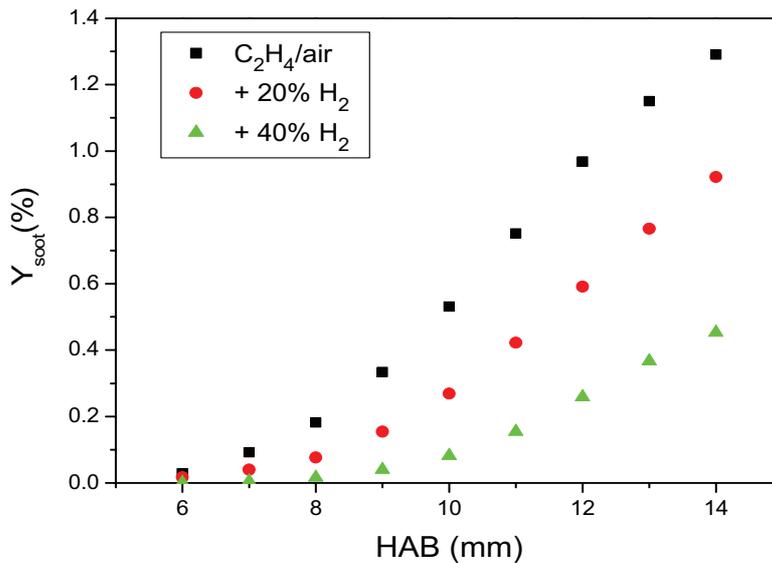
**Fig. III.2.16:** *Soot yield versus the height above the burner for the three flames C$_2$H$_4$/air, C$_2$H$_4$/20%H$_2$/air and C$_2$H$_4$/40%H$_2$/air (see Table II.2.1)*

All curves present a monotonic increase with HAB. Anyway, by increasing hydrogen content a strong reduction of the soot yield is obtained along the whole axial profile. Then, it is important to stress that the soot yield decreases with increasing hydrogen addition even in the case where the following conditions are fulfilled:

- C/O is constant
- The equivalence ratio increases as hydrogen is added

Comparing the shape of the three curves it is observed that, increasing hydrogen addition, the axial location where soot starts (the soot inception region) is shifted towards higher heights above the burner. This inception region results to occur at HAB = 7 mm for non-doped flame, at 8 mm for 20% H$_2$ flame, and between 9 mm and 10 mm for 40% H$_2$ flame. For that, in the following the axial profiles of the soot parameters will be represented starting from the heights above the burner where soot inception starts.

Soon after the inception region, soot particles growth seems to be different for the three flames, being the related curves characterized by different slopes.

From scattering measurements at 30° and 150° the dissymmetry ratio is calculated and reported in Fig. III.2.17 versus the height above the burner for the three flames.

As already shown in the case of pure ethylene/ air flame, the dissymmetry ratio presents a behavior versus HAB characterized by three different slopes. With 20% H$_2$ addition, a shift

of these three slopes towards higher height above the burner is detected. Finally, with 40% H_2, a further shift is observed, but in this case the last slope is not seen anymore, or it is too small to be detected.
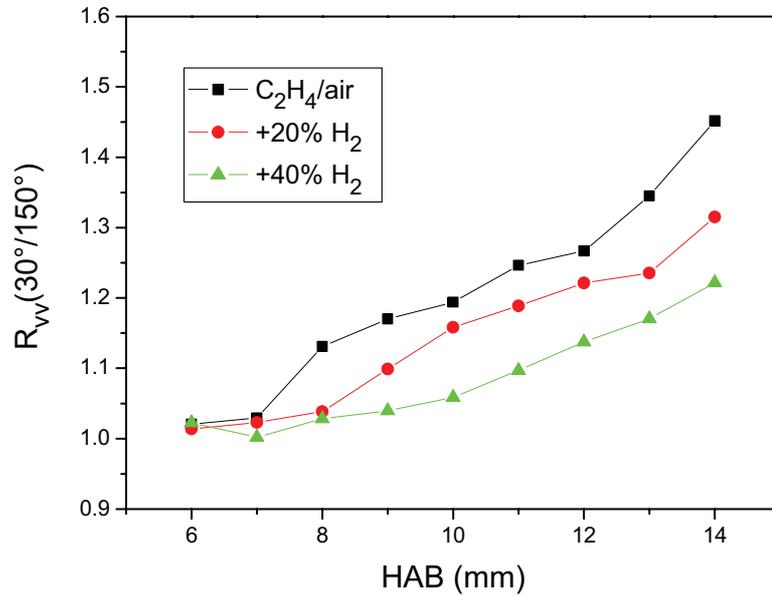
Fig. III.2.17: *Dissymmetry ratio versus the height above the burner for the three flames (C_2H_4/air, C_2H_4/20%H_2/air and C_2H_4/40%H_2/air; see Table II.2.1).*

From the dissymmetry ratio by using the polynomial expression, the radius of gyration R_{gm1} is derived and in Fig. III.2.18 the axial profiles for the three flames are reported.
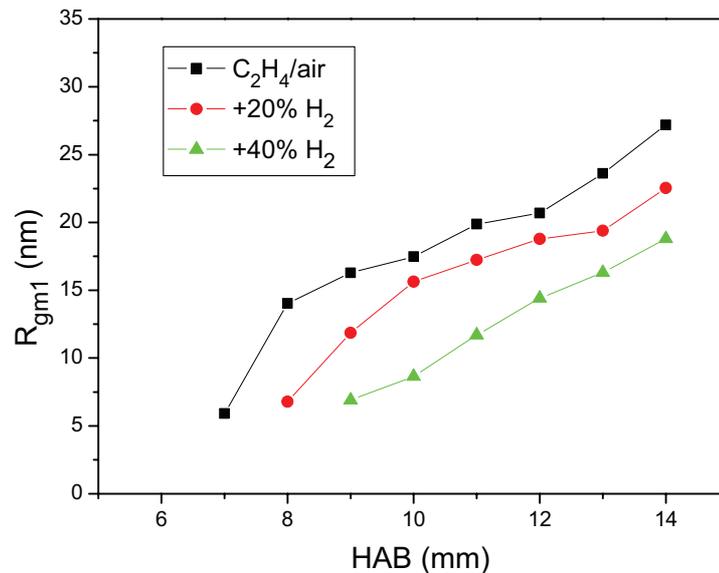
Fig. III.2.18: *R_{gm1} vs HAB for the three flames (C_2H_4/air, C_2H_4/20%H_2/air and C_2H_4/40%H_2/air; see Table II.2.1)*

It is obtained the same trends already described for the dissymmetry ratio.

Concerning the volume-mean diameter, in Fig. III.2.19 the axial profile of D_{30} is shown
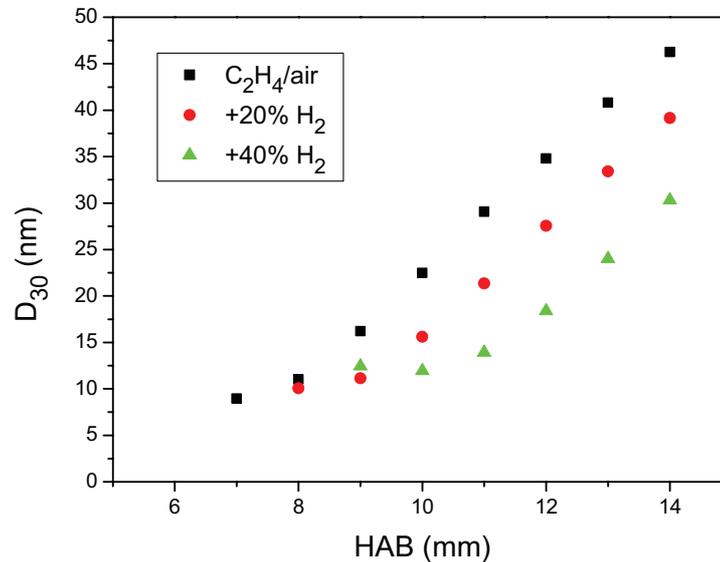
Fig. III.2.19: *Volume-mean diameter versus the height above the burner for the three flames (C_2H_4/air, C_2H_4/20%H_2/air and C_2H_4/40%H_2/air; see Table II.2.1).*

Again, a significant reduction of the volume-mean diameter has been detected by increasing hydrogen content. In this case the trend of the curves is almost regular for all flames. Being obtained from extinction and scattering, the same shifts at higher heights above the burner are observed as shown in the previous figures.

The axial profiles of the soot particle diameter versus the height above the burner are reported in Fig. III.2.20. The same trend as the volume-mean diameter is obtained. A severe reduction is observed with hydrogen addition: at HAB=12 mm particle diameter results to be 17 nm in non-doped flames and 6 nm in 40% H_2 flame. Then, it is possible to infer that hydrogen addition has an affect also on soot surface growth rate.
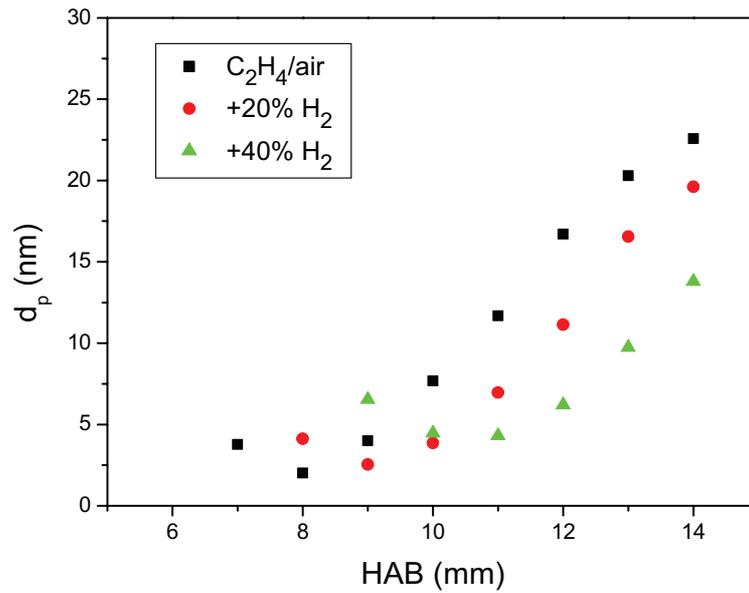
Fig. III.2.20: *Soot particle diameter versus the height above the burner for the three flames (C$_2$H$_4$/air, C$_2$H$_4$/20%H$_2$/air and C$_2$H$_4$/40%H$_2$/air; see Table II.2.1).*

Finally in Fig. III.2.21 the particle number density is reported versus the height above the burner. With hydrogen addition the typical well-defined peak due to the occurrence of the nucleation process followed by the coagulation mechanism observed in the ethylene/air flame presents the following changes:

- it is shifted at higher height in the flame,
- it presents a strong reduction in intensity (number of primary particle per unit volume).

In order to explain the total behavior of hydrogen addition on such flames, a comparison between all parameters obtained and shown previously (soot volume fraction, radius of gyration, volume-mean diameter, soot particle diameter and number density) has to be performed.

The general trend is a total reduction of the soot particulate, both in terms of volume fraction and in terms of dimension.
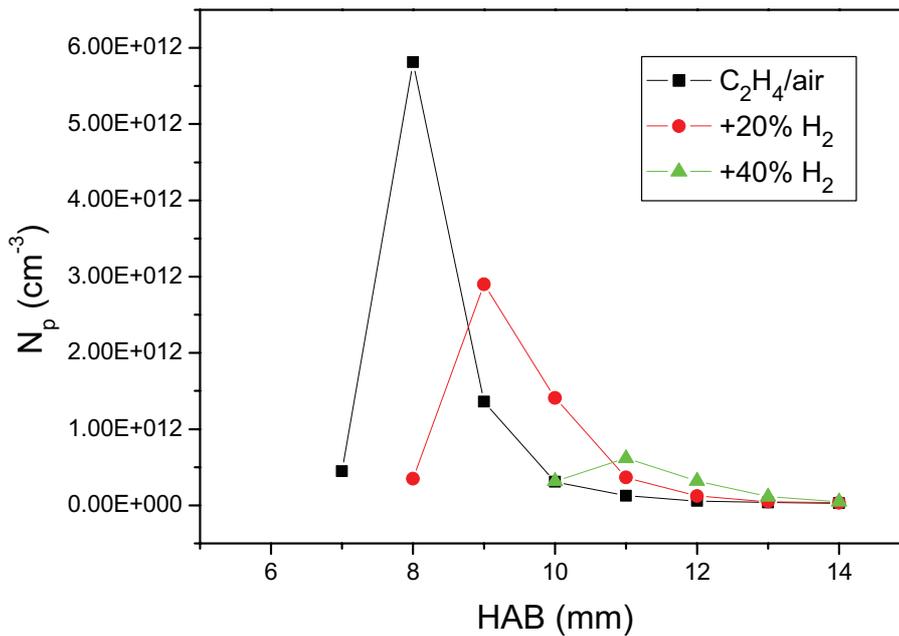
Fig. III.2.21: *Soot number density versus the height above the burner for the three flames (C₂H₄/air, C₂H₄/20%H₂/air and C₂H₄/40%H₂/air; see Table II.2.1).*

Such a reduction can be linked to two different processes important in soot formation, reported in the following.

1. The first one is the delay time necessary to form soot precursors. In fact, a long delay will lead to less soot, being shorter the residence time (and higher the laminar flame velocity with hydrogen addition).

2. The second parameter is linked to the concentration level of soot precursors that can decrease drastically with hydrogen addition, leading to a decrease in the nuclei concentration and, consequently, in the number of particles.

Measurements in the shock tube, presented in the next Chapter, allow to have information about the induction delay time and its dependence on hydrogen addition. Then, it will be possible to discriminate between the two scenarios.

As a further observation, while for the three flames an increasing trend with different slopes is exhibited by the soot volume fraction, the volume-mean diameter and the primary particle diameter present almost the same slope in the increasing behavior.

Concerning the radius of gyration, the very fast increase detected already at HAB=7 mm accounts for the starting of the aggregation process at this height. As this occurs close to the inception region, it is possible to infer that soot formation and growth via aggregation are not really separated phenomena, due to their fast occurrence in premixed flames. Such observation is confirmed by the fact that at low heights above the burner D_{30} and R_{gm1} are larger than the value of the primary particle diameter.

To conclude, hydrogen addition has an effect on soot concentration, dimension and aggregation.

2.3 Discussion about soot parameters rate

In order to gain more information about the influence of hydrogen addition on soot formation in premixed flames, the results of soot parameters obtained in the three investigated flames are further processed as follows.

Soot parameters can be expressed as a function of the reactions time, converting in time the height above the burner. At the value of the reactant flow rate (10 Nl/min) used in this work, the flame can be considered dominated by the buoyancy. By assuming constant the acceleration, this speed is given by:

$$a = \left(\frac{\Delta\rho}{\rho}\right)g = 25 - 31 m/s^2 \qquad \text{(III.2.3)}$$

where g is the gravity acceleration and $\left(\dfrac{\Delta\rho}{\rho}\right)$ the density variation due to the increase in temperature.

Then, it is possible to derive the reaction time t(HAB) as a function of the height above the burner as follows

$$t(HAB) = \sqrt{\frac{2\,HAB}{a}} \qquad \text{(III.2.4)}$$

Once soot parameters are reported versus time, for each curve the relative derivative is evaluated. In Fig. III.2.22 and in Fig. III.2.23 the derivative of the soot yield is reported versus time and versus the soot yield values, respectively.
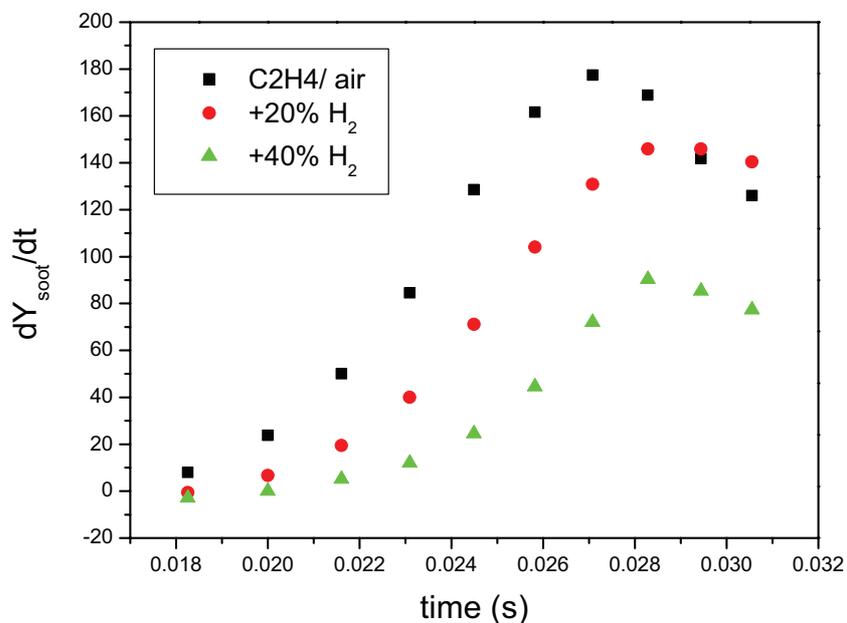
Fig. III.2.22: *Derivative of the soot yield versus time for the three flames (C_2H_4/air, C_2H_4/20%H_2/air and C_2H_4/40%H_2/air; see Table II.2.1).*

In Fig. III.2.22 the three curves, corresponding to the three flames under study, are shifted in time and present a quite regular increase up to a certain height above the burner, followed by a slow decrease.

In Fig. III.2.23, for small values of Y_{soot}, the curves are almost overlapped, while a deviation is observed for higher Y_{soot}. Due to the lower value in the soot yield, the flame with 40% H_2 reaches a maximum before the others, followed by the one with 20% H_2 and the last without hydrogen.
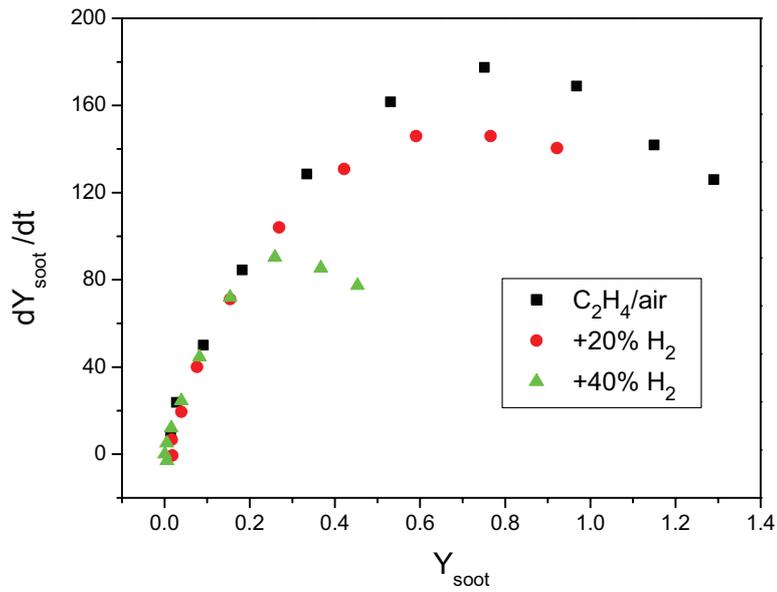
Fig. III.2.23: *Derivative of the soot yield versus soot yield for the three flames (C_2H_4/air, C_2H_4/20%H_2/air and C_2H_4/40%H_2/air; see Table II.2.1).*

In Fig. III.2.24 and Fig.III. 2.25 the derivative of the soot particle diameter versus time and versus the particle diameter values are reported, respectively.
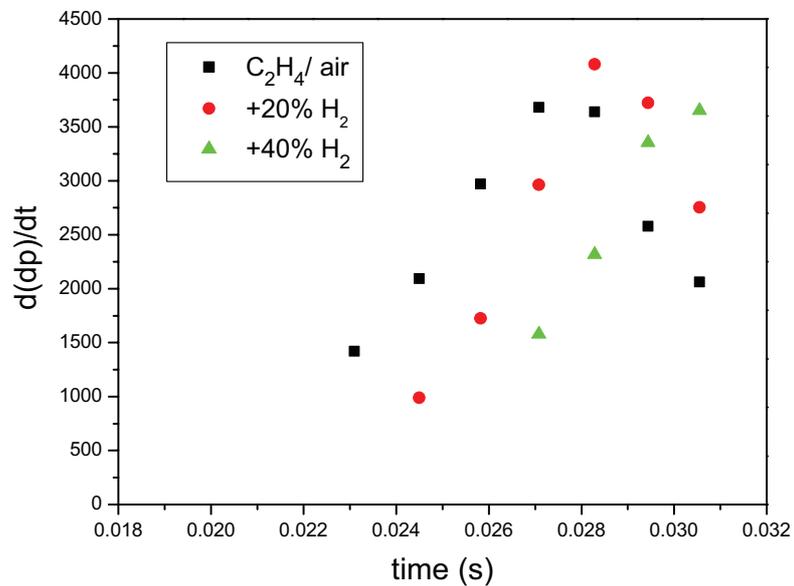

Fig. III.2.24: *Derivative of particle diameter versus time for the three flames (C_2H_4/air, C_2H_4/20%H_2/air and C_2H_4/40%H_2/air; see Table II.2.1).*
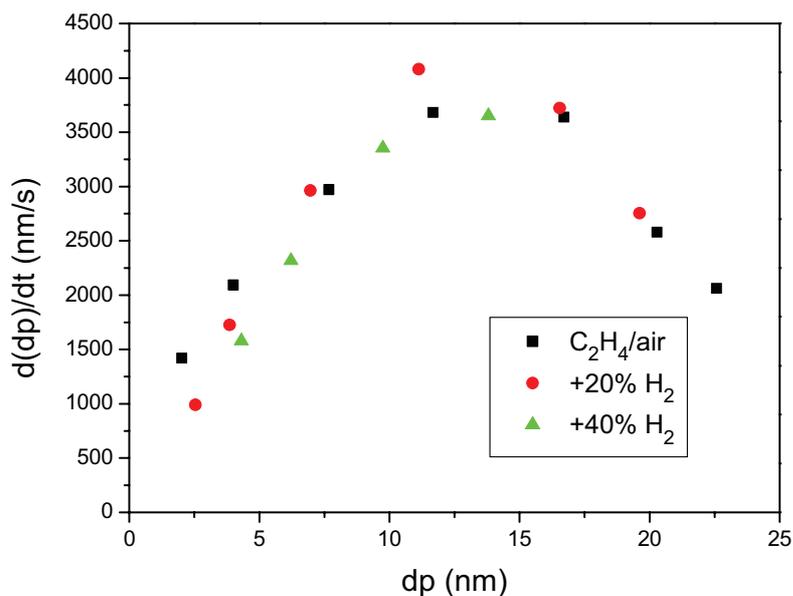
Fig.III. 2.25: *Derivative of particle diameter versus particle diameter for the three flames (C₂H₄/air, C₂H₄/20%H₂/air and C₂H₄/40%H₂/air; see Table II.2.1).*

For clarity also the derivative of the soot volume, V, versus the volume is shown in Fig. III.2.26.
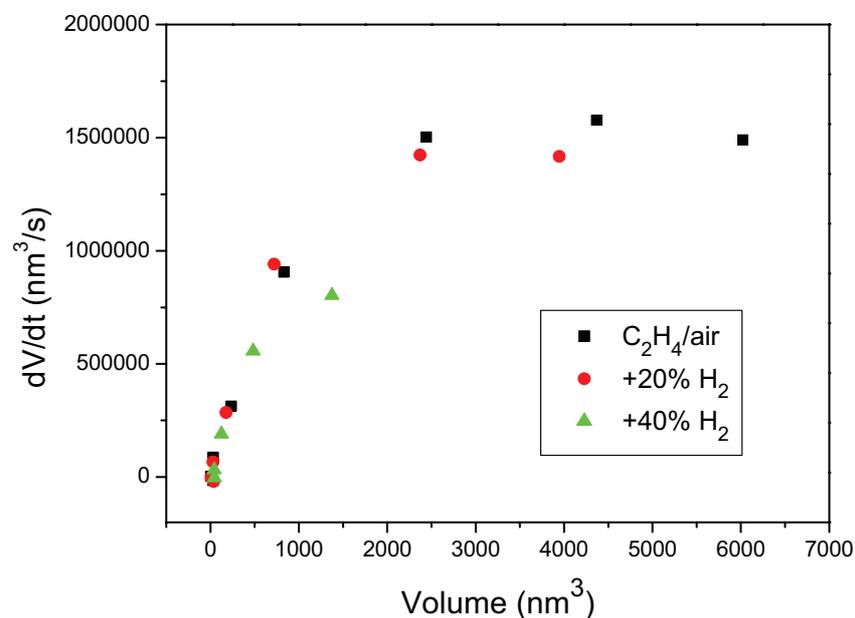
Fig. III.2.26: *Derivative of soot particle volume versus volume values for the three flames (C₂H₄/air, C₂H₄/20%H₂/air and C₂H₄/40%H₂/air; see Table II.2.1).*

The three figures considered (Fig. III.2.24, Fig.III. 2.25 and Fig. III.2.26) allow to derive interesting information about the soot particle growth and the effect of hydrogen addition on it, which are reported in the following.

- In Fig. III.2.24 the derivative of particle diameter versus time presents almost the same slope, only shifted in time, for the three flames.
- In Fig.III. 2.25 and Fig. III.2.26, the curves are practically overlapped, and no influence of hydrogen addition is detected.

Moreover, from the comparison of the last two figures (the d_p and V derivative) a congruent description is obtained. As for d_p derivative, it is obtained an increase with the diameter up to a maximum, after which a decrease is observed. This reduction occurs when particles are already more than 15 nm, and consequently is consistent with an almost constant value of the particle volume.

Finally in Fig. III.2.27 the derivative of particle number density is reported versus time. Considering the ethylene/air flame, at low reaction time and due to coagulation processes, a fast decrease is detected.
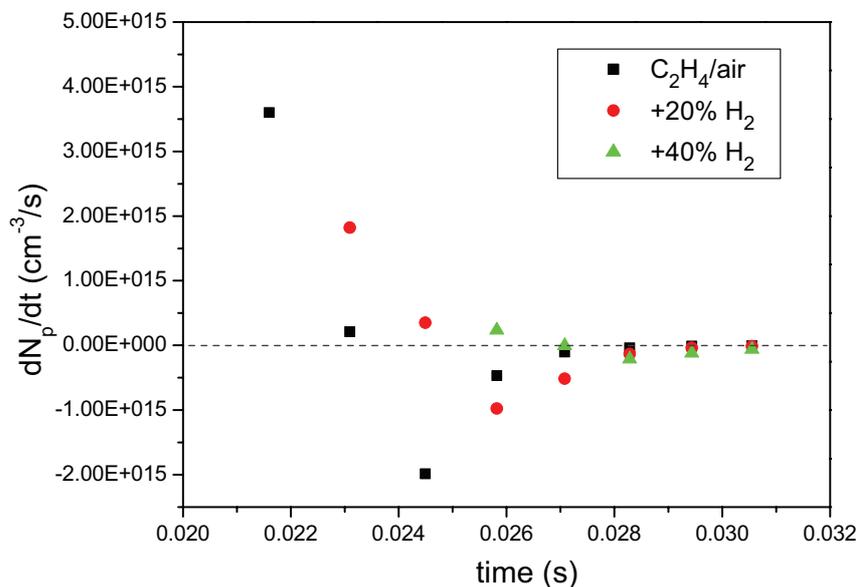
Fig. III.2.27: *Derivative of particle number density versus time for the three flames (C₂H₄/air, C₂H₄/20%H₂/air and C₂H₄/40%H₂/air; see Table II.2.1).*

The curve goes to zero after few milliseconds, that is in few millimeters in the flame. After this time, the number density remains constant. With hydrogen addition a reduction in the rate of the number density is detected. This reduction is less and less important by

increasing hydrogen content. In all cases, the derivative tends to zero as already observed for the non-doped flame.

2.4 TEM measurements

In order to validate the optical measurements and to derive the values of some parameters used in the fractal-like approach, soot sampling technique and TEM analysis has been performed. Measurements are carried out in the no-doped flame at only one location on the axis, at HAB = 14 mm.

Typical images of the soot cluster collected on TEM grids are reported in Fig. III.2.28.

In the two pictures the calibration bar is reported; as different magnification is used, the related bar lengths are different. These images clearly show the soot structure in the flame. At this position, the aggregation process is important: soot aggregates present a typical fractal-like structure, with a characteristic cluster polydispersity.
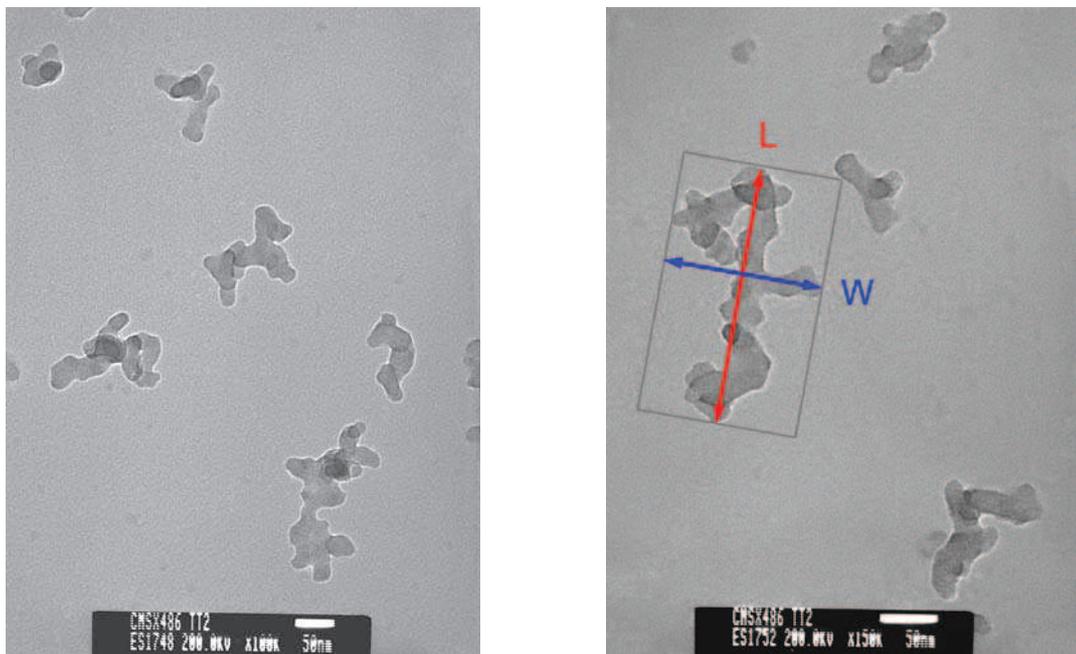
Fig. III.2.28: *TEM images of soot cluster detected at HAB=14 mm in the C_2H_4/air flame.*

In order to obtain soot parameters with a good statistics, different images are taken and processed. From the measurements of the area of each particle, the primary particle diameter

is obtained. A value of 24.7 nm has been derived by averaging more than one hundred particles.

This result is in good agreement with the value of 22.5 nm obtained with optical measurements (see Fig. III.2.20) in the same flame ethylene/air (equivalence ratio =2.34) and at the same height above the burner (HAB = 14 mm).

For the evaluation of the parameters linked to the fractal aggregates, pictures are processed by applying the procedure described in the Chapter I [132]. Considering a single cluster, the following geometric features can be directly measured:

- the length (L) and the width (W), shown for clarity in the right picture of Fig. III.2.28,
- the area of the aggregate.

Then, it is possible to calculate the radius of an aggregate (R_L, defined as the half of the cluster length), the number of primary particles in an aggregate (by using Eq. I.3.42), the equivalent radius of the aggregate surface (R_a). By considering Eq. (I.3.43), the number of primary particle is expressed versus the ratio R_L/a, where a is the primary particle radius. The result is shown in Fig. III.2.29, in a bi-logarithmic scale.

$$\ln(N) = 0.0208 + 1.6855 \ln(R_L/a)$$
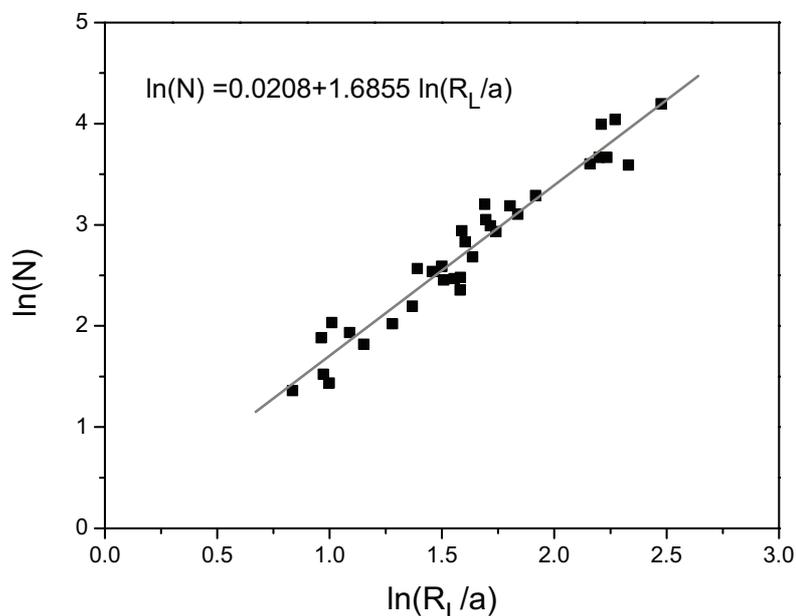
Fig. III.2.29: *Ln-Ln behavior of the number of primary particles in an aggregate versus R_L/a. Data relative to the measurements at HAB=14 mm in the C_2H_4/air flame.*

In the figure the linear fitting is overlapped to the data and the analytical expression is also reported. The slope of the fitting curve gives directly the fractal dimension, that is, in our case, equals to 1.68. This result is in agreement with the data of D_f found in the literature, usually between 1.7-1.9 (Oh et al. [124], Samson et al. [125]).

Moreover, from the intercept of the fitting linear curve with the y-axis, the correlation constant k_L is calculated. By applying Eq. (3.4.4) an estimation of the radius of gyration is derived and finally, by using Eq. (3.4.3), the fractal prefactor K_f is obtained. Unfortunately, a wide range of prefactor value is given in the literature, spreading from 5.8 to 9.4 (De Iuliis et al. [181], Mountain et al. [122], Koylu et al. [193]). The value obtained in this work, and used in our optical measurements, results to be K_f=6.3.

It is interesting to make some further considerations. From one side TEM analysis allows to validate optical measurements by comparing the primary particle diameter obtained with the two different approaches. From the other side the TEM analysis is also used to obtain the value of fractal parameters, such as K_f and D_f. As already observed, these data have been widely measured by other authors and, in fact, several values are reported in the literature. Then, in this context such measurements have been carried out just to confirm these values.

3 Conclusions on flame measurements

In this work, soot formation has been studied in the ethylene/air premixed flame with an equivalence ratio 2.34 and at atmospheric pressure.

Concerning the diagnostic technique implemented, the following conclusions can be draw.

- A novel approach of the scattering/extinction technique has been developed, based on the fractal theory. By considering the scattering measurements performed at three angles indication on the soot structure, as the radius of gyration, the soot yield, the soot primary particle and the number density have been retrieved.

- The sensitivity of the technique at two different parameters, not derived with optical measurements, the fractal prefactor and the fractal dimension, is evaluated.

- These last parameters are, anyway, measured in this work by means of sampling and TEM analysis. Results are in agreement with the values reported in the literature.
- From TEM analysis the primary particle diameter is measured and found to be in agreement with the one optically measured.
- In order to measure the soot volume fraction, the influence of the wavelength of the used source on the extinction measurements is presented.

As for the effect of hydrogen addition on soot formation it is obtained that:
  - with C/O constant and
  - increasing the equivalence ratio

the following conclusions about the role of hydrogen addition can be drown:
- Flame temperature slightly decreases
- Thermodynamic equilibrium is faster reached
- Laminar flame speed increases
- All soot parameters (soot volume fraction, volume-mean diameter, radius of gyration, soot particle diameter and number density) decrease significantly
- Due to the reduction in both D_{30} and R_{gm1} it is inferred that the aggregation processes become less important with hydrogen addition.
- A shift in the curve of all parameters is detected at higher height above the burner by increasing hydrogen content. This can be due to a longer induction delay time or to a decrease in the concentration of the soot precursors, and then on the nuclei formed.

In the next Chapter the dependence of the induction delay time on the hydrogen addition as obtained with measurements in the shock tube will be investigated, and then it will be possible to understand better such behavior.

IV. Shock Tube Measurements: Results and Discussion

INTRODUCTION

In this chapter scattering/extinction measurements performed in the shock tube are presented. The chapter is essentially divided in two sections. In the first part, the applicability and the limitations of the technique are investigated by performing measurements in the small tube. To this purpose, mixtures of ethylene/argon and toluene/argon at relatively low pressure (about 500 kPa) are studied. Toluene mixture is here investigated as it is considered as a reference fuel. In fact, many works can be found in the literature, and consequently many data are available for the comparison.

In the second section measurements performed in the big tube, where the previously assessed experimental scattering/extinction apparatus is built up, are presented. This tube is more appropriate for chemical kinetics studies as the effects of boundary layers can be considered as negligible. Here the role of hydrogen addition to an ethylene mixture in the soot formation mechanisms is investigated. In particular, information about global soot growth parameters, as soot yield and induction delay time, as well as the soot structure and dimension are presented. In order to analyze the morphology of soot particles, scattering measurements

are performed at three angles (20°, 90°, 160°) and the value of the dissymmetry ratio is evaluated.

1 Methodology

One of the main objectives of this work is to develop and to assess the technique based on the coupling of the extinction method to Rayleigh scattering to study soot formation behind reflected shock waves.

In order to be able to fulfill this task, it was decided to use the shock tube of 38 mm in diameter (4 m long) which presents numerous advantages:

- its small volume allowing to vacuum in short time,
- the short handling time between two consecutive runs.

Thanks to these observations, the technique can be assessed in a no time-consuming experimental apparatus.

However, the major drawback of this shock tube is in its diameter. In fact, for such small diameters, the boundary layer developing behind the incident shock wave can constitute a problem in defining the ideal conditions that are usually found in larger shock tubes.

Due to the very low amount of soot produced from ethylene pyrolysis, its molar percent was fixed to 3 % in argon. However, this concentration of the fuel in argon is high, especially considering the small tube diameter. Moreover, the time for the soot to be formed was very long compared to the observation time in the shock tube. Given these conditions, measurements performed with ethylene are considered just to investigate the characteristics of the signals and the procedure to derive the results. No kinetic parameters of soot formation, such as induction delay times or soot yield, will be derived from the experiments performed with the mixture of 3 % ethylene in argon mixture. On the contrary such analysis will be carried out with the toluene mixture, and in this case also a comparison with literature data can be performed.

1.1 Procedure and technical assessment

For each shock wave run the following measurements are obtained:

- three pressure signals from the corresponding pressure transducers;
- scattering signal detected at 90° and transmitted intensity across the tube of both blue and red laser beam.

For signals detection two different fast digital oscilloscopes are used, both triggered by the signal from the last pressure transducer positioned close to the tube-end wall. In the following, examples of these measurements are reported, which refer to the conditions of 3% C_2H_4 in Ar, at $P_5 = 4.63$ bar and $T_5 = 2140$ K.

In Fig. IV.1.1, pressure signals versus time are shown.
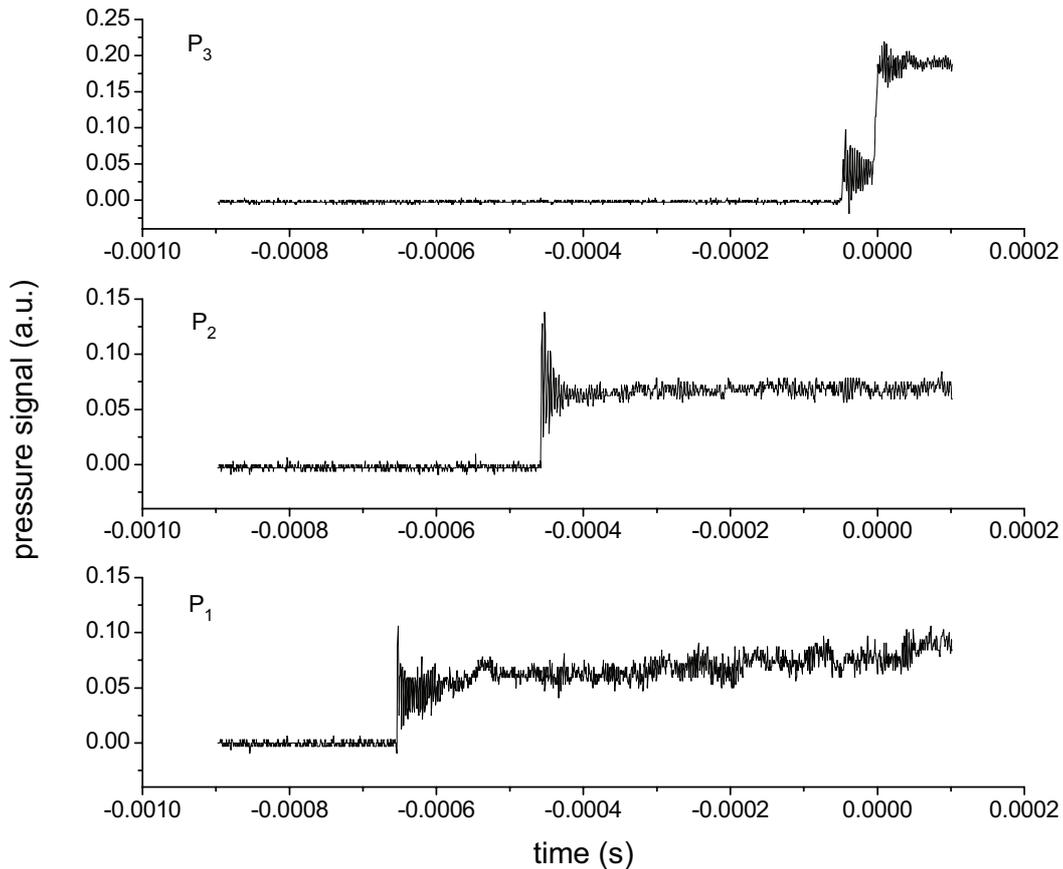
Fig. IV.1.1: *Pressure signals versus time - 3% C_2H_4 in Ar, at $P_5 = 463$ kPa and $T_5 = 2140$ K.*

Starting from the bottom, there are represented the signals detected from the pressure transducers P_1, P_2 and P_3. As for P_3 signal, the reflected wave front is also visible. These curves allow to evaluate the time occurrence of the shock wave. Then, by knowing the distance between two consecutive pressure transducers, for each run the shock wave velocity is calculated. In Fig. IV.1.2 the scattering and extinction measurements are reported.
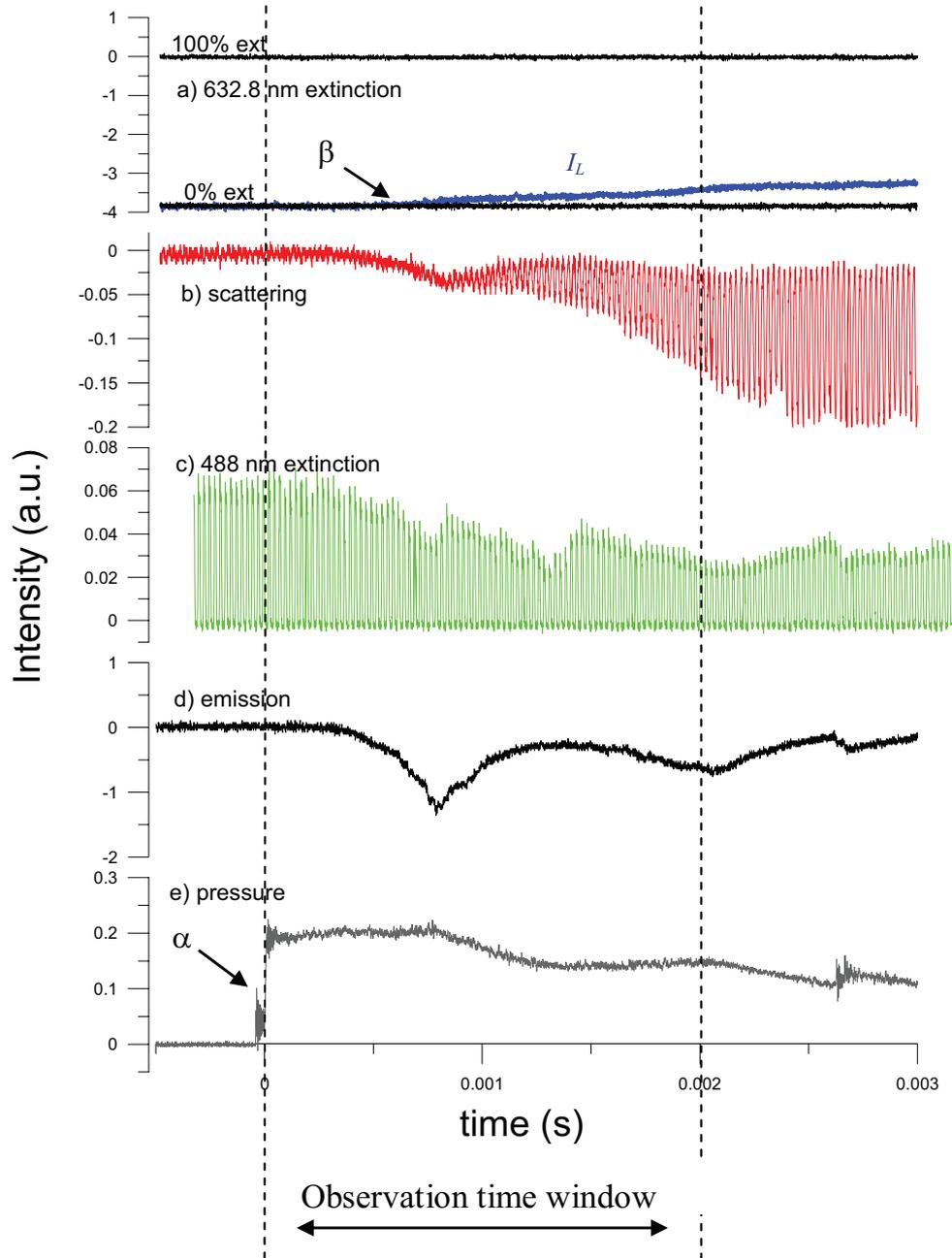
Fig. IV.1.2: *Time-resolved scattering/extinction measurements – raw data. 3% C_2H_4 in Ar, at $P_5 = 463$ kPa and $T_5 = 2140$ K.*

At the bottom the pressure signal versus time is shown, which is used to trigger the acquisition and to fix the initial time scale for the observation behind the reflected shock wave. In the panel a) and c) the extinction signals of the red ($\lambda = 632.8$ nm) and blue ($\lambda = 488$ nm) beam are reported. Due to the use of the chopper, the 488 nm transmittance results to be laser-modulated. As clearly observed in the figure, the value of extinction of the blue laser beam increases significantly with the time, reaching the value of about 0.5, in the conditions

here analyzed. This high extinction in the blue spectral region affects scattering measurements and consequently a correction has to be performed, as it will be shown in the paragraph of scattering processing procedure. In the panel d) the horizontally polarized component of the emitted radiation is shown. This signal, which is not modulated and consequently not related to the laser, is due to emission from soot or other gas-phase species produced in the tube at high temperature (e.g. the polycyclic aromatic hydrocarbons, PAH). Finally panel b) shows the modulated, vertically polarized scattered signal from soot particles. It is important to notice that the shape of the emission curve reproduces quite well, in different scale, the baseline of the scattering signal, over which the modulated curve is placed. This confirms the nature of the emission curve in panel d).

As it can be seen from the figure, an induction delay time, discussed in the following, is detected between the reflected shock wave and the beginning of soot formation (compare e.g. points α and β in the figure).

In the figure the temporal trend up to 3 ms is reported. Anyway, the observation time has to be limited at about 2 ms behind the reflected shock wave, the period when pressure and the temperature remain almost constant. At longer times strong scattering signals were observed, probably due to the passage in the probe volume of small fragments of the diaphragm transported by the driven gas.

1.1.1 Scattering signal processing procedure

The modulated signal, shown in panel b) of Fig. IV.1.2, presents the following characteristics.

- Each raw signal consists of 10,000 samples in 10 ms as resulting from the sampling frequency of the oscilloscope, then giving a resolution of 1 μs.
- Being the signal modulated at 40 kHz, 400 cycles are obtained, each consisting of 25 dots.

By keeping these features in mind, a proper procedure is developed to derive the vertically polarized scattering signal, which is described in the three points below.

1. Signal smoothing. An averaging process over ten adjacent points performed by using the ORIGIN software allows to reduce the ripple in the initial modulated curve and to improve the signal to noise ratio of the following step 2).

2. Modulated signal evaluation. The averaged data file is processed by using a MATHCAD program (see in the Appendix) in order to determine the maximum (upper envelop) and the minimum (lower envelop) value of the time-dependent signal in each cycle (see Fig. IV.1.3). The corresponding difference gives the scattering signal. As each measure corresponds to one cycle, the derived signal consists of 400 points.

3. Background subtraction. The background is measured largely before the occurrence of the modulated signal and subtracted to the scattering.

4. Scattering smoothing procedure. A further averaging process over ten adjacent points is performed on the scattering signal obtained from step 2. Even in this case the ORIGIN software is used.
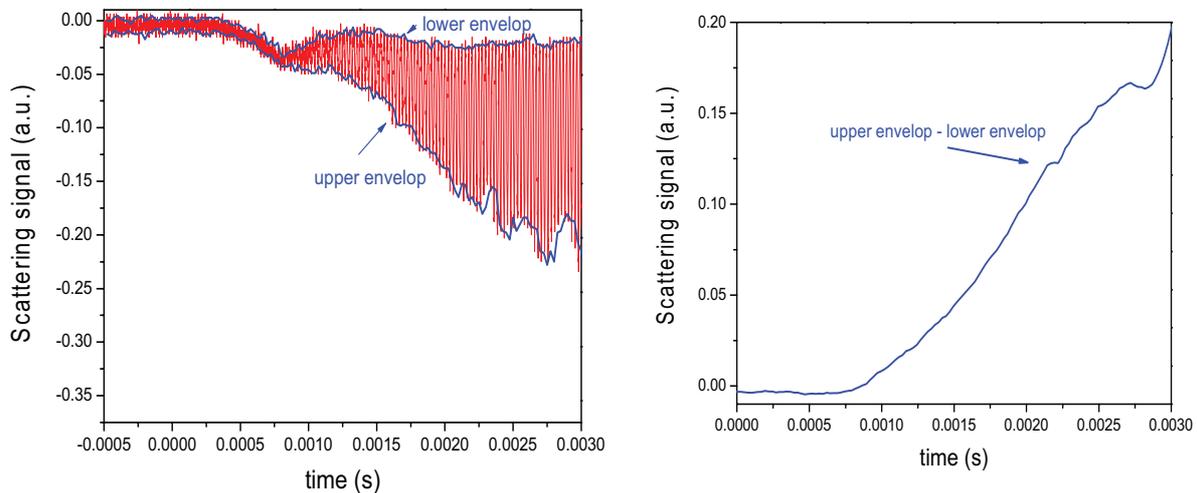
Fig. IV.1.3: *Scattering signal evaluation. 3% C_2H_4 in Ar, at $P_5 = 463$ kPa and $T_5 = 2140$ K.*

In the right side of Fig. IV.1.3, the obtained scattering signal is shown.

In order to derive soot scattering coefficient the calibration procedure with propane, of which the scattering cross section is known, is performed as reported in the Paragraph 2.3 of Chpater II.

Finally, soot scattering coefficient is corrected for self-absorption effects. In fact, considering the transmittance of the 488 nm laser beam reported in the panel c) of Fig. IV.1.2 of about 0.5, a significant extinction of the signal is obtained. This is not surprising considering both the path length of 38 mm crossed by the laser and the soot concentration in the tube. Then, as the scattering signal is proportional to the intensity of the incident laser

beam, and being this last absorbed in the medium, an underestimation of the scattering signal is obtained (pre-filter). To avoid these effects a correction for the absorption of the laser beam has to be performed. Moreover, considering the collecting pathway of the scattering signal, an absorption of this intensity from soot in the tube can also result (post-filter).

Then, in brief two effects have to be considered: the absorption of the laser beam intensity across half the diameter of the tube and the absorption of the scattering intensity on the collecting pathway, that is again half diameter long. Due to the supposed homogeneous distribution of soot in the tube section, this is equivalent to considerg the transmittance of the blue laser beam across the whole diameter. In fact, if I_o and I' are the incident intensity and the one in the probe volume of the laser beam and I_{VV} the scattering signal detected at the tube exit, we can write:

$$I' \approx I_0 \exp(-K_{ext}L/2) \tag{IV.1.1}$$

$$I_{VV} \approx I' \exp(-K_{ext}L/2) \approx I_0 \exp(-K_{ext}L/2)\exp(-K_{ext}L/2) \approx I_0 \exp(-K_{ext}L) \tag{IV.1.2}$$

Then, the correction is performed simply dividing the scattering signal with the transmittance of the blue laser beam evaluated from panel c). In Fig. IV.1.4 the scattering coefficient obtained directly from the calibration (red line) and the corresponding one corrected for the absorption (blue line) are reported.
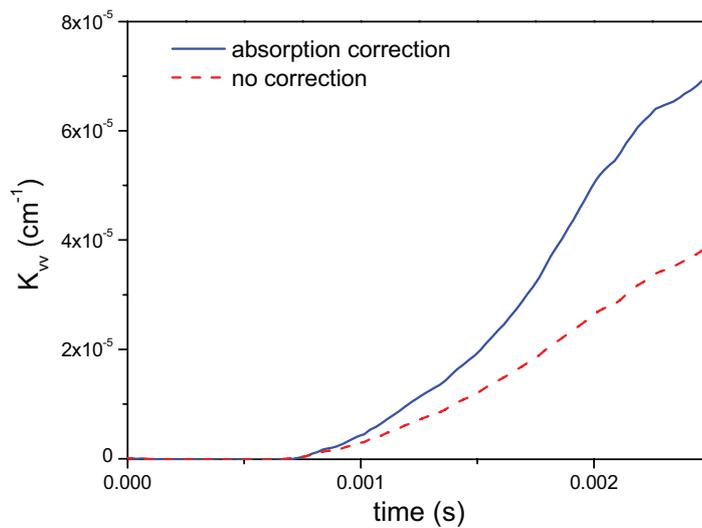

Fig. IV.1.4: *Scattering coefficient versus time with (continuous line) and without (dash line) absorption correction – 3% C$_2$H$_4$ in Ar, at P$_5$ = 463 kPa and T$_5$ = 2140 K*

As observed from the figure, a significant difference is obtained: the scattering coefficient reaches a value 50% higher with the absorption correction. As our knowledge its is the first time that such correction is performed in shock tube scattering measurements.

1.1.2 Extinction signal processing

Now the transmitted intensity of the 632.8 nm laser beam reported in the panel a) of Fig. IV.1.2 is considered. In order to increase the signal to noise ratio and reduce the ripple, an averaging procedure is applied to this curve.

The extinction coefficient and the soot volume fraction can be derived as follows.

Defining the parameters (Fig. IV.1.2):

- I_0= the signal intensity corresponding to 0% absorption (which is the incident laser beam intensity value)

- I_{100}= the signal intensity corresponding to 100% absorption

- I_L= the signal intensity of the transmitted laser beam, depending on time.

The monochromatic transmittance, TR_λ is calculated as

$$TR_\lambda = \frac{I_L - I_{100}}{I_0 - I_{100}} \qquad\qquad (VI.1.3)$$

Then, applying the relationships reported in Paragraph 2.1 of Chapter I, the scattering coefficient and soot volume fraction are calculated. For these measurements the transmittance of the red beam is considered. In fact, as it can be easily verified, the use of the extinction of the 488 nm beam produces results for f_v that are overestimated. This is due to the contribution to the extinction from species absorbing in the blue spectral region. Similar results have been obtained by Graham et al [74, 32, 75] and Migliorini et al. in rich premixed flames [76]. The presence of these species is also confirmed by measurements, here not reported, where the strong emission signal detected at 488 nm, increases by increasing the temperature and is present even when the red extinction is practically zero. This proves that emission is not related to soot particles, but to gas-phase species, like PAH, assumed to be soot precursors.

In this chapter we will come back on this point to show deeply our results concerning the evaluation of the soot volume fraction by using different wavelengths. There, it will be widely proved the dependence of the extinction measurements on the wavelength related to the different experimental conditions. While in the case of pyrolysis in the shock tube the use

of the 632.8 nm wavelength gives the right value of f_v, for measurements in premixed flames the use of red line is not enough, but an IR source is needed.

1.1.3 Global soot parameters and soot structure

From the time-dependent behavior of the soot volume fraction, information about global soot kinetic parameters, such as the soot yield and the induction delay time, are obtained. In Fig. IV.1.5, the f_v curve is traced and the related soot parameters shown.
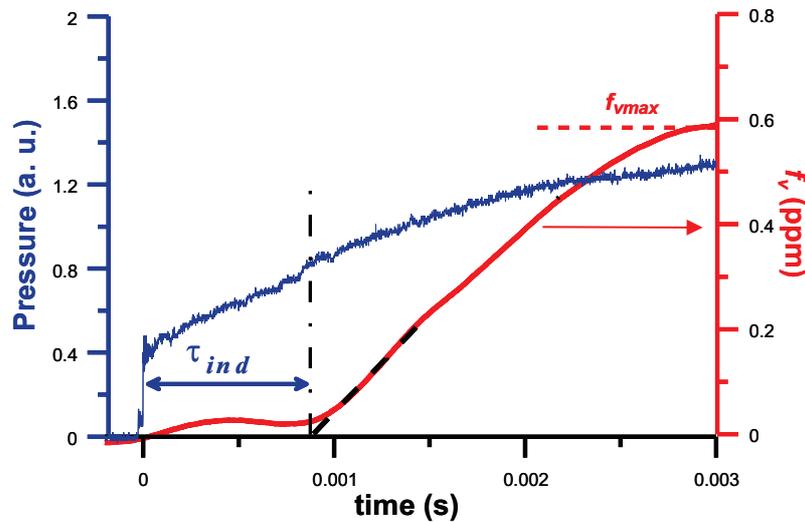
Fig. IV.1.5: *Induction delay time and f_{vmax} obtained from f_v time-dependent behavior –*
3% C_2H_4 in Ar, at P_5 = 463 kPa and T_5 = 2140 K.

By using the *ORIGIN* software, the time-resolved curve of f_v is fitted with the logistic function given by the following expression:

$$f_v = \frac{f_{v\max}}{1 + Q\exp(k_g(\tau_{ind} - t))} \qquad (IV.1.4)$$

where Q is a parameter of the mathematical procedure implemented. The other parameters in the equation, f_{vmax}, k_g and τ_{ind} represent the maximum soot volume fraction, the soot global growth constant and the soot induction delay time, respectively. From this figure it is clear the definition of the induction delay time, which is the interval between the wave front of the reflected shock wave, and the interception of the tangent of the transmission curve at the deflection point and the axis corresponding to 100% transmission. Eq. (VI.1.4) has been

obtained on the basis of numerous experiments carried out for different types of fuels (Mathieu [194], Mathieu et al. [195], [169], [165]).

From the maximum soot volume fraction, the relative soot yield, Y_{soot}, already defined in the Chapter III is evaluated.

In Fig. IV.1.6, the scattering and the extinction coefficients are reported versus time together with the pressure signal from the last pressure transducer.
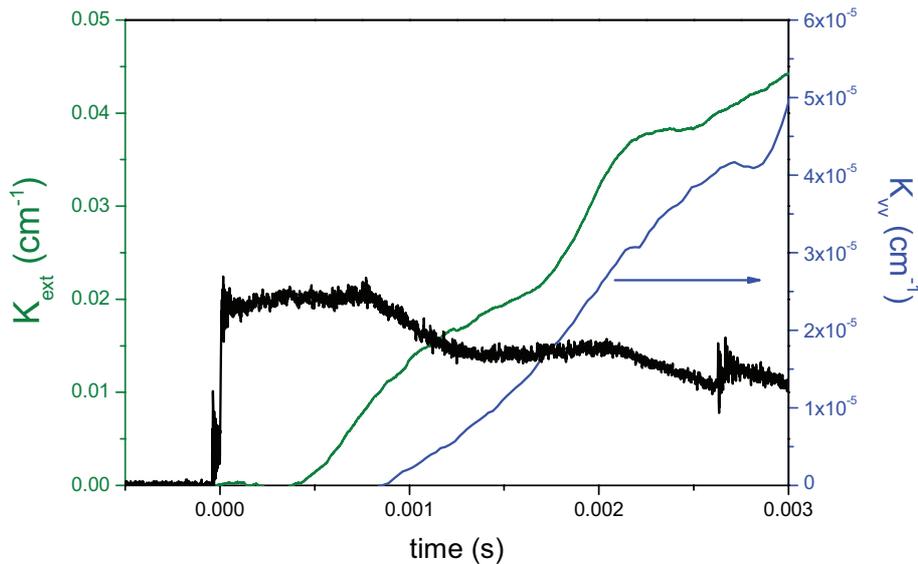
Fig. IV.1.6: *Scattering and extinction coefficients versus time.*
3% C_2H_4 in Ar, at P_5 = 463 kPa and T_5 = 2140 K.

A well defined delay is evident between the wave front of the reflected shock wave and the beginning of soot formation as detected with the extinction coefficient. As already observed, this corresponds to the induction delay time. A further delay is present between the extinction and scattering coefficients curves. In fact, being the scattering coefficient proportional to the sixth power of the soot particle diameter, and being this last quite small at the beginning of the formation, the related signal is negligible. Then, this delay can be due to the limited dynamic range of such measurements. Same trends have been obtained for scattering and extinction coefficients derived from measurements in flames (see Fig. III.3.5).

By combining extinction and scattering measurements, soot particle diameter and number density are derived and an example is show in Fig. IV.1.7. The overall temporal trend is in agreement with the few results reported in the literature [113, 163, 164, 10-12].
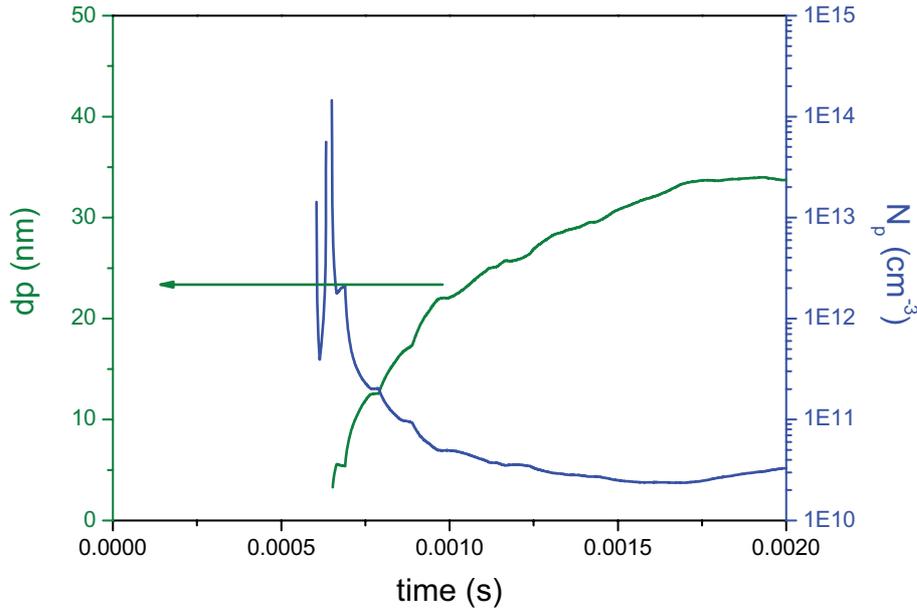
Fig. IV.1.7: *Temporal trend of soot particle diameter and number density.*

3% C_2H_4 in Ar, at P_5 = 463 kPa and T_5 = 2140 K.

At the beginning of their formation, soot particles present a quite fast increase in diameter and in number density. This behavior is related to soot nucleation processes. The growth in the particle size is then characterized by a slower increase up to about 35 nm, in correspondence of which a significant decreasing in N_p is detected. This trend accounts for surface growth and coagulation mechanisms.

1.2 Uncertainties of scattering/extinction measurements

1.2.1 Uncertainties of scattering/extinction coefficients

In order to evaluate the uncertainties of our measurements, the error propagation theory is applied by starting from the errors in the raw data.

As already observed in the Chapter I, the values of the refractive index used in data reduction are the main uncertainties of the optical measurements. For the moment, we neglect such a contribution.

The uncertainties of the incident laser beam intensity, I_0, and the transmitted one, I_L, are evaluated. Both signals are collected during the observation time on the order of few

milliseconds, the incident laser beam intensity being measured before each shot. The relative error of the I_0 value is obtained by a time-averaging over the whole observation time and it is found to be 0.77%. As for the uncertainties of I_L, as it changes with time, it was estimated when the intensity reaches the minimum value of transmittance, where a plateau, as it will be shown in the following, is observed. A value of 0.89% is obtained for the uncertainty on I_L. The error on the extinction coefficient and on the soot volume fraction (see Paragraph 2.1 in Chapter I) is then easily evaluated. By applying the propagation theory, we use for the monochromatic transmittance $TR_\lambda = I_L/I_0$ (see Eq. (2.1.1) in Chapter I) and the extinction coefficient the relationships reported in the Paragraph 2.3 of Chapter III .

Same expression is obtained for f_v and K_{ext}, which differ for a constant factor of proportionality. The resulting error for soot volume fraction is 5.28%.

As for the calculus of the soot yield (Eq.(III.2.2)), the carbon atom concentration in the initial mixture is determined, which is given by

$$[C]_{tot} = \frac{X_{HC} P_5}{k_B T_5} n_c 10^{-6} \tag{IV.1.5}$$

where P_5 and T_5 are the pressure and temperature behind the reflected shock wave, X_{HC} the ethylene mole fraction, n_c the number of the carbon atoms in the initial molecule, and k_B the Boltzman constant. As the error on the pressure and the temperature is 1.5%, an error of 2.12% is obtained for the carbon atom concentration. To evaluate the error in the soot yield, the uncertainties on the soot density has to be considered. By taking the values reported in the literature, spreading from 1.8 to 2 g/cm^3, an uncertainty of 10% is obtained, which results in an overall error of 10% in the evaluation of the soot yield.

Soot particle diameter is obtained by combining extinction and scattering measurements. Then, applying the error propagation theory, the relative error is given by

$$\frac{d(d_p)}{d_p} = \sqrt{\left(\frac{dK_{ext}}{K_{ext}}\right)^2 + \left(\frac{dK_{vv}}{K_{vv}}\right)^2} \tag{IV.1.6}$$

The uncertainty on the scattering coefficient is evaluated from the raw signal to be 4%. Then, recalling that the extinction coefficient error is 5.28%, an error of 6.62% is derived for the size diameter.

1.2.2 Dependence of extinction measurements on laser wavelength

Considering soot volume fraction measurements in shock tubes, extinction is carried out at 488 nm (Ar^+ laser), 632.8 nm (He-Ne laser) and 810 nm (diode laser). In Fig. IV.1.8, the curves of the corresponding estimation of the soot volume fraction versus time are reported.
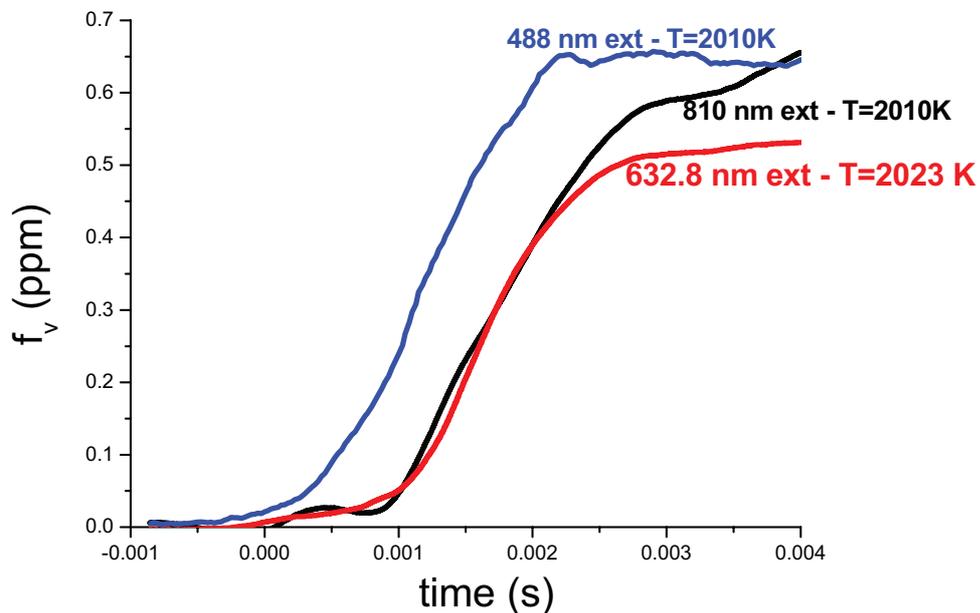
Fig. IV.1.8: *Fv versus time using 488nm, 632.8 nm and 810 nm –2%C_2H_4 in Argon.*

The three measurements refer to almost the same experimental conditions for the pressure and the temperature, which are reported in the figure for each curve.

The graphs related to 632.8 and 810 nm laser beams are overlapped all along the investigation time, the slight difference presented at the maximum being essentially due to the small difference in the temperature and pressure of the two runs. On the contrary, the curve of soot volume fraction obtained with the blue laser beam starts before the others, revealing the presence of species absorbing in this spectral region and responsible of an overestimation of f_v. This contribution is significant at the beginning of soot formation and becomes negligible at the maximum of f_v, where the conversion in soot particulate takes place.

For this reason, we can conclude that in the case of shock tube measurements, the use of 810 nm laser beam in the big tube is a non-necessary choice, and also 632.8 nm wavelength (used in the small tube) could be used for such measurements.

Anyway, as already observed for extinction measurements in flames, the use of an IR source results to be the safest choice for whatever experimental conditions.

1.2.3 Dependence of scattering/extinction measurements on refractive index

Finally the uncertainties due to the value of the soot refractive index are considered. To this purpose the discussion performed in the Chapter I is recalled and here only few values are selected at the wavelengths used in scattering/extinction measurements. In Table IV.1.1 the real (n) and imaginary part (k) of the refractive index (m), proposed by different authors, together with the related evaluation of $E(m)$ and $F(m)$ functions, are reported.

Authors	Extinction at 800 nm		Scattering at 488 nm	
	m	E(m)	m	E(m)
Chang. Char.[81]	1.78- i 0.56	0.2188	1.72 – i 0.62	0.274
Dalzell, Sar. [101]	1.59 – i 0.60	0.267	1.56 – i 0.57	0.218
Lee and Tien [99]	1.82 – i 0.49	0.1570853	1.98 – i 0.54	0.29413
Hab.(mature soot) [100]	1.81 – i 0.37	0.1616034	1.86 – i 0.44	0.25869
Hab. (young soot) [100]	1.46 – i 0.23	0.14497409	1.45 – i 0.28	0.10355

Table IV.1.1: *List of the values of the refractive index and E(m) from different authors.*

The corresponding curves of f_v vs time are shown in Fig. IV.1.9. As already observed in Chapter I, a significant change in the soot volume fraction is obtained, with a spread of almost 100%.

To evaluated the uncertainty on the soot particle diameter, the ratio E(m)/F(m) has to be considered, which gives an error of about 60%. These results confirm once more the strong

influence of the refractive index on such measurements. Anyway, it is important to point out that the aim of the present thesis is the study of the effect of hydrogen addition on soot formation, and consequently, this comparison can be carried out keeping constant the value of the refractive index used and so neglecting its influence.
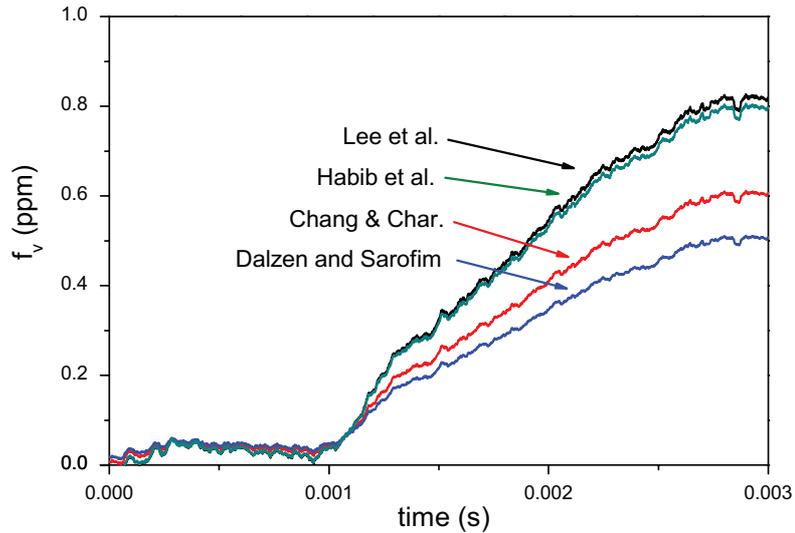
Fig. IV.1.9: *Soot volume fraction vs time calculated using the values of E(m) in*

.

As already reported, in this work the refractive index values proposed by Chang and Charalampopoulos are used [81].

1.3 Signal analysis

In the previous paragraphs the procedure to derive scattering signal and scattering coefficient has been described. It is important to point out once more the difficulties of this kind of measurements, where transient phenomena are involved, taking very few milliseconds. In this section some observation regarding the kind of signals obtained and their characteristics, as for example their repeatability for given conditions, are presented. In the frame of the technique assessment, these investigations are important as it allows to gain experience on the kind of measurements involved.

1.3.1 Repeatability of scattering measurements and dependence on the temperature

It is investigated the repeatability of the signal by fixing all the other experimental conditions, as temperature and pressure. For shock tube measurements, this means to fix the initial pressure of the mixture and its concentration. Anyway, even in this case, temperature and pressure behind the reflected shock wave are not unambiguously determined, as they depend on the way in which the membrane will brake. Then, it is practically impossible to have exactly the same experimental conditions. For that, to perform such analysis among the whole set of raw data obtained the shots characterized by a quite close temperature are considered and the related scattering coefficients compared.

In Fig. IV.1.10, an example is shown for the ethylene/argon mixture at the temperature 2110 K. Both the signal obtained after MATHCAD processing and the corresponding smoothing averaging are reported (see the processing procedure in Paragraph 2.1.1).
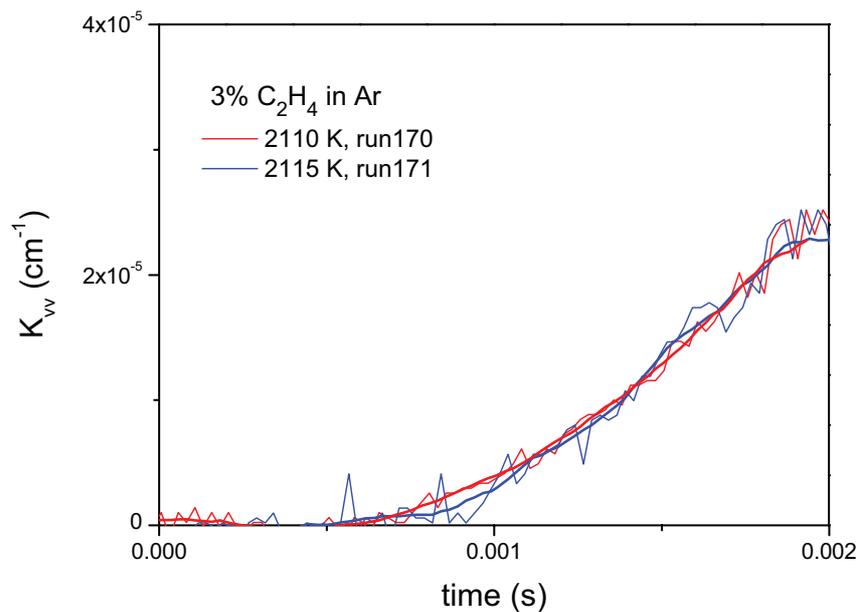
Fig. IV.1.10: *Comparison of the scattering coefficients versus time detected at close temperature*

The two sets of curves are quite well overlapped, confirming a good repeatability of the scattering signal at a given condition of temperature.

The sensitivity of the scattering coefficient on the temperature has been investigated for the two mixtures (3% ethylene and 0.3% toluene in argon). To this purpose three different

regions of the temperature (low, medium and high) range are taken into account and the related scattering coefficients represented versus time. In Fig. IV.1.11 and Fig. IV.1.12 are reported data referring to ethylene and toluene, respectively.
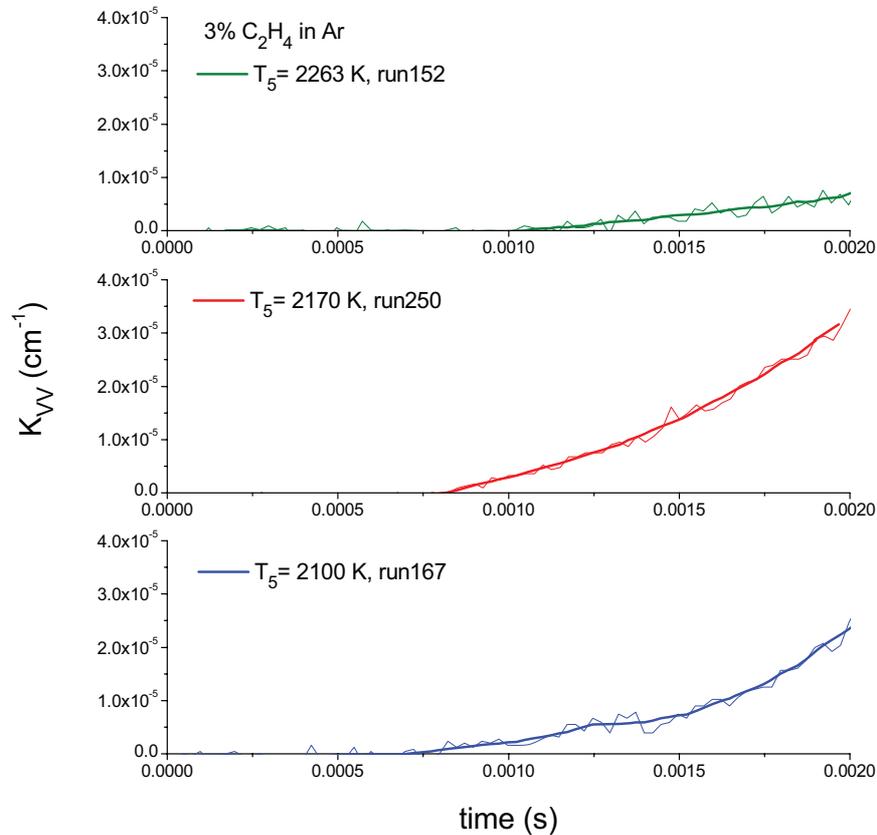
Fig. IV.1.11: *Scattering coefficient versus time at different temperature range – 3% C_2H_4 in Argon (T_5=2100 K P_5=447 kPa – blue line; T_5=2170 K P_5=518 kPa – red line; T_5=2263 K P_5=435 kPa – green line) in 38 mm i.d. tube*

From these figures some observation can be made.

1. Scattering signal increases with the time in a quite regular way for the both mixtures.

2. Increasing the temperature, a reduction of the delay in the appearance of scattering signal is observed. The same trend is obtained for the two mixtures.

3. Even if the scattering is almost in the same range of values, with the ethylene mixture presenting a slightly lower signal than the toluene mixture, a different trend is observed by increasing the temperature. In fact, considering ethylene mixture in Fig. IV.1.11 and starting from the bottom a first increase is detected

moving at higher temperature (curve in the middle), followed by a substantial decrease (upper curve). An opposite trend is obtained for toluene/argon mixture.
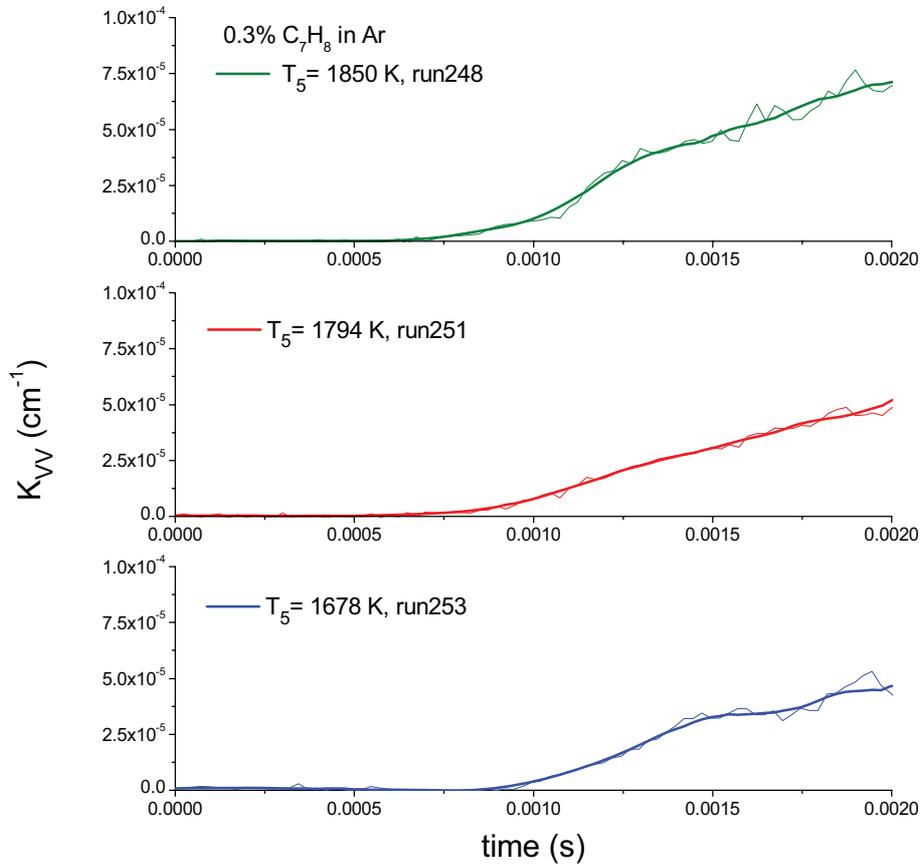
Fig. IV.1.12: *Scattering coefficient versus time at different temperature range – 0.3% C$_7$H$_8$ in Argon (T$_5$=1678 K P$_5$=592 kPa – blue line; T$_5$=1794 K P$_5$=569 kPa – red line; T$_5$=1850 K P$_5$=596 kPa – green line) in 38 mm i.d. tube*

.

1.3.2 Soot volume fraction dependence on temperature

In order to investigate the dependence of the soot volume fraction on the temperature, the time-behavior of f_v in the low, medium and high temperature regions are considered. In Fig. IV.1.13 and in Fig. IV.1.14 the measurements obtained with ethylene and toluene are reported, respectively.
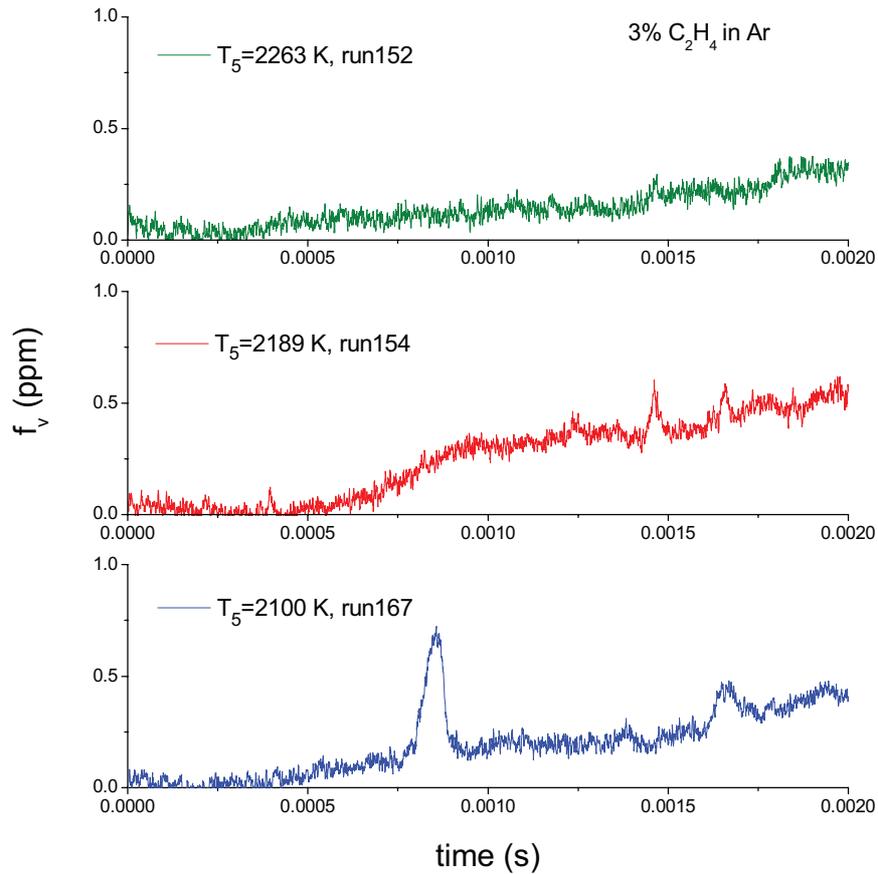
Fig. IV.1.13: *Soot volume fraction vs time as a function of the temperature –3% C₂H₄ in Ar (T_5=2263K P_5=534 kPa – blue line; T_5=2189 K P_5=516 kPa – red line; T_5=2100 K P_5=447 kPa – green line) in 38 mm i.d. tube*

By comparing the time behavior of the soot volume fraction obtained for ethylene and for toluene, significant differences are shown. In fact, for toluene mixture, besides the absolute value of the soot volume fraction (higher in this case), f_v curves exhibit a smaller delay with respect to the reflected shock wave (at time zero).
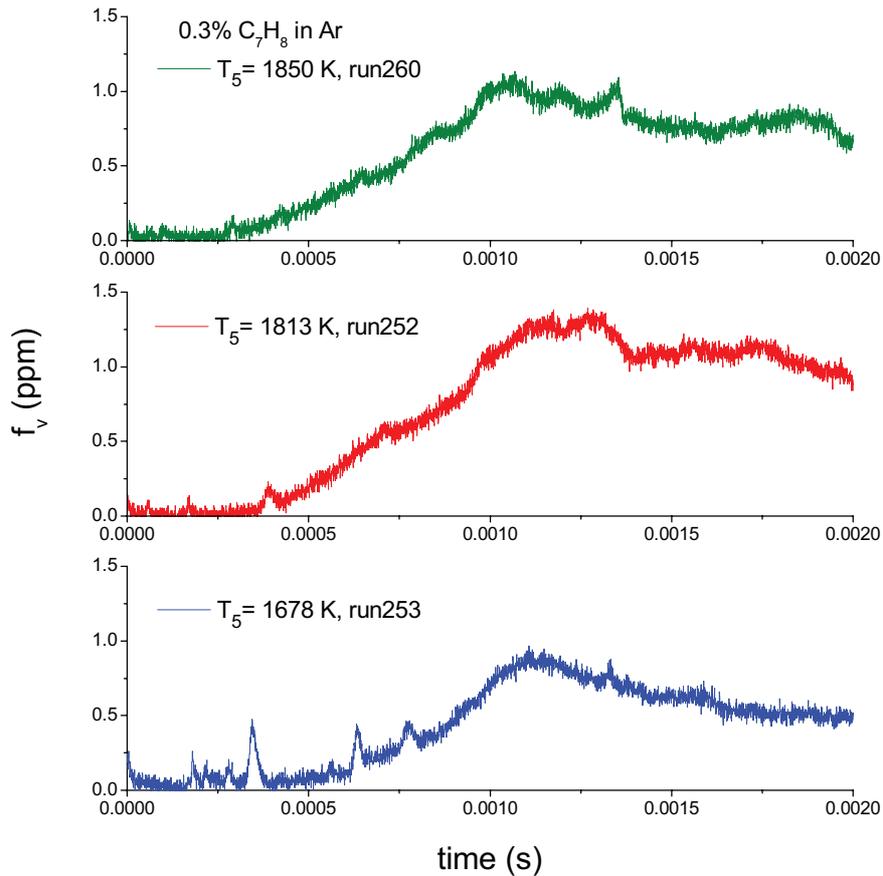
Fig. IV.1.14: *Soot volume fraction vs time as a function of the temperature – 0.3% C_7H_8 in Ar (T_5=1678 K P_5=592 kPa – blue line; T_5=1813 K P_5=569 kPa – red line; T_5=1850 K P_5=596 kPa – green line) in 38 mm i.d. tube*

1.4   Validation of the technique

To validate the technique soot parameters obtained according to the methodology already described are reported versus the temperature and the results corresponding to toluene pyrolysis are finally compared with literature data.

1.4.1   Primary particle diameter

In Fig. IV.1.15 the mean values of the primary particle diameter versus temperature are shown for the two mixtures. As from scattering/extinction measurements, the behavior of soot diameter versus time is obtained, the comparison is performed at a given time. In this case 1.5 ms beyond the reflected shock wave is chosen, for comparison with literature data.
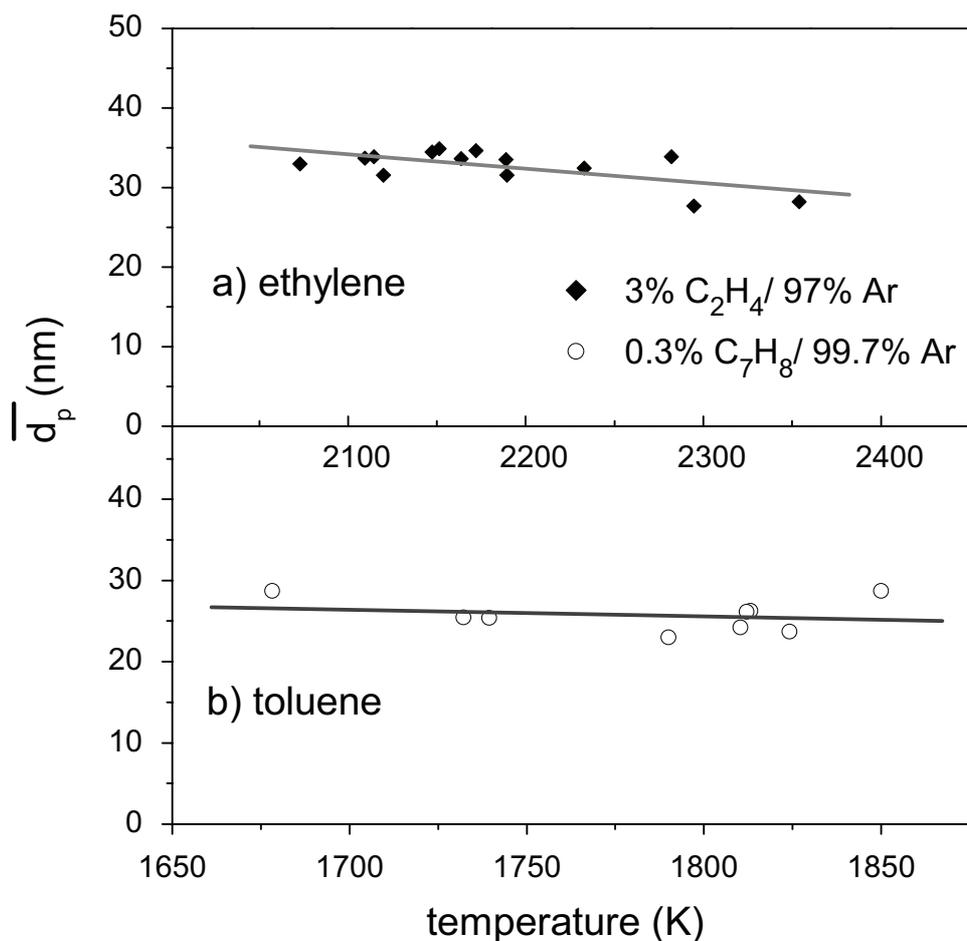
Fig. IV.1.15: *Dependence of the mean particle diameter on the temperature. 3% C₂H₄ and 0.3% C₇H₈ in Ar – measurements in 38 mm i.d. tube.*

Both trends are quite linear, with the diameter decreasing with the increasing of the temperature, which is in agreement with TEM measurements of soot performed in a shock-tube. Anyway, this decrease is not significant, at least in the range of the temperature investigated. The observed diameter is in the range of 20-35 nm in agreement with previous measurements (Kellerer [113]). From the comparison of our results with the measurements by Kellerer et al. some further considerations are necessary. These authors investigated soot formation and particle size growth in a wide pressure range, both for pyrolysis and oxidation of different hydrocarbons. Concerning the dependence of soot diameter with the temperature only the results of the oxidation of toluene and n–heptane are reported. The behavior of toluene is in agreement with our results, even if in our case pyrolysis is investigated. On the contrary, for n-heptane soot diameter presents a different dependence. No comments or suggestions have been given to discuss these differences. Unfortunately no results were shown for ethylene or other hydrocarbons.

1.4.2 Induction delay time

In this and in the following sections global kinetic parameters of soot formation in the toluene mixture are considered. In Fig. IV.1.16 the dependence of the induction delay time τ_{ind} versus the inverse of the temperature is shown in logarithmic scale.
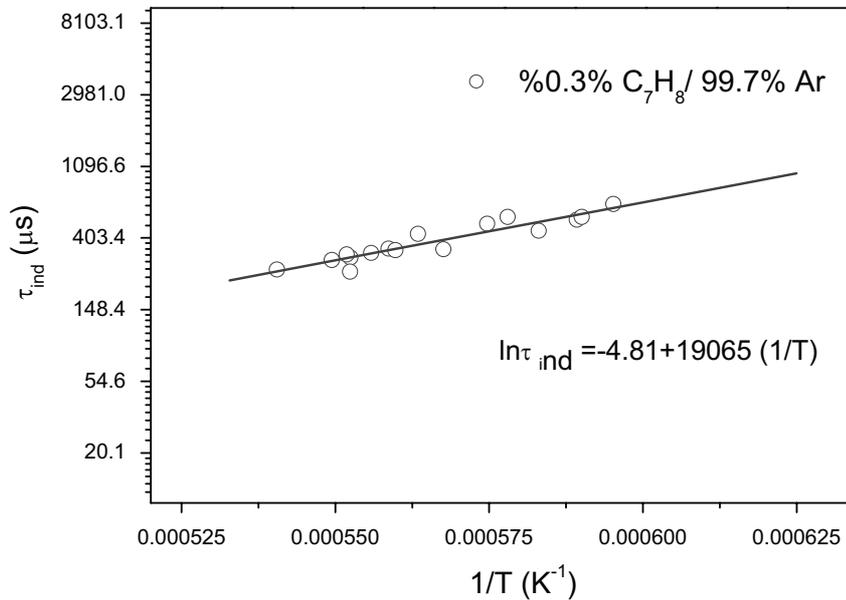
Fig. IV.1.16: *Induction delay time versus inverse of the temperature for 0.3% toluene in Argon*

It is obtained a typical linear trend in logarithmic scale, that means the exponential Arrhenius's law. In the same figure, the linear fitting curve is overlapped to the corresponding measurements. From the slope the activation energy (*E*) can be derived. Considering the following equation

$$\ln(\tau_{ind}) = 19065 * 1/T - 4.81 \qquad \text{(IV.1.7)}$$

and multiplying the slope for the gas constant (8.314 J K^{-1} mol^{-}1), the corresponding activation energy results to be E = 19065*8.314 /1000 = 158 kJ.mol^{-1}. This value is in a good agreement with other data from the literature and reported in
Table **IV.1.2**.

References	E (kJ/mol^{-1})
This work	158
Wang [166]	149
Douce et al. [114]	189
Kellerer [113, 163]	235

Table IV.1.2: *Comparison of C$_7$H$_8$ activation energy obtained in this work with literature data.*

1.4.3 Soot yield

The dependence of the soot yield on the temperature is reported in Fig. IV.1.17 for toluene/argon mixture.

A typical Gaussian-like distribution with a characteristic peak is found. As it was introduced by Mathieu and co-workers [195], the evolution of the soot yield as a function of the temperature is described using the following equation:

$$Y_{soot} = Y_{max} \exp\left[A_{rdt} \left(\frac{T_{max} - T}{T} \right)^2 \right] \qquad \text{(IV.1.8)}$$

where Y_{max} is the maximum soot yield obtained at the temperature value T_{max}. In this case the values of the maximum soot yield and the related temperature are 24.26% and 1796 K, respectively. It is important to observe that this trend, with this value of the maximum soot volume fraction occurring at the maximum temperature, is in agreement with results reported in the literature obtained in the same conditions (Mathieu et al. [195]).
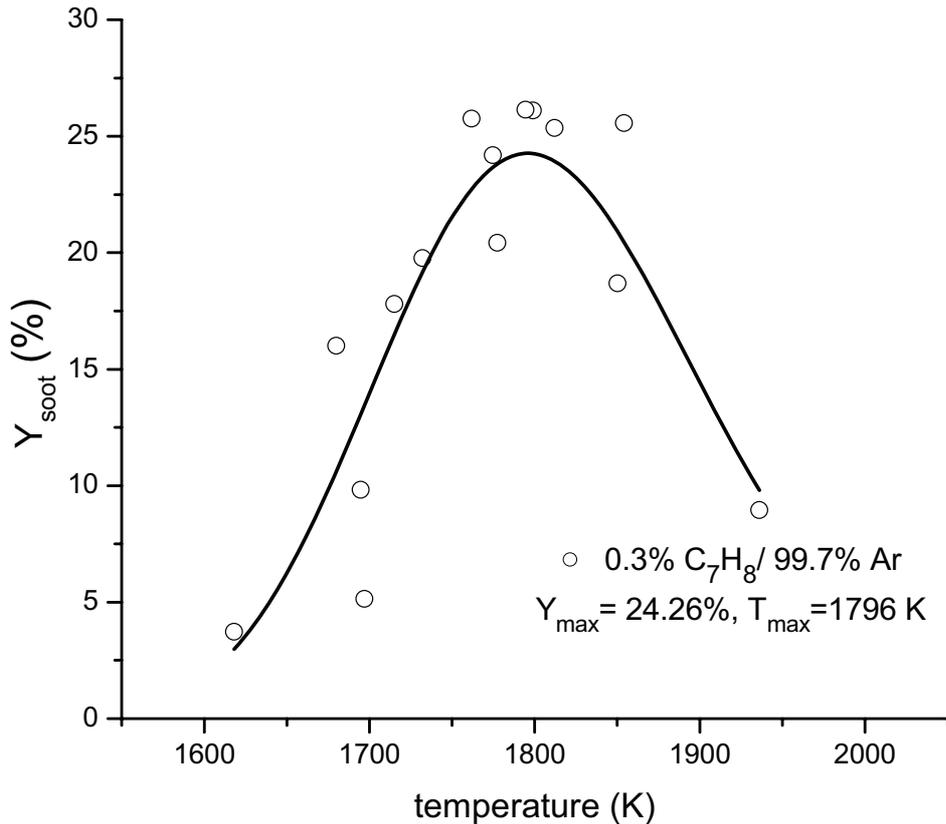
Fig. IV.1.17: *Dependence of the soot yield from the temperature. 0.3% toluene in Argon*

1.5 Conclusions on the applicability of the technique

The scattering measurements performed in the 38 mm shock tube allow the following observations.

- Care has to be taken for the evaluation of the scattering signal. Here a wide description of the processing procedure applied to derive the signal from the raw data has been presented.

- In order to take into account pre-filter and post-filter effects, correction for absorption of both the laser beam and the scattering radiation has to be performed. This correction can be very significant, depending on the soot load and on the path length crossed by the laser beam.

- The agreement of the results obtained, especially for the global kinetics parameters of soot formation like induction delay time and soot yield in the toluene/argon mixture, allows to be confident on the actual applicability of this technique.

Moreover, in the case of high soot load, the hypothesis of isolated primary particles could no longer be verified, and aggregation processes can occur.

Then, with the detection of the scattering signal at 90° soot dimension can be derived, without any information on its morphology. In order to take into account further growth mechanism, more scattering data are needed.

2   Results on 78 mm i.d. tube

In this sections measurements performed in the shock tube with 78 mm internal diameter are described. Here the role of hydrogen in the soot formation mechanisms is investigated, by using a mixture of 2% ethylene in argon, at which two hydrogen contents have been added.

Both the global parameters of soot formation kinetics (as the soot yield, the induction delay time and the soot growth) and the characteristics of the soot structure (as the soot particle diameter and the number density) have been investigated in dependence on the temperature, according to the experimental conditions reported in Table II.2.1. Concerning the soot diameter, moreover, as a time-resolved curve is obtained for each condition, its dependence on the temperature is performed by considering the value reached 3 ms, which is also the end of the observation time.

2.1   Improvement added to the extinction / scattering technique

Once the technique has been assessed on the 38 mm tube, scattering/extinction measurements are then carried out in the 78 mm diameter tube, with the addition of the following improvements.

1. In order to analyze soot morphology due to aggregation processes, the scattering at three angles is performed, at 20°, 90° and 160°.
2. For extinction measurements, the He-Ne laser beam has been changed with an infrared laser, in order to be sure to neglect absorption from other gas-phase species.

For each run the following measurements are obtained:

- pressure signals from four pressure transducers;

- scattering signal detected at 20°, 90° and 160°

- transmitted intensity across the tube of both blue (488 nm) and infrared (810 nm) laser beam.

In Fig. IV.2.1, typical raw signals are shown.
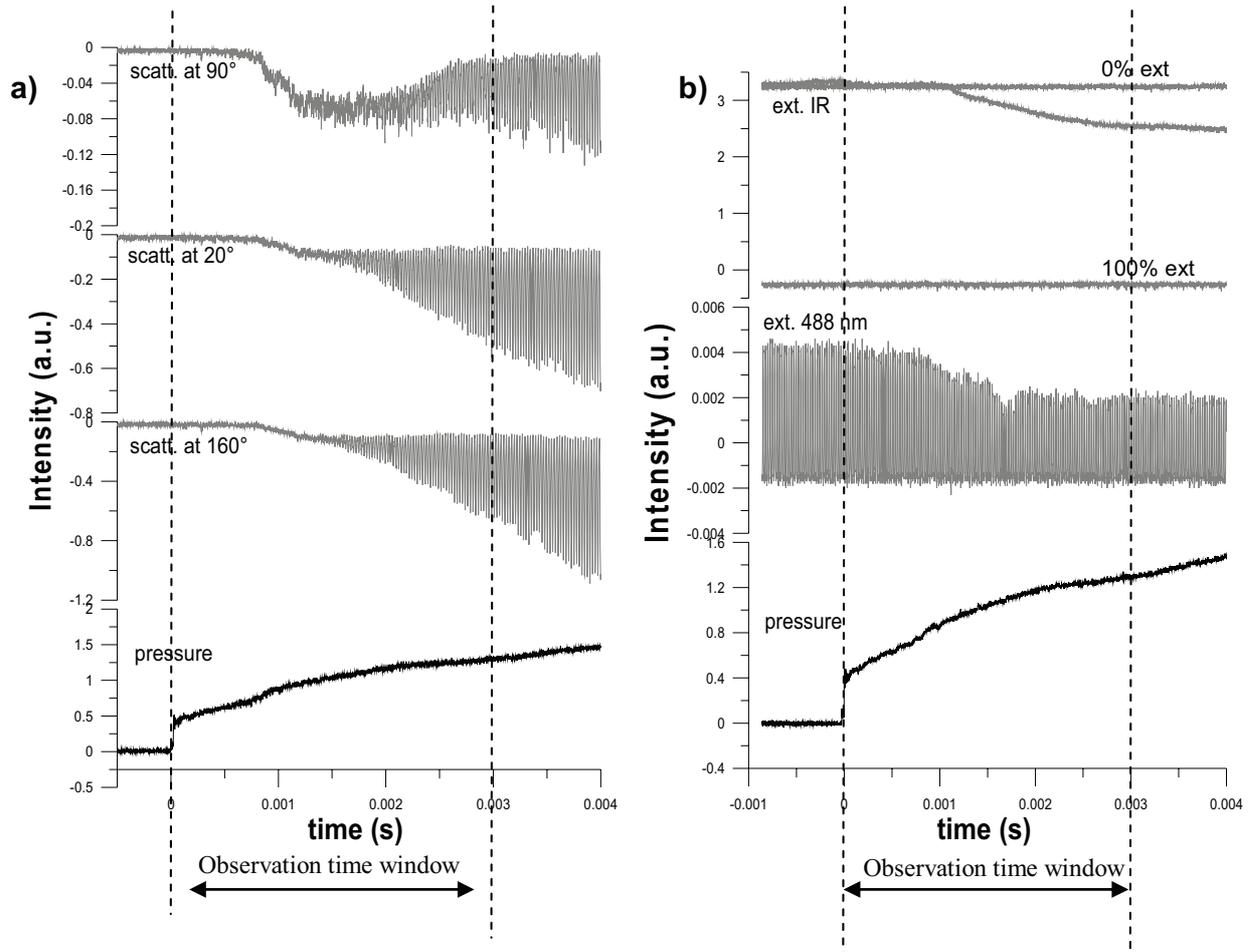
Fig. IV.2.1: *Extinction/scattering measurements (2% C_2H_4 in Ar, $T_5 = 2010$ K e $P_5 = 555$ kPa)*

The data refer to the case of 2% ethylene in Argon at $P_5 = 555$ kPa and $T_5 = 2010$ K. Here pressure signals used to measure the wave speed are not reported as they are similar to the ones in Fig. IV.1.1.

For both panels, at the bottom, the time dependent pressure signal is reported from the fourth pressure transducers, which is used to trigger the acquisition and to fix the initial time

scale behind the reflected shock wave. In the panel a), the scattering signals at the three angles are shown versus the time, whilst in b) the signals transmitted across the tube related to the two laser beams are reported. In both panels, the observation time window is shown with two dotted lines, starting from t = 0 s in correspondence of the flame front of the reflected shock wave and up to t = 3 ms. In this interval, the pressure and the temperature can be considered constant.

The raw data of extinction and scattering measurements are processed by applying the same methodology developed and carried out in the 38 mm tube, and here briefly recalled.

From the temporal behavior of the transmitted laser intensity, the extinction coefficient and then the soot volume fraction are calculated. From the time-resolved soot volume fraction soot kinetics parameters, as the induction delay time, the soot yield, and the soot growth rate are obtained.

As the scattering signals are detected at the three angles, three signals have to be processed and calibrated according to the same procedure previously reported for the scattering signal at 90°. Correction for absorption has been performed as in the measurements in 38 mm i.d. tube. Then, three scattering coefficients versus time are derived, which will be analyzed as follows:

1. The scattering signal collected at 90° allows, in conjunction with extinction measurements, to evaluate the temporal evolution of the particle diameter and the number density.

2. With scattering measurements at the other two angles information about aggregation processes involved in the soot growth is derived. In fact, by calculating the value of the dissymmetry ratio versus the time (di Stasio [196], Riefler et al. [197], di Stasio et al. [120], [198]), the occurrence of aggregation in the evolution of soot growth can be monitored.

2.2   Scattering coefficients

2.2.1   Signal repeatability

As a first analysis the repeatability of scattering measurements is checked. To this purpose, considering the runs characterized by close temperature, a comparison of the scattering coefficient versus the time is analyzed. In Fig. IV.2.2 the results relative to the

mixture of 2% ethylene in argon are shown. With a spread in the temperature of about 15° of the shots, no significant differences in the curves are detected, which proves the good repeatability of scattering measurements.
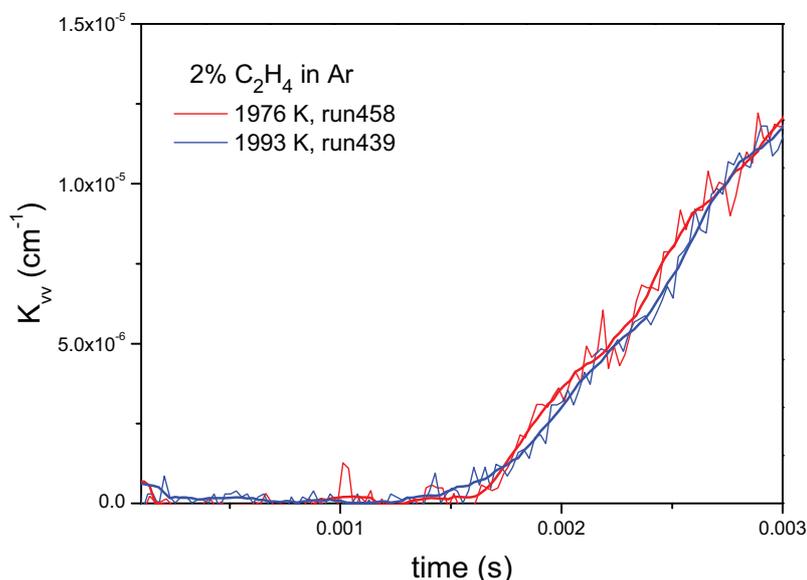
Fig. IV.2.2: *Comparison of K_{vv} versus time in the same temperature range – 2% C_2H_4 in Ar (T_5=1976 K P_5=470 kPa - blue line; T_5=1993 K P_5=465 kPa - red line)*

2.2.2 Dependence on the temperature

The same procedure already described for the 38 mm i.d. shock tube is here applied. Three different regions at low, medium and high temperature in the range of the investigated values. In Fig. IV.2.3 the related scattering signals as detected at 90° are reported versus time. The same behavior, here not reported for brevity, is obtained for the signals collected at the other scattering angles (20° and 160°).

In each condition, signals obtained by MATHCAD processing are taken into account and overlapped to the corresponding smoothing averaging.
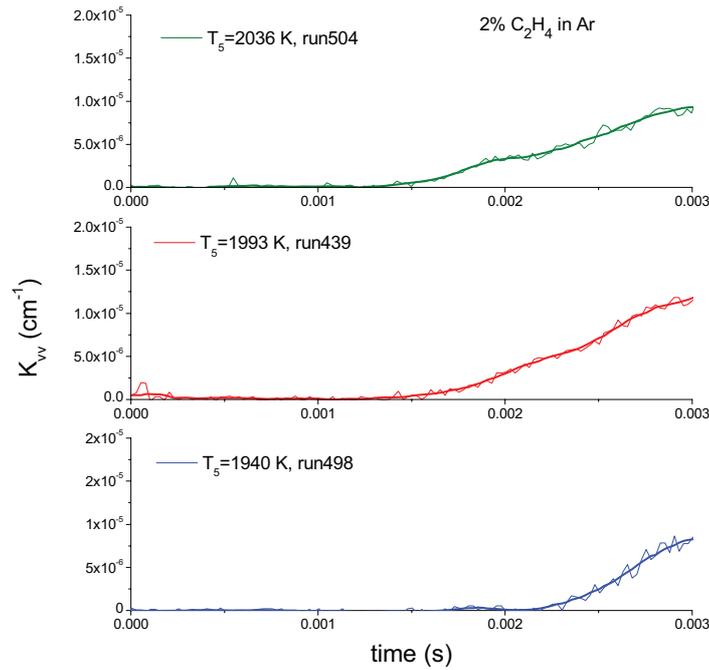
Fig. IV.2.3 : *Scattering coefficient versus time at different temperature range. 2% C₂H₄ in Argon (T₅=1940 K P₅=508 kPa – blue line; T₅=1993 K P₅=465 kPa – red line; T₅=2036 K P₅=463 kPa – green line)*

Signals are very similar to the scattering one detected in the 38 mm i.d. tube. They present a regular behavior, which increases with the time, corresponding to an increase in soot size. It is also evident how the beginning of scattering coefficient is shifted in time by changing temperature conditions.

2.2.3 Dependence on hydrogen addition

In the same way, the dependence of the scattering coefficient on hydrogen addition is investigated at a given value of the temperature, and the curves versus time are reported Fig. IV.2.4. Scattering coefficients increase almost regularly with the time. Moreover, a significant decrease of K_{vv} is detected with hydrogen addition during all the observation time.
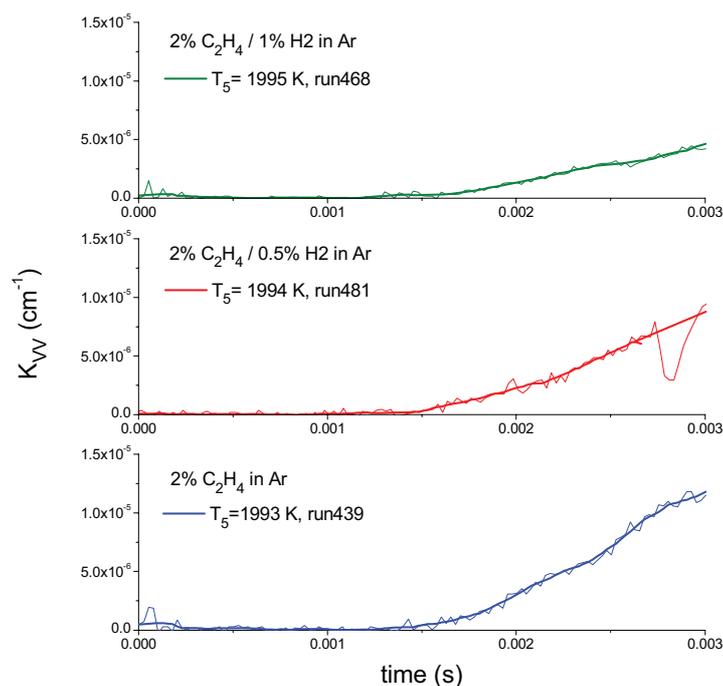
Fig. IV.2.4: *Dependence of scattering coefficient on hydrogen addition – 2% C$_2$H$_4$ in Ar (T$_5$=1994 K, P$_5$=465 kPa) and with 0.5%(T$_5$=1994 K, P$_5$=448 kPa and 1% H$_2$ (T$_5$=1995 K, P$_5$=458 kPa)*

As a general observation, by comparing Fig. IV.2.4 and Fig. IV.1.11 and Fig. IV.1.12, the signals obtained in the 38 mm i.d. tube are definitively noisier than the ones performed in the 78 mm i.d. shock tube. Such behavior can be attributed to the effects of boundary layer negligible in the big tube. This confirms that the use of a large tube to perform kinetics studies results to be mandatory.

2.3   Dissymmetry ratios

In order to investigate soot morphology, for each run the dissymmetry ratios R$_{VV}$ (20°/90°) and R$_{VV}$ (20°/160°) are calculated. Considering the measurements reported in Fig. IV.2.1, the dissymmetry ratio versus time is shown in Fig. IV.2.5.

Even if the dissymmetry ratio R$_{VV}$(20°/90°) is quite spread out, no real trend is detectable from the figure. The two curves can be considered almost constant around the value of 1, which is the straight line overlapped to the symbols.
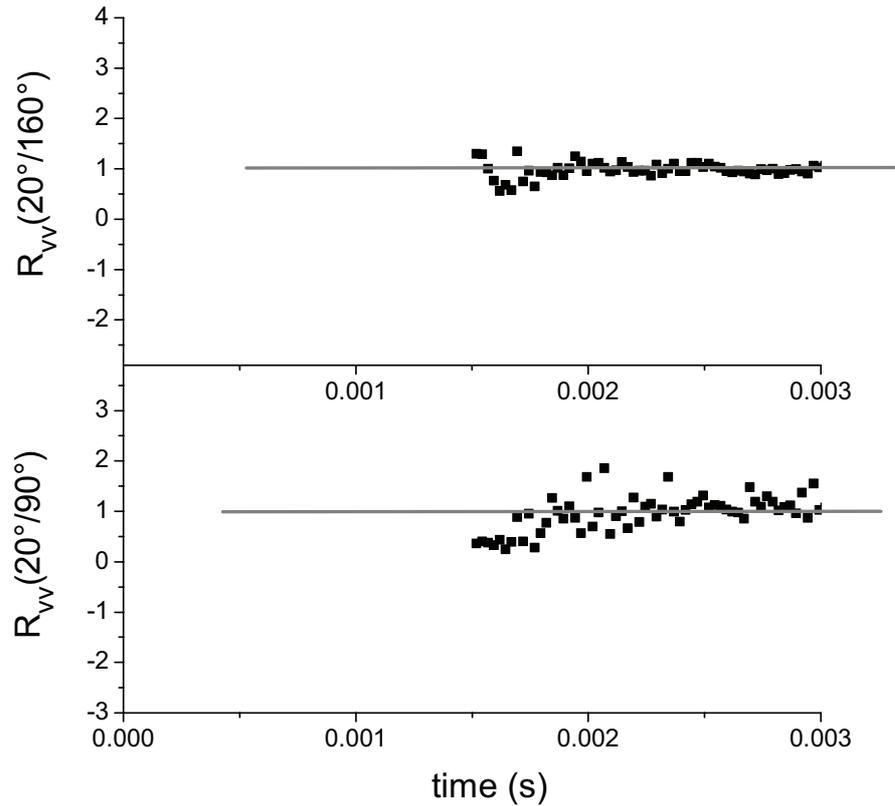
Fig. IV.2.5: *Dissymmetry ratios $R_{vv}(20°/160°)$ and $R_{vv}(20°/90°)$ versus time*
(2% C_2H_4 in Ar, $T_5 = 2010$ K e $P_5 = 555$ kPa)

By considering the discussion reported in the first chapter, this behavior confirms that, at least in the initial stage of soot formation, the aggregation can be considered negligible. The same trend has been obtained for all range of temperature investigated in the present work. Then, we can infer that, in the experimental conditions under study, no aggregation effects are present and the formation and growth of a single soot particle can be monitored.

This results seems to be in contrast with data obtained by di Stasio et al. [119], where a significant linear increase has been obtained for the dissymmetry ratio $R_{vv}(30°/150°)$. The measurements have been carried out to study ethylene pyrolysis, even if no indication about the exact experimental conditions are there given. Moreover, the observation time is extended up to 8 ms, too much long for such analysis. In fact, the same authors affirm that after 2 ms the expansion fan arrives in the measurements section, producing a quick cooling of aerosol and making dominant the aggregation processes. Then, if the observation time is limited at 2 ms, the behavior of the dissymmetry ratios should have been completely different.

2.4 Primary particle diameter

The dependence of the temporal trend of the particle diameter on hydrogen addition is evaluated and reported in Fig. IV.1.1. The behavior of the three curves is very similar. Besides having the same structure, the curves are almost overlapping. Few differences are detected at the beginning of soot formation, where signals are usually noisy, and after 3 ms, that is the limit of the observation time. This result is very interesting: at this temperature conditions, by adding hydrogen a reduction in both soot volume fraction and scattering coefficient is observed, while no effect is detectable in the soot particle diameter. In the same figure the time in correspondence of which the diameter is taken for comparison is shown with star symbols.
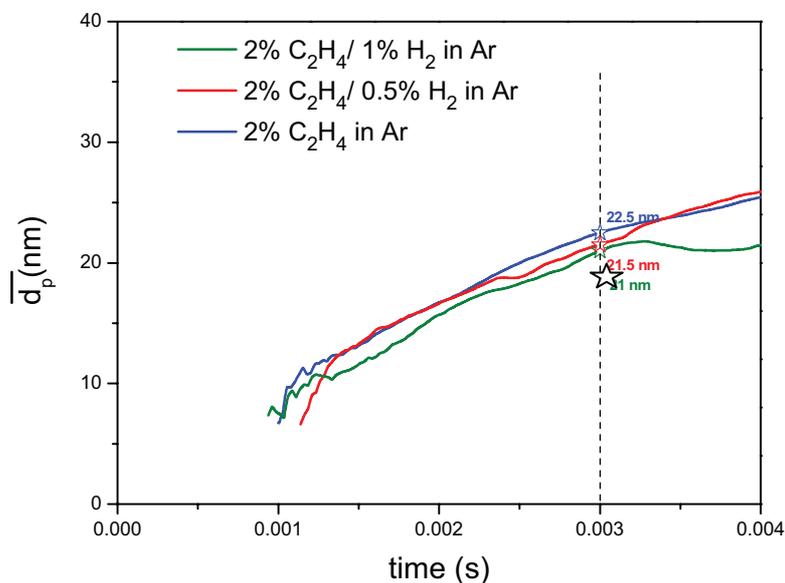
Fig. IV.2.6: *Effect of hydrogen addition on the curve of particle diameter versus the time. – 2% C_2H_4 in Ar (T_5=1994 K, P_5=465 kPa) and with 0.5%(T_5=1994 K, P_5=448 kPa and 1% H_2 (T_5=1995 K, P_5=458 kPa).*

As particle diameter is obtained by ratioing scattering and extinction coefficients, this curve versus the time is particularly noisy at the beginning of soot formation where the two signals are both low. Then, it is difficult to establish the real beginning of such curve, that means to measure the diameter of the actual initial soot particles. Anyway, it makes sense to evaluate with this technique the lowest detectable value of the soot particle diameter, which is related to the minimum signal level of the scattering and extinction. To this purpose two aspects have to be considered. First of all the errors related to the raw data, and then the fact

that, as shown in Fig. IV.2.6, due to the low dynamic range, the scattering signal starts always after the extinction one.

At this stage, where the scattering signal becomes significant with respect to the error bar, the particle diameter is about 8 nm, which is the lowest detectable value of d_p.

In Fig. IV.2.7 the effect of hydrogen addition is considered. Here are reported results obtained with the mixture of 2% ethylene in argon, at which 0.5% and 1% H_2 is added.
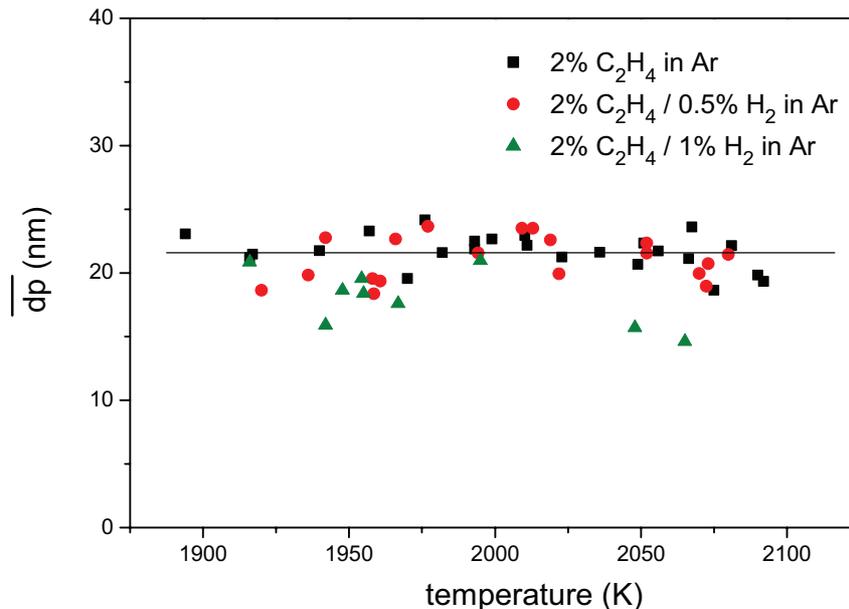
Fig. IV.2.7: *Mean soot particle diameter versus the temperature.*
2% C_2H_4 / 98% Ar – black square; 2% C_2H_4 / 97.5% Ar/ 0.5% H_2 – red circle; 2% C_2H_4 / 97% Ar/ 1% H_2 – green triangle. Measurements in 78 mm i.d. tube.

As observed from the figure, by adding hydrogen to the mixture no significant change in the trend of particle diameters versus the temperature is detected. In fact, considering the mixtures with 0.5% and without hydrogen, the values spread out around about 21 nm (black line in the figure). As for the mixture with 1% H_2 content, some differences are present: the values are much more scattered and with a slight deviation from the trend of the other mixtures. Anyway, it is important to point out that in this last case hydrogen amount is very significant, being the half in volume of the ethylene content.

2.5 Soot formation and growth parameters

For each run, the global parameters of soot formation kinetics (as the soot yield, the induction delay time and the soot growth rate) and the characteristics of the soot structure have been measured.

2.5.1 Soot volume fraction

Dependence on temperature

In order to investigate the dependence of the soot volume fraction on the temperature, the time-behavior of f_v in the low, medium and high temperature regions is compared. In Fig. IV.2.8 measurements versus time are shown.
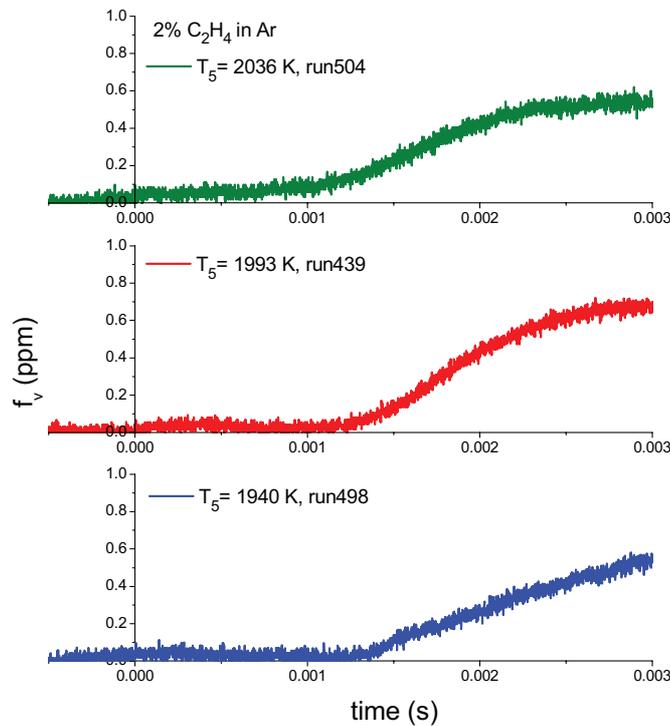
Fig. IV.2.8: Soot volume fraction vs time as a function of the temperature – 2% C₂H₄ in Ar (T₅=1940 K P₅=508 kPa – blue line; T₅=1993 K P₅=465 kPa – red line; T₅=2036 K P₅=463 kPa – green line) – measurements in the 78 i.d. shock tube

The observations already made for the measurements carried out in the small tube are valid also in this case. Moreover, a further consideration has to be pointed out. In all f_v curves versus time a double plateau is detected. This behavior is more evident in the highest temperature conditions (T=2036 K).

Dependence on hydrogen content.

By fixing now the value of the temperature, the dependence of the temporal behavior of the soot volume fraction on hydrogen content in the mixture is considered, and shown in Fig. IV.2.9.
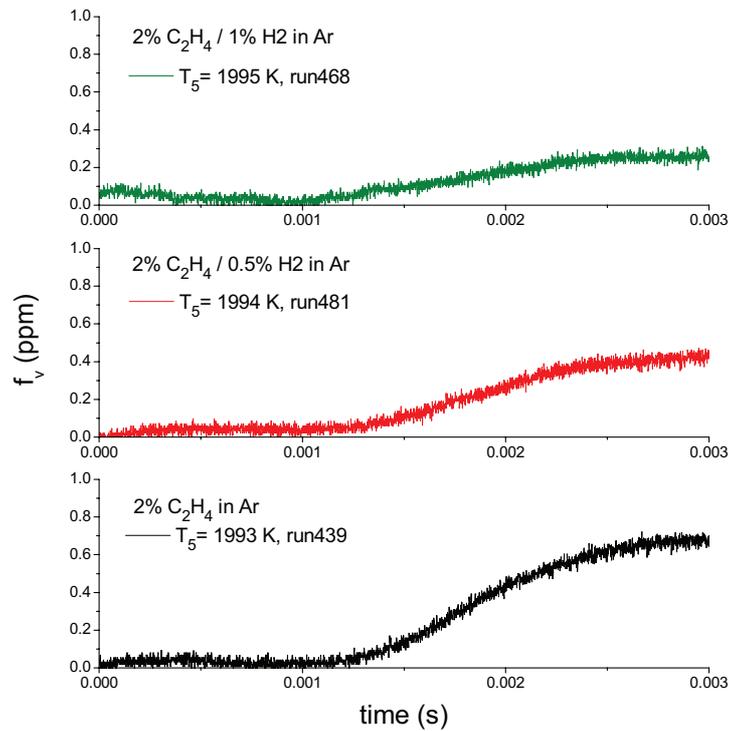
Fig. IV.2.9: *Influence of hydrogen addition on the soot volume fraction vs time 2% C_2H_4 in Ar (T_5=1994 K, P_5=465 kPa) and with 0.5%(T_5=1994 K, P_5=448 kPa and 1% H_2 (T_5=1995 K, P_5=458 kPa)*

From the figure the following observations can be made.

- The curves are very similar. Soot volume fraction starts to increase almost at the same time (above 1.2 ms). This regular increase is similar for the three mixtures, and present a well-defined plateau.

- By increasing hydrogen addition a significant reduction of the value of f_v reached at the plateau is detected.

168

2.5.2 Induction delay time.

Concerning the effect of hydrogen addition, in Fig. IV.2.10 the induction delay time (in logarithmic scale) versus the inverse of the temperature is reported for the three mixtures (2% C_2H_4/ 98% Ar, 2%C_2H_4/ 0.5% H_2/ 97.5% Ar, 2% C_2H_4/ 1% H_2/ 97% Ar). For all curves, the same linear trend, that means an exponential Arrhenius law, has been obtained as the curve shown in Fig. IV.1.16. Overlapped to the symbols the related linear fitting are shown for each mixture, and also the resulting fitting equations are reported.
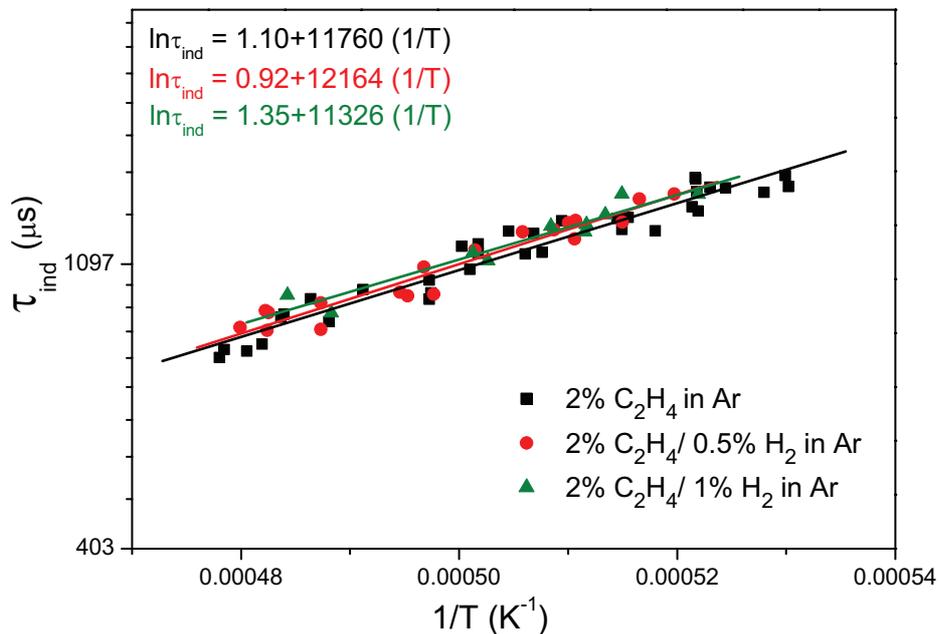
Fig. IV.2.10:*Effect of hydrogen addition on the induction delay time versus the inverse of the temperature. 2% C_2H_4 / 98% Ar – black square; 2% C_2H_4 / 97.5% Ar/ 0.5% H_2 – red circle; 2% C_2H_4 / 97% Ar/ 1% H_2 – green triangle*

From the slope of the straight lines, the activation energy (E) can be derived and reported in Table IV.2.1. Unfortunately, no comparison with the results reported in the literature is possible. In fact, as for the ethylene mixture, the literature data are obtained in different pressure conditions (Kellerer et al. [163]), while no results can be found for the mixtures with hydrogen content. From both the figure and the table, we can see that, by adding 0.5 and 1% H_2 at the mixture ethylene/argon, no significant differences appear in the slope of the induction delay time, and consequently on the activation energy. In fact, the

spread between the maximum and the minimum value is less than 7%. We can then infer that hydrogen addition produces no effect on the induction delay time.

mixture	slope	E (kJ/mol)
C_2H_4	11760.25485	97.7277
+0.5%H_2	12164.57516	101.0876
+1%H_2	11326.19714	94.1207

Table IV.2.1*: Values of the activation energy for the three mixtures.*

2.5.3 Soot yield.

In Fig. IV.2.11 the dependence of the soot yield on the temperature is reported for the three mixtures (ethylene/argon and with hydrogen addition).

The measurements (symbols in the figure) present the same Gaussian-like behavior already observed in the 38 mm i.d. shock tube, and can be described by using the relationship reported in Eq.3.5.2. By fitting these measurements with such function, the maximum soot yield and the temperature at which this maximum occurs can be obtained. In Fig. IV.2.11 these values of T_{max} and Y_{max} as well as the fitting curves are reported for each mixture.

Comparing these results the following observations can be made.

- The global structure is similar for the three mixtures and it is characterized by a maximum of the soot yield falling at almost the same temperature of 1990 K.

- By increasing the percentage in volume of hydrogen, a significant reduction of the soot yield results. In fact, Y_{max} is around 8.7% in the case of pure ethylene, and it reduces at less than the half by adding 1% H_2.
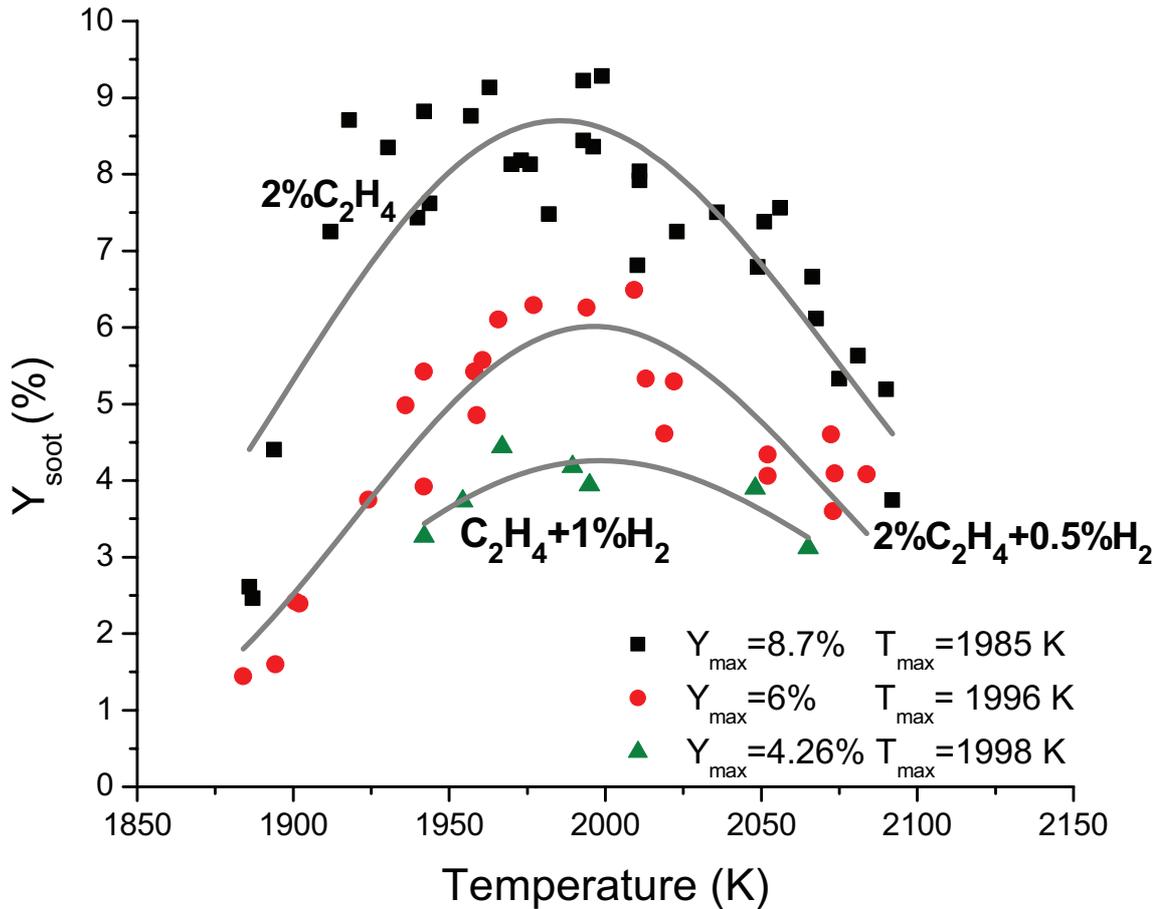
Fig. IV.2.11: *Soot yield versus temperature for the three mixtures: . 2% C₂H₄ / 98% Ar – black square; 2% C₂H₄ / 97.5% Ar/ 0.5% H₂ – red circle; 2% C₂H₄ / 97% Ar/ 1% H₂ – green triangle*

2.5.4 Total soot growth

As a further analysis of the effect of hydrogen in the ethylene pyrolysis investigated in the shock tube, the total soot growth rate is considered. As observed from Fig. IV.1.5 in this Chapter, after soot inception and before reaching a constant value in the plateau region, soot volume fraction exhibits a fast growth. In laminar flames at atmospheric pressure, the increasing in soot volume fraction can be well described by a first-order growth model as (Matzing et al. [31], Eq. (I.1.3) in Chapter I).

Considering measurements in a shock tube, such model can be applied only in the first stages of soot growth. In our case, the soot growth is evaluated for each run and the results shown in Fig. 7.1 as a function of the inverse of the temperature. By using the logarithmic

scale for the y-axis, the typical Arrhenius's dependence is obtained with an apparent activation energy E_g. The three sets of symbols, one for each mixture, are linearly fitted and the relationships are shown in the same figure
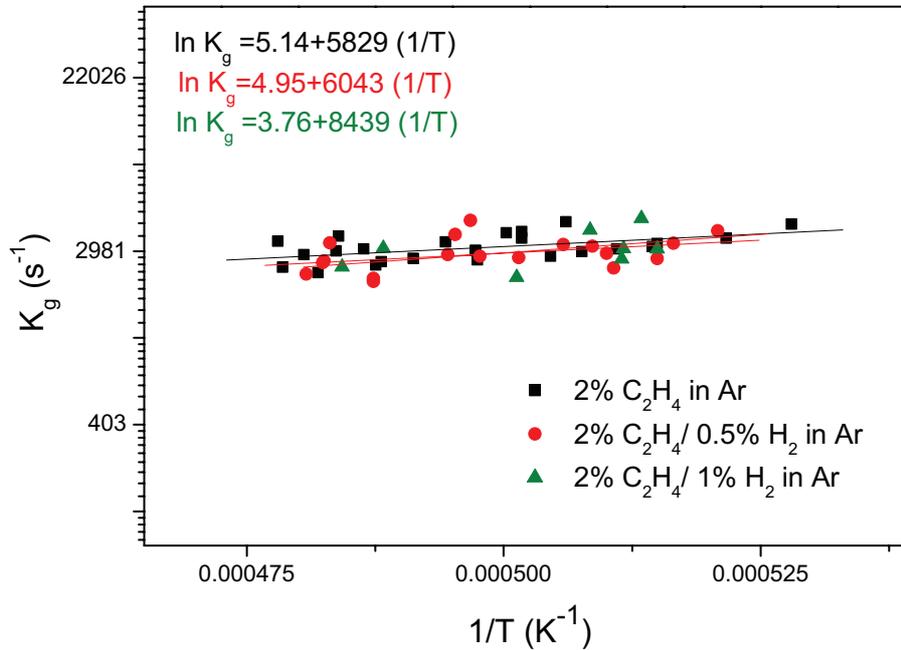
Fig. 2.1: *Total soot growth rate versus the inverse of the temperature for the three mixtures: 2% C_2H_4 / 98% Ar – black square; 2% C_2H_4 / 97.5% Ar/ 0.5% H_2 – red circle; 2% C_2H_4 / 97% Ar/ 1% H_2 – green triangle.*

Considering for each mixture the curve slope, E_g can be calculated and reported in Table 3.I. As it can be seen from the figure, the symbols are quite spread and it is difficult to estimate a difference in the trend. In fact, by comparing the activation energy in the mixtures without hydrogen and with 0.5% addition, the values are quite close. The different value obtained in the last mixture in the table is due to the large uncertainties of the data. With 1% H_2 , that is half the amount of ethylene in the mixture, very law concentration of soot volume fraction is detected; with a maximum value of $f_v = 0.3$ ppm.

3   Conclusions on shock tube measurements

During this work, we have assessed the applicability of the scattering technique at multiple angles, coupled with the extinction one, in order to derive the main parameters

characterizing the soot tendency of ethylene / argon mixtures and the effect of adding hydrogen on the soot production.

It has been shown that special care must be taken when measuring the scattered light from soot particles formed in shock tubes. Moreover, due to the strong absorption of both the incident laser light and of the scattered intensity by soot particles in the tube, a correction procedure has to be applied, otherwise an undervaluation of scattering coefficients can result.

Considering the evaluation of the dissymmetry ratio versus time, it has been proved that during the during the observation time behind reflected shock waves, no aggregation effects have been detected. Then, it is possible to infer that the evolution of isolated particles can be followed.

As for the effect of hydrogen on soot tendency, in Table 3.I a summary of the results concerning the role of hydrogen addition in the ethylene pyrolysis is reported for the three investigated mixtures: 2% C_2H_4 / 98% Ar; 2% C_2H_4 / 97.5% Ar/ 0.5% H_2; 2% C_2H_4 / 97% Ar/ 1% H_2.

Mixture in Ar	Y_{max}, T_{max} (K)	dp (nm)	E (kJ/mol^{-1})	E_g (kJ/mol^{-1})
2% C_2H_4	8.7%, 1985K	22	97.74	48.44
2% C_2H_4/0.5% H_2	6%, 1996	21	101.09	50.22
2% C_2H_4/1% H_2	4.26%, 1998	20	94.12	70.13

Table 3.I: *Soot particle diameter, maximum soot yield and related temperature, activation energy related to the induction delay time and soot growth rate for the mixtures: 2% C_2H_4 / 98% Ar; 2% C_2H_4 / 97.5% Ar/ 0.5% H_2; 2% C_2H_4 / 97% Ar/ 1% H_2.*

For each mixture, the following parameters are shown: the characteristic parameters of the soot yield (that is the maximum soot yield, Y_{max}, and the related temperature, T_{max}), the mean particle diameter occurring at an average value of temperature (detected at 3 ms after the reflected shock wave in the 78 mm i.d. tube), the activation energy relative to the induction delay time (E) and the one of the total soot growth (E_k).

These overall results presented here allow to obtain a clear and consistent picture of the role of hydrogen addition to the ethylene/argon mixture. We can synthesize in brief that:

- Soot induction delay times are not changed by adding hydrogen to the mixture, this result indicates that the time needed to form soot precursors and the first nuclei is the same whether hydrogen is added or not to the mixture. (see Fig. III.2.9 and Fig. III.2.14).

- Soot yield is strongly modified. Hence, from this finding, one can conclude that hydrogen is responsible for the depletion in the soot precursors and must play a role in the chemical routes to PAHs and soot nucleii as a scavenger.

- As for the effect of hydrogen on the soot diameter, it seems that hydrogen did not affect the size of the primary spheres.

- Finally, the fact that the soot growth constant is not affect by the presence of hydrogen indicates that the mechanism of surface growth is the same and that only the concentration of soot precursors is lower.

Conclusions and perspective

In this work the effect of hydrogen addition on soot formation is investigated in the reactors and according the experimental conditions reported in the following.

-    Premixed combustion is studied on the laminar premixed flame at atmospheric temperature, with an equivalence ratio of 2.34 and constant C/O ratio of 0.77

-    Pyrolysis condition is investigated in the shock tube at wide temperature range and pressure around 500 kPa.

In both cases ethylene is used as fuel, and in the shock tube also toluene is studied. For these studies the experimental investigation has been carried out by means of the scattering/extinction technique. This diagnostic allows to determine soot parameters in terms of soot concentration, particle dimension, number density and aggregation. The technique has been widely applied in flames, but the implementation on the shock tube requires many efforts. For that, in this work scattering/extinction technique have been developed in the flame and then the extension to the shock tube has been deeply investigated. In the following the main conclusions will be presented, for both the technique and for the role of hydrogen in soot formation.

All over the following, the very different environment have to be kept in mind.

Conclusions on scattering/extinction technique

From scattering/extinction measurements the following results are obtained.

▪ A novel scattering technique has been proposed to describe soot formation and structure and, consequently, to derive soot parameters in the premixed flame, where strong agglomeration is present. The approach is based on the fractal like soot model and R-D-G scattering theory. By performing scattering measurements at three angles a numerical procedure was developed to derive, in conjunction with extinction measurements, soot structure and morphology as well as soot volume fraction and soot yield.

▪ Concerning the extinction technique, for soot volume fraction measurements, it was found that the use of the red laser line in the premixed flame conditions investigated in this study is not appropriate to derive soot volume fraction. An overestimated value is obtained, due to contribution of other gas-phase species absorbing in this spectral region. In this case, an IR source is needed. On the contrary, in pyrolysis measurements performed in the shock tube, it has been proved that, in the range of temperature and pressure under study, same results are obtained by using laser beams in the red and IR spectral region. Anyway, it is suggested the use of an IR source as safer, whatever the hydrocarbons and the experimental conditions.

▪ The extension of the technique to the shock tube has been developed and widely discussed concerning both the experimental set-up and the theoretical approach. Extinction and three angles scattering technique at have been applied to the shock tube. Soot morphology has been investigated by applying a dissymmetry ratio technique, in order to follow aggregation processes along soot formation and growth stages. The processing procedure to retrieve soot parameters has been presented and discussed.

By comparing the scattering/extinction technique as applied in the two reactors the following conclusions can be drawn:

- The first major result of this study is that special care must be taken when measuring the light scattered from soot particles produced in shock tubes. Indeed, unlike in flames where the intensity of the incident laser light does not decrease as it crosses the reaction zone, in the case of shock tube experiments, the absorption of the incident laser, as well as the scattered light, can strongly affect the results leading to a misevaluation of the scattering coefficient. As far as we know, this is the first study which has demonstrated this effect.

- The second major result is that, during the observation time behind reflected shock waves (in this case around 3 ms), the primary soot particles do not aggregate as it is observed in flames, but grow as individual particles. One has to keep in mind that very small particles (lower than 5 nm) are not measurable in this configuration and hence, the coagulation of these small particles is not identified using the scattering ratios at different angles. But when the soot particles reach a size around 10 nm, the main growth process is surface growth.

Conclusions on soot formation

The results concerning soot formation in the two systems can be synthesized as follows:

In the flame

- From overall results of the soot parameters along the flame axis, it can be inferred that as soon as soot particles are formed, coagulation and aggregation processed occur almost at the same time. In fact, fast increase of the dissymmetry ratio and of the radius of gyration are detected simultaneously with the first extinction (inception) and number decrease (coagulation).
- Moreover, the growth of the particle diameter and of the volume-mean diameter is almost continuous along the flame

In the shock tube

- The global soot parameters and the soot primary particles are derived in this case. The values obtained for the soot yield and for the primary particles obtained with toluene

are in agreement with literature data. No data are available in the literature for ethylene, at least at the conditions under study.

Conclusions on the effect of hydrogen addition

Concerning the role of hydrogen addition on soot formation, from the results obtained in the two reactors, the following conclusions can be drawn.

In the flame

- By adding hydrogen an overall reduction of soot concentration, volume-mean diameter, primary particle and number density is obtained. In particular the reduction in the soot yield is found, even if the C/O is constant and the equivalence ratio increases. As for aggregation, a reduction in the radius of gyration accounts for the formation of less ramified soot structures.
- Moreover, by considering the derivative with time of soot parameters, it can be deduced that with hydrogen addition the rate at which soot primary particle diameter and soot yield change are the same with and without hydrogen.

In the shock tube

- With hydrogen addition no significant effects on the induction delay time and on the soot particle diameter are detected.
- As for soot volume fraction and soot yield, the effect of hydrogen addition is a significant reduction of the soot yield at any temperature values under study. Moreover, the curve of soot yield versus the temperature presents the same shape with and without hydrogen, and is characterized by the same value of the temperature at which the maximum soot yield occurs.
- As for the soot growth, the same values are obtained with and without hydrogen addition, and the same dependence on soot temperature is found as well.
- The decrease in soot volume fraction (soot yield) appears to be mainly related to a decrease in number of inception sites, being the particle growth substantially unchanged with hydrogen addition.

These important results obtained from shock tube measurements give complementary insights on the flame findings. Indeed, from flame measurements it was observed that two different parameters could be responsible for soot reduction: the delay time necessary to form soot precursor and the concentration level of such precursors, that could account for a decrease in the nuclei concentration. From shock tube measurements, no effect on the induction delay time was observed. On the contrary, as soot yield is strongly modified, one can conclude that hydrogen is responsible for the depletion in the soot precursors and must play in the chemical routes to PAHs and soot nuclei as a scavenger.

Concerning the diameter, in shock tube measurements hydrogen did not affect the size of the primary spheres, unlike it was observed in flames. However, the effect of hydrogen is noticeable in flames only for HAB above 10 mm, where the agglomeration exists. But, for lower HAB, where agglomeration is negligible, while inception and coagulation dominate, the effect of hydrogen is hardly noticeable, as in shock tubes.

Finally, the fact that the soot growth is not affect by the presence of hydrogen indicates that the mechanism of surface growth remains the same and that only the concentration of soot precursors is lower.

As a perspective work, in order to derive a complete understanding of these processes, it would be interesting to study oxidation conditions in the shock tube.

REFERENCES

1 http://www.epa.gov/air/oaqps/eog/bces/module3/category/category.htm

2 T. Nussbaumer, C. Czaschi, N. Klipper, L. Johansson, C. Tullin, On behalf of International Energy Agency (IEA) Bioenergy Task 32, Swiss Federal Office of Energy (SFOE) (2008)

3 D.C. Chalupa, P.E. Morrow, G. Oberdörster, M.J. Utell, M.W. Frampton, *Ultrafine Particle Deposition in Subjects with Asthma,* Environ Health Perspec. **112**(8), 879–882 (2004)

4 http://www.eia.doe.gov/iea/

5 D.B. Kittelson, W.F. Watts, J.P. Johnson, *Ultrafine and Nanoparticle Emissions: A New Challenge for Internal Combustion Engine Designers*, Intern. Conf. "Engines of Sustainable Development", Naples, 2003.

6 D.B. Kittelson, *Engines and nanoparticles: a review,* Journal of Aerosol Science **29**, 575–588 (1998).

7 H. Jung, D.B. Kittelson, M.R. Zachariah, *The influence of engine lubricating oil on diesel nanoparticle emissions and kinetics of oxidation*, SAE Paper n. 2003-01-3179 (2003).

8 R.L. Vander Wal, *Soot Precursor Material: Visualization via Simultaneous LIF-LII and Characterization via TEM*, Proceedings of the Combustion Institute **26**, 2269–2275, (1996)

9 F. Xu, G.M. Faeth, *Soot formation in laminar acetylene/air diffusion flames at atmospheric pressure,* Combustion and Flame **125**, 804-819 (2001)

10 U.O. Koylu, G.M. Faeth, T.L. Farias, M.G. Carvalho, *Fractal and Projected Structure Properties of Soot Aggregates*, Combustion and Flame **100**, 621-633 (1995)

11 J. Lahaye, G. Prado, *Physical Aspects of Nucleation and Growth of Soot Particles*, Plenum Edition (1981)

12 H. Gg Wagner, *Soot formation in combustion*, Proceedings of the Combustion Institute **17**, 3-19 (1978)

13 B.S. Haynes, G.G. Wagner, *Soot Formation*, Progress in Energy and Combustion Science **7**, 229-273 (1981)

14 O.I. Smith, *Fundamentals of Soot Formation in Flames with Application to Diesel Engine Particulate Emissions*, Progress in Energy and Combustion Science **7**, 275-291 (1981)

15 H. Bockhorn, *Introduction to Soot Formation in Combustion – Mechanisms and Models*, H. Bockhorn Edition (1994)

16 J. S. Lighty, R. Pugmire, A. Sarofim, A. Violi, G. Voth, *Nano Carbon Particles in the Atmosphere: Formation and Transformation,* NSF Nanoscale Science and Engineering Grantees Conference, Dec 13-15, 2004

17 H. Richter, J.B. Howard, Formation of polycyclic aromatic hydrocarbons and their growth to soot – a review of chemical reaction pathways, Progress in Energy and Combustion Science **26**, 565-608 (2000)

18 R.A. Dobbins, R.A. Fletcher, H.C. Chang, *The evolution of soot precursor particles in a diffusion flame*, Combustion and flame **14**, 285-298 (1998)

19 M. Frenklach, D.W. Clary, Jr W.C. Gardiner, S.E. Stein, *Detailed kinetic modeling of soot formation in shock-tube pyrolysis of acetilene,* Proceedings of the Combustion Institute **20**, 887-901 (1984)

20 M. Frenklach and H. Wang, *Detailed modeling of soot particle nucleation and Growth,* Proc. Comb. Inst. **23**, 1559–1566 (1991)

21 M. Frenklach, H. Wang, *Detailed kinetic modeling of soot particle formation*, Springer **59**, 1994

22 J.A. Miller, C.F. Melius,. *Kinetic and thermodynamic issues in the formation of aromatic compounds in flames of aliphatic fuels,* Combust. Flame **91**, 21–39 (1992).

23 A.M. Dean, *Detailed kinetic modeling of autocatalysis in methane pyrolysis*, J Phys Chem. **94,** 1432–1439 (1990)

24 N.M. Marinov, W.J. Pitz, C.K. Westbrook, M.J. Castaldi, S.M. Senkan, *Modeling of aromatic and polycyclic aromatic hydrocarbon formation in premixed methane and ethane flames*, Combust Sci Technol **116/117**, 211 (1996)

25 M.J. Castaldi, N.M. Marinov, C.F. Melius, J. Huang, S.M. Senkan, W.J. Pitz, C.K. Westbrook, *Experimental and modeling investigation of aromatic and polycyclic aromatic hydrocarbon formation in a premixed ethylene flame*, Proceeding sof the Combustion Institute **26**, 693–702 (1996)

26 I. Glassman, *Soot Formation in Combustion processes*, Proceedings of the Combustion Institute **22**, 295-311 (1988)

27 I.M. Kennedy, *Models of soot formation and oxidation*, Progress in Energy and Combustion Science **23**, 95-132 (1997)

28 J.T. McKinnon, J.B. Howard, *The role of PAH and Acetylene in Soot Nucleation and Growth*, Proceedings of the Combustion Institute **24**, 965-971 (1992)

29 M. Frenklach, *On surface growth mechanisms of soot particles*, Proceedings of the Combustion Institute **26**, 2285-2293 (1996)

30 H. Bockorn, T. Schafer, *Soot Formation in Combustion*, Springer Series in Chemical Physics (1994)

31 H. Matzing, H.Gg. Wagner, *Measurements about the influence of pressure on carbon formation in premixed laminar C_2H_4-air flame*, Proceedings of the Combustion Institute **21**, 1047-1055 (1986)

32 S.C. Graham, J.B. Homer, J.L.J. Rosenfeld, *The formation and coagulation of soot aerosols generated by the pyrolysis of aromatic hydrocarbons*, Proceedings of Royal society of London **2**, 259-285 (1975)

33 K. Oh, H. D. Shin, *The effect of oxygen and carbon dioxide concentration on soot formation in non-premixed flames*, Fuel **85**, 615–624 (2006)

34 F. Liu, H. Guo, G. Smallwood, O.L. Gulder, *The Chemical Effects of Carbon Dioxide as an Additive in an Ethylene Diffusion Flame: Implications for Soot and NOx Formation,* Combustion and Flame 125, 778-782 (2001)

35 P.A. Tesner, *Formation of Dispersed Carbon by Thermal Decomposition of Hydrocarbons*, Proceedings of the Combustion Institute **7**, 546-553 (1958)

36 M. Karbasi, I. Wierzba, *The effects of hydrogen addition on the stability limits of methane jet diffusion flames*, Int. J. Hydrogen Energy **2**, 123-129 (1998)

37 R.W. Schefer, *Hydrogen Enrichment for Improved Lean Flame Stability*, Int.J. Hydrogen Energy **28**, 1131-1141 (2003)

38 G.S. Jackson, R. Sai, J.M. Plaia, C.M. Boggs, K.T. Kiger, *Influence of H_2 on the response of lean premixed CH_4 flames to high strained flows*, Combustion and Flame **132**, 503-511 (2003)

39 F. Cozzi, A. Coghe, *Behavior of hydrogen-enriched non-premixed swirled natural gas flames*,Int. J. Hydrogen Energy **31**, 669-677 (2005)

40 G. Yu, C.K. Law, C.K. Wu, *Laminar flame speedsof hydrocarbon and air mixtures with hydrogen addition*, Combustion and Flame **63**, 339-347 (1986)

41 F. Halter, C. Chauveau, I. Gokalp, *Characterization of the effects of hydrogen addition in premixed methane/air flames,* Int. J. Hydrogen Energy **32**, 2585-2592 (2007)

42 C. Tseng, *Effects of hydrogen addition on methane combustion in a porous medium burner*, Int. J. Hydrogen Energy **27**, 699-707 (2002)

43 A.R. Choudhuri, S.R. Gollahalli, *Combustion characteristics of hydrogen-hydrocarbons hybrid fuels*, Int. J. Hydrogen Energy **25**, 451-462 (2000)

44 F. Migliorini, S. De Iuliis, L. Leone, F. Cignoli, G. Zizak, *Soot volume fraciton measurements in methane/hydrogen diffusion flames*, Proceedings of the 24th Meeting of Italian Section of The Combustion Institute, Pisa, Giugno (2006)

45 O.L. Gulder, D.R. Snelling, R.A. Sawchuk, *Influence of Hydrogen Addition to Fuel on Temperature Field and Soot Formation in Diffusion Flames*, Proceedings of the Combustion Institute **26**, 2351-2357 (1996)

46 H. Guo, F. Liu, D.J. Smallwood, O.L. Gulder, *Numerical study on the influence of hydrogen addition on soot formation in a laminar ethylene-air diffusion flame*, Combustion and Flame **145**, 324-338 (2006)

References

47 M. Yahyaoui, N. Djebaïli-Chaumeix, P. Dagaut, C.-E. Paillard, S. Gail, *Experimental and modelling study of gasoline surrogate mixtures oxidation in jet stirred reactor and shock tube*, Proceedings of the Combustion Institute **31** 385–391 (2007)

48 P. Dagaut, *On the kinetics of hydrocarbons oxidation from natural gas to kerosene and diesel fuel*, Phys. Chem. Chem Phys. **4**, 2079-2094 (2002)

49 I. Kitsopanidis, W.K. Cheng, *Soot formation study in a rapid compression machine,* J. Eng. Gas Turbines Power **128**, 942-950 (2006)

50 W. Clauss, V. I. Fabelinsky, D. N. Kozlov, V. V. Smirnov, O. M. Stelmakh, K. A. Vereschagin, *Dual-broadband CARS temperature measurements in hydrogen-oxygen atmospheric pressure flames*, Appl. Phys. B **70**, 127-131 (2000)

51 S. Cheskis, *Quantitative measurements of absolute concentrations of intermediate species in flames*, Prog. Energy Comb. Sci. **25**, 233-252 (1999)

52 Y.–L. Chen, J. W. L. Lewis, C. Parigger, *Probability distribution of Laser-Induced Breackdown and ignition of ammonia*, J. Quant. Spectrosc. Radiat. Transfer **66**, 41-49 (2000)

53 R. S. Barlow, C. D. Carter, *Raman/Rayleigh/LIF measurements of nitric oxide formation in turbulent hydrogen jet flames*, Combust. Flame **97**, 261-280 (1994)

54 W. Meier, A. O. Vyrodov, V. Bergmann, W. Stricker, *Simultaneous Raman/LIF measurements of major species and NO in turbulent H_2/air diffusion flames*, Appl. Phys. B **63**, 79-90 (1996)

55 S. Prucker, W. Meier, W. Stricker, *A flat flame burner as calibration source for combustion research: Temperatures and species concentrations of premixed H_2/Air flames*, Rev. Sci. Instrum. **65** (9), 2908-2911 (1994)

56 G. Sutton, A. Levick, G. Edwards, D. Greenhalgh, *A combustion temperature and species standard for the calibration of laser diagnostic techniques*, Combust. Flame **147,** 39-48 (2006)

57 A. D'Alessio, G. Gambi, P. Minutolo, S. Russo, A. D'Anna, *Optical characterization of rich premixed CH_4/O_2 flames across the soot formation threshold*, Proceedings of the Combust. Inst. **25,** 645-651 (1994)

58 F. Xu, P. B. Sunderland, G. M. Faeth, *Soot formation in laminar premixed ethylene/air flames at atmospheric pressure,*Combust. Flame **108,** 471-493 (1997)

59 F. Xu, K.-C. Lin, G. M. Faeth, *Soot Formation in Laminar Premixed methane/oxygen flames at atmospheric pressure*, Combust. Flame **115,** 195-209 (1998)

60 A. Tregrossi, A. Ciajolo, R. Barbella, *The combustion of benzene in rich premixed flames at atmospheric pressure – Formation during Combustion*, Combust. Flame **117,** 553-561(1999)

61 B. Atakan, A. Lamprecht, K. Kohse-Hoinghaus, *An experimental study of fuel-rich 1,3-pentadiene and acetylene/propene flames,* Combust. Flame **133,** 431-440 (2003)

62 B. Apicella, M. Alfè, R. Barbella, A. Tregrossi, A. Ciajolo, *Aromatic structures of carbonaceous materials and soot inferred by spectroscopic analysis*, Carbon **42,** 1583-1589 (2004)

63 A. V. Menon, S.-Y. Lee, M. J. Linevsky, T. A. Litzinger, R. J. Santoro, *Addition of NO2 to a Laminar Premixed Ethylene-air Flame: Effect on Soot Formation*, Proc. Comb. Inst. **31,** 593-601 (2007)

64 B. Axelsson, R. Collin, P. –E. Bengtsson, *Laser-Induced Incandescence for Soot Particle Size Measurements in Premixed Flat Flames*, Appl. Opt. **39** (21), 3683-3690 (2000)

65 V. Kruger, C. Wahl, R. Hadef, K. P. Geigle, W. Stricker, M. Aigner, *Comparison of laser-induced incandescence method with scanning mobility particle sizer technique: the influence of probe sampling and laser heating on soot particle size distribution*, Meas. Sci. Technol. **16,** 1477-1486 (2005)

66 C. Schulz, B. F. Kock, M. Hoffmann, H. Michelsen, S. Will, B. Bougie, R. Suntz, G. Smallwood, *Laser-Induced Incandescence: recent trends and current questions*, Appl. Phys. B **83**, 333-354. (2006)

67 U. Koylu, *Quantitative Analysis of In Situ Optical Diagnostics for Inferring particle/Aggregate Parameters in Flames: Implications for Soot Surface Growth and Total Emissivity*, Combustion and Flame **109**, 488-500 (1996)

68 C. Janzen, H. Kleinwechter, J. Knipping, H. Wiggers, P. Roth, *Size analysis in low-pressure nanoparticle reactors: comparison of particle mass spectrometry with in situ probing transmission electron microscopy*, J. Aerosol Science **33**, 833-841 (2002)

69 R.A. Dobbins, .M. Megaridis, *Morphology of Flame-Generated Soot as Determined by Thermophoretic Sampling*, Langmuir **3**, 254-259 (1987)

70 J. Cai, N. Lu, C.M. Sorensen, *Comparison of size and morphology of soot aggregates as determined by light scattering and electron microscope analysis*, Langmuir **9**, 2861-2867 (1993)

71 C.J. Dasch, *One-dimensional tomography: a comparison of Abel, onion-peeling, and filtered backprojection methods*, Appl. Opt. **31**, 1146-1152 (1992)

72 P.S. Greenberg, J.C. Ku, *Soot volume fraction imaging*, Applied Optics **36**, 5514-5522 (1997)

73 D.R. Snelling, K.A. Thomson, G.J. Smallwood, O.L. Gulder, *Two-dimensional imaging of soot volume fraction in laminar diffusion flames*, Applied Optics **38**, 2478-2485 (1999)

74 S.C. Graham, *The collisional growth of soot particles at high temperatures*, Proceedings of the Combustion Institute **16**, 663-668 (1976).

75 S.C. Graham, J.B. Homer, J.L.J. Rosenfeld, *The formation and coagulation of soot aerosols*, 10th Int. Shock Waves Symposium, 621-631 (1975)

76 F. Migliorini, G. Lo Castro, F. Cignoli, S. De Iuliis, G. Zizak, *Laser extinction/scattering technique at different wavelengths in a rich premixed flame*, Italian Section of the Combustion Institute, Napoli, Italy, July 2005

77 R.G. Siddal, I.A. McGrath, *The Emissivity of Luminous Flames*, Proceedings of the Combustion Institute **9**, 102-110 (1962)

78 Y. Matsui, T. Kamimoto, S. Matsuoka, Publ. 790471 Society of Automotive Engineers, Warrendale, PA (1979)

79 F. Cignoli, S. De Iuliis, V. Manta, G. Zizak, *Two-Dimensional Two-Wavelength Emission Technique for Soot Diagnostics,* Applied Optics **40**, pp.5370-5378 (2001)

References

80 S. De Iuliis, M. Barbini, S. Benecchi, F. Cignoli, G. Zizak, *Determination of the soot volume fraction in an ethylene diffusion flame by multiwavelength analysis of soot radiation*, Combustion and Flame **115**, 253 – 261 (1998)

81 H. Chang, T.T. Charalampopoulos, *Determination of the wavelength dependence of refractive indices of flame soot*, Proc. Royal Soc. **430,** 577-591 (1990)

82 L. A. Melton, *Soot diagnostics based on laser heating,* Appl. Opt. **23**, 2201-2208 (1984)

83 A.C. Eckbreth, *Effects of Laser-Modulatedparticulate incandescence on raman scattering diagnostics,* J. Appl. Phys. **48**, 4473-4479 (1977)

84 S. De Iuliis, F. Cignoli, G. Zizak, *Two-color laser-induced incandescence (2C-LII) technique for absolute soot volume fraction measurements in flames*, Appl. Opt. **44,** 7414-7423 (2005)

85 C.R. Shaddix, K.C. Smyth, *Laser-induced incandescence measurements of soot production in steady and flickering methane, propane, and ethylene diffusion flames*, Combustion and Flame **107**, 418-452 (1996)

86 B. Axelsson, R. Collin and P.E. Bengtsson, *Laser-induced incandescence for soot particle size and volume fraction measurements using on-line extinction calibration*, Appl. Phys. B **72**, 367–372 (2001)

87 D.R. Snelling, G.J. Smallwood, O.L. Gulder, F. Liu, W.D. Bachalo, *A Calibration-Independent Technique of Measuring Soot by Laser Induced Incandescence Using Absolute Light Intensità,* Second Joint Meeting of the U.S. Sections of The Combustion Institute, Oakland, Calif. (2001)

88 S. De Iuliis, F. Migliorini, F. Cignoli, G. Zizak, *Peak soot temperature in laser-induced incandescence measurements,* Appl. Physics B **83**, 397-402 (2006)

89 S. De Iuliis, F. Migliorini, F. Cignoli, G. Zizak, *2D soot volume fraction imaging in an ethylene diffusion flame by two-color laser-induced incandescence (2C-LII) technique and comparison with results from other optical diagnostics*, Proceedings of the Combustion Institute **31**, 869-876 (2007)

References

90 D.R. Snelling, G. J. Smallwood, F. Liu, O.L. Gulder, W.D. Bachalo, *A calibration-independent laser-induced incandescence techniqeu for soot measurements by detecting absolute light inetnsity*, Applied Optics **44**, 6773-6785 (2005)

91 H.A. Michelsen, P.O. Witze, D. Kayes, S. Hochgreb, *Time-resolved laser-induced incandescence of soot: the influence of experimental factors and microphysical mechanisms*, Applied Optics **42**, 5577-5590 (2003)

92 H.A. Michelsen, *Understanding and Predicting the Temporal Response of Laser-Induced Incandescence from Carbonaceous Particles*, J.Chem.Phys. **118**, 7012-7045 (2003)

93 T.T. Charalampopoulos, *Morphology and dynamics of agglomerated particulates in combustion systems using light scattering techniques*, Prog. Energy Comb. Sci. **18**, 13-45 (1992)

94 C.M. Sorensen, *Light scattering by fractal aggregates: a review*, Aerosol Science and Tehnol. **35**, 648-687 (2001)

95 C.M. Megaridis, R.A. Dobbins, *Morphological Description of Flame-Generated Materials*, Combustion Science and Technol. **71**, 95-109 (1990)

96 R.A. Dobbins, R. J. Santoro, H.G. Semerjiian, *Analysis of light scattering from soot using optical cross sections for aggregates*, Proceedings of the Combustion Institute **23**, 1525-1532 (1990)

97 P.A. Bonczyk, R.J. Hall, *Measurement of the fractal dimension of soot using UV laser radiation*, Langmuir **8**, 1666-1670 (1992)

98 R. Puri, T.F. Richardson, R.J. Santoro, R.A. Dobbins, *Aerosol Dynamic Processes of Soot Aggregates in a Laminar Ethene Diffusion Flame*, Combustion and Flame **92**, 320-333 (1993)

99 S.C. Lee, C.L. Tien, *Optical constants of soot in hydrocarbon f*lames, Proceedings of the Comb. Institute **18**, 1159-1166 (1980)

100 Z.G. Habib, P. Vervish, *On the Refractive Index of Soot at Flame Temperature*, Combust. Science Technol. **59**, 261-274 (1988)

101 W.H. Dalzell, A. F. Sarofim, *Optical Constants of Soot and Their Application to Heat-Flux Calculations,* J. Heat Transf. **91**, 100-104 (1969)

102 A. B. Pluchino, S. S. Goldberg, J. M. Dowling, C. M. Randall, *Refractive-index measurements of single micron-sized carbon particles,* Appl. Opt. **19**, 3370-3372 (1980)

103 B. M. Vaglieco, F. Beretta, A. D'Alessio, *In situ evaluation of the soot refractive index in the UV-visible from the measurement of the scattering and extinction coefficients in rich flames,* Combust. Flame **79,** 259-271 (1990)

104 C. E. Batten, *Spectral optical constants of soots from polarized angular reflectance measurements,* Appl. Opt. **24**, 1193-1199 (1985)

105 J. Mullins, A. Williams, *The optical properties of soot: a comparison between experimental and theoretical values,* Fuel **66**, 277-280 (1987)

106 T. T. Charalampopoulos, *Automated light scattering system and a method for the in situ measurement of the index of refraction of soot particles*, Rev. Sci. Instrum. **58**, 1638-1646 (1987)

107 T. T. Charalampopoulos, H. Chang, *In situ optical properties of soot particles in wavelength range from 340 nm to 600 nm*, Combust. Sci. Technol. **59**, 401-421 (1988)

108 B. J. Stagg, T. T. Charalampopoulos, *Refractive indices of pyrolytic graphite, amorpous carbon and flame soot in the temperature range 25o to 600° C*, Combust. Flame **94**, 381-396 (1983)

109 A. D'Alessio, P. Minutolo, G. Gambi, A. D'Anna, Phys. Chem. **97**, 1574-1583 (1993)

110 S. S. Krishnan, K. C. Lin, G. M. Faeth, *Optical properties in the visible of overfire soot in large buoyant turbulent diffusion flames,* J. Heat transfer **122**, 517-524 (2000)

111 M. Kerker, *The Scattering of light*, Academic Press 1969

112 U.O. Koylu, G.M. Faeth, *Optical properties of soot in buoyant laminar diffusion flames*, Transactions of ASME **116**, 152-159 (1994)

113 R. Kellerer, S. Koch, S Witting, *Measurements of the growth and coagulation of soot particles in a high-pressure shock tube,* Combustion and Flame **120**, 188-199 (2000)

114 F. Douce, N. Djebaili-Chaumeix, C.E. Paillard, C. Clinard, J.N. Rouzaud, *Soot formation from heavy hydrocarbons behind reflected shock waves*, Proceedings of the Combustion Institute **28**, 2423-2529 (2000)

115 St. Bauerle, Y. Karasevish, St. Slavov, M. Tanke, Th. Thienel, H.Gg. Wagner, *Thermal and chemical influences on the soot mass growth*, Proceedings of the Combustion Institute **21,** 627-634 (1994)

116. V.G. Knorre, D. Tanke, Th Thienel, H.Gg. Wagner*, Soot formation in the pyrolysis of bezene/acetylene and acetylene/hydrogen mixtures at high carbon concentrations*, Proceedings of the Combustion Institute 26, 2303-2310 (1996)

117 D.E. Fussey, A.J. Gosling, D. Lampard, *A shock-tube study of induction times in the formation of carbon particles by pyrolysis of the C_2*, Combustion and Flame 32 181-192 (1978)

118 J. Felske, P.F. Hsu, J.C. Ku, *The effect of soot particle optical inhomogenity and agglomeration on the analysis of light scattering measurements in flames*, J. Quant. Spectrosc. Radiat. Transfer **35**, 447-465 (1986)

119 S. di Stasio, P. Massoli, M. Lazzaro, *Retrieval of soot aggregate morphology from light scattering/extinction measurements in a high-pressure high-temperature environment*, J.Aerosol Sci. **27**, 897-913 (1996)

120 S. di Stasio, P. Massoli, *A dissymmetry ratio optical technique as applied to scattering pattern recognistion of differently shaped soot aggregates*, Part.Part. Syst. Charact. **15**, 90-99 (1998)

121 S. di Stasio, P. Massoli, *Morphology, monomer size and concentration of allomerates constituted by Rayleigh particles as retrieved from Scattering/Extinction measurements*, Comb. Sci. Technol. **124,** 219-247 (1997)

122 R.D. Mountain, G.W. Mulholland, *Light scattering from simulated smoke agglomerates,* Langmuir **4**, 1321-1326 (1988)

123 R. Botet, R. Jullien, *A theory of aggregating systems of particles : the clustering of clusters process*, Annales de Physics **13**, 153-221 (1988)

124 C. Oh, C.M. Sorensen, *The Effect of Overlap between Monomers on the Determination of Fractal Cluster Morphology*, J.Colloid Interface Sci. **193(1)**, 17-25 (1997)

125 R.J. Samson, G.W. Mulholland, J.W. Gentry, *Structural analysis of soot agglomerates*, Langmuir **3**, 272-281 (1997)

126 R.K.Chakrabarty, H. Moosmuller, W. P. Arnott, M.A. Garro, G. Tian, J.G.Slowik, E.S.Cross, J.Han, P.Davidovits, T.B. Onash, D:R.Worsnop, *Low Fractal Dimension Cluster-Dilute Soot Aggregates from a Premixed Flame*, Physics Review Letter **102** (2009)

127 U.O. Koylu, G.M. Faeth, *Radiative properties of flame-generated soot*, J. Heat Transher **115**, 409-417 (1993)

128 R.A. Dobbins, C.M. Megaridis, *Absorption and scattering of light by polydisperse aggregates*, Appl. Optics **30**, 4747-4754 (1991)

129 C.M. Sorensen, J. Cai, N. Lu, *Test of static structure factors for describing light scattering from fractal soot aggregates*, Langmuir **8**, 2064-2069 (1992)

130 Y. Teng, U.O.Koylu, *Optical sizing of aggregated combustion particles: computational development of a two-angle laser scattering technique*, Applied Optics **45**, 4396-4403 (2006)

131 U.O. Koylu, G.M. Faeth, *Structure of overfire soot in buoyant turbulent diffusion flames at long residence times,* Combustion and Flame **89**, 140-156 (1992)

132 U.O. Koylu, G.M. Faeth, T.L. Farias, M.G. Carvalho, *Fractal and projected structre porperties of soot aggregates*. Combustion and Flame **100**, 621-633 (1995)

133 A.J. Hurd, W.L. Flower, *In Situ Growth and Structure of Fractal Silica Aggregates in a Flame,* J. Colloid. Interface Sci. **122**, 178-192 (1988)

134 D'Alessio, G. Gambi, P. Minutolo, S. Russo, A. D'Anna, *Optical characterization of rich premixed CH4/O2 flames across the soot formation threshold,* Proceedings of the Combustion Institute **25**, 645-651 (1994)

135 N.M. Marinov, W.J. Pitz, C.K. Weastbrook, A.M. Vincitore, M.J. Castaldi, S.M. Senkan, C.F. Malius, *Aromatic and Polycyclic Aromatic Hydrocarbon Formation in a Laminar Premixed n-Butane Flame*, Comb. Flame **114**, 192-213 (1998)

136 A. Tregrossi, A. Ciajolo, R. Barbella, *The combustion of benzene in rich premixed flames at atmospheric pressare,* Comb. Flame **117**, 553-561 (1999)

137 T.R. Melton, F. Inal, S.M. Senkan, *The effects of equivalence ratio on the formation of polycyclic aromatic hydrocarbons and soot in premixed ethane flames*, Comb. Flame, **121**, 671-678 (2000)

138 A. Ciajolo, R. Barbella, A. Tregrossi, L. Bonfanti, *Spectroscopic and compositional signatures of PAH-loaded mixtures in the soot inception region of premixed ethylene flame,* Proceedings of the Combustion Institute **27**, 1481 (1998)

139 A. D'Alessio, A. D'Anna, G. Gambi, P. Minutolo, *The spectroscopic characterisation of UV absorbing nanoparticles in fuel rich soot forming flames*, J. Aerosol Sci. **29**, 397 (1998).

140 P. Minutolo, G. Gambi, A. D'Alessio, *Properties ofcarbonaceous nanoparticles in flat premixed C_2H_4/Air flames with C/O ranging from 0.4 to soot appearance limit,* Proceedings of the Combustion Institute **27**, 951 (1998)

141 A. Ciajolo, A. Tregrossi, R. Barbella, R. Ragucci, B. Apicella, M. De Joannon, *The Relation Between Ultraviolet-Excited Fluorescence Spectroscopy and Aromatic Species Formed in Rich Laminar Ethylene Flames,* Comb. Flame **125**, 1225-1220 (2001)

142 P. Minutolo, G. Gambi, A. D'Alessio, *The optical band gap model in the interpretation of the UV-visible absorption spectra of rich premixed flames,* Proceedings of the Combustion Institute **26**, 951-957 (1996)

143 P. Minutolo, A. D'Anna, A. D'Alessio, *On detection of nanoparticles below the sooting threshold,* Comb. Flame, **152**, 287-292 (2008)

144 P. Minutolo, G. Gambi, A. D'Alessio, S. Carlucci, *Spectroscopic Characterisation of Carbonaceous Nanoparticles in Premixed Flames*, Atmospheric Env., **33**, 2725 (1999)

145 L.A. Sgro, P. Minutolo, G. Basile, A. D'Alessio, *UV-visible spectroscopy of organic carbon particulate sampled from ethylene/air flames,* Chemosphere **42**, 671-680 (2001)

146 L.A. Sgro, G. Basile, A.C. Barone, A. D'Anna, P. Minutolo, A. Borghese, A. D'Alessio, *Detection of combustion formed nanoparticles,* Chemosphere **51**, 1079-1090 (2003)

147 P. Weilmunster, A. Keller, K.-H. Homann, *Large molecules, radicals, ions, and small soot particles in fuel-rich hydrocarbon flames. Part I: Positive ions of polycyclic aromatic hydrocarbons (PAH) in low-pressure premixed flames of acetylene and oxigen,* Comb. Flame **116**, 62-83 (1998)

148 H. Richter, T.G. Benish, O.A. Mazyar, W.H. Green, J.B. Howard, *Formation of Polycyclic Aromatic Hydrocarbons and their Radicals in a Nearly Sooting Premixed Benzene Flame*, Proceedings of the Combustion Institute **28**, 2609-2618 (2000)

149 J. Appel, H. Bockhorn, M. Frenklach, *Kinetic modeling of soot formation with detailed chemistry and physics: laminar premixed flames of C2 hydrocarbons,* Comb. Flame **121**, 122-136 (1995)

150 A. D'Anna, A. Violi, A. D'Alessio, *Modeling the Rich Combustion of Aliphatic Hydrocarbons*, Comb. Flame **121**, 418-429 (2000)

151 A.V. Krestinin, *Detailed Modeling of Soot Formation in Hydrocarbon Pyrolysis*, Comb. Flame **121**, 513-524 (2000)

152 H. Richter, W.J. Grieco, J.B. Howard, *Formation Mechanism of Polycyclic Aromatic Hydrocarbons and Fullerenes in Premixed Benzene Flames*, Comb. Flame **119**, 1-22 (1999)

153 U. Bonne, K.H. Homann, H. Gg. Wagner, *Carbon formation in premixed flames*, Proceedings of the Combustion Institute **10**, 503-512 (1965)

154 K.H. Homann, H. Gg. Wagner, *Some new aspects of the mechanism of carbon formation in premixed flames*, Proceedings of the Combustion Institute **11**, 371-379 (1967)

155 A. D'Alessio, A. Di Lorenzo, A.F. Sarofim, F. Beretta, S. Masi, C. Venitozzi, *Soot formation in methane-oxygen flames*, Proceedings of the Combustion Institute **15,** 1427 (1975)

156 A. D'Alessio, F. Beretta, C. Venitozzi, *Optical Investigations on Soot Forming. Methane-Oxygen Flames,* Comb. Sci. Technol. **5**, 263-272 (1972)

157 W.L. Flower, *Optical measurements of soot formation in premixes flames,* Comb. Sci. Technol. **33**, 17-33 (1983)

158 P.A. Bonczyk, *Suppression of soot in flames by alkaline-earth and other metal additives*, Comb. Sci. Technol. **59**, 143 (1988)

159 D.W. Hahn, T.T. Charalampopoulos, *The role of iron additives in sooting premixed flames*, Proceedings of the Combustion Institute **24,** 1007-1014 (1992)

160 J. Hodges, D. Foster, *Soot Coagulation with Surface Growth Kinetics,* Comb. Sci. Technol., **51**, 235-249 (1987)

161 A. Kazakov, M. Frenklach, *Dynamic Modeling of Soot Particle Coagulation and Aggregation: Implementation With the Method of Moments and Application to High-Pressure Laminar Premixed Flames,* Comb. Flame **114**, 484 501 (1998)

162 W.J. Hooker, *Shock tube studies of acetylene decomposition*, Proceeding of the Combustion Institute **7,**. 949-952, (1958)

163 H. Kellerer, A. Muller, H.-J. Bauer et S. Wittig, *Soot formation in a shock tube under elevated pressure conditions*, Combustion Science and Technology **113 – 114**, 67 – 80 (1996)

164 H. Kellerer et S. Wittig, *Growth and coagulation of soot at high pressures*, Proceeding of the 21st International Symposium on Shock Waves (1997)

165 O. Mathieu, N. Djebaïli-Chaumeix, C.-E. Paillard, F. Douce, *Experimental study of soot formation from a diesel fuel surrogate in a shock tube,* Combustion and Flame **156** (8) 1576-1586 (2009)

166 T. S. Wang, R. A. Matula et R. C. Farmer, *Combustion kinetics of soot formation from toluene*, Proceeding of Combustion Institute **18**, 1149 – 1158 (1981)

167 A. Alexiou et A. Williams, *Soot formation in shock-tube pyrolysis of toluene-methanol, toluene-ethanol, and toluene-oxygen mixtures*, Combustion and Flame **104**, 51-65 (1996)

168 F. Douce, N. Djebaïli-Chaumeix, C.-E. Paillard, C. Clinard, J.-N. Rouzaud, *Soot formation from heavy hydrocarbons behind reflected shock waves*, Proceeding of the Combustion Institute **28** (2), 2523-2529 (2000)

169 O. Mathieu, G. Frache, N. Djebaïli-Chaumeix, C.-E. Paillard, G. Krier, J.-F. Muller, F. Douce, P. Manuelli, *Characterization of adsorbed species on soot formed behind reflected shock waves*, Proceedings of the Combustion Institute **31** (1), 511-519 (2007)

170 A. Muller et S. Wittig, *Influence of temperature and pressure on soot formation in a shock tube under high pressure conditions*, Proceeding of the 18th International Symposium on Shock Waves, 759-764 (1991)

171 D. Tanke, ''Rußbildung in der Kohlenwasserstoffpyrolyse hinter Stoßwellen,'' Ph.D. thesis, Universitat Gottingen, 1995.

172 H. Mätzing et H.Gg. Wagner, *Measurements about the influence of pressure on carbon formation in premixed laminar C_2H_4-air flames*, Proceeding of the Combustion Institute **21**, 1047-1055 (1986)

173 H. Böhm, D. Hesse, H. Jander, B. Lüers, J. Pietscher, H. Gg. Wagner et M. Weiss, *The influence of pressure and temperature on soot formation in premixed flames*, Proceeding of the Combustion Institute **22**, 403-411 (1988)

174 M. Frenklach, S. Taki, M. B. Durgaprasad et R. A. Matula, *Soot formation in shock-tube pyrolysis of acetylene, allene, and 1,3-butadiene,* Combustion and Flame, **54**, 81-101 (1983)

175 S. M. Hwang, P. Vlasov, H.Gg. Wagner et Th. Wolff, Zeitschrift für Physikalische Chemie **173**, 129-139 (1991)

176 E. Goos, F. Douce, N. Djebaili-Chaumeix, M. Braun-Unkhoff, *Experimental and numerical investigation focusing on early soot formation of toluene and 1-methylnaphthalene at high pressures,* Proceedings of European Combustion Meeting 2003.

References

---

177 O. Mathieu, N. Djebaili-Chaumeix and C.-E. Paillard, *Soot formation behind reflected shock waves from a Fischer-Tropsch diesel fuel*, Proceedings of the European Combustion Meeting 2005

178 T. Tsuboi, K. Ishii, H. Omura, *Spectral intensity measurement for soot formation of benzene behind reflected shock waves*, Shock Waves **12**, 121-128 (2002)

179 A. Emelianov, A. Eremin, H. Jander, H.Gg Wagner, Ch. Borchers, *Spectral and structural properties of carbon nanoparticle forming in C_3O_2 and C_2H_2 pyrolysis behind shock waves,* Proceedings of the Combustion Institute **29**, 2351-2357 (2002)

180 M. Evans, A. Williams, *Shock tube studies on the formation of soot from the combustion and pyrolysis of some hydrocarbons*, Fuel **60**, 1047-1056 (1981)

181 S. De Iuliis, F. Cignoli, S. Benecchi, G. Zizak, *Determination of soot parameters by a two-angle scattering/extincion technique in an ethylene diffusion flame*, Appl. Opt. **37**, 1865-7874 (1998)

182 H. Kellerer, A., Muller, H-J. Bauer, S. Witting, *Soot formation ina shock tube under elevated pressure conditions*, Comb. Sci. and Tech. **113**, 67-80 (1996).

183 http://www.flatflame.com/index_copy(1).htm

184 W. Meier, A. O. Vyrodov, V. Bergmann, W. Stricker, *Simultaneous Raman / LIF Measurements of Major Species and NO in Turbulent H2/Air Diffusion Flames*, Appl. Phys. B **63**, 79-90 (1996)

185 F. Migliorini, S. De Iuliis, F. Cignoli, G. Zizak, *How "flat" is the rich premixed flame produced by your McKenna burner?*, Combustion and Flame **153**, 384-393 (2008).

186 K. Wegner, S.P. Pratsinis, *Scale-up of nanoparticles synthesis in diffusion flame reactors*, Chemical Engineering Science **58**, 4581-4589 (2003)

187 A.G. Gaydon, I.R.Hurle, *The shock tube in high-Temperature Chemical Physics*, Chapman & Hall Ltd. London 1963

188 C. Paillard, S. Youssefi, G. Duprè, *The Explosive Decomposition of Chlorine Dioxide Behind Shock Wave - Dynamics of Reactive Systems Part II: Modeling and Heterogeneous Combustion*, Progr. Astronaut. Aeronaut. **105**, 394-406 (1986)

189 R.E. Mitchell, R.J. Kee, *A general-purpose computer code for predicting chemical kinetic behaviour behind incident and reflected shocks*, Sandia International Laboratories Report No. SAND82-8205, 1992

190 R.J. Kee., F.M. Rupley, J.A. Miller, CHEMKIN-II: *A Fortran Chemical Kinetics Package for the Analysis of Gas Phase Chemical Kinetics*, Sandia International Laboratories Report No. SAND89-8009B, 1993

191 F. Migliorini, S. De Iuliis, F. Cignoli, G. Zizak, *Comparison of soot volume fraction measurements performed with laser-induced incadescence and laser extinction at different wavelengths in a McKenna burner*, Elettroottica 2008

192 F. Migliorini, S. Mancarella, S. Bianchi, S. De Iuliis, F. Cignoli, G. Zizak, *Preliminary investigation on the influence of hydrogen addition in air/C_2H_4 premiixed flames,* Italian Section of the Combustion Institute **30** (2007)

193 U.O. Koylu, C.S. McEnally, D.E. Rosner, L.D. Pferfferle, *Simultaneous Measurements of Soot Volume Fraction and Particle Size / Microstructure in Flames Using a Thermophoretic Sampling Technique,* Combustion and Flame **110**, 494-507 (1997)

194 O. Mathieu, *Etude cinétique de la formation des particules de suie dans les conditions de fonctionnement des moteurs automobiles*, PhD thesis, Université d'Orléans 2006

195 O. Mathieu, N. Djebaïli-Caumeix, F. Douce, P. Manuelli and C.-E. Paillard, *Study of early soot formation from alkyl-aromatics fuels,* Proc. European Combustion Meeting, ECM2007, 2007

196 S. di Stasio, *Experiments on depolarized scattering to sense in situ the onset of early agglomeration between nano-size soot particles*, J. Quantitative Spectroscopy and Radiative Transfer **73**, 423-432 (2002).

197 N. Riefler, S. di Stasio, T. Wriedt, *Structural analysis of clusters using configurational and orientational averaging in light scattering analysis*, J. Quantitative Spectroscopy and Radiative Transfer **89**, 323-342 (2004)

198 S. di Stasio, A.G. Konstandopoulos, M.Kostoglou, *Cluster-cluster aggregation kinetics and primary particle growth of soot nanoparticles in flame by light scattering and numerical simulations*, J. Colloid and Interface Science **247**, 33-46 (2002)

NOMENCLATURE

a	primary particle radius
L, W	maximum projected length (L) and width (W) of an aggregate
$A_a, (R_a)$	aggregate projected area: $A_a = \pi R_a^2$
A_p	primary particle cross section
d_p	soot particle diamter
C_{VV}^P	scattering cross section of a single particle
C_{VV}^a	scattering cross section of an aggregate
K_{VV}	soot scattering coefficient
$K_{vv,pol}$	soot scattering coefficient for a polydisperse ensemble of aggregates
N_p	number of primary particles per unit volume
N_a	number of aggregates per unit volume
N	number of particles per aggregate
f_v	soot volume fraction
K_{abs}	absorption coefficient
$K_{abs,pol}$	absorption coefficient for a polydisperse ensemble of aggregates
K_{ext}	extinction coefficient
$K = 2\pi/\lambda_{scatt}$	wave vector
q	scattering wave vector
$x_p = \pi dp/\lambda_{scatt}$	particle size parameter
$F(m)$	function of the soot refractive index m
$E(m)$	function of soot refractive index m
$m = n + ik$	soot refractive index: n real and k imaginary part
$S(qR_g)$	optical structure factor
$I_{vv}(\theta)$	vertically polarized scattering signal
$I_{VV}^p(\theta)$	vertically polarized scattering signal for a polydisperse ensemble of aggregates
$p(d_p)$	probability distribution function for primary particles with different size

d_{pm}	geometric mean diameter of the $p(dp)$ distribution
σ_g	standard deviation of the $p(dp)$ distribution
dp_{mn}	generalized mean diameter or moment ratio of the $p(d_p)$
$\overline{d_p}$	mean diameter, equals to first order moment, dp_{10}
$R_{vv}(\theta)$	dissymmetry ratio
TR_λ	monochromatic transmittance
η	instrumental factor
$p(N)$	probability distribution function, giving the fraction of aggregates with a number N of primary particles.
N_m	geometric mean of the primary particles per aggregate
σ	standard deviation of $p(N)$
$\overline{m_q}$	qth moment of the probability distribution function: $\overline{m_q} = \int_0^\infty N^q p(N)dN$
R_g	radius of gyration
D_f	fractal dimension
K_f	fractal prefactor
τ_{ind}	induction delay time
K_g	soot growth rate
Λ	particle thermal conductivity toward the surrounding gases
ΔH_v	the heat of vaporization of carbon
W_s	is the molecular weight of carbon vapor species
dM/dt	the mass vaporization rate
c_s	the specific heat of carbon
ρ	soot density
U_v	thermal velocity
N_{av}	Avogadro's number

APPENDIX

Measurement of the scattering signal from a modulated one at 40KHz

The scattering signal is derived from the vertically polarized signal modulated at 40 kHz collected with the oscilloscope as follows.

The signal to be processed is read and plotted

:=   💾

F:\..\C3scatt16000000.xls

$i := 0 .. 250000$

$j := 0 .. 250000$
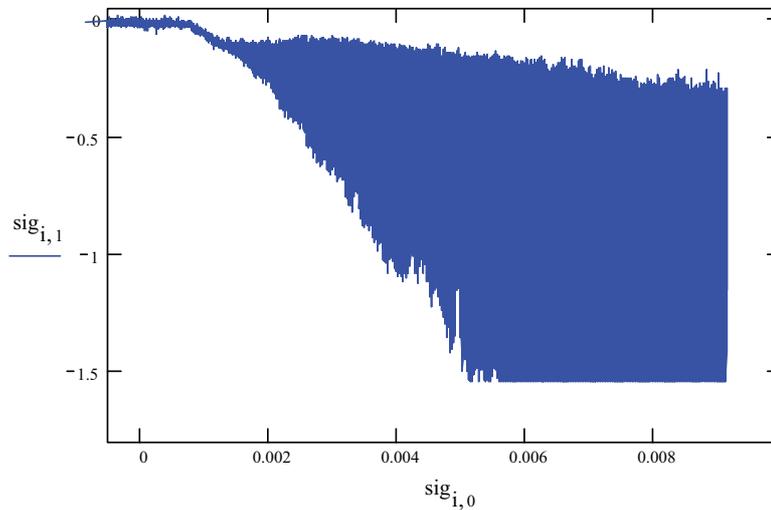
The signal presents the following characteristics:

- 10,000 sampling
- measurement time: 1 ms
- modulation at 40 kHZ
- # cylces: 400

Then the calculation is applying:

(a) Evaluation of the lower envelop

(b) Evaluation of the upper envelop

(c) Evaluation of the scattering signal (from the difference of the previous ones)

(d) Backgroungsubtraction

(a) $\quad$ lim_min(f) :=

$\Big|$ $L \leftarrow \text{trunc}\left(\dfrac{\text{rows}(f)}{40000 \cdot 0.01}\right)$

$L1 \leftarrow 40000 \cdot 0.01$

for $i \in 0 .. L1 - 1$

$\quad\Big|$ for $j \in 0 .. L - 1$

$\qquad\Big|$ $s_j \leftarrow f_{j + L \cdot i, 1}$

$\qquad\Big|$ $r_j \leftarrow f_{j, 0}$

$\quad$ $mm \leftarrow \min(s)$

$\quad$ $mm1 \leftarrow \max(s)$

$\quad$ $h \leftarrow 0$

$\quad$ while $s_h < mm1$

$\qquad$ $h \leftarrow h + 1$

$\quad$ $hfin \leftarrow h$

$\quad$ $sh_i \leftarrow \dfrac{\displaystyle\sum_{g=0}^{1} f_{hfin + L \cdot i + g, 1}}{2}$

$\quad$ $k \leftarrow 0$

$\quad$ while $s_k > mm$

$\qquad$ $k \leftarrow k + 1$

$\quad$ $kfin \leftarrow k$

$\quad$ $ss_i \leftarrow f_{kfin, 0}$

$\quad$ $sk_i \leftarrow \dfrac{\displaystyle\sum_{g=0}^{1} f_{kfin + L \cdot i + g, 1}}{2}$

$\quad$ $res_{L1 - 1 - i, 1} \leftarrow sh_i$

for $i \in 0 .. 399$

$\quad$ $res_{L1 - 1 - i, 0} \leftarrow ss_0 - \dfrac{1}{40000} \cdot i$

res

(b) $\text{lim\_max}(f) :=$

$$L \leftarrow \text{trunc}\left(\frac{\text{rows}(f)}{40000 \cdot 0.01}\right)$$

$L1 \leftarrow 40000 \cdot 0.01$

$\text{for } i \in 0..\, L1 - 1$

$\quad \text{for } j \in 0..\, L - 1$

$\qquad s_j \leftarrow f_{j + L \cdot i,\, 1}$

$\qquad r_j \leftarrow f_{j,\, 0}$

$\quad mm \leftarrow \min(s)$

$\quad mm1 \leftarrow \max(s)$

$\quad h \leftarrow 0$

$\quad \text{while } s_h < mm1$

$\qquad h \leftarrow h + 1$

$\quad hfin \leftarrow h$

$$sh_i \leftarrow \frac{\displaystyle\sum_{g=0}^{1} f_{hfin + L \cdot i + g,\, 1}}{2}$$

$\quad k \leftarrow 0$

$\quad \text{while } s_k > mm$

$\qquad k \leftarrow k + 1$

$\quad kfin \leftarrow k$

$\quad ss_i \leftarrow f_{kfin,\, 0}$

$$sk_i \leftarrow \frac{\displaystyle\sum_{g=0}^{1} f_{kfin + L \cdot i + g,\, 1}}{2}$$

$\quad res_{L1 - 1 - i,\, 1} \leftarrow sk_i$

$\text{for } i \in 0..\, 399$

$\quad res_{L1 - 1 - i,\, 0} \leftarrow ss_0 - \frac{1}{40000} \cdot i$

res

(c) $\text{rest}(f) := $

$\left|\begin{array}{l} L \leftarrow \text{trunc}\left(\dfrac{\text{rows}(f)}{40000 \cdot 0.01}\right) \\[2mm] L1 \leftarrow 40000 \cdot 0.01 \\[2mm] \text{for } i \in 0 .. \text{cols}(f) - 1 \\[1mm] \quad \text{for } j \in 0 .. \text{rows}(f) - 1 \\[1mm] \qquad nf_{j,i} \leftarrow f_{\text{rows}(f) - j - 1, i} \\[2mm] \text{for } i \in 0 .. L1 - 1 \\[1mm] \quad \left|\begin{array}{l} \text{for } j \in 0 .. L - 1 \\[1mm] \quad s_j \leftarrow nf_{j + L \cdot i, 1} \\[2mm] mm \leftarrow \min(s) \\[1mm] mm1 \leftarrow \max(s) \\[1mm] h \leftarrow 0 \\[1mm] \text{while } s_h < mm1 \\[1mm] \quad h \leftarrow h + 1 \\[1mm] hfin \leftarrow h \\[3mm] sh_i \leftarrow \dfrac{\displaystyle\sum_{g=0}^{1} nf_{hfin + L \cdot i + g, 1}}{2} \\[4mm] k \leftarrow 0 \\[1mm] \text{while } s_k > mm \\[1mm] \quad k \leftarrow k + 1 \\[1mm] kfin \leftarrow k \\[1mm] ss_i \leftarrow nf_{kfin, 0} \\[3mm] sk_i \leftarrow \dfrac{\displaystyle\sum_{g=0}^{1} nf_{kfin + L \cdot i + g, 1}}{2} \\[4mm] res_{L1 - 1 - i, 1} \leftarrow sh_i - sk_i \end{array}\right. \\[2mm] \text{for } i \in 0 .. 399 \\[1mm] \quad res_{L1 - 1 - i, 0} \leftarrow ss_0 - \dfrac{1}{40000} \cdot i \\[2mm] res \end{array}\right.$

(d) $\quad$ sobc(f, val) := $\quad\left|\begin{array}{l}\text{for } i \in 0..1\end{array}\right.$

$$\text{for } i \in 0..1$$
$$\quad \text{for } j \in 0..\text{rows}(f) - 1$$
$$\quad\quad \left|\begin{array}{l} r_{j,i} \leftarrow f_{j,i} \\ res_{j,i} \leftarrow f_{j,i} \end{array}\right.$$
$$\quad \text{for } m \in 0..0 + \text{val}$$
$$\quad\quad avg_m \leftarrow \left(r_{m,i}\right)$$
$$av \leftarrow \text{mean}(avg)$$
$$\text{for } k \in 0..\text{rows}(f) - 1$$
$$\quad res_{k,1} \leftarrow r_{k,1} - av$$
$$\text{for } e \in 0..1$$
$$\quad \text{for } h \in 0..\text{rows}(f) - 1$$
$$\quad\quad rres_{h,e} \leftarrow res_{h,e}$$
$$rres$$

ris := rest(sig)
ris_back := sobc(ris, 30)

The signal is then plotted and saved.

C:\..\scattering_signal

ris_back

205
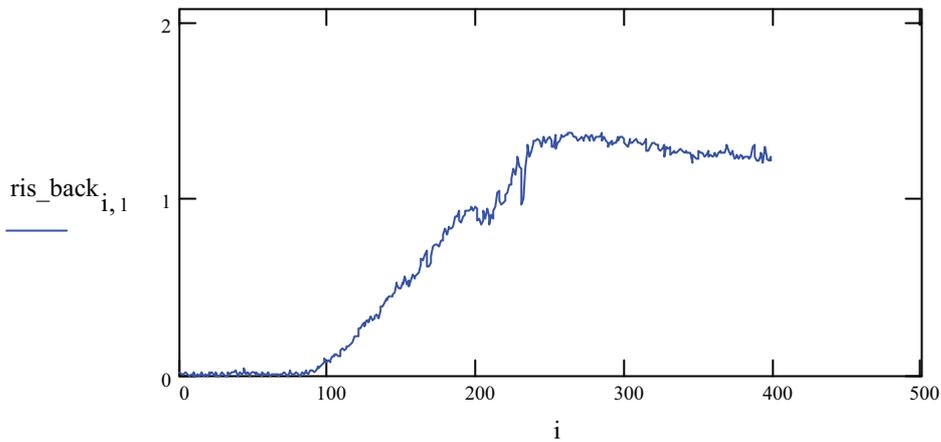
Pubblications on ISI journals

1. S. De Iuliis, F. Migliorini, F. Cignoli, G. Zizak, *Peak soot temperature in laser-induced incandescence measurements*, Applied Physics B, 397-402 (2006)

2. F. Migliorini, S.De Iuliis, F. Cignoli, G. Zizak, *Absorption correction of two color laser-induced incandescence signals for soot volume fraction measurements*, Applied Optics **45**, 7706 (2006).

3. S. De Iuliis, F. Migliorini, F. Cignoli, G. Zizak, "*2D soot volume fraction imaging in an ethylene diffusion flame by two-color laser-induced incandescence (2C-LII) technique and comparison with results from other optical technique*", Proceedings of the Symposium (Inter.) on Combsution, The Combustion Institute **31,** pag. 869-876 (2007).

4. F. Migliorini, S. De Iuliis, F. Cignoli, G. Zizak, "*How flat is the rich premixed flame produced by your McKenna burner?*", Combustion and Flame **153**, 384-393 (2008)

5. S. De Iuliis, N. Chaumeix, M. Idir, C-E. Paillard, *Scattering-extinction measurements of soot formation in a shock tube*, Experimental Thermal and Fluid Science **32 (7)** 1354-1362 (2008)

6. S. Maffi, F. Cignoli, C. Bellomunno, S. De Iuliis, G. Zizak, *Spectral effects in laser induced incandescence application to flame-made titania nanoparticles*, Spectrochimica Acta B **63,** 202-209 (2008)

7. F. Migliorini, S. De Iuliis, S. Maffi, F. Cignoli, G.Zizak, *Investigation on the influence of soot size on prompt LII signals in flames*, Applied Physics B **96 (4)**, 637-643 (2009)

Contributions to Conferences

1. C. Bellomunno, F. Cignoli, S. De Iuliis, S. Maffi, G. Zizak, *Investigation of the Synthesis of Titania, Silica and Vanadia Nanoparticles in a Hybrid Flame Reactor,* Italian Section of the Combustion Institute, Pisa (2006)

2. F. Migliorini, S. De Iuliis, L. Leone, F. Cignoli, G. Zizak, *Soot volume fraction measurements in methane/hydrogen diffusion flames,* Italian Section of the Combustion Institute, Pisa (2006)

3. F. Liu, F. Migliorini, F. Cignoli, S. De Iuliis, G. Zizak, "*Effect of Hydrogen and helium addition to fuel on soot formation in axisymmetric coflow laminar methane-air diffusion flame*", Proceeding of HT2007, ASME-JSME Thermal Engineering Summer Heat Transfer Conference, July 8-12 2007 Vancouver, Canada.

4. F. Migliorini, S. Mancarella, S. Bianchi, S. De Iuliis, F. Cignoli, G. Zizak, "*Preliminary Investigation on the Influence of Hydrogen Addition in Air/C$_2$H$_4$ Premixed Flames*", Proceedings of the 30th Meeting of the Italian Section of the Combustion Institutte, Ischia 2007.

5. F. Migliorini, S. De Iuliis, F. Cignoli, G. Zizak, "*Non-uniform distribution in a "flat" rich premixed ethylene-air flame produced by a McKenna burner*", Proceedings of the European Combustion Meeting, Creta 2007.

6. S. De Iuliis, N. Chaumeix, C-E. Paillard, "*Scattering-extinction measurements of soot formation in a shock tube*", Proceedings of the Mediterranean Combustion Meeting, Tunisia 2007.

7. F. Cignoli, S. Maffi, C. Bellomunno, S. De Iuliis, G. Zizak, "*LII experiments in a hybrid flame for TiO$_2$ Synthesi*s", Proceedings of the Mediterranean Combustion Meeting, Tunisia 2007

8. F. Cignoli, S. De Iuliis, F. Migliorini, G. Zizak, "*2D soot volume fraction measurements in a ethylene diffusion flame by two-dimensional two-color laser-induced incandescence technique*", Combustion Generated Nanoparticles Meeting, ETH Zurigo 2007.

9. S. De Iuliis, N. Chaumeix, M. Idir, J-C Paillard, *Effect of hydrogen addition on soot formation in a shock tube*, GDRE meeing, Milano (2008)

10. F. Migliorni, S. De Iuliis, F. Cignoli, G. Zizak, M. Sirignano, A. D'Anna, *Effect of Hydrogen Addition on Soot Formation in Rich Premixed Ethylene/Air Flames,* 31° Incontro Annuale della Sezione Italiana del Combustion Institute, Torino, giugno 2008.

11. S. De Iuliis, N. Chaumeix, M. Idir, J-C. Paillard, *Effect of Hydrogen Addition on Soot Formation in a Shock Tube*, GDRE Meeting, Torino, giugno 2008.

12. F. Migliorini, S. De Iuliis, F. Cignoli, G. Zizak, *Comparison of Soot Volume Fraction Measurements performed with Laser-Induced Incandescence and Laser Extinction at different wavelengths in a McKenna burner*, Congresso di Elettroottica, Milano, Aprile 2008.

13. F. Migliorini, S. De Iuliis, F. Cignoli, G. Zizak, M. Sirignano, A. D'Anna, *Effect of H$_2$ Addition on Soot and Nanoparticles Formation for Rich Premixed Ethylene/Air Flames*, Simposio Europeo del Combustion Institute, Aprile 2009

Silvana DE IULIIS

Etude de la vitesse de formation des suies à partir de l'éthylène en présence d'hydrogène par les méthodes du tube à choc et du brûleur au moyen de différentes techniques optiques

Cette thèse a pour objet d'améliorer la connaissance du mécanisme de formation de suie. Deux méthodes ont été utilisées pour produire des particules de suie dans des conditions contrôlées : le brûleur à flamme plat où les particules se forment par combustion de mélanges d'éthylène/air riches et le tube à choc dans lequel la suie est produite par pyrolyse de C_2H_4 à haute pression (5 bar) et dans un large domaine de température (1850-2100 K). Ces deux systèmes ont été équipés avec un dispositif original de diffusion laser à trois angles couplé à l'extinction laser pour suivre la croissance de particules, identifier les différentes étapes de leur mécanisme de formation et en déduire l'évolution de la fraction volumique des suies, leur rendement, leur structure et leur morphologie. Dans la flamme, l'addition de H_2 entraîne une réduction globale de la concentration des suies, de leur diamètre moyen des particules et leurs agglomérats, de la densité en nombre de particules. Dans le tube à choc, on n'observe pas de dépendance significative du délai d'induction à la formation des particules par addition de H_2. La courbe de rendement en suie en fonction de la température présente la même forme avec et sans hydrogène mais le rendement maximal est fortement abaissé en présence d'hydrogène pour une concentration initiale fixée en atomes de carbone. Le rôle de l'hydrogène sur la croissance des particules et les caractéristiques des suies est discuté en comparant les résultats obtenus dans le cas de la flamme de prémélange et derrière l'onde de choc réfléchie respectivement.

Mots clés : Formation des suies, Ethylène, Hydrogène, Diffusion laser à trois angles, Extinction laser,

A Shock Tube and Burner Study on Soot Growth Rate from Ethylene in Presence of Hydrogen by Different Optical Diagnostics

Abstract : The aim of this thesis was to improve the knowledge of the soot formation mechanism. Two methods have been used to produce soot particles in controlled conditions: flat flame burner where particles were formed by combustion of rich ethylene/air mixtures and shock tube in which soot was produced by C_2H_4 pyrolysis at high pressure (5 bar) and in a large range of temperature (1850-2100 K). Both systems have been equipped with a novel technique of scattering at three angles coupled with laser extinction device in order to follow particles growth, to identify different steps of their formation mechanism and to deduce soot volume fraction evolution, soot yield, structure and morphology. In the flame, an overall reduction of soot concentration, mean volume diameter, particles number density was observed when hydrogen was added to combustible mixture. In shock tube, induction delay time of particle formation does not depend on H_2 addition. The typical curves of soot yield versus temperature present the same shape with and without H_2 ; the maximum yield occurs at the same temperature (near 2000 K) but the yield is strongly lower in presence of H_2 for a given C atom concentration. The role of hydrogen on particles growth rate and soot characteristics was discussed by comparing the results obtained respectively in the premixed flames and behind reflected shock waves.

Keywords : Soot formation, ethylene, hydrogen, laser extinction, laser scattering at three angles

ICARE – CNRS– UPR 4030
1c Av. de la Recherche Scientifique,
45071 ORLEANS CEDEX 2

Politecnico di Milano
Dip. Energia, Via Lambruschini, 4
20156 Milano, Italy

POLITECNICO
DI MILANO